The population of close double white dwarf binary stars

by

James Munday

Thesis

Submitted to the University of Warwick

for the degree of

Doctor of Philosophy

Department of Physics

June 2025

THE UNIVERSITY OF
WARWICK

Contents

Acknowledgments

I am forever grateful for the help of all of my peers that have assisted me throughout this journey both scientifically and mentally. My incredible mentors were Dr. Ingrid Pelisoli and Prof. Pier-Emmanuel Tremblay, who have supported me with all projects, ideas and gallivants over the last 3 years with no hesitation. Without their guidance, I would not be the scientist I am today on the cusp of obtaining a Doctorate of Philosophy qualification and much of this amazing work has revolved around bouncing ideas between us. Words cannot accurately describe how thankful I am to work with and have met them both.

Alongside my studies, I spent a year living in La Palma teaching the Isaac Newton Telescope to visiting observers. I wish to thank Ovidiu Vaduvescu and Lucía Suarez for their sharing of telescope expertise during these times. I also wish to thank Dr. David Jones for his continued advice and support both professionally and personally. The encouragement and guidance that he has given over the last years has gone above and beyond what I could ever ask and I am incredibly grateful for him being a part of my journey.

Near the beginning of my PhD, I had a distressing period of time for a whole host of reasons and I want to thank the support of Prof. Peter Wheatley, Prof. Elizabeth Stanway and Dr. James McCormac with all my heart. I also appreciate the introduction to the field and topics of my PhD research by the late Prof. Thomas Marsh.

A PhD is not just about the work but the experience and impact it has on life. In that regard, I wish to say how grateful I am to have met my PhD brothers Dr. Gareth Jones and Dr. Jorge Fernández Fernández and for the ups, downs, laughs and rants throughout. It was amazing to have each other by our sides. In the same sense, a few to mention from the extensive list of wonderful people I have met in this little world of astronomy: Harry Dawson, Viktoria Pinter, Joonas Viuho and Dario Gonzalez Picos.

Declarations

I submit this thesis to the University of Warwick graduate school for the degree of Doctor of Philosophy. This thesis was written by me and has not been submitted to any other institution.
Much of this thesis includes material from published work that I wrote in academic journals, being:

- J. Munday et al. “Two decades of optical timing of the shortest-period binary star system HM Cancri". In: MNRAS (Feb. 2023), arXiv: 2211.09834
- J. Munday et al. "An Eclipsing 47 minute Double White Dwarf Binary at 400 pc". In MNRAS (Aug. 2023), arXiv: 2308.00036
- J. Munday et al. "The DBL Survey I: discovery of 34 double-lined double white dwarf binaries". In MNRAS (Aug. 2024), arXiv: 2407.02594
- J. Munday et al. “There is a super-Chandrasekhar mass type Ia supernova progenitor located 49 pc away that will detonate in 23 Gyr". In Nature Astronomy (June 2025), arXiv: 2504.04522
- J. Munday et al. “The DBL Survey II: towards a mass-period distribution of double white dwarf binaries". In: MNRAS (Aug. 2025), arXiv: arXiv:2507.14123

There will be some overlap with the following papers as I was an integral part of the study carrying out some of the outlined methodology, being:

- Amaral, Munday et al. "The double low-mass white dwarf eclipsing binary system J2102-4145 and its possible evolution". In A&A (May 2024), arXiv: 2402.10159
- Budaj et al. "A swarm of dusty objects in orbit around the central star of planetary nebula WeSb 1”. In Nature Astronomy (March 2025)

Abstract

Close to 40% of all stars are locked in the form of a binary pairing. By sheer number and the exotic products that come from binary star evolution, they are fascinating objects with many unanswered questions regarding their lifetimes and their effect on Galactic evolution. In this doctoral thesis, I present much undertaken research in the field of double white dwarf binary star systems, which are some of the end products of binary evolutionary. They are vital in addressing the evolutionary conditions that made these objects and in unravelling the phenomena that occur close to or during merger. A particular focus is set on compact (having undergone mass transfer stages) or ultra-compact (also with an orbital period close to or less than one hour) systems, having pairs of stars that orbit each other on the timescale of days to mere minutes.

The first and second chapter set the tone for the thesis. In Chapter 1, I introduce white dwarf binaries as a field and the essential physical components, while in Chapter 2 I outline key concepts used to analyse observational datasets. Chapter 3 focuses on my research of HM Cancri, the shortest period binary star system known to date, and the now extremely precise measurement of its orbital decay. In Chapter 4, I present the shortest-period detached source ever discovered through the Transiting Exoplanet Survey Satellite. Chapters 5, 6 and 7 are based on the double-lined double white dwarf (DBL) survey that I initiated, which crucially uncovered a population of high-mass double white dwarfs that were hiding in plain sight, including the most massive double white dwarf discovered to date. Lastly, in Chapter 8, I conclude the research presented in my thesis and address the prospects for the future of the field, including the upcoming era of space-based gravitational wave detectors.

Abbreviations

ADU	Analogue to Digital Units
BJD	Barycentric Julian Date
BMJD	Barycentric Modified Julian Date
CCD	Charge-Coupled Devices
CMOS	Complementary Metal Oxide Semiconductor
CV	Cataclysmic Variable
DBL	Double-lined double white dwarf
DWD	Double White Dwarf
ELM	Extremely Low Mass
FIES	FIbre-fed Echelle Spectrograph
GMOS	Gemini Multi-Object Spectrograph
GTC	Gran Telescopio Canarias
HJD	Heliocentric Julian Date
HR	Hertzsprung-Russell
INT	Isaac Newton Telescope
ISIS	Intermediate-dispersion Spectrograph and Imaging System

JD	Julian Date
LISA	Laser Interferometer Space Antenna
LTE	Local Thermal Equilibrium
MCMC	Markov Chain Monte Carlo
MESA	Modules for Experiments in Stellar Astrophysics
MS	Main Sequence
MTRR	Mass-Temperature-Radius Relationship
NLTE	Non-Local Thermal Equilibrium
NOT	Nordic Optical Telescope
NTT	New Technology Telescope
PHOEBE	PHysics Of Eclipsing BinariEs
PSF	Point Spread Function
RV	Radial Velocity
SAAO	South African Astronomical Observatory
SNR	Signal-to-Noise Ratio
TAI	International Atomic Time
TDB	Barycentric Dynamical Time
TESS	Transiting Exoplanet Survey Satellite
TNG	Telescopio Nazionale Galileo
TNO	Thai National Observatory
UTC	Coordinated Universal Time

UVES	UV-Visual Echelle Spectrograph
VLT	Very Large Telescope
WD	White Dwarf
WD-BASS	White Dwarf Binary And Single Star
WHT	William Herschel Telescope
ZTF	Zwicky Transient Facility

Chapter 1

Introduction

1.1 Properties of white dwarfs

1.1.1 Formation

A star will begin its life in a molecular cloud that exceeds the Jeans mass [the critical mass for gravity to dominate; Jeans, 1902], causing the gravitational collapse of material into a protostar. Continued gravitational collapse increases the core temperature of the material to around 10^7 K where nuclear fusion is initiated and a zero-age main sequence star is born when the mass of the protostar is above approximately $0.08\,\mathrm{M}_{\odot}$, otherwise the protostar will become a brown dwarf. For single, isolated stars with a total mass up to approximately 8–10 $\mathrm{M}_{\odot}$, prolonged periods of core hydrogen fusion, followed by core helium (if the initial core mass is above $\approx 0.45\mathrm{M}_{\odot}$) and shell hydrogen fusion progressively push the star to traverse the main sequence branch, the red giant branch and the thermally pulsating asymptotic giant branch, with pulses induced from the turning off and on of hydrogen shell burning. In this environment, large convective winds cause the spewing of material into the interstellar medium becoming unbound from the host star, whereby it is briefly photoionised in the form of a planetary nebula. A hot, dense and exposed core remains in the form of a pre-white dwarf (pre-WD, alternatively named a post-asymptotic giant branch star) which slowly cools along the WD cooling sequence over the span of gigayears, where fusion ceases but the gravitational pressure is withstood by electron degeneracy pressure. This is the evolution for around 95–98% of all stars in the Milky Way. The less massive a main sequence star is, the longer it takes to evolve along the main sequence. Many stars that formed at the beginning of the Galaxy still have not had sufficient time to become WDs. In turn, this symbolises that WDs can only exist in our galactic neighbourhood with a mass of roughly $0.53\,\mathrm{M}_{\odot}$ or more through single star stellar evolution [Marsh et al., 1995; Cummings et al., 2018], corresponding to an initial star mass of about $0.8\,\mathrm{M}_{\odot}$.

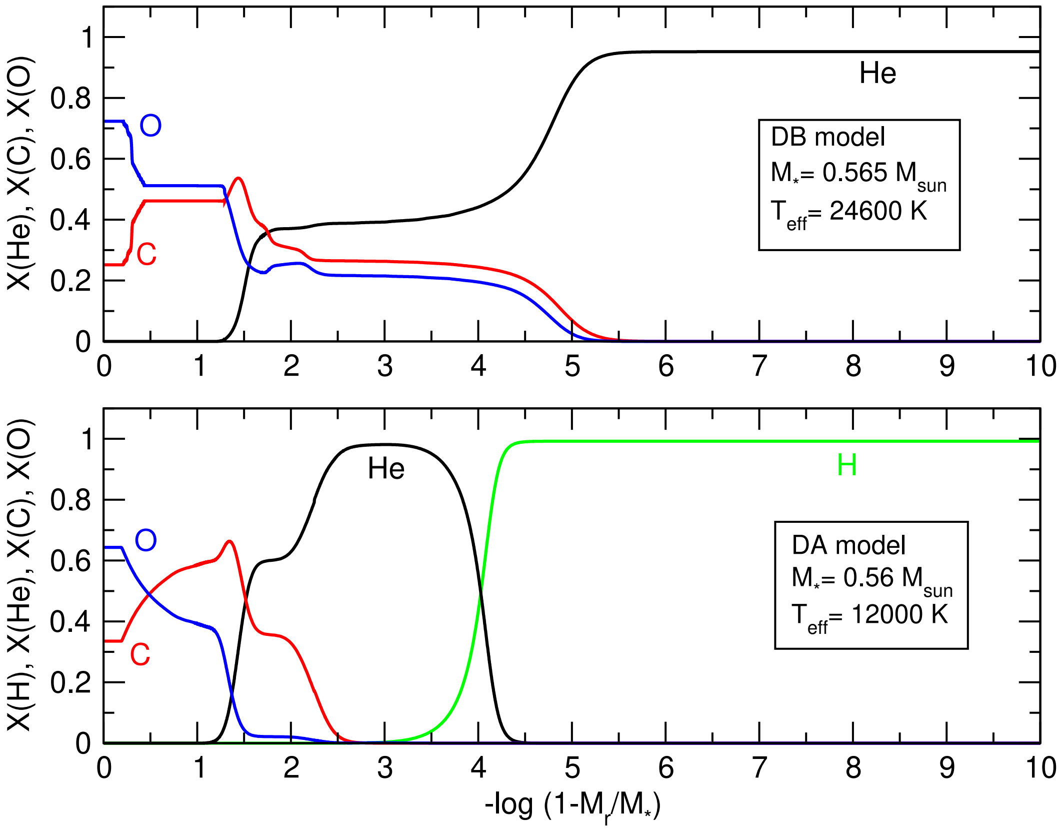

Figure 1.1: The internal structure of a hydrogen atmosphere (spectral type DA) and helium atmosphere (spectral type DB) WD for the labelled masses and effective temperatures. I draw particular attention to the logarithmic x-axis, since here the carbon-oxygen cores contain the vast majority of mass, while the envelopes are thin in radius. Figure presented in Althaus et al. [2010].

1.1.2 White dwarf structure

Before becoming a WD, where all fusion ceases, core nuclear fusion forms carbon and oxygen after sequential *pp*-chain, carbon-oxygen-nitrogen cycle and triple-alpha process nuclear fusion. For shell burning, gravitational settling naturally causes the heavy elements that are created to sink to the centre of the star, stratifying its structure. A graphical representation of the stratification is depicted in Fig. 1.1. The atmospheres of the stars are close to a pure mixture and the fact that the optical depth is so shallow in these high-density environments means that the photosphere solely encompasses the near-pure mixture close to the surface. Binary evolution, which will be spoken about further in Section 1.2, can strip the star envelope early, skipping any carbon/oxygen formation since the core temperature never rises high enough to the point where the cross section is significant, and with this a helium core WD with a hydrogen envelope can exist. There is a further case for initial star masses close to $8\,\mathrm{M}_\odot$ where it may be possible to form oxygen-neon or oxygen-neon-magnesium core white dwarfs, representing the densest environment.

1.1.3 The mass-radius relationship

An important characteristic of white dwarfs is their predictable radius because of their equation of state. Chandrasekhar [1931] considered an equation of state where the pressure, P is related to the density, ρ, by

$$P \propto \rho^{1+n} \tag{1.1}$$

with n the polytropic index. For relativistic electron gases, $n = 3$, and for non-relativistic gases, $n = 3/2$. In the fully degenerate, relativistic case, this in turn gives rise to a maximum mass of a WD before gravitational collapse, which Chandrasekhar 1931a discovered to be $0.91\,\mathrm{M}_\odot$ for a radius tending to zero. Chandrasekhar [1935] revised this concept and presented a full mass-radius relationship for WDs which is depicted in Fig. 1.2 and set a maximum WD mass of

$$M_3 = 5.728 M_\odot/\mu^2 \tag{1.2}$$

where the subscript represents a polytropic index of $n = 3$ and μ is the nucleon to electron ratio. For an ionised carbon-oxygen composition, $\mu = 2$, giving rise to the well-known Chandrasekhar mass limit of $M_{Ch} = 1.44\,\mathrm{M}_\odot$ at which gravitational collapse will occur as electron degeneracy pressure is overcome. These points rely on the assumptions of a zero-temperature (as an outward thermal pressure will relieve collapse) and a non-rotating star (which will allow for higher masses as rotation generates an outwards centrifugal force).

1.1.4 Spectral signatures

WDs can show varied atmospheric compositions and observationally they are distinguishable through their spectral features, as depicted in Fig. 1.3. As for the naming conventions, the initial D stands for degenerate and is common for all WD spectral types, DAs exhibit hydrogen absorption lines in their spectra, DBs have He I absorption present, DCs are featureless, DOs have He II absorption, DQs show signs of atomic or molecular carbon and DZs show metal lines that originate from metals in the star's atmosphere. Following these, there are the added letters at the end of each acronym being 'H' if Zeeman splitting is present, 'e' if there is emission on the respective line or 'P' for signatures of polarisation. In the case of a mix of lines, the choice of ordering very much depends on the interpretation of the author where one example naming system is for the spectral type with lines of larger equivalent width to appear first [Doyle et al., 2023].

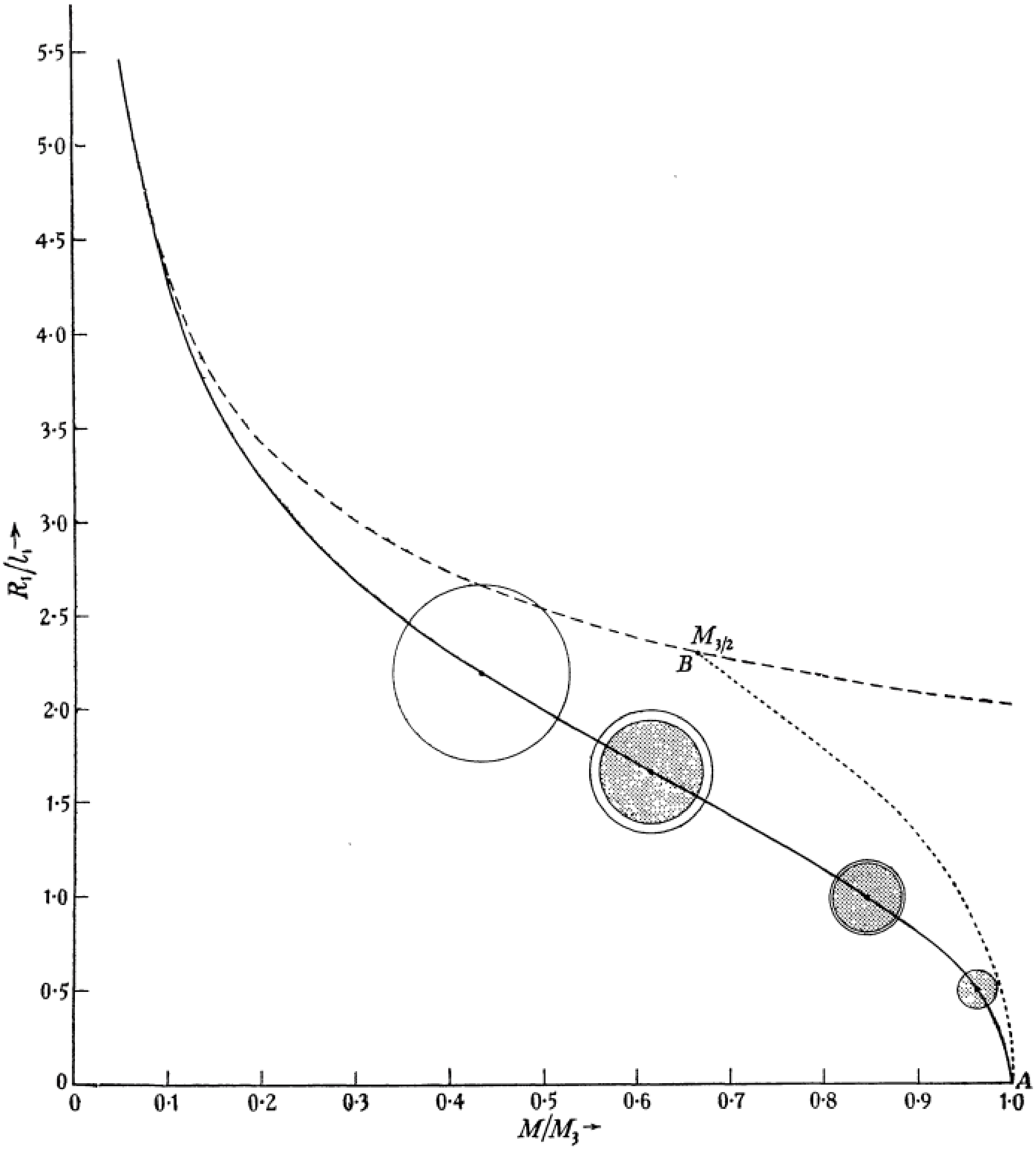

Figure 1.2: The mass-radius relationship for WDs presented by Chandrasekhar [1935]. To highlight, the smaller the mass of the WD for a given composition, the larger its radius, which is the opposite of the trend in younger stars. The solid line represents the relationship for a collapsed configuration. The dotted and dashed lines are for non-relativistic and fully relativistic polytropes, respectively. Smaller star masses have an asymptotic increase in radius.

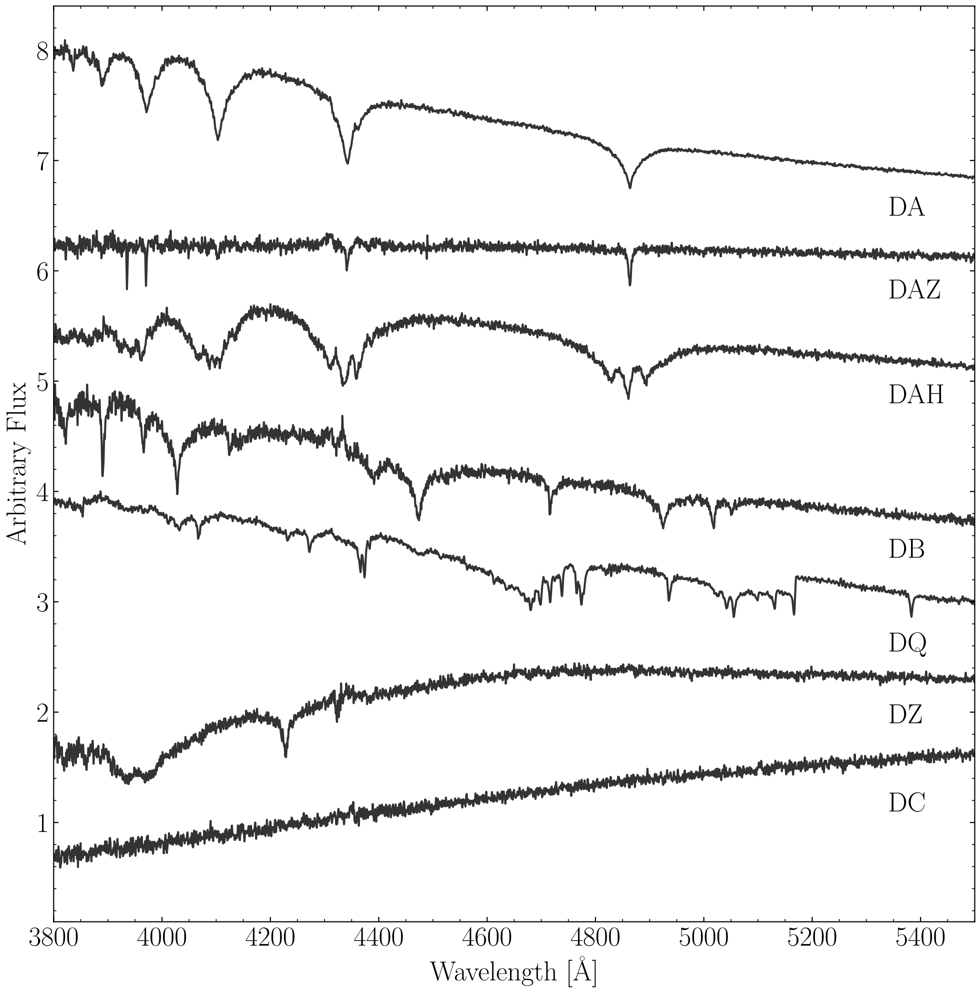

Figure 1.3: A depiction of all WD spectral types mentioned in Section 1.1.1. The spectra shown are from the Dark Energy Spectroscopic Instrument (DESI) and the plot is a modified version of that presented in Manser et al. [2024].

1.1.5 Population of white dwarfs

DAs constitute about 60% of WDs in volume complete populations [O'Brien et al., 2024], or about 80% in magnitude limited ones [Kilic et al., 2020b, 2024]. DBs and DOs exist due to a lost hydrogen envelope during its evolution, from hydrogen being mixed inside larger helium convection zones or from the presence of an extremely thin hydrogen layer. DCs exist from the cool effective temperature of a WD to the point where faint/no visible spectral lines are apparent (≈ 5000 K for hydrogen lines, $\approx 14\,000$ K for helium) and DQs are the result of convective dredge-up/mixing of carbon from deeper layers or from a lost hydrogen/helium layer. Additionally, the subclass of hot DQs are thought to originate from stellar mergers [Shen et al., 2023; Kawka et al., 2023; Kilic et al., 2023]. In hot DZ WDs, metal lines can arise from radiative levitation, while at temperatures of up to a couple of tens of thousand of Kelvin they can originate from the active accretion of orbiting material which may be due to e.g. asteroid scattering [Bonsor et al., 2011] or planet accretion [Gänsicke et al., 2019].

A few billion WDs are predicted to exist in the Galaxy [Napiwotzki, 2009]. Observationally, we have identified 1.3 million candidates thanks to the precise astrometry and photometry from the Gaia mission [Gentile Fusillo et al., 2021]. Out of those, around 50 000 are currently spectroscopically confirmed [Kepler et al., 2021; Manser et al., 2024]. In the local population of WDs, we are currently volume-complete out to a radius of 40 pc from the Sun [McCleery et al., 2020; O'Brien et al., 2023, 2024] with a sample of approximately 1000 stars. These and many other works have revealed a mass distribution of WDs with a median mass of approximately 0.6 $\mathrm{M}_\odot$ [e.g. Hollands et al., 2018; Kilic et al., 2020b], originating from an initial star mass of approximately 1.4 $\mathrm{M}_\odot$ [Cummings et al., 2018]. At the same time, subdivisions in the population exist that are not fully expected from single star stellar evolution. One of these is for larger mass WDs, where we see an abundance at approximately 0.8 $\mathrm{M}_\odot$ that is expected to arise from the remnant mergers of two low mass WDs, but may be explainable via star formation rates or differences in the treatment of the asymptotic giant branch phase in the WD's evolution [Kilic et al., 2020b]. Secondly, we see multiple cases of apparently single, low-mass WDs (< 0.45–$0.5\,\mathrm{M}_\odot$) that, as mentioned before, are physically unable to form from a single star evolutionary path given the age of the Galaxy[1]. The presence of a close companion can fathom such a low mass WD, where I will now describe how by introducing the formation of WD binaries.

---

[1] Note that in metal rich environments, the minimum mass of a WD can be pushed lower still [Romero et al., 2015], but accurate qualification of this circumstance is still an active area of research.

1.2 White dwarfs in binaries

1.2.1 Evolutionary scenarios

Approximately 30–40% of stars form in binary star systems [Raghavan et al., 2010] with a varying binary fraction depending on the stellar type/mass of the stars and on the metallicity [Sana and Evans, 2011; Chini et al., 2012]. The two stars typically form from the same circumbinary disc at the same time and with the same metallicity. At orbits of 100s of AUs (with the exact value dependant on the star masses), stars can evolve in near-completely isolated conditions, never coming into contact. Conversely, if the orbital separation is smaller, one star will naturally evolve faster than the other for different initial masses and will arrive at the giant branch first, at which point the outer shells of the star expand and the radius increases. As the stars formed close together, the faster evolving star reaches a point where it fills and overfills the region at which matter is bound to its gravitational field, namely the Roche lobe, and matter is accreted onto the companion through the first Lagrangian point [Kopal, 1959; Paczyński, 1971]. This event occurs for intermediate mass stars when the initial orbital period is $\lessapprox 100\,$days. The transfer of material is not perfectly conservative. Mass and with it angular momentum is lost from the binary, all the while material is still overflowing from the faster evolving star, causing the companion to grow in size. The next interactions depend on whether the mass transfer is stable or unstable, which is largely governed by the response of the donor to mass loss through the donor's core mass.

In the case of stable mass transfer, the mass-losing star continues getting stripped until the decrease in radius causes the star to stop overflowing (accelerating the evolution of the donor), the system detaches, and the binary carries on evolving. Though in the case of unstable mass transfer, the orbital separation continues to decrease, the Roche lobe of the accretor fills and hence overflowing material can no longer pass through the first Lagrangian point. The material instead surrounds the binary in what is referred to as a common envelope. Friction between the contact binary and the envelope due to a lack of co-rotation sends the binary into a rapid inspiral. To survive, a critical amount of angular momentum must be imparted into the common envelope to be able to eject it completely from the binary which is highly sensitive to the initial conditions [Toonen and Nelemans, 2013; Bours et al., 2013; Ivanova et al., 2013b] and, if the binary is able to do so, the abrupt ejection of mass will lead to a re-stabilised orbit at a wider than before but still compact separation. If the common envelope cannot be ejected, the stars will merge in the form of a luminous red nova [Ivanova et al., 2013a].

The general outline for compact binary evolution, including the timing of common envelope phases, is depicted in Fig. 1.4. The focus of this thesis is close double white dwarf (DWD) binaries, whose formation requires two phases of mass transfer to exist at

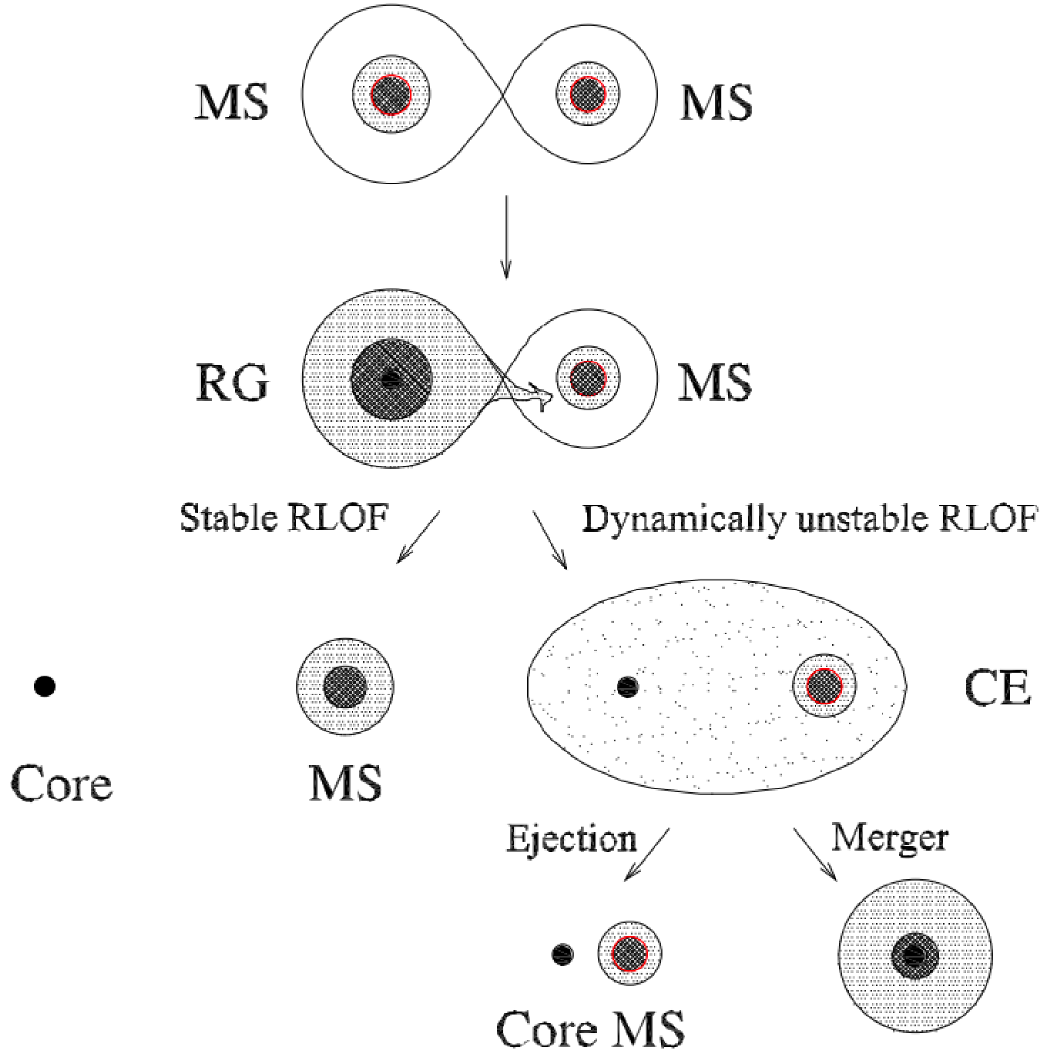

Figure 1.4: A graphic of compact binary star evolution from the start to the final stages of its lifetime, presented in Han et al. [2020]. MS refers to the main sequence phase, whereas RG represents a red giant.

an orbital separation on the scale of hundredths to tenths of astronomical units; at least one common envelope event must have occurred with both stars surviving. All of these channels contribute to the formation of DWDs, though some stronger than others, and we can divide the evolutionary scenarios into the following categories:

1) Roche lobe + common envelope: The more massive star is first to evolve, mass is transferred stably exposing the core of the donor. Mass transfer seizes and the star cools into a WD. The second star then evolves, initiates Roche lobe overflow and unstable mass transfer, a common envelope event occurs and the envelope is ejected, leaving behind the DWD. Such an ejection of mass allows low mass ($< 0.45\,\mathrm{M_\odot}$) WDs to exist [Iben and Tutukov, 1987; Bergeron et al., 1992; Marsh et al., 1995] even though a $0.8\,\mathrm{M_\odot}$ star, or a WD below $\approx 0.53\,\mathrm{M_\odot}$, would not be able to form through single star evolution within a Hubble time. The premature stripping of the star, leaving a hot and dense core, speeds up the stellar evolution, arriving at the WD phase early.

2) Common envelope + common envelope: The same as before, but there is unstable mass transfer in the first phase and two common envelopes occur. The Roche lobe + common envelope and the common envelope + common envelope evolutionary channels are dominant in the formation of the population of DWDs [Han, 1998; Nelemans et al., 2001c].

3) Common envelope + Roche lobe: The first phase of mass transfer is unstable leading to a common envelope. The binary restabilises at a larger orbit and the second star evolves and the binary undergoes stable mass transfer. This is an evolutionary path, though we can tweak it by adding a further nuance that Roche lobe overflow in the second mass transfer phase happens relatively soon after the common envelope phase. The star has not had long to continue its typical evolution and the core mass is relatively small ($<0.3\,\mathrm{M_\odot}$). Here, dynamo activity in the second star induced from binary interaction introduces a magnetic field and magnetic braking becomes the dominant cause of the orbital separation decreasing further (see Section 1.2.2). This tends to be the driving factor in bringing the stars into contact for orbital periods between approximately 4–24 hrs. Roche lobe overflow now occurs in the second star, shredding the outer layers and leaving behind an exposed core. This is the evolutionary path in which the majority of binaries with an extremely low mass WD form [Li et al., 2019].

4) Roche lobe + Roche lobe: This route to form DWD binaries is relevant for systems that began on wider orbits [separations of a couple of astronomical units, see Korol et al., 2022b, for examples]. These systems are difficult to identify, but are possible through astrometric deviations to the centre of light for non-equally luminous systems.

5) No mass transfer: stars evolve practically as if they were isolated. These are very wide systems with periods of hundreds of days, possible to be resolved or detected through common proper motion pairs [El-Badry and Rix, 2018; El-Badry et al., 2021a]. That said, recent work has hinted at systematic difference in the cooling age of wide DWDs compared to single star evolutionary tracks [Heintz et al., 2022, 2024], but the extent of the effects of a wide companion on its partner remains somewhat unclear or if the state of these DWD systems comes from an earlier merger event.

Normally, the second formed WD has a shorter cooling age, which is to say that in a system with two WDs of identical mass and composition, the hotter WD is the younger one. This is a natural expectation since it more recently donated material to the accretor, exposing the inner layers of the star. Given the series of mass transfer events, one can expect the second formed WD to be less massive also. There is a special but significant case where this perception can be deceiving. Picture a binary where the first mass transfer phase is stable through the Roche lobe situation. The donor gets stripped while in the Hertzsprung gap to become a low mass helium star of around 0.5–0.8 $\mathrm{M}_\odot$ and has a long cooling time on the order of 10^8 yr. The second star transfers mass onto this low-mass helium star unstably and we get a common envelope (scenario #1) that is expelled, the orbit restabilises, and then we get a third mass transfer phase to leave behind an exposed core that cools into a WD. The second star here has formed a WD before the helium star has been able to evolve to a WD itself, presenting an apparent mass inversion or reversed set of formation events. This evolutionary scenario was discussed in [Toonen et al., 2012], including example starting masses and separations of the two stars needed, and permits a hotter and more massive WD.

1.2.2 Orbital angular momentum transfer

I will now introduce the orbital angular momentum transfer mechanisms at play which lead to the aforementioned events and describe the orbital trajectory of a DWD binary. The rate of change of orbital angular momentum transfer in a binary can be modelled as

$$\dot{J}_{\mathrm{orb}} = \dot{J}_{\mathrm{gr}} + \dot{J}_{\mathrm{ml}} + \dot{J}_{\mathrm{mb}} + \dot{J}_{\mathrm{ls}} + \dot{J}_{\mathrm{di}} \tag{1.3}$$

With the J's here representing the angular momentum and J_{orb} being that of the orbit, J_{ml} being that due to mass loss, J_{gr} due to gravitational wave radiation, J_{mb} due to magnetic braking, J_{ls} due to spin-orbit coupling (tidal heating) and J_{di} due to direct impact accretion. Explaining these terms in order:

Magnetic braking

In the binary evolution phase when one star is a WD and the other a main sequence star, magnetic braking is the primary cause of orbital decay due to gradual orbital angular momentum loss[2]. Here, a magnetic main sequence star has an outward-flowing stellar wind. Charged particles in the stellar wind follow the magnetic field lines and become accelerated, but being in a compact binary become trapped and dragged in a co-rotating orbit. This carries away angular momentum from one of the stars, slowing down its rotation. The implication on the binary is that orbital angular momentum is spent in re-synchronising the spin of the main sequence star with the orbit [spinning it up, Zahn, 1977; Verbunt and Hut, 1983] and ultimately drives orbital decay. Eventually, the stars come into contact again, initiating mass transfer, to form a cataclysmic variable (CV) – a system where the WD accretes mass from its main sequence (or slightly evolved) companion. Following the prescription of Verbunt and Zwaan [1981]; Rappaport et al. [1983],

$$\dot{J}_{\rm mb} = -3.8 \times 10^{-30} M_{\rm MS} R_{\odot}^{4} \left(\frac{R_{\rm MS}}{R_{\odot}}\right)^{\gamma} \left(\frac{2\pi}{P_{\rm orb}}\right)^{3} \tag{1.4}$$

where in CV evolution, $\gamma = 2$ is often used [see e.g. Schreiber and Gänsicke, 2003]. When the period has shrunk to approximately 3 hours, magnetic braking ceases from the donor becoming fully convective. The absence of magnetic braking causes the stars to detach [Knigge et al., 2011], creating an apparent 'period gap' between orbital periods of 2–3 hours. Gravitational wave radiation is then the leading factor that brings the two stars back together.

In DWD binaries on the other hand, which come from a WD plus red giant branch or asymptotic giant branch star that overflows onto the WD, observations tell us that practically no compact systems in the Galaxy are magnetic. There is one exception [NLTT 12758 Kawka et al., 2017] that is the only magnetic DWD, but such a system has been proposed to be extremely rare [Schreiber et al., 2022], supported by magnetic fields expected to dissipate in an astrophysically short timescale for recently formed WDs [before any potential reappearance as the white dwarf ages Bagnulo and Landstreet, 2022; Camisassa et al., 2024]. Hence, magnetic braking has a smaller, but non-negligible, effect on the evolution towards becoming and after creation of a DWD binary. One of the multiple CV evolutionary paths has however been proposed as a means to form AM CVn binaries with helium donor stars [El-Badry et al., 2021b].

---

[2] While still the case, I note the recent study of El-Badry et al. [2022] who find observational evidence favouring magnetic braking at a much lower degree than has been applied in past evolutionary models.

Gravitational wave radiation

Two stars in orbit continuously radiate gravitational waves, which is parameterised by [Landau and Lifshitz, 1971]

$$\frac{\dot{J}_{\rm gr}}{J} = -\frac{32}{5}\frac{G^3}{c^5}\frac{M_1 M_2 (M_1 + M_2)}{a^4} \tag{1.5}$$

with G the gravitational constant, c the speed of light, M_1 and M_2 the mass of the two stars and a the orbital separation. Gravitational wave radiation becomes significant as a loss of orbital angular momentum for close orbital separations, and so is small up until the later stages of binary evolution. Following an orbital evolution solely impacted by the emission of gravitational waves, the orbital period evolves as

$$\dot{P}_{\rm GW} = -\frac{96}{5}\frac{G^3}{c^5}\frac{M_1 M_2 M_{\rm T} P_{\rm orb}}{a^4} = \frac{3\dot{J}_{\rm GW}}{J_{\rm orb}} P_{\rm orb} \tag{1.6}$$

with M_T the total mass $M_1 + M_2$. Taking the derivative of equation 1.6, we see that the second derivative of the orbital period is

$$\ddot{P}_{\rm GW} = \dot{P}_{GW}\left(-\frac{4\dot{a}}{a} + \frac{\dot{P}}{P}\right) = \dot{P}_{GW}\left(-\frac{8}{3}\frac{\dot{P}}{P} + \frac{\dot{P}}{P}\right) = -\frac{5}{3}\frac{\dot{P}}{P}\dot{P}_{GW} \tag{1.7}$$

and when gravitational wave emission dominates the orbital trajectory, $\ddot{P}_{GW} = -\frac{5}{3}\dot{P}^2_{GW}/P_{\rm orb}$. Evidently, $\ddot{P}_{\rm GW}$ becomes significant only at small orbital periods when $\dot{P}_{\rm orb}/P_{\rm orb}$ is minimised.

Then two stars will merge after a critical time [Peters, 1964]

$$T_c(a_0) = \frac{5}{256}\frac{a_0^4 c^5}{G^3 M_1 M_2 (M_1 + M_2)} \tag{1.8}$$

with the assumption that the orbit is circularised (an eccentricity of zero) as is the case for DWD binaries since their orbits quickly circularise following a common envelope phase; at the time of writing, no eccentric DWDs are known, with typical maximum constraints being about $e = 0.001$ [e.g. Chandra et al., 2021].

The gravitational wave frequency is parameterised as $f_{GW} = 2/P_{\rm orb}$ because the shape of the quadrupole pattern (that describes how mass distributions stretch/squeeze space in two directions simultaneously) repeats twice per orbit. Under solely gravitational-wave orbital angular momentum loss

$$\dot{f}_{GW} = \frac{96}{5}\,\pi^{8/3}\left(\frac{G\mathcal{M}}{c^3}\right)^{5/3} f_{GW}^{11/3} \tag{1.9}$$

and the dimensionless gravitational wave amplitude is

$$\mathcal{A} = \frac{2(G\mathcal{M})^{5/3}}{c^4 d}(\pi f_{GW})^{2/3} \tag{1.10}$$

that are also dependent on the distance to the source, d, and the chirp mass

$$\mathcal{M} = \frac{(M_1 M_2)^{3/5}}{(M_1 + M_2)^{1/5}} \tag{1.11}$$

For detection with gravitational wave spacecrafts, the characteristic strain of a binary can then be calculated as [Moore et al., 2015]

$$h_c = \sqrt{N_{\text{cycle}}}\mathcal{A} \tag{1.12}$$

where $N_{\text{cycle}} = f_{GW} T_{\text{obs}}$ is the number of observed cycles of the binary over a time T_{obs} of gravitational wave monitoring.

During the last tens of megayears of orbital decay, the rate of change of J_{GR} becomes large enough that the gravitational waves radiated by the source remain strong enough to be detected above the noise profile of upcoming gravitational wave detectors in the millhertz regime. Crucially, gravitational waves propagate through space-time following a $1/d$ relation, whereas the emitted flux from photons propagates as $1/d^2$. This hence signifies that sources at further distances can still be detected and located via triangulation when not possible in the optical. This is exemplified by Fig. 1.5 and there are multiple systems that will serve as test subjects to calibrate the detectors, commonly referred to as gravitational wave "verification binaries".

A plot of the known verification binaries that the Laser Interferometer Space Antenna (LISA) will depend on, all of which lie significantly above the noise instrumental background of the detector, are plotted in Fig. 1.6, ranging from orbital periods of approximately 1 hour to 5.4 minutes. These can be detached systems, or the shrinking of the orbit can cause one star to overflow its Roche lobe like in AM CVn binaries, which are ultracompact binaries composed of a white dwarf accreting hydrogen-deficient material from its companion.

Tidal effects/spin-orbit coupling

DWDs hence in-spiral to ultra-compact orbital periods through the sustained emission of gravitational waves. At approximately sub-10 min periods, tidal braking becomes influential on the loss of orbital angular momentum to a similar magnitude [the torquing timescale scales as P^3 whereas the gravitational wave timescale scales as $\mathrm{P}^{8/3}$, e.g. Piro, 2011]. When

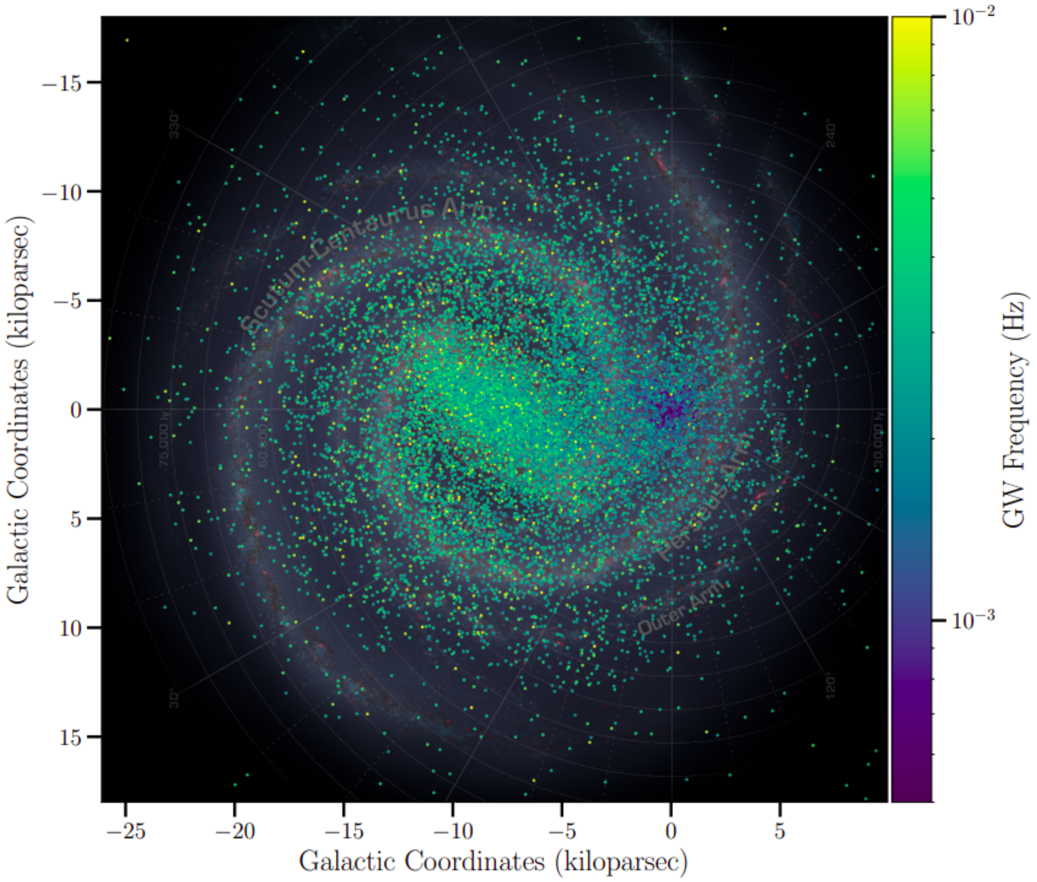

Figure 1.5: A prediction of the distribution of DWD binaries that will be detectable by the LISA spacecraft with a signal to noise ratio greater than 7. The coordinate system is zeroed on the location of the solar system, where the increase of blue sources is apparent due to the improved sensitivity of nearby, longer period systems. Once detected, the distribution of such systems will prove vital in constraining the distribution of mass and the structure of the Galaxy [Breivik et al., 2020; Ebadi et al., 2024] and its dwarf galaxies Korol et al. [2020]. Figure presented in Amaro-Seoane et al. [2022] with credit to Valeriya Korol.

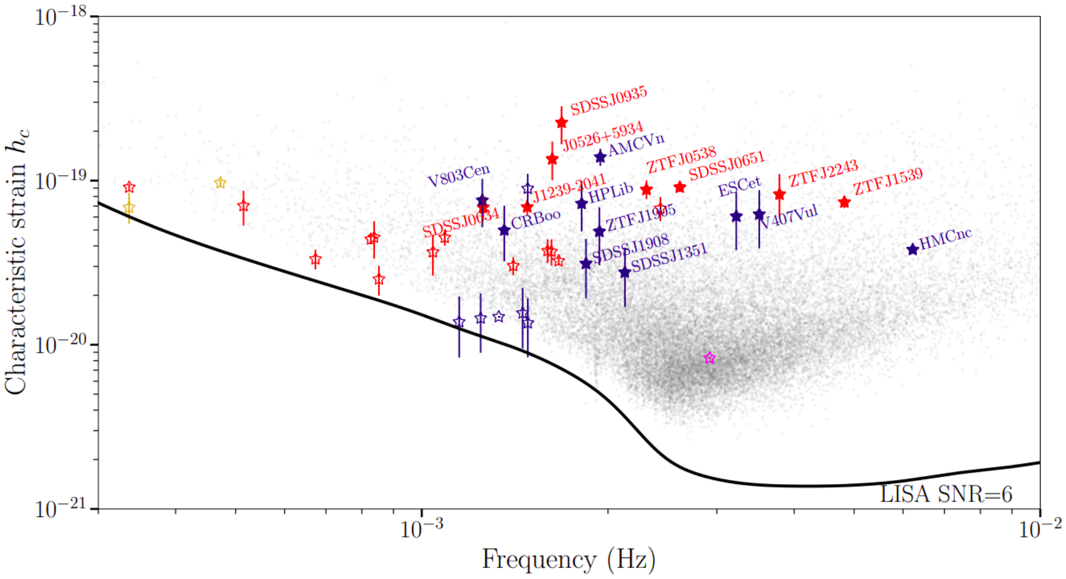

Figure 1.6: LISA verification binaries, figure taken from Fig. 4 of Kupfer et al. [2024]. The characteristic strain of the binaries is computed with an assumed $T_{\rm obs} = 4\,{\rm yr}$ LISA mission lifetime. The black line is the detection threshold for sources with a signal-to-noise ratio greater than 6. Points plotted in blue, red, yellow and magenta are AM CVns, detached DWDs, hot subdwarfs (which are stripped, core-helium burning stars) and ultra-compact X-ray binaries.

both tides and gravitational wave radiation are acting on the binary, it can be parameterised as [Piro, 2019]

$$\dot{P}_{\text{tide}} = \frac{\dot{P}_{\text{GW}} - 3(\dot{\eta}/\eta)(J_{\text{WD}}/J_{\text{orb}})P}{1 - 3J_{\text{WD}}/J_{\text{orb}}} \tag{1.13}$$

where η corresponds to a tidal locking factor for which $\eta = 0$ signifies no tidal effects and $\eta = 1$ signifies total tidal locking. When negligible tidal effects are at play, most orbital energy goes into gravitational waves and when there is total tidal locking most of the lost orbital energy goes into spinning up the WDs, while the heating of the two stars remains small (tidal heating is more significant in between). The second period derivative due to tides can also be written as [Piro, 2019]

$$\ddot{P}_{\text{tide}} \left(1 - \frac{3J_{\text{WD}}}{J_{\text{orb}}}\right) = -\frac{4}{3}\frac{\dot{P}_{\text{tide}}\dot{P}_{\text{GW}}}{P} - \frac{\dot{P}^2_{\text{tide}}}{P}\left(\frac{1}{3} + \frac{3J_{\text{WD}}}{J_{\text{orb}}}\right) \tag{1.14}$$

Tidal interactions in DWDs are yet to be directly measured given the need to a) be detached b) have short orbital periods where its contribution is significant c) the need for long-term orbital tracking of the binaries for $\dot{P}$ and $\ddot{P}$ measurements d) the need for precise masses of the two stars to separate tidal from gravitational wave effects. This ultimately limits us to eclipsing detached DWDs since pronounced eclipses grant an increased precision in orbital timing measurements. Eclipsing sources are still often troublesome for obtaining precise masses, though inferences through the second period derivative are more forgiving on mass errors. There are two exemplar candidates that should directly reveal clear orbital decay due to tidal effects: J0651+2844 ($\mathrm{P_{orb}} = 12.75\,\mathrm{min}$) and J1539+5027 ($\mathrm{P_{orb}} = 6.9\,\mathrm{min}$). These systems will reveal a direct measurement of the second derivative term on the timescale of decades, proving crucial in quantifying tidal effects in real systems. This is particularly important given the deviation from purely general relativistic inspiral, as without better knowledge its effect renders the masses inferred from detached systems using the chirp mass found from gravitational wave or $\dot{P}_{\text{orb}}$ observations as inaccurate. A well-understood orbital trajectory from orbital angular momentum components is required to predict and understand the final state of the binary, having strong applications to the number of detectable Galactic DWDs for future gravitational wave detectors [Toubiana et al., 2024].

Direct impact accretion

While direct impact accretion does have immediate parallels with mass transfer, the novelty of it occurring for only the most ultra-compact of systems ($\mathrm{P_{orb}} < 15\,\mathrm{min}$) merits a separate discussion.

When the donor of a binary initiates mass transfer, mass follows a ballistic trajectory flowing out of the first Langrangian point and forms an accretion disc around the accretor star. However, in ultra-compact DWD binaries, the onset of mass transfer occurs at very small (tenths of solar radii) orbital separations owing to the tiny radii of WDs. In the case that an accretion disc does form, the material would orbit at an equivalent radius [Verbunt and Rappaport, 1988]

$$\frac{r}{a} \approx 0.0883 + 0.04858 \log q + 0.11489 \log^2 q - 0.020475 \log^3 q \tag{1.15}$$

with $q = M_d/M_a$, and the radius at which the accretion stream would initially pass the surface of the WD is approximately [Nelemans et al., 2001a]

$$\frac{r_{\text{min}}}{a} \approx 0.04948 - 0.03815 \log(q) + 0.04752 \log^2(q) - 0.006973 \log^3(q) \tag{1.16}$$

If the radius of the star is larger than r_{min}, mass flows through the first Lagrangian point with a trajectory that coincides with the accretor, such that accreted material directly impacts its surface (Fig. 1.7). This acts as a further orbital angular momentum sink acting to accelerating the inspiral, given as

$$\dot{J}_{\text{di}} = J_{\text{orb}} \sqrt{r_h\,(1+q)} \frac{\dot{M}_d}{M_d} \tag{1.17}$$

The sudden impact of the stream onto the WD accretor introduces an intense emission of X-rays at the impact site. To date, just 3 direct impact sources have been discovered, largely owing to the fact that the duration of the direct impact phase is merely a few tens of thousands of years. These are HM Cancri [Ramsay et al., 2002], V407 Vul [Marsh and Steeghs, 2002] and perhaps the recently discovered source eRASSU J060839.5-704014 [Maitra et al., 2024] but further confirmation is required to ascertain its physical nature as a DWD. HM Cancri and V407 Vul are currently inspiraling [Hakala et al., 2003; Barros et al., 2007] and the period derivative of eRASSU J060839.5-704014 is not known, such that there is no known source that is still directly impacting that has survived through a period minimum. However, there is one source, ES Ceti [Noguchi et al., 1980; Downes and Shara, 1993], that is oustpiraling [de Miguel et al., 2018] and has formed an accretion disc [Bąkowska et al., 2021].

Mass loss

For completeness, it should be mentioned that orbital angular momentum loss from wind Roche lobe overflow causing an orbital shrinkage occurs too, but further discussion is not necessary for the theme of this thesis [see e.g. Abate et al., 2013, for more details]. There is also the situation where two WDs could experience a head-on collision driven by the quasi-secular changes of the orbital evolution from a tertiary component, but this has been shown

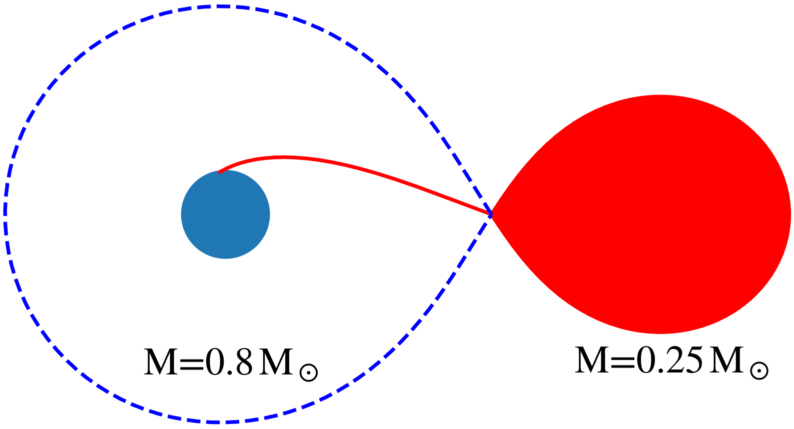

Figure 1.7: A graphical representation of direct impact mass transfer from an accretor with mass $0.8\,M_\odot$ and radius $0.01\,R_\odot$, a $0.25\,M_\odot$ donor and an orbital separation of $0.1\,R_\odot$. The donor's Roche lobe is full and the ballistic trajectory of the accretion stream is shown, coinciding with the surface of the accretor. The blue dotted region is the Roche lobe of the accretor. A 1:1 aspect ratio is maintained in the vertical/horizontal direction.

to be relatively infrequent [Toonen et al., 2018, and references therein]. Non-conservative mass transfer will be touched on in the following section.

1.3 Detonation, merger or a surviving AM CVn? The final moments of binary evolution

I have touched on the formation of DWDs and their orbital evolution through various angular momentum transfer mechanisms. Now, I will discuss their fate. From equation 1.6, any DWD with an initial orbital period between 9–13 hrs will come back into contact within a Hubble time. Broadly speaking and as has been long adopted, a binary with $q > 2/3$ leads to unstable mass transfer [e.g. Marsh et al., 2004], but the most important aspect of the binary's stability is the synchronisation of the two stars with the orbit. During inspiral, tidal forces or magnetic coupling act to synchronise the spin of the WDs with the orbit. Once mass transfer initiates, the accretion stream naturally acts to spin up the accretor, so the key to survival is the percentage of gained angular momentum that can be fed back into the orbit [Marsh et al., 2004; Fuller and Lai, 2012].

1.3.1 Survival

All mechanisms above exclaim that orbital angular momentum is continuously being lost from the system. Yet, this does not necessarily imply that the DWD's destiny is catastrophic. As mass is transferred from the donor, the mass ratio continuously changes, and a larger mass ratio obtains a stable orbit at larger orbital separations. Hence, a decreasing orbital separation from orbital angular momentum loss is met by mass transfer. If mass can be exchanged rapidly enough, the orbit stabilises by increasing the orbital separation.

Contrary to the typical dynamics of mass transfer between non-degenerate stars, the smaller mass, larger radius WD is first to overflow its Roche lobe as the donor star, with the larger mass, smaller radius WD the accretor in a DWD binary. Mass transfer from one star to a higher mass companion acts to expand the orbit, counteracting the shrinkage caused by gravitational wave losses with angular momentum transfer playing an important role in the fate of these systems [Marsh et al., 2004].

The mass transfer rate of a binary is set by [e.g. Kaplan et al., 2012]

$$\frac{\dot{J}}{J} = \frac{\dot{M}_a}{M_a} + \frac{\dot{M}_d}{M_d} + \frac{\dot{a}}{2a} - \frac{\dot{M}_t}{2M_t} \tag{1.18}$$

with subscripts a, d and t being the accretor, donor and total, and, for conservative mass transfer, does not alter the orbital angular momentum of a system. However, in ultra-compact binaries, the build up of material on the accretor can lead to episodes of hydrogen or helium flashes that eject material in nova eruptions, accelerating in-spiral. Considering $\dot{M}_t = f\dot{M}_d$ to track the total mass lost by the system, with f being a dimensionless quantity equal to 0 if the accretor keeps all accreted mass and 1 if all mass accreted is ejected, the mass transfer rate and the orbital angular momentum are related via

$$\frac{\dot{J}}{J} = \frac{\dot{M}_d}{M_d}\left(1 + (f-1)\frac{M_d}{M_a} - f\frac{M_d}{2M_t}\right) + \frac{\dot{a}}{2a} \tag{1.19}$$

Converting all into units of the orbital separation with $r_L = R_L/a$, accounting both the response of the donor, $\zeta_{r_d} = d\ln r_d/d\ln M_d$, and the evolution of the Roche lobe, $\zeta_{r_L} = d\ln r_L/d\ln M_2$, equation 1.19 becomes

$$\frac{\dot{J}}{J} = \frac{\dot{M}_d}{M_d}\left(1 + \frac{\zeta_d - \zeta_{r_L}}{2} + (f-1)\frac{M_d}{M_a} - f\frac{M_d}{2M_t}\right) \tag{1.20}$$

Now we must also consider when mass transfer itself is stable, i.e. when the donor remains within its Roche lobe and only overflows through the first Lagrangian point. If we consider an overfill factor of $\Delta = R_2 - R_{r_L}$, $d\Delta/dt$ shows whether the response of the donor is causing the inspiral to speed up or not. Marsh et al. [2004] show that to a good approximation

$$\frac{1}{2R_d}\frac{d\Delta}{dt} = -\frac{\dot{J}_{GR}}{J_{\text{orb}}} - \frac{kM_1R_1^2}{\tau_s J_{\text{orb}}}\omega + \left(1 + \frac{\zeta_d - \zeta_{r_L}}{2} - q - \sqrt{(1+q)r_h}\right)\frac{\dot{M}_d}{M_d} \tag{1.21}$$

where the first term on the right hand side of the equation corresponds to the gravitational waves component, the second to the spin-orbit coupling, and the third addresses mass transfer. $kM_1R_1^2$ is the moment of inertia of the accretor, τ_s is the synchronisation timescale and ω is the difference between the spin of the accretor and the orbital frequency. The donor is synchronised with the orbit [Zahn, 1977; Verbunt and Hut, 1983], hence is negligible. Collecting all non-mass transfer related terms to the left, we will have stable mass transfer when the mass transfer is larger than this value, hence when

$$\left(1 + \frac{\zeta_2 - \zeta_{r_L}}{2} - q - \sqrt{(1+q)r_h}\right)\frac{\dot{M}_d}{M_d} > 0 \tag{1.22}$$

$$q < 1 + \frac{\zeta_d - \zeta_{r_L}}{2} - \sqrt{(1+q)r_h} \tag{1.23}$$

in the case of direct impact accretion, or without the final term in equation 1.23 in the case of disc accretion, and the extra orbital angular momentum sink of direct impacting material clearly causes instability.

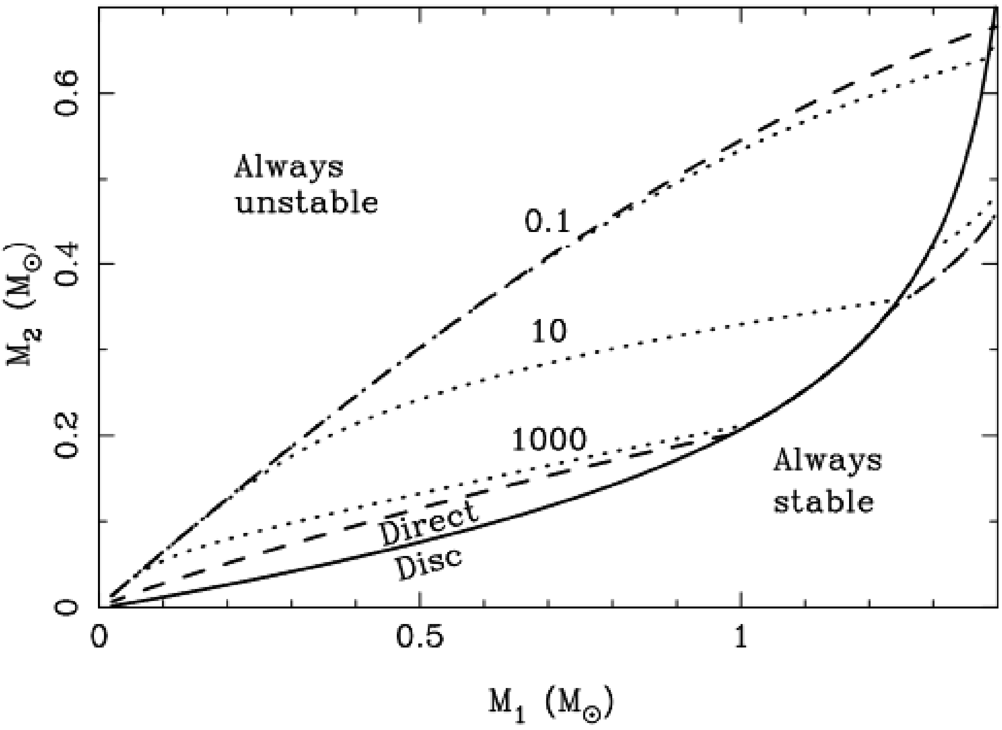

Figure 1.8: Figure 1 from Marsh et al. [2004] showing the limits of direct vs disc accretion (solid black line). The dashed lines show the conditions for stable/unstable mass transfer dependent on the synchronisation timescale, which is the timescale on which angular momentum is able to be fed back into the orbit. Combinations towards the left of each dashed/dotted line lead to instability and towards the right for stability. Each number is in years (the faster it can resynchronise, the more stable the system). M_1 here is the mass of the accretor.

As a WD's response to mass transfer is to expand, ζ_2 is negative and a typical value is approximately $-0.6 < \zeta_2 < -0.3$ [Wong and Bildsten, 2021], but the donor's response depends highly on the mass of the WD. Performing this, we run into a problem fast - the permitted mass ratios that would allow a binary to survive period minimum are very small and direct impact accretion is the primary reason. With unstable mass transfer, we should see an accelerating inspiral in direct impact accreting binaries, and hence only systems with tiny mass ratios would be able to survive a period minimum (see Fig. 1.8).

Two big issues came from this. The first issue is the need to find progenitors of the observed AM CVn population, which – as previously mentioned – are compact accreting binaries with often strong gravitational wave emission. Nelemans et al. [2001a] noted how direct impact accretion severely decreases the galactic population of AM CVn binaries to the point where their simulation would not be able to reproduce observed period-minimum survivors through the double degenerate channel. In the worst case scenario where all angular momentum from directly impacting material works to spin up the accretor and is not fed back into the orbit, Nelemans et al. [2001a] show how any DWD would require an e.g. $0.5\,\mathrm{M}_\odot$ accretor with a $< 0.14\,\mathrm{M}_\odot$ donor or a $1\,\mathrm{M}_\odot$ accretor with a $< 0.2\,\mathrm{M}_\odot$ donor (see their figure 1). In their synthetic population of AM CVn's, this resulted in practically all DWDs leading to unstable mass transfer and hence no contribution to the AM CVn population. The second issue is that, in the 1990s, 3 candidate ultra-compact binaries were discovered: V407 Vul (P=9.5 min), HM Cancri (P=5.4 min) and ES Ceti (P=10.3 min). Given their orbital periods and if they all are ultra-compact binaries, they have to be DWDs as a helium star or larger donor would not be able to fit for an orbital separation this small, and these were the first candidate systems that show that ultra-compact DWDs can form and do exist. All three showed an X-ray profile that could be due to direct impact accretion [in recent years, ES Ceti has been discovered to harbour an accretion disc Bąkowska et al., 2021]. However, the issue is that a system undergoing unstable mass transfer should do so at a much larger rate than the flux of the X-ray signals indicate, disfavouring the DWD model (see Chapter 3 for discussion of other models).

D'Antona et al. [2006] [see also Deloye and Taam, 2006; Kaplan et al., 2012] proposed a model in which a large hydrogen envelope could act to make the donor star semi-degenerate, and hence the donor would maintain a similar radius instead of expanding due to mass transfer. This allows for much smaller accretion rates that are consistent with the observed X-ray fluxes for sub-10 min orbital periods (as will be discussed in Chapter 3). Once the hydrogen envelope is depleted, we return to the degenerate equation of state for the donor star as pure helium is donated and the mass transfer rate climbs significantly ($\dot{M} = 10^{-7} - 10^{-5}\,\mathrm{M}_\odot\,\mathrm{yr}^{-1}$). At this high of a mass transfer rate, the mass loss repels the decrease in orbital separation induced from the aforementioned orbital angular momentum losses due to a change in mass ratio. Hypothetically, the system has the potential to lead to an expanding orbit, surviving through a period minimum, and existing as an AM CVn binary with an extremely stripped donor having lost hundredths of solar masses.

The knowledge of whether a DWD can indeed survive period minimum is still largely unclear, where it is worth mentioning that some authors advocate that no/very few DWDs will survive a period minimum [e.g. Shen, 2015; Polin et al., 2019]. Not only this, but observational evidence of the impact and efficiency of tidal interactions is uncharted territory, and the same applies for the synchronisation timescale. Thus, it is unclear how much angular momentum can be re-pumped into the orbit during mass transfer which ultimately is the key for achieving stability[3]. What is clear though is that ultra-compact DWDs

---

[3] Clear evidence exists for outspiraling (surviving) AM CVn's that arose through the non-degenerate helium star channel or the cataclysmic variable channel with an evolved donor, which are able to reach minimum orbital periods of roughly 12 min.

do exist for prolonged periods of time, show evidence in favour of their ability to resist orbital inspiral and may still be responsible for the population of expanding orbit AM CVn binaries. The study of ultra-compact DWDs and AM CVn binaries is still a highly active area of research, and discovery of outspiraling, directly-impacting accretion stream binaries would be revolutionary to show direct and unmistakable observational evidence that DWDs can survive inspiral.

1.3.2 Demise

I address here all cases where the binary is not able to survive inspiral. The result of the merger depends strongly on the initial mass of the two WDs and the total mass of the system. The knowledge of which remnants are formed from a merger is guided by population synthesis of DWDs that match relatively well the subsequent populations [Han, 1998; Nelemans et al., 2001c; Han et al., 2002; Toonen et al., 2012] and/or where no other known stellar types can explain the remnants. Approximately speaking, two low mass WDs will merge to form a sdO/sdB star [Zhang and Jeffery, 2012], a hot subdwarf which is core helium burning, an R Coronae Borealis [Webbink, 1984] star, which is a hydrogen-deficient and carbon-rich, or a carbon-oxygen WD from the two individual star masses combined at merger. A carbon-oxygen WD with a low mass WD companion may form a new larger mass, carbon-oxygen core WD for the lower total mass boundary, or an ONe WD/SN .Ia supernova for the upper. Equal mass WDs with a total mass approaching the Chandrasekhar mass limit are theorised to either detonate or, if an oxygen-neon WD is present, lead to an accretion induced collapse [Nomoto et al., 1979; Nomoto and Kondo, 1991] and the formation of a neutron star. Such a large mass merger has also been considered as a formation mechanism for large mass WDs with a strong magnetic field [Cheng et al., 2019; Gvaramadze et al., 2019; Hollands et al., 2020].

Anything with a total mass above approximately 1.5 $M_{\odot}$ will maintain enough mass during merger to exceed the Chandrasekhar mass limit, inevitably implying that in some way an explosion of a star will occur. What likely happens in reality is that, in these high total mass systems, the explosion of one star occurs before merger which may lead to the explosion of the donor as well [Pakmor et al., 2012b]. Exploration of these conditions are purely theoretical with no type Ia supernova model able to explain the wealth of identified type Ia's [e.g. Maoz et al., 2014; Liu et al., 2023; Soker, 2024], primarily found through transient surveys. Popularity has grown in recent years for the existence of sub-Chandrasekhar mass detonations, where the larger the mass of the accretor, the more likely a detonation and consequently explosion is to happen. The key to setting off a detonation is whether ignition of carbon fusion can be initiated, leading to runaway thermonuclear reactions, explosion of the star and dispersion of metals into the interstellar medium. A sub-

Chandrasekhar mass double-detonation can occur through stable mass transfer from a He WD or a helium star if the accreted helium reaches ≈0.02–0.2 $M_\odot$ [Neunteufel et al., 2016; Polin et al., 2019], detonates and initiates a second detonation in the core [e.g. Nomoto, 1982]. Or, sub-Chandrasekhar mass type Ia can occur through unstable mass transfer. Here, compressional heating from the accretion stream can lead to a core detonation of the carbon-oxygen WD [Pakmor et al., 2010, 2011, 2012b]. Alternatively but again through unstable mass transfer, there is the dynamically driven double-degenerate double-detonation (dubbed the D^6 scenario) in which a thin ($\approx 0.01\,M_\odot$) helium layer detonates on the accretor's surface and consequently triggers the core detonation as well [Boos et al., 2021; Shen et al., 2021]. In the sub-Chandrasekhar mass situation, the initial detonation is triggered through accumulation of a helium shell from the donor's material.

1.4 The observed population of double white dwarfs

There are expected to be hundreds of millions of DWD binaries in the Galaxy [e.g. Nelemans et al., 2001c; Marsh, 2011; Korol et al., 2022b]. DWDs in compact configurations are of particular galactic interest, long suspected to contribute towards a large fraction of type Ia supernovae [see Maoz et al., 2014, for a review] that are responsible for the enrichment of the interstellar medium, and to be an explanation for the existence of exotic merger remnants [e.g. Webbink, 1984; Zhang and Jeffery, 2012]. Furthermore, compact DWD binaries serve as surviving test subjects of the common envelope phase [Nandez et al., 2015], which can be used to probe the conditions that may lead to the survival or demise of a binary through population modelling [Toonen et al., 2012, 2017; Korol et al., 2022b]. However, only a small fraction of the observable population has been conclusively identified to date. This is largely the result of observational biases from the intrinsic dimness of WDs and from a detection biases in each method.

Ongoing and recent attempts to exploit all-sky variability surveys to find DWD and other compact binaries has resulted in an acceleration in the detection of such systems [e.g. Burdge et al., 2020b; van Roestel et al., 2021, 2022; Kosakowski et al., 2022; Keller et al., 2022; Ren et al., 2023]. These searches are highly sensitive to eclipsing systems, or near-edge-on binaries that can have large photometric amplitudes. They are also extremely biased towards the most compact of sources owing to the increased eclipse probability, large ellipsoidal modulation effects to the two stars making photometric variability more severe, and the ability to survey more orbital cycles in the same amount of telescope time.

Many radial velocity searches have been conducted over the last decades (see Table 1.1 for full references). Focusing on two large-scale and recent searches, the extremely low mass (ELM) WD survey [Brown et al., 2022] and the supernovae type Ia progenitor survey [Napiwotzki et al., 2020] have provided population statistics on the DWD sample from the DWDs discovered in their surveys. In particular, Napiwotzki et al. [2020] reveal a DWD fraction of 6% compared to their observed WD sample and from other studies the overall percentage of DWDs in the Milky Way compared to the number of WDs is predicted to be ≈5–10% [Maxted and Marsh, 1999; Maoz and Hallakoun, 2017; Maoz et al., 2018; Napiwotzki et al., 2020; Korol et al., 2022a; O'Brien et al., 2024], which are consistent with the fraction expected from close DWD population synthesis [Toonen et al., 2017]. A couple of dozen other radial-velocity variable or eclipsing DWD systems have been discovered separately to these surveys [see e.g. Kilic et al., 2010; Hallakoun et al., 2016; Brown et al., 2020b; Kilic et al., 2021a; Kosakowski et al., 2023, and references therein] which typically have orbital periods between a few hours and a day. However, the most compact of DWD binaries with an orbital period less than one hour are rare. Brown et al. [2022] find that $\approx 10\%$ of low-mass WD binaries alone have sub-hour orbital periods in the ELM WD survey. Approximately 20 out of a total of 200 DWDs have been found to be this compact, an excessive fraction compared to the $\approx 5\%$ predicted [Nelemans et al., 2001c] that is likely consistent when considering observational biases.

Multi-object spectroscopic (MOS) surveys have proven capable of surveying thousands of WDs that are ideal for bulk population analyses [e.g. Tremblay et al., 2011, 2016; Kilic et al., 2020b; Manser et al., 2024]. Within, multi-epoch observations allow the possibility to flag considerably RV variable binaries. Searches have been carried out to resolve the orbits of such sources [Breedt et al., 2017], but from the knowledge of a maximum RV difference between the two stars alone, predictions of synthetic populations can be put to the test. Studies by Maoz et al. [2012]; Badenes and Maoz [2012]; Maoz et al. [2018] have presented and utilised a method to simulate the observed RV shift of a population, being able to place limits on the DWD fraction and merger rate in the Milky Way. Tangential to this, synthetic observables based on mock populations have been utilised to study the frequency of type Ia supernovae aiming to address the gawping difference between the observed and predict rates [Rebassa-Mansergas et al., 2019], with no DWD candidate known that will merge in a Hubble time that have a total mass that exceeds the Chandraskehar mass limit (see discussion in Chapters 5 and 6 for supernova mechanisms and candidates).

A new means of detecting thousands of wide binary companions to a WD has lately become possible through astrometric solutions using *Gaia* [Gaia Collaboration et al., 2016a, 2023]. El-Badry and Rix [2018]; El-Badry et al. [2021a] revealed hundreds of wide DWD binaries through the means of a common proper motion and parallax between the two stars ($\gtrsim$100 AU). As for the more compact systems, signatures of binarity in the local population can be predicted through a low-amplitude astrometric wobble of the centre of light, which has often been used to select strong candidates through the so called Renormalised Unit

Weight Error [RUWE, Belokurov et al., 2020]. Of the likes, Korol et al. [2022a] analyse RUWE-excessive candidates to identify a gap in the separation distribution of DWDs at approximately 1 au while finding a consistent DWD fraction with the spectroscopic sample analyses and indicating a sensitivity in the detection of DWDs with orbital separations 0.01 au $< a <$ 2 au.

Looking towards the near future, there are many DWD binaries with orbital frequencies in the mHz frequency band ($\approx$ sub-hour periods) scattered across the full Milky Way that are waiting to be discovered by upcoming space-based gravitational wave detectors like *TianQuin* [Luo et al., 2016] and the *Laser Interferometer Space Antenna* [LISA, Amaro-Seoane et al., 2017, 2022]. DWDs will be the dominant foreground sources [Nissanke et al., 2012; Korol et al., 2017; Lamberts et al., 2019; Amaro-Seoane et al., 2023; Staelens and Nelemans, 2024], with recent simulations expecting about 10 000 DWDs to be detected in the mission's lifetime. These observations should mark a leap in our understanding of DWDs from an order of magnitude more systems being discovered alone, will permit the unravelling of the full structure of the Milky Way [Georgousi et al., 2023] and will reveal the DWD fraction in various Milky Way satellites [Korol et al., 2020] that are tricky with other types of observation due to their high star density and crowding.

In the present day, we know of about 300 compact DWDs, with their location on a Hertzsprung-Russel diagram plotted in Fig. 1.9. A cumulative distribution function of the orbital periods of these systems compared to synthetic population predictions is additionally displayed in Fig. 1.10, clearly conveying the preferential bias in the observed population towards short orbital periods. To be confirmed as a DWD, a source needs to show the clear detection of both WDs, for fitted atmospheric parameters and/or masses for a given period to only be consistent with the binary harbouring two WDs, or for the stars to be spatially resolved. For compact, the exact definition is open to an individual's opinion, but I do and will describe these as cases where there has been a mass transfer episode in the past, which drives the stars to a more compact orbit. The first definitive discovery of a compact DWD binary was L870$-$2, identified as a DA+DA and double-lined system with an orbital period of 1.6 d [Saffer et al., 1988], sparking the inspiration for dedicated searches in the decade that followed [Robinson and Shafter, 1987; Bragaglia et al., 1990; Foss et al., 1991; Marsh et al., 1995; Marsh, 1995; Moran et al., 1997]. As we see in Fig. 1.11, the increase in DWDs appears exponential, in such a way that, if the trend continues, we can expect an observed population of approximately 1100 compact DWDs on the launch date of LISA.

Early attempts to model systems in the observed population of DWDs, starting with a mere 10-15 discovered systems, quickly identified that a double common envelope evolution is unable to explain the mass distribution of double helium core DWDs [Nelemans et al., 2000, 2001c]. Problematically, stable Roche lobe overflow or a combination of Roche lobe overflow and common envelope evolution is not able to either, leading to the introduction of a formalism that acts on a dynamical timescale, consisting of the components γ and $\alpha\lambda$. The purpose of the γ parameter is to take away extra angular momentum from the binary to create the correct period distribution after each mass transfer event, while $\alpha\lambda$ is the common envelope efficiency parameter, α, times a parameter that depends on the structure of the giant star, λ. This approach best fit the observations and can explain the full mass-period distribution of DWDs, but a physical reason for this extra angular momentum sink in the orbital evolution is unclear. The results and usefulness of employing such an approach was later corroborated by van der Sluys et al. [2006], while Woods et al. [2012] advocate that a better approach is to consider non-conservative mass transfer during a first mass transfer phase, which is stable Roche lobe overflow, followed by a single common envelope phase that creates compact enough orbits that match DWD observations. To date, the γ formalism holds strongest with a much increased population size [Nelemans et al., 2025], and the testing of non-conservative mass transfer on the population of DWDs is actively pursued [Li et al., 2023].

Continued efforts to increase the sample of well-characterised DWDs covering the full mass-period range is crucial to accurately model the Galactic population of DWDs, and with that their role in creating the various stellar products described in Section 1.3 and the role of WD explosions in enriching the interstellar medium. This is especially relevant for DWDs that have a total mass above approximately $1.0\,\mathrm{M}_{\odot}$ which are predicted by synthetic populations but have been missing in the observed population.

1.5 Thesis overview

The work presented in the following chapters of this thesis outline my contribution to the advancement of our understanding of compact DWD binaries. The first projects of my doctoral degree focussed around the ultra-compact cases, motivated by pre-gravitational wave detector preparation. Later, I focussed on compact but several hour orbital periods to obtain a reflective sample of the general DWD population and reveal a ‘missing’ observed population of high total mass systems. The majority of the methodology used in my studies is described in Chapter 2, while some details specific to each study is mentioned in the respective chapters. In Chapters 3 and 4, I present a major augmentation to the sample of precisely constrained DWDs in Chapter 5 which turn out to be some of the most massive DWD systems ever discovered, performed through the double-lined double white dwarf (DBL) survey. In Chapter 6, I present a devoted study on the largest total mass DWD binary which came from the DBL survey, which is the largest mass system discovered to date. In Chapter 7, I present a continuation of DBL survey by obtaining full orbital solutions

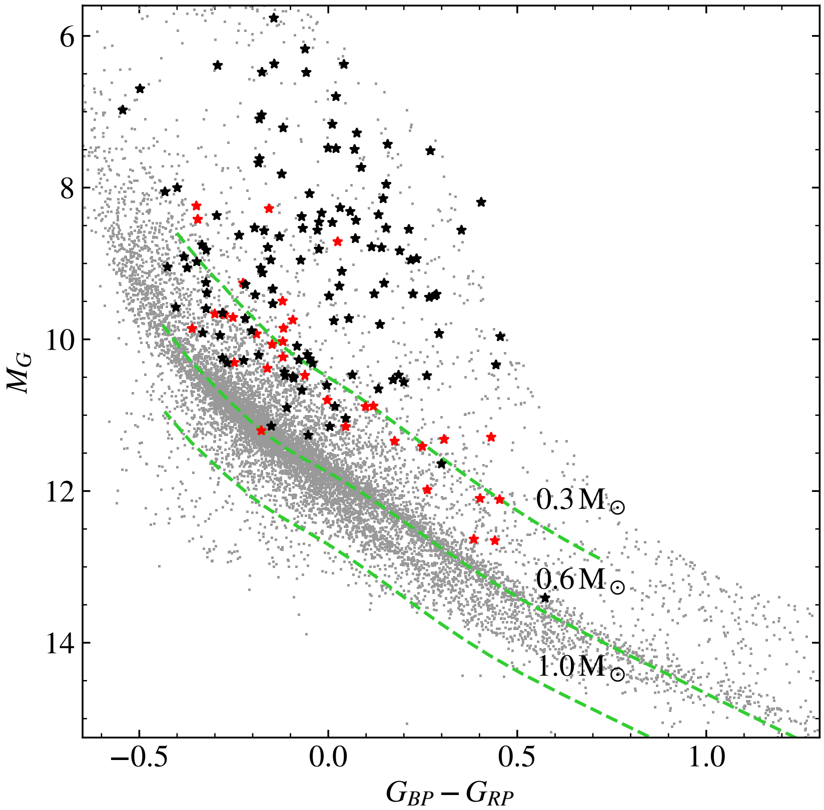

Figure 1.9: A Hertzsprung-Russell diagram zoomed-in on WDs. Plotted in grey are all WDs detected in Gaia DR3 [Gentile Fusillo et al., 2021], where star shaped points are confirmed and compact DWD binaries. In red are double-lined DWDs (both stars are visible in its spectrum) and in black are single-lined DWDs (only one star is visible in its spectrum). Dashed green lines represent the cooling sequences of an isolated 0.3 M$_\odot$, 0.6 M$_\odot$ or 1.0 M$_\odot$, starting at the top left and cooling down to the bottom right. The clear bias in the DWD population is emphasised by the vast number of systems that fall above the 0.3 M$_\odot$ cooling sequence, being ELM DWD binaries in which the ELM dominates the luminosity of the system and outshines its companion.

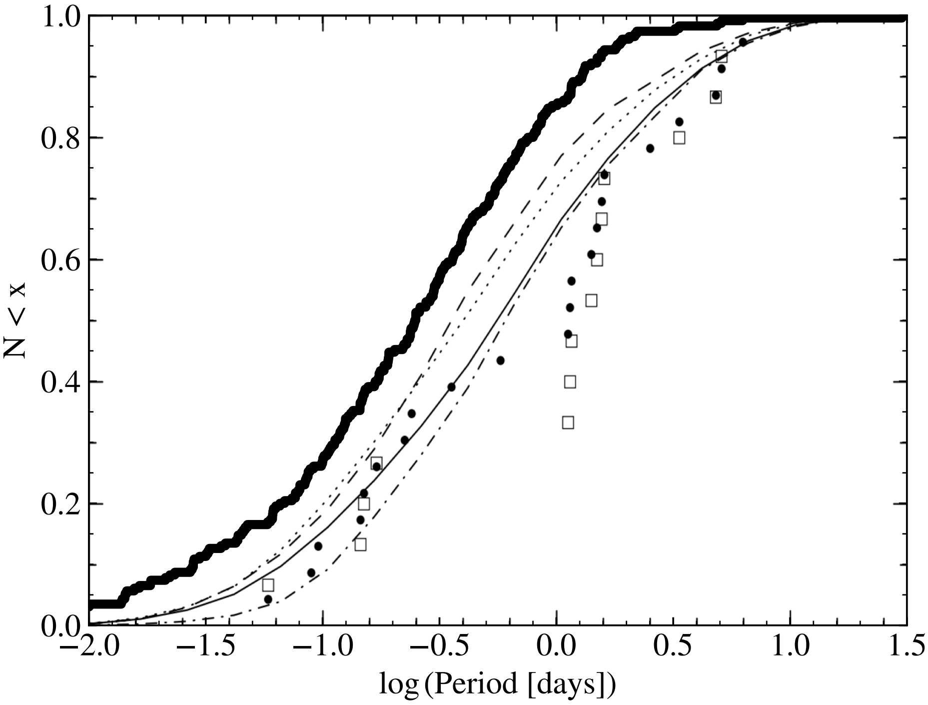

Figure 1.10: A cumulative distribution function of the orbital period of DWDs, presented in Fig. 4 of Nelemans et al. [2001c], with the cumulative distribution function of the present-day observed DWD sample in thick, solid black. The thin lines in this plot are used to provide an error margin in the cooling of the WDs. Evidently, there is a strikingly large over-prediction of systems at shorter orbital periods, consequential of the observing biases towards shorter orbital periods described in Section 1.4. The data points are the observed sample of DWDs (squares) and sdB binaries (circles) at the time of this article being published.

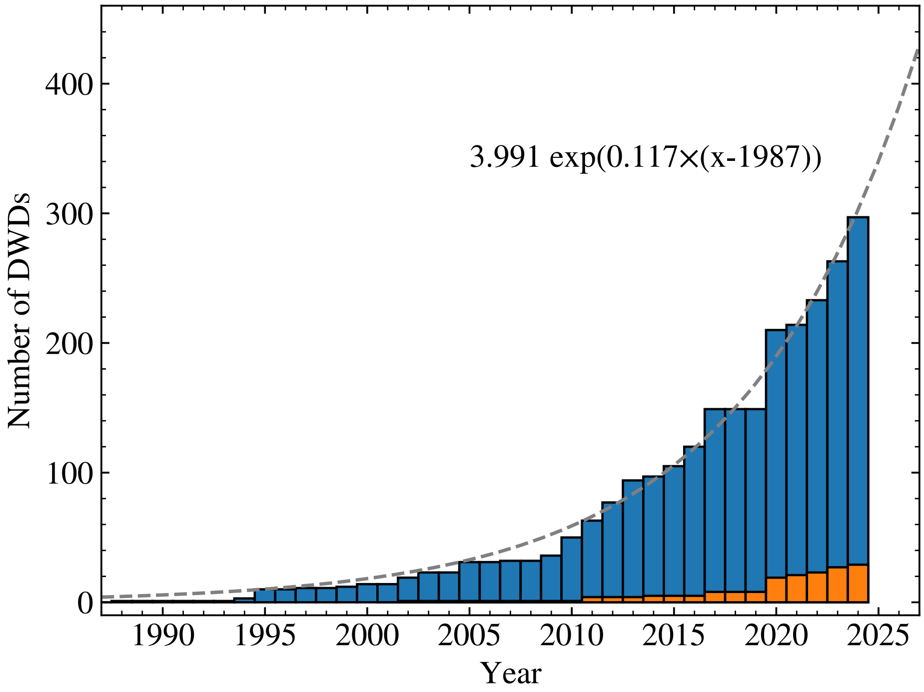

Figure 1.11: A cumulative distribution of the number of compact DWD binary discoveries at the end of each respective year (according to the publication date). The general trend follows an exponential increase thanks to developments in astronomical instrumentation, capabilities and surveys. If we imagine that this exponential trend continues, which may be possible owing to the upcoming spectroscopic MOS surveys and greatly increased photometric depth with the LSST, we will reach an observed population of approximately 1100 DWD binaries at the time of the launch of LISA in 2035. In orange are the discovery of DWDs with orbital periods below 60 min for each year. A large increase in these ultracompact source detections is witnessed in recent years owing to the invent of deeper all-sky surveys.

for many of the newly presented systems.

Table 1.1: A table of all compact DWDs found to date. This list will be regularly maintained at `https://github.com/JamesMunday98/CloseDWDbinaries` and more details of each system is stored within, including the right ascension and declination of sources. See Fig. 5.1 for the Hertzsprung-Russell diagram location of all of these.

Name	P_{orb} [min]	M_1 [$M_\odot$]	M_2 [$M_\odot$]	Distance [pc]	Reference
HM Cnc	5.36	1.00	0.20	>1500	[1] [2] [3] [4]
eRASSU J060839.5–704014	6.23	-	-	>5000	[5]
ZTF J1539+5027	6.91	0.21	0.61	-	[6]
ZTF J0546+3843	7.95	-	-	3707	[7]
ZTF J1858-2024	8.68	-	-	2895	[6]
ZTF J2243+5242	8.80	0.35	0.38	2120	[8]
V407 Vul	9.48	-	-	-	
ES Cet	10.33	-	-	-	[9]
WD J0651+2844	12.75	0.26	0.50	993	[10] [11]
ZTF J0538+1953	14.44	0.32	0.45	1040	[5]
WD 0931+444	19.80	0.31	0.75	370	[12] [13]
SDSS J232230.20+050942.06	20.02	0.27	0.24	865	[14]
J0526+5934	20.51	0.26	0.71	847	[15] [16] [17]
PTF J0533+0209	20.60	0.17	0.65	1266	[5]
ZTF J2029+1534	20.90	0.30	0.32	8063	[5]
J1239-2041	22.51	0.29	>0.61	824	[18]
ZTF J0722-1839	23.70	0.33	0.38	1429	[5]
ZTF J1749+0924	26.40	0.28	0.40	-	[5]
SDSS J063449.92+380352.2	26.50	0.45	0.21	435	[19]
SMSS J033816.16-813929.9	30.60	0.23	0.38	533	[18]
J2322+2103	31.97	0.25	>0.19	884	[17]
ZTF J1946+3203	33.56	0.31	0.27	5225	[5]
WD J0106-1000	39.10	0.19	0.57	833	[20] [12]
WD J1630+4233	39.83	0.30	0.76	851	[21] [12]
SDSS082239+304857	40.28	0.30	0.52	881	[22] [23]
J1526-2711	40.29	0.37	>0.4	621	[24]
ZTF J1901+5309	40.60	0.36	0.36	911	[25] [5]
J2049+3351	42.84	-	-	1961	[23]
SDSS J104336.28+055149.9	45.65	0.18	>0.07	-	[21]
J1506-1125	46.54	0.43	>0.18	413	[23]
WDJ 022558.21-692025.38	47.19	0.40	0.28	403	[26]
J1235+1543	52.88	0.35	≥0.17	444	[27] [28]
ZTF J2320+3750	55.25	0.20	0.69	1443	[5]
WD J1053+5200	61.29	0.20	0.75	3817	[29] [30] [31] [12]
J0056-0611	62.47	0.18	0.82	626	[32] [12]
SDSS J1056+6536	62.65	0.33	0.76	1510	[33] [12]
J0923+3028	64.73	0.28	0.76	287	[30] [34] [12]
WD J1436+5010	65.95	0.23	0.78	948	[35] [12]
J1832+2031	67.16	0.29	>0.47	621	[23]

... continued

Name	P_{orb} [min]	M_1 [$M_\odot$]	M_2 [$M_\odot$]	Distance [pc]	Reference
J1738+2927	68.69	0.26	>0.55	780	[36]
WD J0825+1152	83.79	0.28	0.80	2378	[32] [12]
J1812+0525	86.18	0.28	0.73	1176	[23]
WD0957-666	87.83	0.37	0.32	164	[37] [38]
WD J1741+6526	88.00	0.17	1.17	1154	[39] [12]
J0221+1710	88.25	0.26	0.62	279	[23] [40]
J2013-1310	88.73	0.37	>0.51	452	[23]
WD J0755+4906	90.75	0.18	0.96	-	[30] [12]
J1758+7642	94.56	-	-	620	[41]
SDSS J1337+3952	99.00	0.51	0.32	114	[42]
J1313+5828	106.49	0.27	>0.56	678	[17]
WD J2338-2052	110.07	0.26	0.75	655	[31] [12]
J2309+2603	110.20	0.18	0.96	-	[43] [12]
WD J0849+0445	113.33	0.18	0.86	1784	[34] [12]
WD0019-105	115.06	0.33	>0.19	2844	[33]
J0751-0141	115.22	0.19	0.97	1785	[31] [44] [12]
J1657-0417	120.89	0.27	>0.5	490	[23]
J1121+6052	121.70	0.19	>0.2	752	[23]
J2149+1506	122.99	0.27	>0.51	1055	[17]
J0501-2312	124.69	0.36	>0.14	610	[23]
J2119-0018	124.95	0.16	0.84	1400	[30] [12]
J0930-8107	127.25	0.24	>0.29	855	[45]
J1234-0228	131.62	0.23	0.75	783	[33]
J1808+2723	142.25	0.22	>0.24	355	[23]
J1152+0248	143.81	0.36	0.32	632	[46] [47]
J2102-4145	144.30	0.38	0.31	165	[23] [48]
J1632+4936	146.03	0.27	>0.33	1117	[17]
J1054-2121	150.32	0.18	0.77	1742	[12]
J0725-1245	152.83	0.42	>0.12	662	[23]
J1237+4913	154.99	0.43	≥0.25	959	[27]
J2243-4511	157.65	0.29	>0.46	389	[23]
J0745+1949	161.86	0.16	0.15	919	[49] [12]
J1401-0817	162.71	0.22	>0.79	555	[35]
CSS 41177	167.06	0.38	0.32	435	[50]
J2303-2614	170.20	0.18	>0.58	321	[23]
WD1242-105	171.02	0.56	0.39	40	[51]
J1048-0000	173.71	0.17	>0.62	707	[35]
J1108+1512	177.26	0.18	0.78	825	[12]
J1115+0246	178.63	0.45	>0.26	899	[35]
J0338+4134	180.45	0.22	≈0.7	596	[52] [53]
J2147+1859	185.46	0.16	>0.27	2199	[35]
J0642-5605	189.92	0.18	>0.96	704	[44]

... continued

Name	P_{orb} [min]	M_1 [$M_\odot$]	M_2 [$M_\odot$]	Distance [pc]	Reference
J2257+3023	194.24	0.33	>0.47	277	[17]
J0545-1902	208.04	0.40	>0.25	386	[23]
WD 1101+364	208.40	0.29	0.33	87	[54]
WD1704+481	208.49	0.39	0.56	39	[55]
J0112+1835	211.65	0.16	0.74	757	[38] [12]
J0151+1812	213.29	0.15	>0.47	933	[35]
J0923-1218	214.50	0.34	>0.19	262	[35]
J1233+1602	217.30	0.17	0.98	676	[30] [12]
J1459-1920	218.87	0.26	>0.7	1408	[23]
J1130+3855	225.39	0.29	0.90	675	[12]
GD 251	239.75	0.39	>0.322	246	[56]
J2342+0811	241.75	0.42	$\geq$0.26	575	[27]
J1112+1117	248.37	0.18	0.75	364	[12]
J1553+6736	251.31	0.22	>0.12	424	[23]
J0650-4925	251.32	0.18	>0.67	1042	[44]
SDSS1005+3550	254.19	0.17	0.75	1764	[32] [12]
J0818+3536	263.74	0.16	0.75	-	[30] [12]
J0101+0401	263.98	0.19	>0.35	1245	[17]
SDSS1257+5428	273.30	0.20	>0.95	120	[57] [58] [59]
WD J1443+1509	274.36	0.20	0.99	705	[38] [12]
J0130+5321	276.55	0.19	>0.4	85	[35]
J0450-0145	276.72	0.19	>0.61	1099	[23]
SDSS2103-0027	292.44	0.16	0.88	1078	[32] [12]
HE0225-1912	316.80	0.55	0.23	155	[60]
J1238+1946	320.76	0.21	0.87	2211	[31] [12]
J1249+2626	329.85	0.16	0.76	808	[61] [12]
J1625+3632	331.20	0.20	>0.07	2467	[33]
NLTT 11748	339.13	0.15	0.73	182	[62] [63]
WD J1840+6423	340.88	0.18	0.86	770	[38] [12]
J1708+2225	341.78	0.32	>0.22	1612	[35]
J2104+1712	342.00	0.18	>0.86	357	[17]
J1129+4715	343.91	0.19	>0.37	847	[23]
WD J0822+2753	351.36	0.19	0.93	590	[34] [12]
GALEX J1717+6757	354.44	0.18	0.90	179	[64] [65]
J1631+0605	356.77	0.16	0.79	961	[42] [12]
J1526+0543	360.56	0.16	0.81	3144	[60] [12]
J0517-1153	360.75	0.19	>1.07	680	[23]
J2132+0754	360.81	0.19	1.07	1221	[31] [12]
J1141+3850	373.80	0.18	0.92	1516	[31] [12]
J0256+4405	376.21	0.22	>0.68	714	[23]
J1630+2712	398.10	0.17	0.80	6978	[30] [12]
HE2209-1444	398.78	0.58	0.58	38	[66]

... continued

Name	P_{orb} [min]	M_1 [$M_\odot$]	M_2 [$M_\odot$]	Distance [pc]	Reference
J2306+0224	413.68	0.20	>0.28	1105	[17]
J1557+2823	416.46	0.49	>0.43	247	[31]
J1449+1717	418.68	0.17	0.83	613	[60] [12]
J0042+3103	428.04	0.18	>0.49	545	[35]
J1555+1007	429.17	0.35	>0.38	397	[23]
WD2020-425	432.00	0.81	0.54	99	[67] [68] [59]
J0834+3049	433.14	0.29	$\geq$0.47	757	[27]
SDSS1005+0542	440.06	0.34	>0.66	1640	[32]
J1545+4301	445.41	0.17	>0.3	939	[35]
J0820+4543	454.36	0.41	>0.44	388	[17]
SDSS0917+4638	455.64	0.17	0.75	2222	[69] [12]
PG1114+224	460.80	0.41	>0.07	260	[70]
SDSS J0152+0749	464.95	0.17	0.82	977	[38] [12]
J1906+6239	474.32	0.26	>1.06	246	[17]
J0116+4249	480.96	0.26	>0.81	4506	[17]
J0155-4148	495.17	0.22	>0.67	481	[23]
WD0455-295	516.10	0.40	0.44	97	[71] [59]
J0050+2147	519.25	0.19	>0.46	4102	[35]
J1255-1853	523.78	0.19	>0.73	1818	[23]
J2332+0427	529.80	0.18	>0.61	1087	[35]
J0215+0155	558.64	0.29	>0.58	465	[23]
WD0028-474	560.99	0.60	0.45	97	[72]
J0500-0930	567.86	0.16	>0.3	72	[44] [73]
J1046-0153	569.36	0.37	>0.19	383	[31]
J2245+0750	571.16	0.18	>0.7	1547	[35]
J1240-0958	576.55	0.20	>0.65	769	[23]
J1617+1310	592.19	0.17	0.85	1053	[60] [12]
J1538+0252	603.58	0.17	0.92	1408	[31] [12]
J0027-1516	611.40	0.18	>0.36	518	[35]
WD1013-010	628.60	0.44	>0.38	46	[74] [59]
J0212+2657	646.68	0.17	>0.62	804	[35]
J0837+6648	667.14	0.18	0.76	604	[60] [12]
J0940+6304	697.51	0.18	0.90	4107	[42] [12]
J0022+0031	707.04	0.38	>0.21	631	[33]
HE0410-1137	732.53	0.51	0.39	105	[71]
J2151+2730	742.94	0.19	>0.72	1546	[17]
HE1414-0848	745.65	0.52	0.74	81	[75]
J0840+1527	751.03	0.19	0.75	-	[31] [12]
J0745+2104	777.08	0.40	>0.46	747	[17]
J0755+4800	786.63	0.42	>0.90	183	[31]
J0802-0955	787.49	0.20	0.82	994	[31] [12]
J1104+0918	796.59	0.46	>0.55	189	[31]

... continued

Name	P_{orb} [min]	M_1 [$M_\odot$]	M_2 [$M_\odot$]	Distance [pc]	Reference
J1157+0546	813.60	0.17	>0.44	-	[31]
J1518+1354	830.30	0.15	0.75	3799	[42] [12]
J1514-1436	848.36	0.17	>0.63	1754	[44]
J2151+1614	851.79	0.18	0.80	391	[12]
WD J1518+0658	877.46	0.22	0.83	349	[38] [12]
J0756+6704	889.65	0.18	0.95	2065	[60] [12]
J0130-0530	916.53	0.30	>0.85	4834	[17]
WD1210+140	924.39	0.23	>0.38	212	[73] [59]
HE2200-1341	947.95	0.46	>0.393	138	[59]
J1151+5858	963.39	0.19	0.85	931	[31] [12]
J2339-0347	965.79	0.19	>0.41	1882	[35]
J1236-0444	990.12	0.16	>0.37	524	[44]
SDSS0730+1703	1004.69	0.18	0.76	1330	[32] [12]
J0806-0716	1015.99	0.20	>0.63	1027	[17]
WD 1534+503	1024.26	0.39	0.62	68	[76] [77] [78]
WD 0311-649	1064.98	0.38	0.55	37	[79]
SDSS0845+1624	1088.63	0.40	>0.19	584	[32]
J1439+1002	1114.55	0.18	0.78	726	[30] [12]
J1422+4352	1114.55	0.18	0.78	3215	[30] [12]
J2339+2024	1145.92	0.18	>0.28	1387	[35]
J0308+5140	1160.50	0.15	>0.16	2278	[60]
J0811+0225	1183.59	0.18	1.28	1839	[31] [12]
J1039+1645	1188.00	0.46	>0.31	610	[42]
WD 1606+422	1208.66	0.57	0.45	43	[78] [77]
PG1519+500	1238.83	0.42	>0.14	306	[80]
HE0320-1917	1245.48	0.29	>0.35	115	[73] [59]
J2317+0602	1248.51	0.38	>0.38	558	[35]
J0125+2017	1278.12	0.18	>0.14	4528	[42]
J1638+3500	1304.73	0.70	>0.45	103	[35]
J2348+2804	1324.99	0.22	>0.25	1365	[17]
J1241+0633	1381.13	0.20	0.80	422	[42] [12]
LP 400-22	1454.63	0.19	0.77	366	[81] [82] [12]
J0815+2309	1545.94	0.20	0.80	2117	[31] [12]
PG0934+338	1604.45	0.38	>0.5	322	[79]
GD 360	1623.46	0.35	>0.178	89	[55]
NLTT 12758	1661.77	0.83	0.69	33	[83] [84]
WD1428+373	1665.71	0.35	>0.233	98	[85]
WD1022+050	1666.30	0.39	>0.283	43	[84] [59]
NLTT 16249	1671.84	0.47	0.51	60	[86] [87] [88]
J0135+2359	1695.82	0.21	>1.02	847	[23]
J1021+0543	1799.93	0.23	>0.33	1420	[35]
PG0834+501	1848.96	0.40	>0.22	515	[79]

... continued

Name	$P_{\rm orb}$ [min]	M_1 [$M_\odot$]	M_2 [$M_\odot$]	Distance [pc]	Reference
J0124+3908	1860.64	0.41	>0.69	833	[35]
J0147+0113	1876.87	0.24	>0.74	809	[35]
J0441-0547	1900.76	0.18	>2.28	4733	[35]
PG1036+086	1912.75	0.42	>0.37	231	[79]
WD0136+768	2026.40	0.47	0.37	75	[37]
J1512+2615	2139.36	0.25	0.76	934	[30] [12]
WD1202+608	2149.96	0.49	>0.25	202	[89]
SDSS J022932.28+713002.7	2152.22	0.18	1.19	1625	[90]
L870-2	2240.32	0.47	0.52	13	[91] [92]
J1130+0933	2245.46	0.18	>0.19	-	[42]
WD1204+450	2307.83	0.46	0.52	122	[37]
WD 1447-190	2578.80	0.41	0.33	49	[78]
WD0341+021	2621.80	0.38	>0.33	143	[93]
WD0326-273	2700.58	0.51	0.59	23	[73]
HE0315-0118	2754.43	0.40	0.49	70	[71] [59]
PG 1632+177	2951.81	0.49	0.40	26	[76] [77]
J1128+1743	3117.60	0.18	>0.11	1628	[42]
WD1349+144	3181.54	0.53	0.33	116	[94] [73]
HE1511-0448	4639.68	0.48	>0.46	293	[73]
WD 1241-010	4820.27	0.31	>0.373	83	[55]
PG1317+453	7015.88	0.33	>0.421	49	[55]
PG2032+188	7321.82	0.41	>0.469	109	[55] [84]
WD1824+040	9023.04	0.43	>0.515	45	[84] [59]
PG1115+166	43326.72	0.43	0.52	91	[95] [96]
ZTF J1356+5706	91.93	0.45	0.27	361	[40] [39]
ZTF J1758+7642	189.12	0.29	0.21	624	[40] [39]
WD2253-081	–	0.2	-	36	[97]
HS1334+0701	–	0.35	-	106	[59]
WD0032-317	–	0.35	-	431	[96]
WD2336-187	–	0.36	-	37	[59]
WD0344+073	–	0.39	-	139	[59]
WDJ135342.35+165651.75	–	0.47	0.43	102	[77]
WDJ002602.29-103751.86	–	0.47	0.42	88	[77]
HE0205-2945	–	0.413	-	101	[59]
WDJ183442.33-170028.00	–	0.42	0.46	97	[77]
WDJ141632.84+111003.85	–	0.47	0.42	129	[77]
WDJ212935.23+001332.26	–	0.44	0.44	65	[77]
WD2345-4810	–	0.43	-	247	[59]

... continued

Name	P_{orb} [min]	M_1 [$M_\odot$]	M_2 [$M_\odot$]	Distance [pc]	Reference
WDJ152038.37+390349.32	–	0.61	0.32	94	[77]
HE0031-5525	–	0.45	-	68	[96]
WD2308+050	–	0.45	-	231	[96]
WD2330-212	–	0.45	-	263	[59]
WDJ114446.16+364151.13	–	0.42	0.45	90	[77]
WDJ005413.14+415613.73	–	0.43	0.45	54	[77]
WDJ084457.81+453632.94	–	0.58	0.43	61	[77]
HE0455-282	–	0.47	-	233	[59]
WDJ000319.54+022623.28	–	0.47	0.38	158	[77]
WDJ013446.42+282616.83	–	0.49	0.43	177	[77]
WDJ020119.40-050748.59	–	0.49	0.54	85	[77]
WDJ151109.90+404801.18	–	0.67	0.44	55	[77]
WDJ170120.99-191527.57	–	0.67	0.48	97	[77]
HE0325-4033	–	0.49	-	105	[59]
WD1124-018	–	0.49	-	180	[26]
WDJ211327.98+720814.03	–	0.42	0.38	96	[77]
HE0131+0149	–	0.5	-	48	[59]
WD0114-605	–	0.5	-	97	[96]
HE0417-3033	–	0.5	-	144	[96]
HS1204+0159	–	0.5	-	219	[96]
EGGR 561	–	0.505	-	55	[59]
WDJ221209.01+612906.96	–	0.54	0.55	64	[77]
WDJ182606.04+482911.30	–	0.47	0.54	136	[77]
WDJ141625.94+311600.55	–	0.47	0.42	116	[77]
WDJ014202.72+262354.58	–	0.53	0.45	173	[77]
WD0216+143	–	0.54	-	83	[59]
WDJ231404.30+552814.11	–	0.66	0.38	105	[77]
WD2254+126	–	0.55	-	63	[96]
HE0221-2642	–	0.55	-	179	[96]
HE0344-1207	–	0.55	-	68	[96]
HE0516-1804	–	0.55	-	84	[96]
WD2359-324	–	0.55	-	193	[96]
WDJ013812.93+444252.10	–	0.57	0.53	82	[77]
WDJ180115.37+721848.76	–	0.55	0.62	128	[77]
WD2248-504	–	0.6	-	63	[96]
HE0221-0535	–	0.6	-	112	[96]
WDJ080856.79+461300.08	–	0.6	0.47	118	[77]
WDJ130014.82+181734.41	–	0.68	0.46	84	[77]
HS2216+1551	–	0.64	-	130	[59]
WDJ020847.22+251409.97	–	0.55	0.74	39	[77]
WDJ192420.74+070135.14	–	0.59	0.63	162	[77]
HS0237+1034	–	0.67	-	113	[59]

... continued

Name	P_{orb} [min]	M_1 [$M_\odot$]	M_2 [$M_\odot$]	Distance [pc]	Reference
HS2046+0044	–	0.7	-	216	[96]
HE2148-3857	–	0.7	-	176	[96]
WDJ180150.89+103401.08	–	0.59	0.53	116	[77]
WDJ165935.59+620934.03	–	0.5	0.7	112	[77]
WDJ181058.67+311940.94	–	0.834	0.721	49	[77] [98]
WDJ214323.95-175413.00	–	0.64	0.64	119	[77]
WDJ192002.51-184442.99	–	0.73	0.65	156	[77]
WD1233-164	–	0.75	-	67	[96]
HE0324-1942	–	0.78	-	141	[67]
WD0128-387	–	0.854	-	54	[70] [59]
MCT0136-2010	–	0.86	-	24	[59]
WD1736+052	–	-	-	45	[99]
HS 0213+059	–	-	-	180	
WD0101+048	–	-	-	22	[100] [92] [59]
GD 69	–	-	-	32	[75]
WD 1418-088	–	0.6	0.68	38	[78]
ATLAS J1138-5139	27.69	1.02	0.24	553	[101] [102]

Chapter 2

Methodology

2.1 Charge-coupled devices

Charge-coupled devices (CCDs) are the detector type for the overwhelming majority of astronomical cameras owing to their ability to obtain high quantum efficiency, low readout noise and high charge-transfer efficiency. Photons hit the focal plane and become trapped in a potential well, exciting an electron from the valence band of the metal-oxide semiconductor to the conductance band and creating an electron-hole pair. To maximise the efficiency of electron capture, a bias voltage is applied to cause a deeper depletion region. Over the integration time of an exposure, multiple photons are captured and the charge is stored within the pixel, before being readout as a voltage that is converted to analogue to digital units (ADU). The conversion factor between the number of electrons and one ADU is measured as the 'gain', and this can be used to revert back to the number of electrons obtained (or the number of 'counts'). Furthermore, electronic and thermal noise is present in the readout of an exposure even after instrument cooling which impacts the noise level of all measurements, typically on the order of a few electrons for each pixel in CCDs. Incoming light follows a Poisson noise distribution following a fixed mean rate (fractional error $\propto 1/\sqrt{\text{counts}}$) while the readout noise is a fixed value, and hence the readout is only relevant for low signal-to-noise observations.

Readout times for typical detectors are on the timescale of seconds to tens of seconds and a mechanical shutter blocks light from hitting the surface of the imaging area between science exposures. Each step occurs sequentially in order of finishing the exposure, reading out and starting a new exposure. For fast variable sources where times of interest are short lived (e.g. eclipses, pulsations), the build-up of lost readout time leads to an excessive fraction of the total time on target lost between exposures. More recently, some instruments are being developed with Complementary Metal Oxide Semiconductor

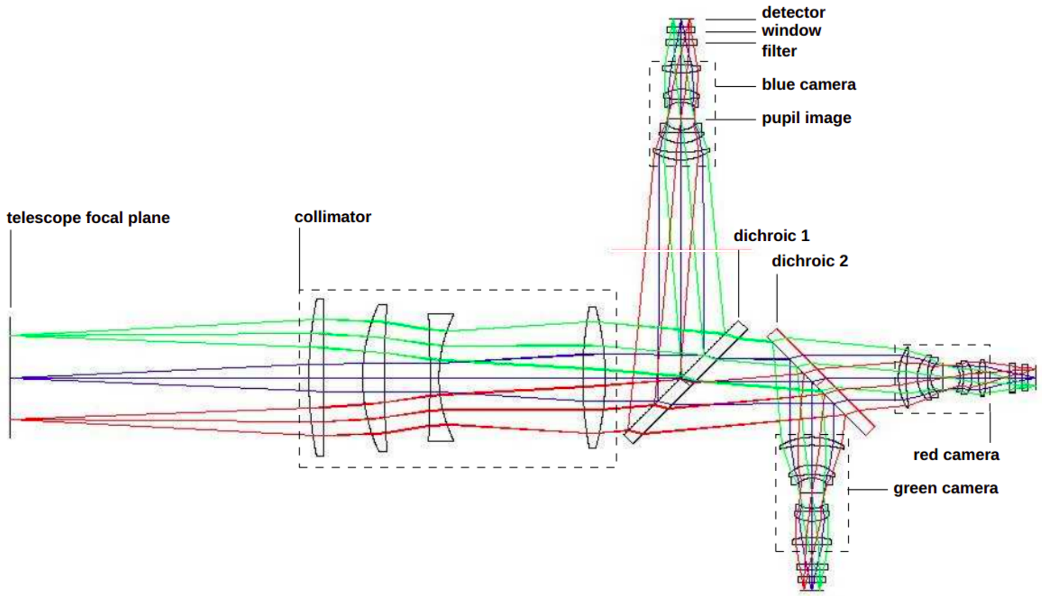

Figure 2.1: Figure 2 of Dhillon et al. [2007] showing the light path entering from the telescope focal plane (left) before having blue, green or red/near-infrared wavelengths split into separate cameras, allowing the simultaneous observation of all.

(CMOS) cameras, where pixels are readout individually, reducing readout time and noise. Though another alternative to bypass this issue comes with frame transfer CCDs. Here, instead of reading out and saving the image instantly, the signal is shuffled from an imaging to a storage area quickly in such a way that there is no need for a mechanical shutter.

This was the original motivation of the ULTRACAM [Dhillon et al., 2007] instrument and the subsequent projects of ULTRASPEC [Dhillon et al., 2014] and HiPERCAM [Dhillon et al., 2016, 2018, 2021] – fast photometry with practically no readout time and low readout noise. An additional motivation is the ability to take simultaneous photometry across multiple bands for maximum science efficiency. ULTRACAM and HiPERCAM use a series of dichroics to split and redirect the incoming beam, where the design of the dichroic controls the wavelengths reflected and transmitted. An image of this design is shown in Fig. 2.1. Light enters from the telescope focal plane and a dichroic splits blue light towards the blue camera, followed by green light towards the green camera and allows red light to be transmitted straight through to the red camera. The blue and green cameras are exclusively used for u_s-band and g_s-band, while the red camera is primarily used for r_s or i_s observations. Exploitation of data from ULTRACAM and HiPERCAM appears in Chapters 3 and 4, utilising data from all cameras for each observation, and the same for the single-colour ULTRASPEC.

2.2 Calibration handling

Regardless of its astronomical purpose, the calibrations required to go from raw data to publication-ready data are near identical for all optical/near-infrared detectors.

Applying a bias voltage causes thermal noise that needs subtracting from all other images to zero the number of electrons observed per exposure. This is subtracted from all frames through a near-zero-second exposure in an environment that is as dark as possible. Along the same lines, further signal can build up over the course of an exposure. The cause of this is primarily through the thermal generation of electrons, but can also be from impurities in the semiconductor material (hot/cold pixels) or inefficiency in the charge transfer process. Thermal generation of electrons is mitigated by cooling the detectors to low temperatures, but can still be a prominent source of noise. Dark images are performed to tackle the issue, where a dark image is the same as a bias but typically lasts for the duration of the exposure time of the science image. The final[1] calibration is flat field images. Here, the detector is shone at a uniformly illuminated light source (the sky during twilight hours or an e.g. Tungsten lamp from within the dome or the optics of the instrument), the measured flux is normalised and divided through the image in order to correct for the relative sensitivity of each pixel. The process of events to obtain a final reduced frame goes

$$\text{Reduced image} = \frac{\text{science} - \text{(dark-bias)} - \text{bias}}{norm(\text{flat} - \text{(dark-bias)} - \text{bias})} \tag{2.1}$$

where the number of counts in the (dark$-$bias) frames are scaled for the exposure time of the relevant science and flat images. The reduced images are then ready for data extraction.

2.3 Photometric observations

The light captured by CCDs can be used to directly study the properties of an astronomical object. In photometry, this is typically used with a filter to gain accurate brightnesses over a defined wavelength range. Stars are observed over the full field of view. Each are measured as the number of counts above zero, such that all observations are placed on an instrumental flux scale with the brightness of stars relative to each other. Stars can be flux calibrated knowing the zeropoint magnitude of the detector (the magnitude of a source that would produce 1 count per second), the flux of a flux standard star and the airmass of observation. Of higher interest for the targets in this thesis is relative photometry. The premise is that, as all stars on the image are observed at the same time, the sky conditions are near identical for any two stars on the frame. This means that relative flux of your target compared to a

---

[1] In the infrared, fringe correcting images can be important to correct for interference between reflections in the optics of the imager but are not crucial for the targets of interest in this thesis.

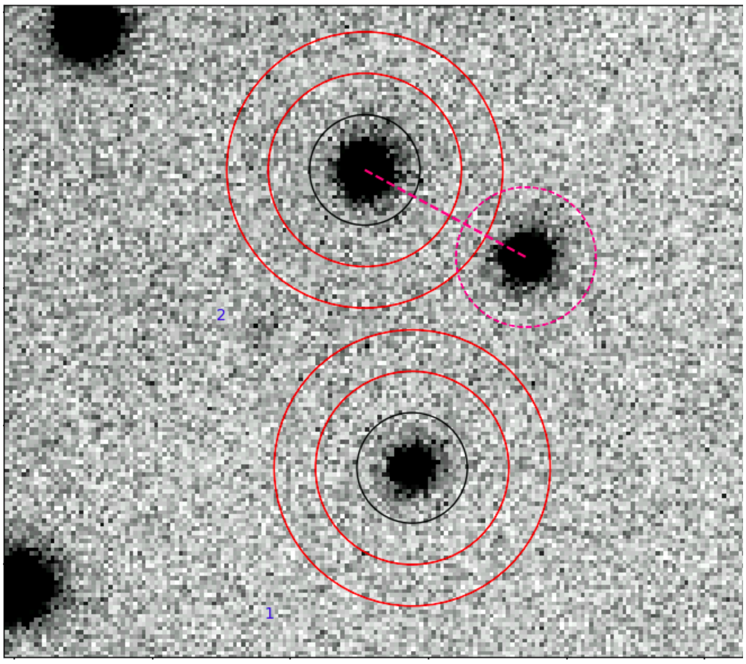

Figure 2.2: A graphical representation of aperture photometry on a frame taken by HiPERCAM. Apertures are drawn around 2 stars in the field and then all flux that falls within is summed, while the red rings represent the inner and outer apertures for sky subtraction. Contamination from nearby sources is not desired, so for the upper star a pink region shows masked pixels from the summing.

bright, non-variable source in the field of similar colour results in a perfect flux calibration compared to that star alone.

To do this, we can perform differential aperture photometry. An aperture is centred on a star with a radius that captures all light within it, and around it are two other annuli. The centre can be found by modelling the point spread function (PSF) of the star, which accounts for the response of the optics and the spreading of light from that of a point source from atmospheric dispersion. Popular examples include a Gaussian function or a Moffat function given their simplicity for fast modelling and their accurate representation of the profile. Then, two annuli mark inner and outer bounds to deduce the sky background level (Fig. 2.2), which is subtracted from the total flux from within the aperture. The same is repeated for a comparison star. With apertures tracking the centre of the stars over multiple images and extracting the sources in the same method, masking any contamination from other objects in the field, a lightcurve is built, as shown in Fig. 2.3.

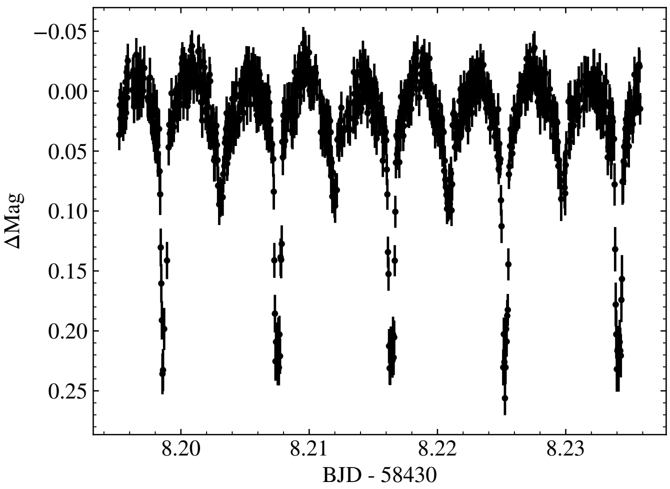

Figure 2.3: The final product of the extracted aperture photometry of the $P = 12.75\,\mathrm{min}$ eclipsing DWD binary J0651+2844 [Hermes et al., 2012] in the g_s-band using HiPERCAM. The exposure time of each image was 3 s and the combined photometry of each image creates this lightcurve.

2.4 Spectroscopic observations

Spectrographs

A spectrograph is the full optics system that leads to light incident on the detector after the final mirror reflection. Light entering a slit passage is incident on a diffraction grating which splits the beam into separate wavelengths in one direction while maintaining its spacial resolution in the other. For long-slit spectroscopy, the angle of incidence of light on the grating is (almost always) positioned such that the first diffraction order shines on the detector, and the location of where the star is placed for the length of the slit is such that the split beam is centred on the detector. The premise is the same for echelle spectrographs, but here multiple refractive orders are viewed simultaneously (usually in the 10s, 20s or larger) to view a larger range of wavelengths at higher resolution but at the cost of a lower efficiency.

2.4.1 Wavelength calibration

Along with the previously mentioned calibrations and actions applied to science frames, one also needs to calibrate the spectral axis of the observations in spectroscopic observations.

For wavelength calibration, we shine light from a lamp with a clear series of discrete energy transitions with known wavelengths. Typical examples are lamps composed of Neon, Argon or Xenon, with the choice of each dependent on the wavelength range of interest. When projected onto the detector after passing through the instrument optics, each energy transition appears as a thin line in the spatial direction. The location of each line is then usable to convert a pixel value to a physical wavelength. A polynomial to the full line series of lines is fit and applied, where, for measurements that require a good wavelength calibration precision, an arc frame is taken just before/after the science observation. The purpose of this arc is to be sensitive to changes in the flexure and temperature of the instrument at the time of observation.

2.4.2 Beam tracing and sky subtraction

The rotation of the spectrograph is aligned to make the beam cover as few rows as possible so that the number of pixels covered (and hence contribution to readout noise) is minimised. But, there is still some tilt in the projected beam because of the $\sin(\theta)$ term in the diffraction grating equation. To model for this, the trace of the beam is first fit. Next, the region of the sky background around the beam is set (in the spatial plane) and a low-order polynomial is fit to predict the imprint of the sky background on the beam, which is then subtracted from each column.

2.4.3 Profiling and extraction

A profile fit of the spectrum should then be considered. Following the trace of the spectrum in shape, this step fits the profile of parallel lines around the beam under the expectation that neighbouring columns are near-parallel [Horne, 1986; Marsh, 1989]. Each profiled line can then be compared to identify the fraction of flux that falls into individual rows and weighted for optimised error calculations. Furthermore, the technique can be used to identify and mitigate bad pixels/cosmics around the beam.

The flux for each column on the spectral axis can be resolved by summing up all the flux in the adjacent rows for which target flux is registered. This is so-called ‘normal extraction’. Better treatment for an optimal flux in each column is given by weighting the pixels within each column. The optimal weight is given by

$$W_i = \frac{P_i/V_i}{\sum_i P_i^2/V_i} \tag{2.2}$$

with P_i the fraction of the total flux in the column i and V_i the variance of all included pixels in column i. The improvement in signal-to-noise from optimal extraction is appreciable [Marsh, 1989], and especially so for lower signal-to-noise observations. Now with these weightings, a weighted sum of the flux can be obtained for every column.

The resultant spectrum considers each step, going from a 2D image to a 1D spectrum, and the wavelength solution determined from the arc frame can be applied. If desired, the flux can be calibrated using a spectro-photometric standard star, where its spectrum is extracted in an identical way and the operation to convert the target brightness to the true brightness of the standard star is applied. A final consideration may be to remove telluric features (originating from light penetrating the Earth's atmosphere) if desiring a good spectrum in the near-infrared/infrared where these features are most prominent.

2.4.4 Converting between time systems

Precisely keeping track of time has been at the heart of variable astronomy for centuries. A year has long been the time taken for the Earth to orbit the Sun and a day as the period of a full rotation of the Earth and a second in modern times is recognised by the radioactive decay time of a cesium-133 atom rather than a fraction of a day. When very high time precision is required however, one should correct not only for the location of the Earth but the location and space velocity of the observer itself. This is a crucial further step because of the motion of the Earth around the Sun and the light travel time depending on the coordinates of the target and the location of Earth.

Even then, the heliocentre is not the best option as the centre of mass of the solar system largely lies between the Sun and Jupiter, hence the best reference frame of choice for extrasolar objects is the barycentre. Observations are easiest tracked by storing the Julian Date (JD), which is an integer number each day, a heliocentric JD (HJD) or a barycentric JD (BJD). These small differences are crucial when considering the sub-second time precision required for orbital decay monitoring or phase folding on an orbital ephemeris.

Additionally, one must consider which reference system should be used for the start of these days. A convenient one that has been adopted worldwide and across astronomy is Coordinated Universal Time (UTC) which relies on a time at the prime meridian that does not vary with daylight saving hours. At the prime meridian, the time is maintained within a second of mean solar time throughout the year and becomes an integer at midnight, making it intuitive too. The one flaw is that UTC requires the addition of leap seconds to compensate for the varying rotational speed of the Earth. Formally, time is kept through the International Atomic Time (TAI) which follows the weighted time from multiple clocks worldwide that measure the frequency of microwaves associated with hyperfine transitions in the ground state of a Caesium-133 atom, which is free of the need for leap second correction. The difference between TAI and UTC is presently 37 seconds, caused by the additions of leap seconds. Barycentric Dynamical Time (TDB) is another time reference system which is commonly used in astronomy when desiring very fine temporal precision, since the time keeping is based at the barycentre and it accounts for gravitational/velocity-related time dilation effects.

2.5 Data analysis

2.5.1 Binary system modelling basics

The orbit of a detached binary is governed by Kepler's third law

$$P^2 = \frac{4\pi^2}{G(M_1 + M_2)} a^3 \tag{2.3}$$

The masses of the two stars and the orbital separation (or period) are the core constraints for a basic model of the system. The primary tools for constraining an orbit are photometric variability and radial velocity variability (see Section 2.5.5). I will primarily address eclipsing binaries as both aspects are applicable. Here, the components constraining the depth of the primary and secondary eclipse are the radii of the stars and their effective temperatures, hence the fraction of light that is contributed in each passband.

Imagining the case where one star is visible in the spectrum and the flux from the companion barely contributes, we can fit the temperature of this seen component using synthetic spectra and maintain this solution fixed in light curve modelling while varying the temperature that adds radiated flux from the companion. The relative depth of eclipses is proportional to the relative radius and temperature of the two stars, allowing an immediate way to probe this constraint with the relative depths of the primary and secondary eclipse in any passband. To break degeneracy between the temperature and radius, we can also obtain multi-colour eclipses that when fitted are sensitive to changes in the relative flux in the relevant wavelength band because of a different shape of the spectral energy distribution of each star.

Then lastly for the eclipses, we can see how quickly ingress/egress occur to deduce the inclination of the system; in a grazing eclipse, the duration of ingress/egress will be much longer than in a total eclipse. These are the primary constraints deduced from fitting photometry, as is later discussed in Section 4.4 with binary star modelling.

For time-series radial velocities of the source, the stars are orbiting with a radial velocity amplitude $K \sin(i)$ and the masses of the stars are found through the binary mass function (see Section 5.5.2). Coupled with photometry that show eclipses, the degeneracy between mass and inclination is crucially broken and precise masses of the stars are solvable. Overall, this leaves us with the most important system and atmospheric parameters for the binary.

This is a generic situation but it is the fundamental logic of all light curve fitting for binaries. That said, there are a few other crucial elements and the most relevant aspects are as follows. 1) Ellipsoidal modulation: the deformation of a star from sphericity due to the pull of the companion's gravitational field. This induces a quasi-sinusoidal trend in the light curve due to a larger surface area of the brighter/dimmer star being shown in the direction of the observer. 2) Irradiation/reflection: the incident light from a star's companion heats the surface of the star, creating a day side and a night side, also causing a sinusoidal photometric trend. Irradiation is often strongest in the red/near-infrared wavelengths. A figure depicting the effect of irradiation and ellipsoidal modulation is found in Fig. 2.4. 3) Limb darkening coefficients: Limb darkening describes the extent to which a star dims when comparing the received flux at the edges to the centre. This is important in eclipsing binaries as the effect causes the amount of occulted light to change over the duration of the eclipse. In total eclipses of planetary systems, this effect causes a pronounced curve leading up to the centre of eclipse because the star dramatically outshines the planet, whereas in binaries limb darkening is relevant at the outermost contact point but during eclipse is often flat-bottomed. 4) Gravity darkening coefficients: Gravity darkening is similar to limb darkening but is caused by the rotation of the star and its gravity, typically making the poles appear darker than its centre.

The effects of 1) and 2) are mainly noticeable at inclinations greater than about 50–60° [e.g. Schaffenroth et al., 2022] [2]. Exposure smearing can at times be relevant due to the fact that ultra-compact DWD eclipses last for minutes at most. All of these aspects can be modelled simultaneously to arrive at a system solution where the synthetic observables best match the observed light and radial velocity curve(s).

In this thesis, I use the PHysics Of Eclipsing BinariEs (PHOEBE) [Prša and Zwitter, 2005; Prša et al., 2016; Horvat et al., 2018; Jones et al., 2020; Conroy et al., 2020] package to minimise a solution with a Markov Chain Monte Carlo (MCMC) algorithm (Section 2.6.2). Apart from gravitational lensing, PHOEBE includes all of these effects and treats the star as a mesh of a couple thousand of triangles that cover the visible surface area of the star and essentially considers each triangle as its own source and own chance of being eclipsed. The meshing algorithm is based on the Wilson-Devinney structure [Wilson and Devinney, 1971] but modified to the Horvat method [Horvat et al., 2019]. As will be seen in Chapter 4, I utilise aperture photometry extracted from ULTRACAM to model a new eclipsing and ultra-compact DWD binary and fit the system parameters through use of this software.

---

[2] Other notable features for DWD binaries are Doppler beaming, the Rossiter-McLaughlin effect, gravitational lensing and additional light from a third source, for example an accretion disc. That said, these are not observable for the systems studied in this thesis.

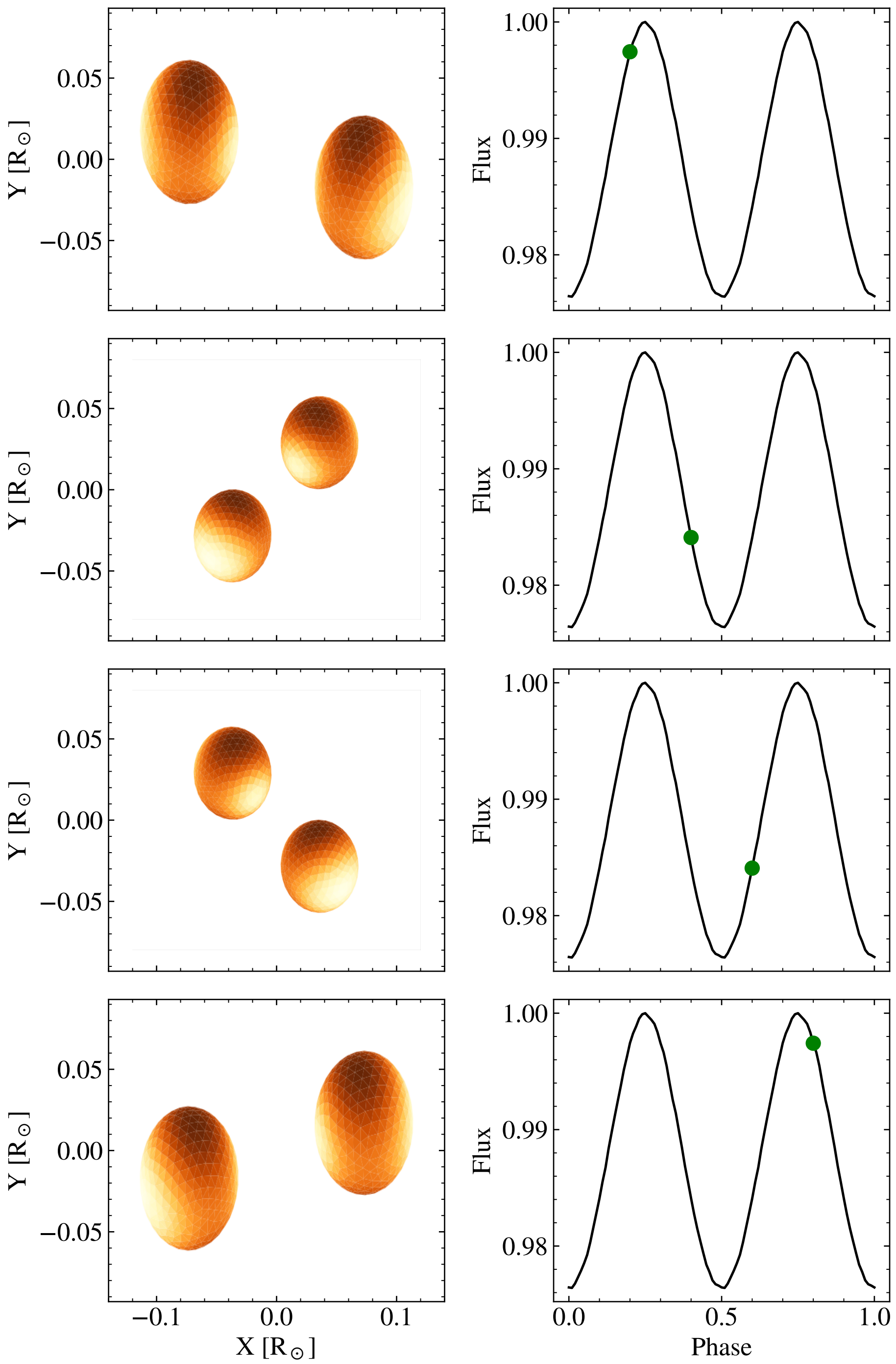

Figure 2.4: A depiction of irradiation and ellipsoidal modulation in a model binary of identical stars synthesised using the PHOEBE package. For illustrative purposes, the temperatures of the stars are high (40 000K) and the orbital period is small (600 s), the masses are 0.5 $M_\odot$, the radii are 0.04 $R_\odot$ and the orbital inclination is 50°. Different orbital phases are shown in each row. Brighter colours in the left column indicate a higher temperature. The orbital phases are indicated with the green point on the model light curve.

2.5.2 Orbital timing

The premise of orbital timing is to monitor the apparent light arrival time of a given phase and search for any deviations away from a constant period. In DWDs as discussed in the introduction, the strongest deviation is typically caused by shrinkage of the orbit due to gravitational wave radiation. Over the course of years the change in the orbital period is miniscule, but the effect of a slight change of period builds up over thousands of orbits and this shift in phasing is observable. The technique is most famous for the double neutron star, Hulse-Taylor pulsar binary system [Hulse and Taylor, 1975], and has many applications in astronomy.

With $\phi(t)$ a function that defines the number of cycles that have occurred in a given amount of time t and T_0 the reference epoch, a Taylor expansion gives

$$\phi\left(t\right) = \phi_0 + f_0\left(t - T_0\right) + \frac{\dot{f}_0}{2}\left(t - T_0\right)^2 + \frac{\ddot{f}_0}{6}\left(t - T_0\right)^3 + \ldots \qquad (2.4)$$

and the orbital frequency evolves as

$$f(t) = f_0 + \dot{f}_0(t - T_0) + \frac{\ddot{f}_0}{2}(t - T_0)^2 + \ldots \qquad (2.5)$$

Furthermore, if we take $E = tf_0$, it can be shown that the observed minus calculated time of a point follows

$$O - C = \Delta T_0 + \Delta P_0 E + \frac{1}{2} P_0 \dot{P} E^2 + \ldots \qquad (2.6)$$

This provides a direct relation between the observed time offset and the orbital derivatives of the binary. Typical and logical phase choices for monitoring are the centre of an eclipse or the photometric maximum of a source. An exemplar case of a DWD binary with significant orbital decay is presented in Fig. 2.5.

Eclipse fitting

For eclipse timing, one can use the model found from light curve modelling and shift the template to obtain the best-matching eclipse centre.

Non-eclipsing sources

The same can be performed with non-eclipsing sources through the timing of photometric maximum or the first harmonic of a Fourier series. For sinusoidal variability, just one harmonic is apparent, and the first and second harmonic can be modelled with

$$d + A\cos\left(\omega(t - T_0)\right) + B\sin\left(2\omega(t - T_0)\right) + C\cos\left(2\omega(t - T_0)\right) \qquad (2.7)$$

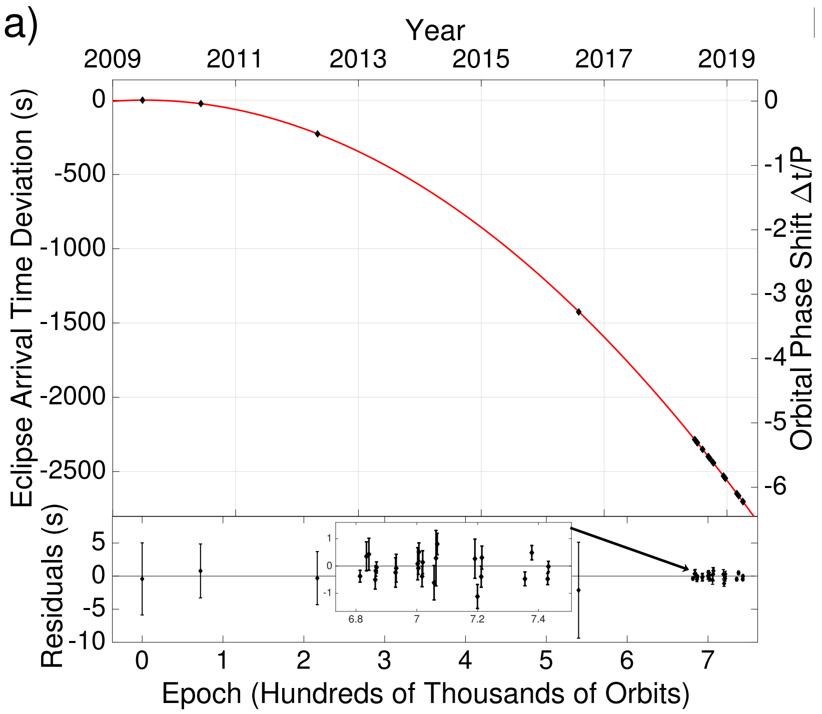

Figure 2.5: Figure 2 from Burdge et al. [2019a] showing the orbital decay of the shortest-period eclipsing DWD binary ZTF J153932.16+502738.8. Points were derived by tracking the centre of eclipse time of the binary with fast photometry. The sloped curve compared to that expected from a constant period represents the orbital decay given in equation 2.6.

where d is an offset term, A the amplitude of the first harmonic, B/C the amplitudes of the second harmonic terms and $\omega = 2\pi f$ the orbital angular frequency. As will be seen in Chapter 3, a second harmonic can be used to model the additional flux from the impact spot of direct-impact accretion (see Section 1.2.2) but is also relevant in compact binaries for accretion discs, superhump periods or magnetic spots.

2.5.3 Obtaining atmospheric constraints

I have mentioned the importance of deriving atmospheric parameters for a WD earlier in this thesis. Now, I will address the technique to do so. While collaborators with previously developed scripts contributed to deriving atmospheric parameters in Chapters 3 and 4, I gained plenty of experience in fitting WD and DWD spectra with the development and publication of my pipeline.

Using spectra

First we take a grid of synthetic spectra. Discussion of the grid's creation is out of the scope of the topic of this thesis, but please see the details in Tremblay et al. [2013a, 2015] and references therein. As DA, DB and DC WDs are solely covered here and are the ones that I have had experience with, these are the spectral types that I will discuss. The unique axes of the synthetic spectra are the effective temperature, the surface gravity and in the case of DBs/DCs the relative hydrogen to helium abundance. For each combination of these variables, the flux per unit stellar surface area supplied is supplied at various wavelengths, with the whole construct acting as a rectangular grid. To sample a given wavelength and atmospheric parameters, the grid can be bilinearly or (for DBAs) trilinearly interpolated between the nearest values of the grid for each variable to trial all solutions for a resultant spectral energy distribution. The spectrum should then be reddened if the reddening coefficients are known to include the impact of light passing through the interstellar medium en-route to the Earth. If required, the flux can be converted from an Eddington to an absolute flux received at Earth.

No broadening effects due to instrumental responses should be included in the grid, but they are in the observations. A convolution using a Gaussian kernel [3] at the same resolution as the observations should be used to smear the synthetic grid to reciprocate the response from the spectrograph. Lastly, the wavelength axis of the convolved spectrum for a set of atmospheric parameters has a finite number of points and should be interpolated to the wavelength of the spectra to allow for a direct comparison between a model and

---

[3] This should be the line spread function of the instrument, but for all cases a Gaussian is sufficient as the line spread function is rarely known/published.

the observations. Multiple synthetic models can be trialed and a best-fitting model can be obtained as described in detail in Section 2.6. This should include the apparent Doppler shift of all stars (see Section 2.5.5) in the fitting procedure.

2.5.4 Using broad/narrow band photometry

While model spectral lines are convolved with a Gaussian kernel to simulate the response of the detector, this is not possible when fitting broad/narrow band photometry because of the non-uniform transmission function associated to each data point. This could be relevant for low resolution spectra as well, but assumed negligible. Single-filter photometry spans a few 10s of angstroms (narrowband) to a couple of hundreds (broadband) and the transmission function including full atmospheric (if relevant), detector and telescope responses are given from the supplier. This simply describes how the throughput of the filter varies over all relevant wavelengths (T(λ)), while the integrated flux of the flux calibrated photometry through the filter (f(λ_{eff})) is measured in an observation. To synthesise photometry from a model spectrum, one needs to integrate over the full passband. For energy counting detectors, this is performed with

$$f(\lambda_{\text{eff}}) = \frac{\int T(\lambda) f(\lambda) d\lambda}{\int T(\lambda) d\lambda} \tag{2.8}$$

while for photon counters

$$f(\lambda_{\text{eff}}) = \frac{\int T(\lambda) f(\lambda) \lambda d\lambda}{\int T(\lambda) \lambda d\lambda} \tag{2.9}$$

and $f(\lambda)$ is the flux of the model spectrum for a specific wavelength. For example, Simpson's integration can be used to integrate the model numerically to obtain $f(\lambda_{\text{eff}})$.

Fitting the absolute fluxes of ground-based spectra is well known to be inaccurate, with typical accuracies to the 10% level. The ability to simultaneously observe many stars with broadband photometry grants a much better calibration of the data as many reference stars can be used to calibrate the absolute fluxes of the target. Eddington fluxes in the model spectrum can be converted to a flux observed at Earth using

$$F_{\text{obs}}(\lambda) = \frac{4\pi R^2}{D^2} F_{\text{Edd}}(\lambda) \tag{2.10}$$

or for scaling the flux of a binary

$$F_{\text{obs}}(\lambda) = \frac{4\pi R_1^2}{D^2} \left(F_{\text{Edd,1}} + F_{\text{Edd,2}} \frac{R_2^2}{R_1^2} \right) \tag{2.11}$$

Given that the photons have penetrated through the interstellar medium and that light scatters more easily in bluer wavelengths, spectra need to be dereddened with interstellar reddening curves. I refer the reader to the work of Gordon et al. [2023] and references within for more information on the generation of the curves, but generally speaking in modelling, a hydrogen column density is assumed (R$_V = 3.1$) and an extinction colour index is quoted (typically E(B$-$V), but this could be E(g$-$r) or any colours). Together, the magnitude of the extinction is calculable for the target of interest (A$_V$) and is used with reddening curves to infer the fraction of lost flux at all wavelengths. Now, the flux of the source and the flux received at Earth can be compared precisely and a solver can be used to minimise the observed and model fluxes. Section 2.6 describes some minimisation processes that can be employed to fit models to the data.

2.5.5 Radial velocity method

The spectral lines of a star shift in wavelength due to the star's surface gravity and motion. From the Schwarzschild metric and employing time dilation, the impact of gravitational redshift to the observed wavelengths of light is given by

$$\frac{\Delta\lambda}{\lambda} = \frac{1}{\sqrt{1 - \frac{2GM}{Rc^2}}} - 1 \tag{2.12}$$

And the phase-dependent radial velocity, V(ϕ) is given by

$$V_{1,2}(\phi) = K_{1,2}\sin(i) + V_{\gamma_{1,2}} \tag{2.13}$$

for a circularised binary, which is always the case for DWDs as they circularise shortly after mass transfer phases. V_γ here is the systemic velocity in the line of sight, and relativistic Doppler shift equation here is writeable as

$$\frac{\Delta\lambda_{1,2}}{\lambda} = \sqrt{\frac{1 + V_{1,2}(\phi)/c}{1 - V_{1,2}(\phi)/c}} - 1 \tag{2.14}$$

with $\Delta\lambda_{1,2}$ being the perceived wavelength shift of spectral lines from each star. In DWD binaries, the radial velocity amplitudes can span from tens to hundreds of kilometres per second, meaning that one requires a spectral resolution, $R = \lambda/\Delta\lambda$, of a couple thousands to detect radial velocity shifts across the orbit of a single-lined source. Double-lined sources comprising two stars with identical spectral type typically need a higher spectral resolution to be disentanglable. In DA+DA DWDs where one is primarily limited to the Balmer line cores, a spectral resolution of at least $R = 5000$ should be used for radial velocity amplitudes of approximately $100\,\mathrm{km\,s^{-1}}$. Increased sensitivity to the double-lined splitting comes with higher resolution observations at the expense of a higher readout noise contribution (because of the need for more pixels in the spectral direction) and often a slightly worse grating efficiency at the blaze wavelength.

I show a comparison plot of the effect of spectral resolution on the detection efficiencies of double-lined DWDs in Fig. 2.6 with resolutions that relate to some low/medium resolution data sources. It can be seen that at $R = 2000$, only systems where the velocity of the two stars exceeds $150\,\mathrm{km\,s^{-1}}$ can be detected as a double-lined DWD, around $100\,\mathrm{km}^{-1}$ for $R = 4000$ and then differences of a few tens of $\mathrm{km\,s^{-1}}$ for higher resolutions to the point where one may become limited by smearing of the spectral signature over the course of the orbit.

There are multiple ways to fit radial velocities to spectra. By far the best approach is to fit a model template that perfectly represents the profile of the spectral lines. In a practical sense however, this is not possible unless a large number of high signal-to-noise observations have been taken of the target and the observations themselves are stacked to obtain a perfect template spectrum. One can solve for an atmospheric solution using synthetic spectra generated from atmospheric grids and use this as a template spectrum to extract radial velocities, but this introduces the issue that state-of-the-art grids have documented imperfections [Tremblay et al., 2013b]. The area most sensitive to the imperfections is unsurprisingly around the line cores where non-local thermal equilibrium effects are at their strongest. Ways around this issue in the literature include isolating the data to fit Gaussian/Lorentzian/Voigt profiles to the line core(s) [Saffer et al., 1988; Maxted and Marsh, 1999], selecting a range that is a few tens of Angstroms around the line cores and fitting a combination of Gaussian profiles and a low-order polynomial to model the broader wings [Kilic et al., 2020a, 2021a], or accepting the imperfections in synthetic grids [Napiwotzki et al., 2020]. The best approach is often subjective to the dataset and typically an increasing spectral resolution amplifies the imperfection in synthetic models. From my personal experience, applying a model template spectrum is the best solution for a spectral resolution $R \leq 10\,000$ to obtain accurate and precise radial velocities. For higher resolution data, where the issue of the line core fitting is more serious, a low order polynomial plus a Gaussian/Lorentzian or a model spectrum plus an additional, narrow Gaussian component to solely improve the line core shape is best (see Chapter 6).

2.5.6 Fitting orbital dynamics with radial velocities

The amplitude of radial velocity (K) is solvable with

$$K_{1,2}^3 = \frac{2\pi G \mathrm{M}_{2,1}^3 \sin^3(i)}{P(\mathrm{M}_1 + \mathrm{M}_2)^2} \tag{2.15}$$

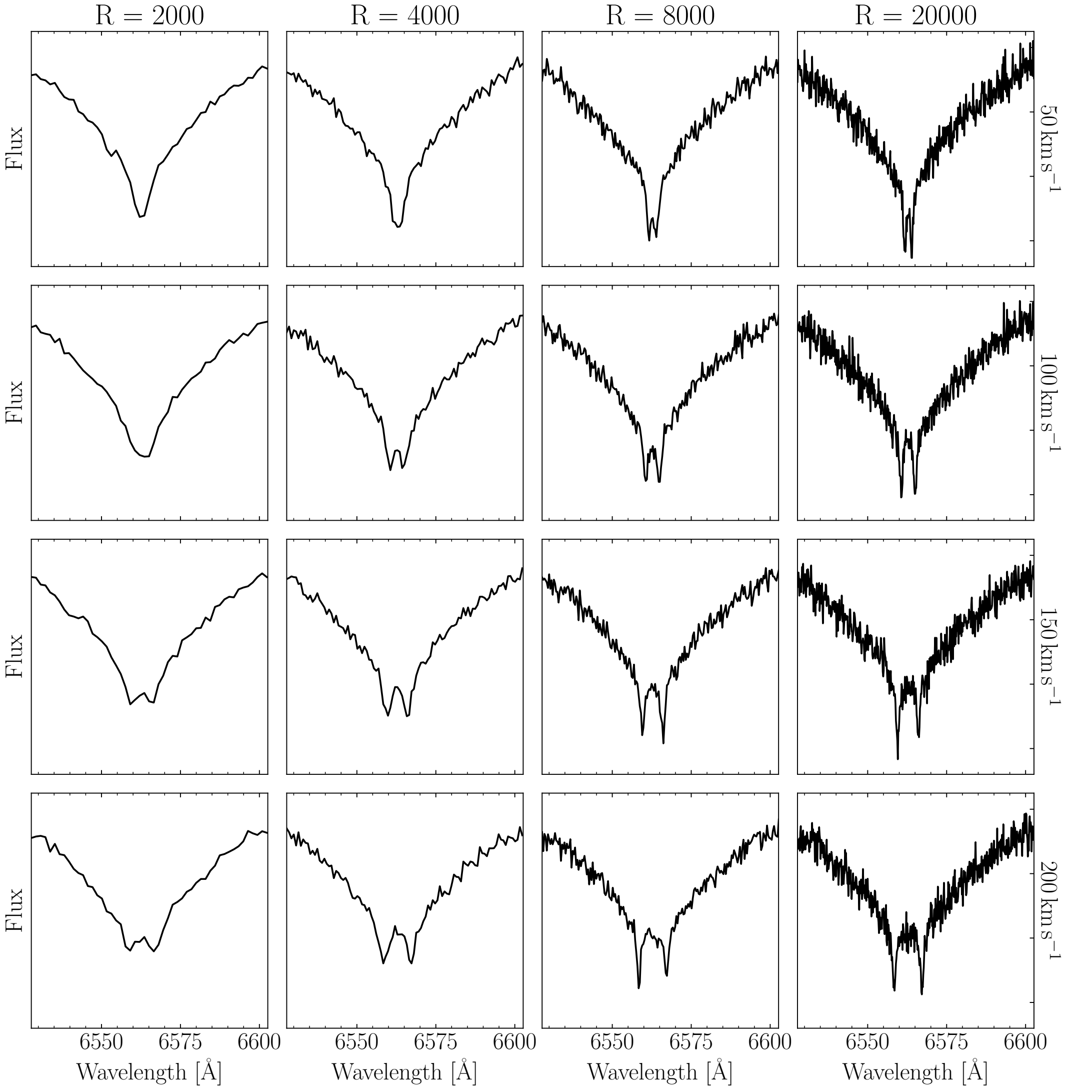

Figure 2.6: A demonstration of the need for higher resolution observations to resolve double-lined signatures in DWD binaries. The spectral resolution of the observations is displayed at the top x-axis and the velocity of each star in opposite direction on the right y-axis. A pixel sampling of 2.2 pixels per resolution element is included to replicate the tendency of long-slit observations sampling slightly above the Nyquist sampling frequency (which is two pixels per resolution element), while the signal-to-noise ratio per angstrom is 100 in all plots. The ability to resolve the narrow line cores of Hα at increasing resolutions is clear by the increased depth of the line core. The resolutions plotted are similar to the resolutions at Hα in SDSS (first column), DESI/4MOST (second column), the data collected in Chapter 5 (third column) and the setup employed by the ESO SPY survey [Napiwotzki et al., 2020] with UVES on the VLT (fourth column). The model spectra used here were two identical $\mathrm{T_{eff}} = 15\,000$ and $\log\,g = 8.0\,$dex DA WDs.

When only one star has radial velocity measurements and the period is well known, there exists a degeneracy in solving for the masses because of the also unknown inclination of the system. In double-lined binaries, this is bypassable solving the simultaneous equation 2.15, becoming

$$\frac{M_1}{M_2} = \frac{K_2}{K_1} \tag{2.16}$$

which obtains an orbitally-derived, model-independent binary mass ratio that can be verified with atmospherically-derived masses of the stars.

Further consistency between the orbital and atmospheric solutions can be obtained with a series of radial velocity measurements for one or both stars. Evidently for two stars with a different surface gravity, the light will be gravitationally blueshifted/redshifted differently to its companion. Through manipulation of equation 2.12, we see that

$$V_{\gamma,1} - V_{\gamma,2} = \frac{G}{c}\left(\frac{M_2}{R_2} - \frac{M_1}{R_1}\right) \tag{2.17}$$

or eliminating the mass of one of the stars from the equation

$$V_{\gamma,1} - V_{\gamma,2} = \frac{G}{c}\left(\frac{K_1 M_1/K_2}{R_2} - \frac{M_1}{R_1}\right) \tag{2.18}$$

Now, the derived V_γ of each star from the radial velocity solution can be compared with the mass of the brighter star and the fitted radii of the two.

Although it is never relevant in this thesis, there is an extra consideration worth mentioning. These equations are valid for a Keplerian orbit and hence assumes that the radial velocities behaves as such. This may not always be the case. The true velocity of the system is measured about the centre of light, meaning that systems with large irradiation profiles deviate the perceived radial velocity towards the day face. The same principle is relevant for eclipsing systems both in terms of the perceived photometric and spectroscopic signature through the Rossiter-McLaughlin effect [Holt, 1893; Rossiter, 1924; McLaughlin, 1924]. As the stars are spinning, eclipses occult either the side of the star spinning away from or towards the observer, making for an asymmetric line profile. Finally, it is hardly relevant for DWD binaries but I mention too that stellar pulsations can induce a fake radial velocity variation which would have to be corrected.

2.6 Computational methods

I have mentioned in this chapter that solutions can be sought with minimisation algorithms. Here, I discuss the process of fitting and obtaining errors through a χ^2 and a Markov Chain Monte Carlo approach.

2.6.1 Least-squares fitting

A mathematical description of least squares fitting will be omitted [see e.g. York, 1968, for details], but its purpose is to take a trial model function and determine how well it fits the data, converging on the solution that fits best. Wide solution boundaries and initial guesses are often supplied to increase the convergence time and avoid local best-fit minima.

Given observed and expected values, the χ^2 can be evaluated with

$$\chi^2 = \sum_{i=1}^{\infty} \frac{(O_i - E_i)^2}{\sigma^2} \tag{2.19}$$

where O_i is the observed data for a point i, E_i is the expected value for that point and σ_i the associated observed error. Convergence can be obtained by trialing solutions and converging at a minimum χ^2 which is the best-fit solution and the fitted error is quoted through the covariance matrix. This approach in deriving errors is analytic and assumes that the structure of the model is correctly specified. This is not always the case where no trial model can perfectly capture the shape of a series of spectral lines.

An alternative and robust approach is to perform bootstrapping. Bootstrapping in this context works in a similar way as mentioned above. The initial starting position of a least-squares fitting algorithm is finely tweaked multiple, e.g. 1000, times while the best-fit solution is again converged upon. In this case however, we obtain a best-fit solution by taking the median of the 1000 iteration distribution of individually-fit values and 1σ errors on the solution are obtained through the 16% and 84% percentiles. This generally does better at producing errors reflective of the uncertainties in the data model at the cost of computing time while, particularly in radial velocity fitting, χ^2 alone can often lead to an underestimated error.

2.6.2 Markov Chain Monte Carlo

Markov Chain Monte Carlo (MCMC) algorithms work to solve a solution by surveying a large initial multi-dimensional parameter space. Independent variables in the model are declared with set boundaries. A number of “walkers” are defined at random starting positions in that parameter space that ‘walk’ over it. The trajectory that they follow create a series of “chains” that converge on a solution of maximised likelihood (which is evaluated by minimising the χ^2 between the data and the model) and trial solutions are chosen by making fine adjustments to the independent variables. Priors on the fit can additionally be enforced to weight solutions by some external information. For example, in light curve fitting, one may apply a prior based on the spectroscopic fit for the effective temperature of that star. These measurements are typically quoted as 1σ errors of a Gaussian distribution (σ_T) with a mean (μ_T), and with this the enforced prior added to the log-likelihood would be

$$\ln(1.0/(\sigma_T\sqrt{2\pi})) - 0.5 * (T_1 - \mu_T)^2/\sigma_T^2 \tag{2.20}$$

Once the chains have converged at minima, all chains are discarded in what finishes a "burn-in" phase. The MCMC algorithm continues and the resultant chains make up the final sample distribution. All of these post-burn-in sample distributions can be used to find the median value and the 32% & 68% percentiles as 1σ errors.

A useful way to visualise the covariance of each parameter is through a corner plot which plots the distributions of each parameter plotted against one another and to inspect density contours within the data. The MCMC algorithm is a far improved option to search for various local minima but is generally a much slower approach to χ^2 fitting. Both algorithms begin to struggle at high dimensions, but are suitable for less than 10–20.

Chapter 3

Two decades of optical timing of the shortest-period binary star system HM Cancri

James Munday, T. R. Marsh, Mark Hollands, Ingrid Pelisoli, Danny Steeghs, Pasi Hakala, Elmé Breedt, Alex Brown, V. S. Dhillon, Martin J. Dyer, Matthew Green, Paul Kerry, S.P. Littlefair, Steven G. Parsons, Dave Sahman, Sorawit Somjit, Boonchoo Sukaum, James Wild

Contribution of co-authors

Observations used in this study were obtained by all authors except #3. Author #3 performed fitting to the HST spectrum presented in Section 3.4.4. All authors contributed with comments on the manuscript during the submission/revision process while authors #2–5 contributed towards the text by supplying key ideas to explore in creating the final version of the study. All other components and the leading of the study were performed by me.

Abstract

The shortest-period binary star system known to date, RX J0806.3+1527 (HM Cancri), has now been observed in the optical for more than two decades. Although it is thought to be a double degenerate binary undergoing mass transfer, an early surprise was that its orbital frequency, f_0, is currently increasing as the result of gravitational wave radiation. This is unusual since it was expected that the mass donor was degenerate and would expand on mass loss, leading to a decreasing f_0. We exploit two decades of high-speed photometry to precisely quantify the trajectory of HM Cancri, allowing us to find that $\ddot{f}_0$ is negative, where $\ddot{f}_0 = (-5.38 \pm 2.10) \times 10^{-27}$ Hz s^{-2}. Coupled with our positive frequency derivative, we show that mass transfer is counteracting gravitational-wave dominated orbital decay and that HM Cancri will turn around within 2100 ± 800 yrs from now. We present Hubble Space Telescope ultra-violet spectra which display Lyman-α absorption, indicative of the presence of hydrogen accreted from the donor star. We use these pieces of information to explore a grid of permitted donor and accretor masses with the Modules for Experiments in Stellar Astrophysics suite, finding models in good accordance with many of the observed properties for a cool and initially hydrogen-rich extremely-low-mass white dwarf ($\approx$0.17 M$_\odot$) coupled with a high accretor mass white dwarf ($\approx$1.0 M$_\odot$). Our measurements and models affirm that HM Cancri is still one of the brightest verification binaries for the Laser Interferometer Space Antenna spacecraft.

3.1 Motivation

Sub-15 min period binaries are extremely scarce because of the short duration (thousands to tens of thousands of years) spent during this evolutionary stage. As discussed in the introduction of this thesis too, the future evolution of many of these systems towards a merger, AM CVn or detonation is unclear and we need devoted analyses of such systems with the tightest of orbits to explore the conditions. Being the shortest-period binary known to date and as the strongest-radiating system of gravitational waves known to date, orbital decay of HM Cancri is rapid and an observed minus calculated trend is detectable in a couple of years of observation. In this study, we strove to improve mass measurements of the binary to unravel its fate using stellar evolutionary code simulations, track the orbital decay extraordinarily precisely to try and derive not only the frequency derivative but the second derivative as well to see at what degree the binary is resisting purely general relativistic inspiral, and obtain a spectral signature of the hotter star in the ultra-violet.

3.2 Deciphering between a unipolar inductor, an intermediate polar or an ultra-compact double white dwarf

These three theories can explain rapid X-ray periodicity, and, most relevant to this chapter, here I will discuss each model before returning to an introduction of HM Cancri.

3.2.1 Unipolar inductor

The most typical and natural comparison for this situation is the Jupiter-Io system. Goldreich and Lynden-Bell [1969] show how the unipolar inductor model can be applied to this system to explain bursts of decametric radiation (radio waves at 22.2MHz) which originate from the planet. The spin of Io is tidally locked with the orbit around the planet while the spin of Jupiter is different to that of the system period. The surface of Jupiter has a magnetic field of around 10 G and Io has a good conductivity, giving rise to an electrical circuit between Io and Jupiter. This difference means that the planet moves across magnetic field lines, inducing an electromagnetic field and an electrical current, and the isotropic ionosphere of Jupiter allows for the current to flow through it, reach the surface and close the loop. Any accelerated electrons along these loops are accelerated in a magnetic field and hence give off cyclotron radiation, causing this sporadic radiowave emission.

In the case of binary star systems, a similar but slightly different effect is witnessed. The logic is the same with a closed circuit being formed between a magnetic and an (assumed to be for simplicity) non-magnetic companion, except that the current flows dissipate in the atmosphere of the magnetic star due to a lesser conductivity, hence applying a resistance and locally heating the magnetic star's surface on the day face. The local heating powers emission and can be detected in the X-ray wavelengths. The total energy budget when dealing with the work done on the orbit from gravitational wave radiation and magnetic effects puts constraints onto the degenerately intertwined star mass and field strength of the magnetic component, for which I refer to the excellent discussion in sections 3 and 4 of Dall'Osso et al. [2007] [see also Dall'Osso et al., 2006]. Importantly, there is no need for any material to be accreted and the orbit may be detached with an orbital period on the timescale of hours. Cyclotron radiation is again expected to give rise to radio waves like in the Jupiter-Io case [1].

3.2.2 Intermediate polar

Intermediate polars originate from a Roche lobe overflowing red dwarf that orbits a magnetic WD of field strength 10^6–10^8 G [e.g. Hellier, 2001]. The orbital periods of these systems range from a couple of hours to a couple of days and mass is accreted in the form of an accretion disc. The magnetic field truncates the inner part of the disc and, in this region, matter flows along the magnetic field lines to be accreted at the poles of the WD rather than steadily flowing onto the WD surface. Periodicity in the lightcurve originates from the orbital period of the binary and the asynchronous rotation of the white dwarf. They can also be bright X-ray emitters owing to the accretion stream crossing the rotating WD's field lines when accreting matter at the poles hits the surface due to Bremsstrahlung radiation.

3.2.3 Double white dwarf

An ultra-compact DWD binary that is Roche-lobe overflowing can explain rapid variability in the X-ray or the optical regime. Naturally, the orbital period is the root of periodicity and would show RV variability on the orbital period, unlike the other two cases. X-rays in this case originate from the Bremsstrahlung radiation of accreted material either through an accretion disc or from direct impact accretion.

3.3 Introduction to HM Cancri

RX J0806.3+1527 [HM Cancri, henceforth HM Cnc, Ramsay et al., 2002, and also independently discovered by Israel et al. 2002] is the shortest-period binary star system

---

[1] A search of radio emission from ultra-compact binaries has been conducted by Ramsay et al. [2007] and would support the unipolar inductor model. Interestingly in this work, although HM Cancri is most definitely a DWD binary, polarised radio emission is detected. The source of this emission is unknown and background contamination can not be ruled out.

known, having a present day orbital period of 5.36 min, equivalent to an orbital frequency of 3.11 mHz. There have been multiple theories suggested to explain the extremely short period of HM Cnc, namely the unipolar inductor model [Wu et al., 2002; Dall'Osso et al., 2007]; the intermediate polar model [Norton et al., 2004]; the AM CVn model [e.g. Nelemans et al., 2001a]. In brief, the unipolar inductor model is similar to the Jupiter-Io system with the binary being detached, the intermediate polar model suggests that the optical period actually represents the spins of magnetic WDs and that the binary's orbital period is much longer, and the AM CVn model involves a compact WD binary mass-transferring helium rich material. In the case of HM Cnc, a DWD binary is required to reach the observed period for an AM CVn without a merger already taking place. The studies of Roelofs et al. [2010] and Mason et al. [2010] helped to reduce the options. They find clear radial-velocity variations on the $5.36\,\mathrm{min}$ optical period, difficult to explain using the intermediate polar model, and a strong indication of an accretion stream via the presence of He II emission lines in the spectrum, which is not predicted by the unipolar inductor model. Strohmayer [2008] fail to detect any signature of metals in the X-ray spectrum, favouring a DWD AM CVn, and a DWD binary is also a natural explanation for the relative phase difference between the peak of X-ray and optical flux [e.g. Barros et al., 2007]. Here, the peak in X-ray flux arrives slightly later than the optical, which arises from the trajectory of the accretion stream directly impacting the surface of the accretor. It would thus seem that only the DWD AM CVn theory can be used to explain all of the present observations.

Follow-up observations of HM Cnc in the X-ray and optical domains have revealed an increase in orbital frequency, f, due to the loss of orbital angular momentum through gravitational wave radiation [Hakala et al., 2003; Israel et al., 2004; Hakala et al., 2004; Strohmayer, 2005; Barros et al., 2007; Esposito et al., 2014; Strohmayer, 2021]. The increase is so much so that HM Cnc will be one of the brightest "verification binaries″ to optimise the performance of the Laser Interferometer Space Antenna [LISA, Amaro-Seoane et al., 2017] spacecraft, given its low-frequency gravitational wave emission, strong signal strength [Kupfer et al., 2018; Amaro-Seoane et al., 2022] and the precise timing measurements that have been used to quantify its orbital decay. Similarly, HM Cnc is planned to be used as the primary reference source for the TianQin spacecraft [Luo et al., 2016; Ye et al., 2019]. While it took two years to detect an increase of HM Cnc's orbital frequency [Hakala et al., 2003], continuous timing measurements over a much longer baseline can prove insightful to determine the second derivative, $\ddot{f}$, which is an indicator of the trajectory of inspiral.

Using X-ray data, Strohmayer [2021] measured the second derivative of the orbital frequency of HM Cnc, finding $\ddot{f} = (-8.95 \pm 1.40) \times 10^{-27}\,\mathrm{Hz\,s^{-2}}$. This was the first significant detection of $\ddot{f}$ for any AM CVn system. The combination of $\dot{f}$ and $\ddot{f}$ can be used to predict the timing of maximum orbital frequency of the binary, which Strohmayer [2021] predicts to occur in 1260 ± 200 yrs from now. In addition, Strohmayer [2021] was able to estimate a mass transfer rate based on the accretion luminosity of the source from X-ray observations. HM Cnc is unfortunately too dim ($G_{\text{mag}} = 20.9$) for a distance constraint with Gaia DR3 [Gaia Collaboration et al., 2016b], though assuming a distance of 5 kpc and donor and accretor masses of 0.27 $\mathrm{M}_{\odot}$ and 0.55 $\mathrm{M}_{\odot}$, Strohmayer [2021] calculated an accretion rate $\dot{M} = -1.6 \times 10^{-8}\,\mathrm{M}_{\odot}\,\mathrm{yr}^{-1}$. However, the calculated mass transfer rate is strongly dependent on the input star masses and the distance to the source. A distance measurement and a precise measurement of $\ddot{f}$ are therefore extremely useful to constrain the binary's evolution with sets of donor and companion masses.

This study of HM Cancri aims to do just that and is set out as follows. Section 3.4 discusses our photometric and spectroscopic observations of HM Cnc and my attempts in deriving a distance measurement. In Section 3.5, I present system timing measurements and derive the orbital ephemeris. I then explored the extent to which the AM CVn channel can match the updated orbital ephemeris with binary evolution simulations in Section 3.6.

3.4 Observations

3.4.1 Photometry

Time-series photometry was obtained using the high-speed cameras ULTRACAM [Dhillon et al., 2007], ULTRASPEC [Dhillon et al., 2014] and HiPERCAM [Dhillon et al., 2016, 2021].Data from HiPERCAM were obtained while mounted on the 4.2m William Herschel Telescope (WHT) and the 10.4m Gran Telescopio Canarias (GTC). We observed with ULTRACAM on the 8.2m Very Large Telescope (VLT), the 3.58m ESO New Technology Telescope (NTT) and the WHT, and we observed with ULTRASPEC mounted on the the 2.4m Thai National Observatory (TNO). Exposure times were varied across the nights to reflect the seeing conditions, the aperture of the telescope and the filters used at the time. A full observing log giving dates, conditions, exposure times and the filters used for each set of observations is given in Table 3.5. All of the data were bias-subtracted and flat-fielded. An additional dark current subtraction was applied to all data from ULTRACAM only as the instrument operates at a temperature high enough for there to be significant dark current. For HiPERCAM, corrections for CCD fringing were performed in the z_s band only using pre-obtained fringe maps for the instrument.

I also accessed VLT FORS1 [Appenzeller et al., 1998], ESO 3.6m Telescope EFOSC2 [Buzzoni et al., 1984] and Telescopio Nazionale Galileo (TNG) DoLoReS archival data that were presented in Israel et al. [2002] prior to our first observation. Extra archival data of HM Cnc were obtained from the TNG DoLoReS instrument from dates following their

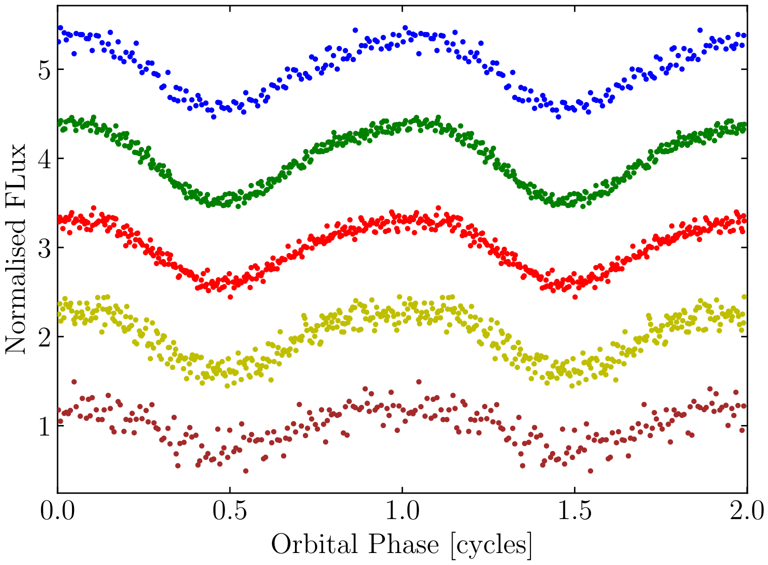

Figure 3.1: Phase-folded HM Cnc light curves from HiPERCAM on the GTC. All filters are displayed. From top to bottom, the super SDSS u_s, g_s, r_s, i_s and z_s. The non-sinusoidal nature of the light curves are noticeable around maximum flux, consequential of the flux contributed by the direct-impact spot. Each band is displaced by an artificial offset for clarity. The peak flux arrives first in the z_s band and last in the u_s.

study. Though the study of Israel et al. [2002] used some of these data before, no timing solutions have been reported, so I used the archival data in this study to take advantage of the longest observational baseline possible[2]. Data obtained with the 2.56m Nordic Optical Telescope (NOT) that was presented in Ramsay et al. [2002]; Hakala et al. [2003, 2004] and with the 2.5m Isaac Newton Telescope (INT) from the RATS survey [Ramsay and Hakala, 2005] were utilised in this study too. The extracted differential photometry obtained in prior studies using data from the NOT were used, whereas raw files were handled from every other source.

Photometry from each instrument, besides data obtained with the NOT, was then extracted using the HiPERCAM pipeline with differential aperture photometry and the application of Naylor [1998]'s optimal photometry algorithm when the target aperture did not need to be linked to a comparison star; otherwise regular aperture photometry was performed. To tackle poorer observing conditions, a variable aperture radius was applied, which was chosen to be a fixed multiple (1.6–1.8×) of the full-width at half-maximum

---

[2] All data presented in Israel et al. [2002] had calibration files and were bias-corrected and flat-fielded with custom scripts. Unfortunately in some cases either windowing setups were not specified or calibration files were not able to be recovered from the TNG archive, meaning that some data extraction was performed without bias or flat-field correction. Whenever HM Cnc overlapped an artefact, or, the image showed a noticeably non-uniform local field, the data from this night were discarded.

of the stars for each individual frame. A non-variable comparison star (Gaia DR3 ID 654873149889859968) was used for all observations when possible, or another (Gaia DR3 ID 654879025405159040) if the main comparison star saturated or coincided with detector defects.

The observation times were corrected to the Barycentric Julian Date (BJD) Barycentric Dynamical Time (TDB) centred on the mid-point of the exposure time. Poor data (e.g. affected by clouds) were rejected by visual inspection with HiPERCAM pipeline routines. I then derived a differential atmospheric extinction term for each filter to correct for the difference in colour between the comparison star and HM Cnc. This was performed by considering the dependence of airmass on the differential flux, which was subtracted to effectively convert to a flux at zenith.

3.4.2 Proper Motion

As of Gaia DR3, there is no measurement of the proper motion of HM Cnc, so I searched for it using our data. To do so, I added world coordinate system information to each FITS file by plate solving each exposure using the backend of Astrometry.net [Lang et al., 2010]. I utilised a custom Gaia DR3 reference star catalogue for the local field containing stars with a right ascension (α) and declination (δ) error of less than 0.1 arcseconds. The catalogue provided the location of stars at the mid-Gaia DR3 epoch. I selected data from the V, r and i bands only to reduce the impact of atmospheric refraction upon the position of HM Cnc relative to the redder stars in the field, though atmospheric refraction still limits our position accuracy. A reliable coordinate calibration was possible for all frames with approximately 20 or more reference stars. Then, I converted the central (pixel) coordinate and error of the centroid for each aperture into a physical α/δ coordinate. All measurements of α/δ from each frame were then combined with a variance weighted mean, giving a measured α/δ for HM Cnc on each night.

From the determined positions (as plotted in Appendix 3.8), I conservatively take the range of the data to find upper limits of $|\dot{\alpha}| < 9.1\,\mathrm{mas\,yr^{-1}}$ and $|\dot{\delta}| < 9.2\,\mathrm{mas\,yr^{-1}}$. The best-fit indicates proper motions of $\dot{\alpha} = 2.0 \pm 1.1$ mas yr^{-1} and $\dot{\delta} = -3.3 \pm 1.1$ mas yr^{-1}, having a reduced χ^2 equal to one. By taking the maximum proper motion, we can derive a loose minimum distance constraint.

The proper motion is inversely proportional to the distance. Using an approximate mean transverse velocity (V_T) of $30\,\mathrm{km\,s^{-1}}$ [Cheng et al., 2019] for a WD in the galactic disc and a maximum absolute proper motion of $\dot{\mu} = \sqrt{|\dot{\alpha}|^2 + |\dot{\delta}|^2 \cos^2(\delta)} \approx 12.7\,\mathrm{mas\,yr^{-1}}$, I find a minimum distance of $D = 500\,\mathrm{pc}$. The best-fit proper motion with $V_T = 30\,\mathrm{km\,s^{-1}}$ gives $D = (1.7 \pm 0.5)\,\mathrm{kpc}$. This result is consistent with a distance limit of $D > 1.1\,\mathrm{kpc}$ if X-rays are responsible for the heating of the donor, but goes against the limit set if

Table 3.1: The measured change in magnitude of HM Cnc in each filter set. HiPERCAM data is excluded from the brightness analysis due to an incompatible comparison star with the ULTRACAM data. This left one single night with the r_s filter, such that no change in magnitude is reported.

Filter	Δmag (mag yr^{-1})	Filter	Δmag (mag yr^{-1})
u$_s$	-0.0149 ± 0.0111	u'	-0.0017 ± 0.0036
g$_s$	-0.0177 ± 0.0080	g'	-0.0013 ± 0.0029
i$_s$	-0.0686 ± 0.0406	r'	-0.0113 ± 0.0041
		i'	0.0080 ± 0.0106

optical/ultra-violet irradiation is responsible, being $d > 4.2\,\mathrm{kpc}$ [Barros et al., 2007]. The best-fitting distance measurement is consistent with the expectation of $D \approx 2\,\mathrm{kpc}$ predicted by Reinsch et al. [2007], although an absolute distance measurement is still relatively unconstrained by my assumption of a disc-like transverse velocity. Halo velocities are often larger [e.g. Pauli et al., 2006; Kim et al., 2020] whereby assuming $V_T = 200\,\mathrm{km\,s^{-1}}$ I obtain a lower limit of $D = 3300\,\mathrm{pc}$ and a best-fitting distance of $D = (11 \pm 3)\,\mathrm{kpc}$. It is hoped that future Gaia data releases will reveal a more precise proper motion and perhaps a parallax measurement, though the $G_{\mathrm{mag}} = 20.9$ target is at the limit of Gaia's capabilities.

3.4.3 Luminosity

If the mass transfer rate of HM Cnc changes as the orbit shrinks, so will the accretion luminosity. I used the ULTRACAM data using the prime and Super SDSS sets of filters to see if the brightness of HM Cnc has changed over the years. I measured HM Cnc's magnitude relative to comparison star Gaia DR3 ID 654873149889859968 using the values of the constant offset d (see Section 3.5.1) from equation (2.7). A difference in colour between HM Cnc and the much redder comparison star was accounted for by subtracting filter-dependent colour coefficients as a function of airmass from the magnitudes obtained, as in Section 3.4.1. The measured changes in magnitude are presented in Table 3.1. Observations with the Super SDSS filters have a total observing span of 4 years, while the SDSS prime observations span 13 years in u' and g', and about 7 years in r' and i', hence the change in magnitude measured with the SDSS prime filters have smaller uncertainties.

For the most part, the measurements favour a small brightening of HM Cnc, but all measurements are within 3σ of no change at all, and so there has been no significant change overall.

3.4.4 Spectroscopy

I utilised the Hubble Space Telescope (HST) Advanced Camera for Surveys (ACS) to obtain slitless spectroscopy of HM Cnc in 2007. We observed with the High Resolution Channel (HRC) with the PR200L prism (R= 300–30) and with the Solar Blind Channel (SBC) with the PR110L prism (R= 60–10), with spectral resolution decreasing as the wavelength increases due to a very non-linear prism dispersion. All spectra were individually reduced and flux calibrated with the HST aXe software and were then stacked[3]. The resultant spectrum was de-reddened using the EXTINCTION python package following the treatment of Fitzpatrick [1999], with $A_V = 0.10$ mag [Esposito et al., 2014] and $R_V = 3.1$. The spectrum obtained is displayed in Fig. 3.2. Some data at both ends of the spectra for each setup were deemed unreliable in the flux calibration due to a degraded resolution, creating a 'winged' effect that is typical in the ACS slitless spectroscopy setup and discussed in detail in the instrument manual. The far ultra-violet end of the impacted regions were masked and are shown as well in Fig. 3.2.

Prior analyses of optical spectra have indirectly suggested that hydrogen is present due to blending of odd terms of the He II Pickering series [Norton et al., 2004; Reinsch et al., 2007]. The stacked spectrum reveals a clear Lyman-α absorption feature in the ultraviolet, which is apparent in all spectra. This is the first direct evidence of hydrogen in the spectrum of HM Cnc and signifies that hydrogen is present in the accretion stream and thus the envelope of the donor. HM Cnc is the only known ultra-compact AM CVn to show any direct trace of hydrogen, with the possible exception of CP Eri [Sion et al., 2006].

Fitting to the observed spectral energy distribution allows us to obtain an improved temperature measurement of the accretor and to predict a hydrogen envelope fraction. The total mass accreted leading up to present day is expected to be approximately 0.01 $M_\odot$ with the majority of mass transferred through direct impact accretion (see Section 3.6), such that the surface composition of both stars will be near identical. The Koester WD atmosphere models [Koester, 2010] were used to constrain these properties from the spectrum. The atmosphere models allow arbitrary atmospheric compositions including hydrogen-helium mixtures to be used in both the atmospheric structure calculation and the spectral synthesis. A least-squares fit to the data was performed including both stellar components, with model inputs being the effective temperature of the donor and accretor, the relative scaling of the donor to the accretor (i.e. R_d^2/R_a^2, with R the radius of the respective star and subscripts d and a the donor and the accretor stars) and a hydrogen-helium abundance which is identical for both stars with no metallicity. Inclusion of a scaling parameter is necessary because,

---

[3] It was not possible to use the typical HST "drizzle″ scheme to combine spectra due to the non-linear dispersion solution. Cosmic rays were flagged by the HST ACS pipeline and were subsequently removed.

[4] https://cds.u-strasbg.fr/

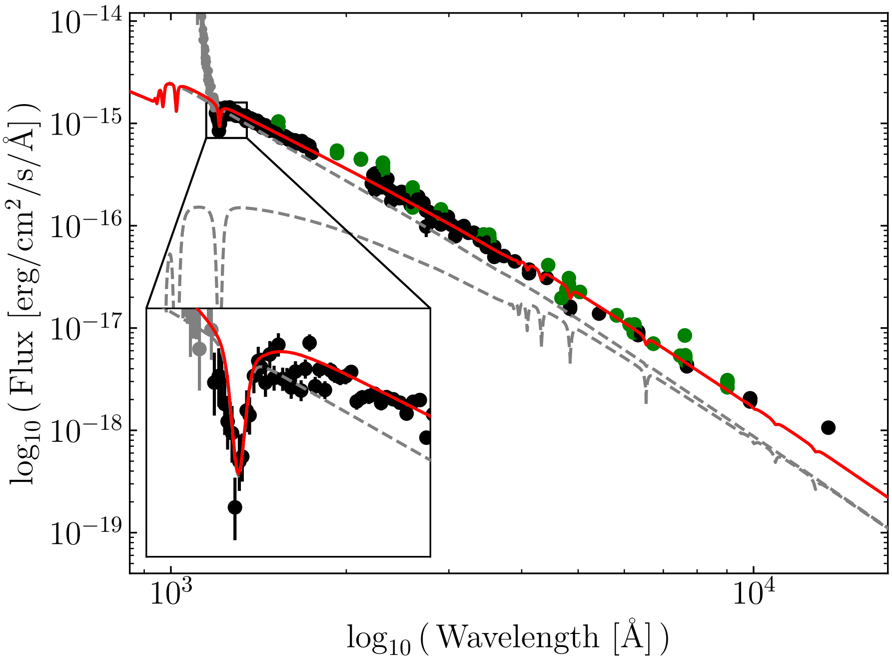

Figure 3.2: The HST stacked spectrum of HM Cnc (black points) with the best spectral fit overplotted in red. Included in the figure is a magnified inset of the Lyman-α absorption feature. In every individual spectrum and at all orbital phases, Lyman-α was recognisable. Other hydrogen absorption lines are not directly visible in the spectrum and blend with helium emission lines [Roelofs et al., 2010], which are not modelled. In dashed grey are the contribution of flux from each star, with the donor contributing less flux. Grey circular points are from the wing of the far-ultraviolet spectrum that were not included in the fit. Green circular points are photometric fluxes from survey data obtained through CDS[4], which were dereddened.

with no firm distance constraint and only one spectral line in the low-resolution spectrum, it is not possible to constrain the surface gravity of either component, and so all calculations were performed at $\log g = 8$. At each step in the least-squares analysis, the atmospheric structures and synthetic spectra of both components were calculated and summed together with the inclusion of the model scaling term. This combined spectrum was then convolved with a Gaussian function to match the instrumental resolution at Lyman-α (R $= 300$). Finally, the model spectrum was scaled from a radiated flux, F, to a flux observed at Earth using equation 2.11, where $\pi R_a^2/D^2 = 4.37 \times 10^{-26}$ is the determined scaling constant.

The derived best-fitting solution is also displayed in Fig. 3.2. From this model, Mark Hollands found a number abundance ratio of $\log(\text{H/He}) = -1.64 \pm 0.05$ dex (H/He $=$ $2.29 \pm 0.26\%$), the hotter star (accretor) temperature to be $42\,500 \pm 800$ K and the cooler star (donor) $18\,600 \pm 300$ K. These quoted errors are purely statistical from the least-squares minimisation and do not reflect the errors in both the choice of reddening coefficients and the flux calibration when combining two instrumental setups, which are such that the cooler component remains largely unconstrained. Furthermore, it is the cooler star that contributes most significantly towards the redder wavelengths, where the spectrum is sparsely sampled and under-fits the observations. The relative contribution from the dimmer donor is $R_d^2/R_a^2 = 2.38 \pm 0.31$, however the radii themselves are unknown with little constraint on the masses of the two stars. If $\text{R}_a = 0.01\,\text{R}_\odot$ is considered with the minimised scaling constant to convert from the radiated flux to the flux at Earth, I find $D = 1.9$ kpc. Doubling the accretor radius would double the inferred distance.

Although difficult at low resolution, other spectral lines were searched for in the stacked spectrum of all exposures and with stacked observations as a function of orbital phase. None were detectable besides the prominent Lyman-α absorption line.

3.5 Timing Solutions

3.5.1 Fitting individual observing runs

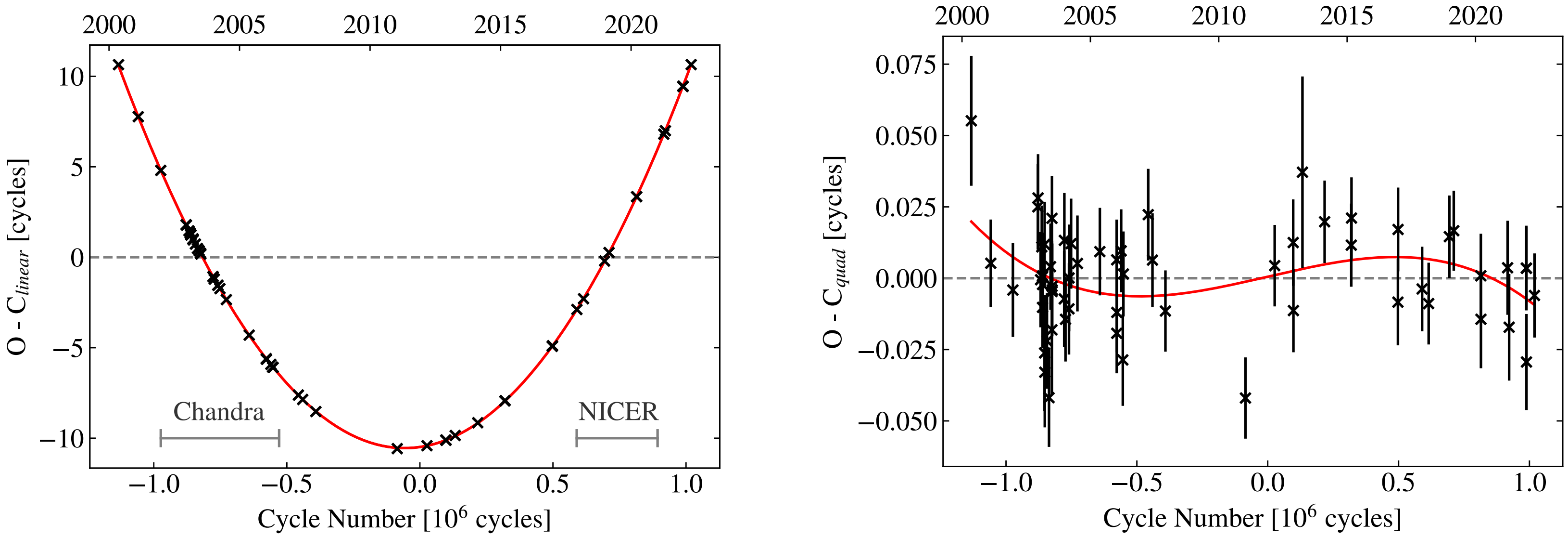

Figure 3.3: *Left:* Timing residuals, observed minus calculated, relative to a linear ephemeris $\phi_0 = 11.1$ cycles, $f_0 = 3.11021829$ mHz, $T_0 = 55849$ BJD TDB. *Right:* Timing residuals relative to the quadratic ephemeris given in Table 3.2. The solid curved line in the right-hand panel shows a cubic ephemeris fit offset relative to the same quadratic ephemeris. The residuals are expressed in terms of orbital cycles. The curvature in the linear ephemeris panel is such that HM Cnc has now advanced by more than 80 entire orbits compared to the period it had at the time of its discovery. The top axes are labelled by the Gregorian year of observation. Multi-filter timing solutions on individual nights are combined to represent a single data point, including a 0.014 cycles error added in quadrature to account for system variability (Section 3.5.4). This was set so that the χ^2 per degree of freedom of the cubic fit equals one. A tabulated list of individual-filter timing solutions is available in Appendix 3.4. Horizontally drawn in grey on the left-hand panel are the spans of cycles covered by X-ray observations. These overlap with the optical observations and are discussed in Section 3.5.4.

Table 3.2: The updated ephemerides for a cubic and quadratic ephemeris, solved with equation 2.4. All errors are quoted to a 1σ uncertainty. The epoch used in these fits was 55849, BJD TDB. This solution is representative of my $u' - g'$ and $r' - g'$ phase offset correction (Table 3.3) and 0.014 cycle flickering correction to the error of each night in quadrature (Section 3.5.4).

Parameter	Cubic	Quadratic
ϕ_0 (Cycles)	0.611 ± 0.004	0.611 ± 0.004
f_0 (Hz)	$0.003110224895 \pm 30\,\mathrm{pHz}$	$0.003110224829 \pm 10\,\mathrm{pHz}$
$\dot{f}_0$ ($\mathrm{Hz\,s^{-1}}$)	$(3.538 \pm 0.001)\times10^{-16}$	$(3.538 \pm 0.001)\times10^{-16}$
$\ddot{f}_0$ ($\mathrm{Hz\,s^{-2}}$)	$(-5.38 \pm 2.10)\times10^{-27}$	–

I fit Fourier series solutions to the extracted photometry of the form using equation 2.7, fitting first and second harmonic terms to account for the non-sinusoidal variability of HM Cnc in the optical (as noticeable in Fig. 3.1). For each night of data with each filter, the terms d, A, B, C and t_0 in equation 2.7 were allowed to vary while ω was held fixed at the expected angular frequency at the time of observation from the cubic ephemeris of Strohmayer [2021]. Including further harmonics to equation 2.7 generated a negligible change in the timing measurement. Uncertainties on t_0 were deduced by taking the standard deviation of 1000 bootstrapping iterations, as used by Pelisoli et al. [2021a]. Example Fourier series solutions and discussion on specific cases can be later found in Section 3.5.4.

For identical filters, if a periodic signal was difficult to detect (e.g. due to poor seeing, short observing time on target), I used the Fourier series solution of the night with the longest observation time for a given filter to search for a timing solution again. I note that there was little difference in t_0 if I allowed the amplitudes of the individual harmonic terms to be free or if I fixed them using a solution to the combined filter dataset. This indicates that there has been no/little detectable change in the periodic signal over the full duration of observations, which may have been induced by a changing accretion spot location. I also note that there was no obvious change in the shape of the Fourier series solution about the peak X-ray flux when comparing nights of observation for identical filters spaced years apart.

I then searched for any filter-dependent offsets to the final timing measurements and present these computed offsets in Table 3.3. Only the $u' - g'$ and $r' - g'$ offsets indicate a relevant deviation from a zero-phase offset at the 1σ level, and so are corrected for all ULTRACAM data using the u' and r' filters. All other observations from data that we have obtained or from archival sources are considered to have a phase offset of zero.

Table 3.3: Phase offsets for each filter used in this study for simultaneous multi-filter observations. The g_s or g' bands are used as a reference.

Filter	$\Delta\phi$ (cycles)	Filter	$\Delta\phi$ (cycles)
$u_s - g_s$	0.0015 ± 0.0040	u' − g'	0.0087 ± 0.0022
$r_s - g_s$	-0.0006 ± 0.0029	r' − g'	-0.0023 ± 0.0016
$i_s - g_s$	0.0019 ± 0.0047	i' − g'	0.0001 ± 0.0090
$z_s - g_s$	0.0020 ± 0.0128		

3.5.2 Constraining the ephemeris

With the full set of filter-offset-corrected (and flickering-considered, see Section 3.5.4) timing solutions, I proceeded by assigning each an integer cycle number, as inferred using the ephemerides of Barros et al. [2007] and Strohmayer [2021] while correcting for the updated epoch, T_0. I chose an epoch $T_0 = 55849$, BJD TDB, as I found that this gave the smallest correlation between the fitting parameters and is located near the centre of the full observing span as expected. Cycle numbers from both of these ephemerides gave the same integer cycle number for all nights and inferred cycle numbers were manually verified for observations taken more recently than those in Strohmayer [2021]. In no case was a jump in cycle number observed, which would be easily noticeable since typical uncertainties are much less than a cycle in magnitude.

It is clear (see Fig. 3.3) that HM Cnc deviates by multiple cycles with respect to a linear fit that has a constant orbital frequency, so I added higher order coefficients to compute a quadratic and then a cubic fit. The set of cycle numbers were fit using equation 2.4. For a linear fit, the first two terms on the right-hand side of equation 2.4 apply, the first three terms for a quadratic and all four for a cubic. The quadratic term corresponds to the parabola that spans 21 cycles from minimum to maximum (Fig. 3.3) which means that HM Cnc has advanced by over 80 orbital cycles relative to the period that it had upon discovery, the result of gravitational-wave driven inspiral.

A fit to the timing measurements was performed using a least-squares analysis through the SCIPY LSTSQ solver in the SCIPY linear algebra package, which I also used to return 1σ statistical errors on all fitted parameters. In the process, the errors on observations were inflated in quadrature so that the reduced χ^2 is equal to one, where flickering in the system largely encourages the inclusion of this procedure (as discussed in Section 3.5.4). The residuals for solutions with a linear and quadratic ephemeris are presented in Fig. 3.3 with the ephemerides for a quadratic and cubic model given in Table 3.2. Corrections of the ephemerides due to the Shklovskii effect [Shklovskii, 1970] and galactic rotation are negligible (see Appendix 3.5.3). The $\dot{f}_0$ coefficient of the quadratic ephemeris is precise to a 0.03% level and is 40 times more precise than that determined by Barros et al. [2007], also derived from optical data.

To check if the $\ddot{f}_0$ term is statistically significant, I performed an F-test between the quadratic and cubic fits. Under the hypothesis that the cubic term is not a significant contribution to the ephemeris, the following F-ratio for n data points

$$F_{\text{ratio}} = \left(\chi^2_{\text{quad}} - \chi^2_{\text{cubic}}\right) \left(\frac{\chi^2_{\text{cubic}}}{n-4}\right)^{-1} \tag{3.1}$$

is expected to have an $F(1,\, n-4)$ distribution, where the 1 in the parenthesis represents the difference in the number of degrees of freedom between the quadratic and cubic fits and $n-4$ reflects the unique degrees of freedom in the cubic fit. I compute the F-ratio to be 6.08 for the $n = 60$ measurements. The cumulative distribution function of an F-distribution can be used to infer at what significance the null-hypothesis that a cubic term is not reflective of the data can be rejected. As such, the cubic term (and so $\ddot{f}_0$) is significant at the 98.3% level (which is significant at 95%, or 2σ, but not at 99.7%, or 3σ). I also carried out an F-test on the digitised X-ray data between the quadratic and cubic solutions specified in Strohmayer [2021] to test the significance of $\ddot{f}$ (see Section 3.5.4). The reduced χ^2 of a cubic fit to the X-ray data was 1.04, so I again inflated the error of all data points in quadrature to gain a reduced χ^2 equal to one. I found $\ddot{f} = -9.41 \pm 1.42 \times 10^{-27}\,\text{Hz}\,\text{s}^{-2}$ and an F-ratio of 44.1 for the X-ray data. From the cumulative distribution of F(1,172), this represents a near 100% significance. Though with sparser sampling, individual measurements for the X-ray data have higher precision since the peak flux per cycle is better defined by a sharp rise towards an intensity maximum, while the optical is more susceptible to variability. Taking the F-test results as evidence that $\ddot{f}$ is a true characteristic of the system, all further mentions of f_0, $\dot{f}_0$ and $\ddot{f}_0$ in this paper assume the cubic solution of Table 3.2.

The optical measurements of $\dot{f}_0$ and $\ddot{f}_0$ allow us to estimate the maximum frequency of HM Cnc before a flip of sign of $\dot{f}$ is observed. If $\ddot{f}_0$ remains constant, equation 2.5 can be used to infer that a maximum frequency is reached when $t = -\dot{f}_0/\ddot{f}_0 + T_0$. I would thus predict the frequency maximum to occur in approximately 2100 ± 800 yrs from now. The timing of this event is consistent with the frequency maximum predicted in Strohmayer [2021]. As always with timing studies, a larger baseline of data would improve the precision of the ephemeris and, in particular, better constrain $\ddot{f}_0$.

Interestingly, $\ddot{f}_0$ is of opposite sign to that predicted in earlier literature, with Deloye and Taam [2006] expecting a *positive* $\ddot{f}$ of magnitude $10^{-28}\,\text{Hz}\,\text{s}^{-2}$. It would be expected that $\ddot{f}$ is positive for almost the entirety of inspiral until merger under purely general relativistic orbital decay, unless a re-stabilisation of the orbit due to mass transfer occurs. Consequently, it is thought that HM Cnc is in a mass transfer turn-on phase that will drive the system to smaller orbital frequencies (longer periods) following the frequency maximum.

Under solely gravitational-wave orbital angular momentum loss for the measured f_0 and $\dot{f}_0$, equation 1.9 can be used to obtain an observed chirp mass of $0.3203 \pm 0.0001\,\mathrm{M}_\odot$. Given that the trajectory of HM Cnc is impacted by the mass accretion rate (which acts to oppose inspiral) and not from gravitational wave radiation alone, this observed chirp mass is a lower bound for the true chirp mass of the system.

3.5.3 Ephemeris corrections

Small corrections can be made to the obtained frequency derivatives obtained in this study. First by considering the Shklovskii effect [Shklovskii, 1970], which can be computed with

$$S_h = V_\perp^2/(c\,D) \tag{3.2}$$

with c the speed of light and D the distance. With our approximate transverse velocity of $30\,\mathrm{km\,s^{-1}}$ and distance of $1.7 \pm 0.5\,\mathrm{kpc}$ from Section 3.4.2,

$$\dot{f}_{\text{Shk}} = f_0\,S_h = (1.8 \pm 0.5) \times 10^{-22}\,\mathrm{Hz\,s^{-1}} \tag{3.3}$$

$$\ddot{f}_{\text{Shk}} \;\approx\; \dot{f}_0\,S_h = (2.0 \pm 0.6) \times 10^{-35}\,\mathrm{Hz\,s^{-2}} \tag{3.4}$$

In addition, one can account for acceleration of the system due to the galactic potential, a_{gal}, as well. I calculated the following galactic corrections to $\dot{f}$ and $\ddot{f}$

$$\dot{f}_{\text{gal}} = f_0\,a_{\text{gal}}/c = 8.3 \times 10^{-22}\,\mathrm{Hz\,s^{-1}} \tag{3.5}$$

$$\ddot{f}_{\text{gal}} \approx \dot{f}_0\,a_{\text{gal}}/c = 9.5 \times 10^{-35}\,\mathrm{Hz\,s^{-2}} \tag{3.6}$$

where a_{gal} was computed using the MILKYWAYPOTENTIAL routine of GALA [Price-Whelan, 2017] with HM Cnc placed at a galactic coordinate 1.7 kpc away from the Sun towards the north galactic pole (in Cartesian coordinates, [-8, 0, 1.7] kpc).

These components can then be subtracted from the measured frequency derivatives, hence the corrected $\dot{f}$ and $\ddot{f}$ are

$$\dot{f}_{\text{corr}} = \dot{f}_0 - \dot{f}_{\text{shk}} - \dot{f}_{\text{gal}} \tag{3.7}$$

$$\ddot{f}_{\text{corr}} = \ddot{f}_0 - \ddot{f}_{\text{shk}} - \ddot{f}_{\text{gal}} \tag{3.8}$$

As evident by the magnitude of each correction, all are negligible compared to the uncertainties quoted in Table 3.2. Increasing the distance to $D = (11 \pm 3)\,\mathrm{kpc}$ for halo-like transverse velocities (Section 3.4.2) results in larger corrections than those stated above. However, neither the correction of $\dot{f}_0$ and $\ddot{f}_0$ due to the Shklovskii effect nor galactic acceleration increase by more than $10\times$ and are still negligible compared to the precision of the ephemerides.

3.5.4 Flickering

I noticed variations in the timing solutions of HM Cnc between adjacent nights with ideal conditions. For data from the VLT with ULTRACAM, observations were performed for a similar duration at similar airmasses over the three nights observed. The observations had a seeing < $1.0''$ and multiple consecutive hours spent on target, resulting in high signal-to-noise ratio (SNR) data with no clear outliers. Fig. 3.4 depicts the changes in the Fourier series solution for sets of observations that were cut to have a one hour duration, with phase-folded light curves included. There are noticeable differences between the solutions of different nights, particularly evident when comparing the phase of minimum flux. Analysis of the full set of VLT nights over an hourly timescale also indicated that there are small changes between solutions with the longest single observing period being three hours, though nightly differences were more apparent. A similar impact to the Fourier solutions and the returned timing solutions was apparent in the (simultaneously observed) u'- and r'-band VLT observations. When I compared the best-quality adjacent nights of NOT data (BJD=52645–52647) each with over 3 hours on target per night, I saw hourly light curve fluctuations at a similar level, though with larger error in individual measurements due to the smaller telescope aperture. I presume that a changing apparent light-curve morphology is a consequence of changes in the system mass transfer rate, creating a flickering effect typical of accreting binaries, while the long-term light-curve morphology is less impacted.

A changing optical periodic signal inherently limits the accuracy of all timing solutions, where, taking the mean of the VLT/ULTRACAM nights to be a reference point, the scatter in t_0 between adjacent nights could be as much as ±0.01–0.015 cycles for all bands. In this study, I thus combined timing solutions from all filters (phase offset corrected where applicable) to obtain a single timing measurement for the night of observations. Then, I added a fixed error in quadrature due to flickering to each night's timing measurement, such that the reduced χ^2 of the ephemerides is equal to one. Overall, this error adjustment was 0.014 cycles.

Also in support of system flickering, Fig. 7 of Strohmayer [2021] compares phase-folded X-ray flux profiles from the Chandra and NICER datasets. A clear difference in flux profile is noticeable after the X-ray peak flux as the flux is decreasing, and to a lesser extent at the peak X-ray flux. This shows deviation over a multiple year time-span, but it is possible that these changes occur on much shorter timescales, e.g. hours.

I then set out to determine whether the flickering was apparent in the X-ray timing solutions as well by comparing the optical data to the nearest X-ray observation. To do this,

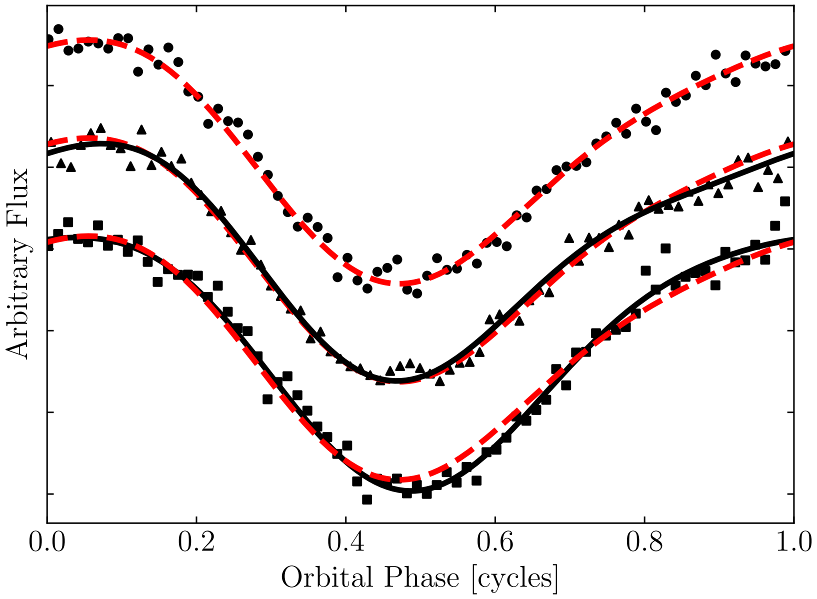

Figure 3.4: Solutions to VLT g-band data, with each plotted light curve representing (binned) data of the first hour of VLT observations each night. Bottom: 2005-11-26 (squares), middle: 2005-11-27 (triangles), Top: 2005-11-28 (circles). The normalised flux is offset between individual nights for clarity. The time at phase 0.0 represents the extracted t_0 for each hour of observations. The Fourier solution for the night of 2005-11-28 is shown in dashed red. The Fourier solutions for other nights are displayed in solid black.

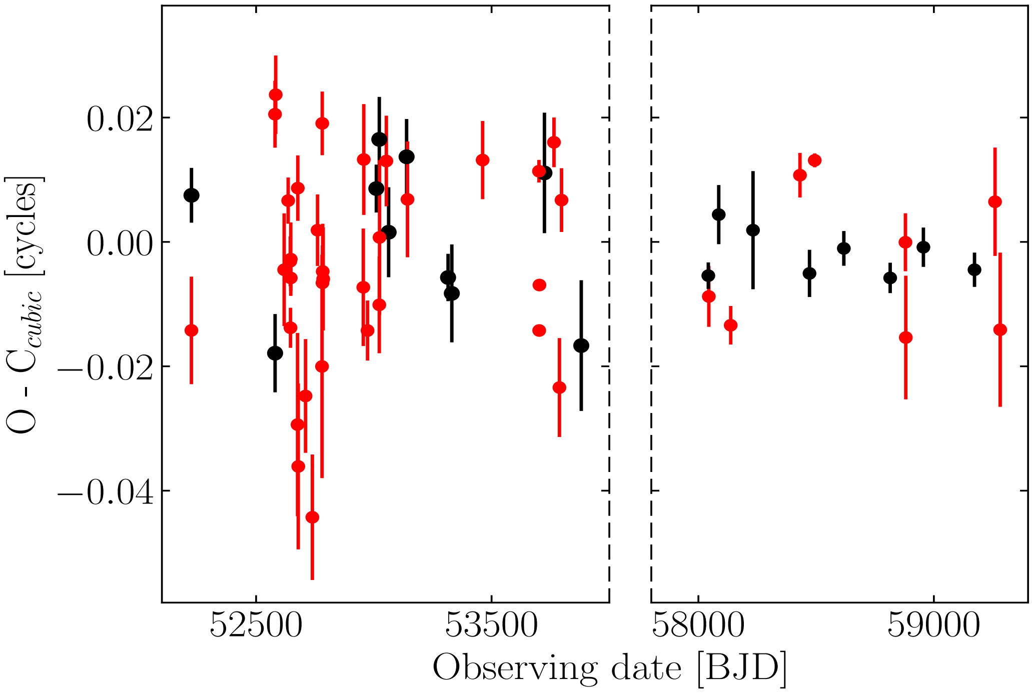

Figure 3.5: A comparison of the X-ray timing solutions (black) of Strohmayer [2021] with our optical measurements (red). Strohmayer [2021] measurements have been binned to represent a single measurement for one observing session, lasting hours at each time. X-ray data on the left of the divide are from Chandra, and on the right are from NICER, with broken axes represented by the dashed line between the plots. The scale is the same in both. Optical measurements within the broken axes are not included in the figure, though are plotted in Fig. 3.3 and comprise a further eight years of coverage. Raw errors are included without the 'flickering correction' described in Section 3.5.4. O-C$_{\text{cubic}}$ was calculated using the cubic ephemeris in Table 3.2 for both the optical and the X-ray measurements.

I utilised the data from Fig. 6 of Strohmayer [2021] by digitising and extracting the plotted data points, followed by a conversion of each to an observed time of peak X-ray flux. After, I compared the optical times with the X-ray times for Chandra and NICER data separately. A phase difference between the time of X-ray peak flux and the derived solutions of t was compensated for by minimising the χ^2 between the optical timing solutions and the X-ray for the cubic-fit ephemeris given in Table 3.2, generating a relative phase difference $\delta\phi \approx 0.14$ cycles from the optical to X-ray. A comparison of the two sets of solutions is plotted in Fig. 3.5, where the 176 individual X-ray measurements have been combined if they coincide with half of a day of each other.

Very few optical/X-ray observations were taken within a day of each other, making a direct comparison difficult. Little scatter is seen in both datasets from the most recent observations, while the earliest show a similar scatter except for the first optical/X-ray measurements. All that I can assert from the data is that an impact on the accuracy of timing solutions at any wavelength cannot be ruled out.

3.6 Evolutionary Modelling

The measured $\ddot{f}_0$ combined with the $\dot{f}_0$ and f_0 is a very strong constraint upon HM Cnc's evolution. I explored simulated binary evolution models with comparison to the observed ephemeris using the Modules for Experiments in Stellar Astrophysics (MESA) 1-D stellar evolution code [Paxton et al., 2011, 2013, 2015, 2018, 2019], release version 15140, to investigate the AM CVn DWD configuration. It has been proposed by D'Antona et al. [2006] that the donor of HM Cnc may be an extremely low mass (ELM) WD that is not fully degenerate and has a thick hydrogen layer, which allows the period to shorten even though accretion occurs. The Lyman-α detection in the HST spectra supports this theory, as well as larger mass, fully-degenerate WD donors with hydrogen in their envelope. Both types of situations are included in the MESA models. Plotted in Fig. 3.6 are the valid mass combinations for each star that our observed chirp mass permits, which I surveyed in the MESA models.

3.6.1 Building a Donor

I approximated the full binary evolution by constructing a He WD from an adaptation of the MAKE_HE_WD MESA test suite. The way this is performed is by evolving a pre-main sequence to a zero age main sequence star, and then by allowing fusion to take place until the core mass reaches the desired mass of a He WD minus the mass of the envelope. We then cut the evolution and gently remove the envelope of the star until only the He core resides. Next, I evolved the star to an effective temperature of 10 kK and then gradually accrete pure hydrogen onto the surface, giving us full control of the total hydrogen envelope mass. What is left is a He core WD with a thin, pure hydrogen layer, which I evolved for 0.5 Gyrs while enabling diffusion, stratifying the layers of the WD to leave a realistic structure[5].

The maximum hydrogen envelope mass in the models was inferred from the Z=0.0001 He WD models of Istrate et al. [2016], choosing models where no hydrogen flash has occurred such that the star maintains a thick hydrogen envelope[6]. For smaller or larger mass

---

[5] My WD models have Z=0.00 due to slow convergence on a solution with the crafted structure in the diffusion process. A couple of test cases of Z=0.02 were evolved as an AM CVn to ensure fair comparisons, where the impact of metallicity in the accreted material was found to be negligible.

[6] Though D'Antona et al. [2006] suggest that larger hydrogen envelope masses of $10^{-2}\,\mathrm{M}_\odot$ could be required for the model, I considered the non-hydrogen-flash Istrate et al. [2016] models to have an improved maximum hydrogen envelope mass.

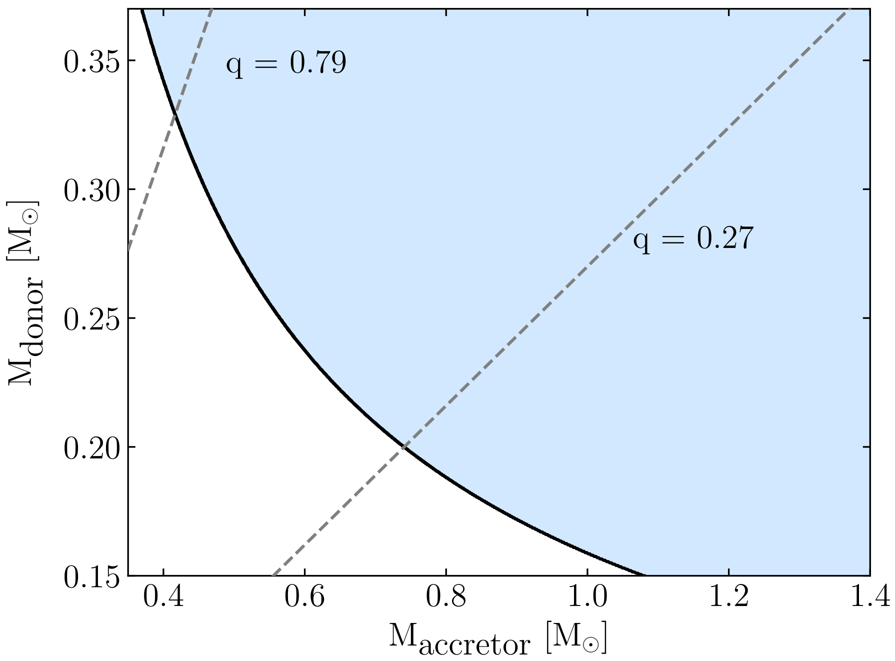

Figure 3.6: Permitted mass combinations for the stars of HM Cnc, given by the shaded blue region. The black solid line represents valid solutions for the observed chirp mass assuming that the orbital decay is solely due to general relativistic effects. Mass transfer permits a smaller $\dot{f}_0$ than purely general relativistic orbital decay in a detached system, meaning that larger system chirp masses (and thus donor and accretor masses) than indicated by the observed chirp mass are possible. Reported boundaries of the mass ratio, $q = M_{\text{donor}}/M_{\text{accretor}}$ from Roelofs et al. [2010] are drawn as dashed grey lines.

WDs than given in the range of models provided by Istrate et al. [2016], I linearly extrapolated their models, with the largest hydrogen envelope used being $\mathrm{M_H} = 6.5 \times 10^{-3}\,\mathrm{M_\odot}$ for models of a $0.16\,\mathrm{M_\odot}$ donor.

While the full set of Istrate et al. [2016] models serves as a good approximation of the amount of hydrogen in the He WD's envelope, the evolution of a compact DWD is very different to their modelling of a neutron star companion to a WD. This, as well as potential hydrogen flashes, suggests that the initial hydrogen envelope could be less than these models. With that in mind, I investigated the compatibility of different masses of hydrogen envelopes by considering my own set of He WD models, whereby a minimum donor hydrogen envelope consists of $\mathrm{M_H} = 0.1 \times 10^{-3}\,\mathrm{M_\odot}$. I sampled hydrogen envelope masses between these limits also, computing models for $\mathrm{M_H} = 1.0 \times 10^{-3}\,\mathrm{M_\odot}$ and $\mathrm{M_H} = 3.0 \times 10^{-3}\,\mathrm{M_\odot}$.

3.6.2 Binary Modelling

I modelled HM Cnc by starting the binary evolution with the fabricated donor He WD and a point mass accretor before any Roche lobe overflow has begun (typically with an initial period of 0.05 days). It is worth noting that Wong and Bildsten [2021] have modelled AM CVn systems with MESA by assuming a pure He donor before any mass transfer and fully evolve two stars rather than one star and a point mass. This would be advantageous here also, however the fact that hydrogen is present in the spectrum and that the hydrogen fraction largely controls the timing of maximum orbital frequency encourages us to include the hydrogen envelope. Though evolving two stars would still be possible, computations including hydrogen to incorporate nuclear burning on the accretor's surface are extremely computationally expensive. Our need to precisely control initial conditions, to simulate a wide grid of models and the fact that nuclear burning on the accretor's surface is important at the onset of mass accretion but less so later in the evolution [Kaplan et al., 2012] led us to proceed with the point mass accretor abstraction, as was similarly initiated by Chen et al. [2022]. The abstraction ignores the possible impact of thermonuclear runaways on the surface of the WD which could result in enhanced angular momentum and mass loss [Shen, 2015]. Given that HM Cnc has not merged and that most of the donor hydrogen envelope has been depleted, the binary has survived hydrogen-rich nova episode(s) and my models are only susceptible to complications from a helium nova episode [Shen, 2015], which may occur in the future. This makes the evolution of my models realistic leading up to f_0, $\dot{f}_0$ and $\ddot{f}_0$, even though the events of the future are uncertain.

Most importantly to the situation at hand, the dynamics revolve around the framework of the Roche lobe approximation of Eggleton [1983] and mass transfer rates following the method outlined in Ritter [1988]. I evolve the orbital angular momentum, J_{orb}, according to equation 1.3 where computed values for the rate of orbital momentum change due to gravitational wave radiation, $\dot{J}_{\rm gr}$, stellar wind mass loss, $\dot{J}_{\rm ml}$, magnetic breaking, $\dot{J}_{\rm mb}$, and spin-orbit (LS) coupling, $\dot{J}_{\rm ls}$, are handled by MESA according to the methods outlined in Paxton et al. [2015]. Mass transfer between the two stars is considered to be perfectly efficient and I applied a tidal synchronisation following the prescription of Hurley et al. [2002] using inbuilt MESA routines.

When an accretion stream feeds into a disc around the accretor, all transferred orbital angular momentum is assumed to return to the orbit of the system; there is no contribution to equation (1.3). When accretion occurs via direct impact, this condition no longer holds. To account for this, I added an extra angular momentum sink to the MESA calculation following the discussion of direct impact accretion in Section 1.2.2 with equation 1.17. Given that I consider a point mass accretor, its radius was computed using a mass-temperature-radius relationship (MTRR) from the Montreal CO WD models [Bédard et al., 2020], where I considered the temperature of the accretor to be 42 500K from the spectrum fit (Section 3.4.4). Hence, direct impact accretion is present if the MTRR radius of the accretor is larger than the radius required for the accretion stream to pass by, or disc-fed accretion on the contrary. In my simulations, this accretor radius is a minimum since the star is likely inflated from mass transfer and partially from irradiation, such that direct impact could begin slightly earlier. For each timestep and model simulated in MESA, I computed whether matter is accreted via direct impact or not and accordingly turned on/off the inclusion of equation (1.17) to the computed $\dot{J}_{\rm orb}$ in equation (1.3).

Diffusion processes were continuously modelled while evolving the binary, before and during mass transfer. The time-step integration itself was variable in the models; longest initially when there is no mass accretion and smallest when the two stars are at their closest separation. The mass transferred in each time-step was calculated implicitly. A test for a merger was analysed for every model with every time-step integration, however unstable mass transfer only occurred for the less-massive-accretor models in the range permitted in Fig. 3.6.

3.6.3 MESA Results

In the DWD configuration, the most significant variables influencing the time of maximum orbital frequency are the donor mass and the amount of hydrogen in the envelope [see e.g. Kaplan et al., 2012]. The mass of the donor significantly affects the duration of Roche lobe overflow, whereas a larger hydrogen fraction induces a larger donor radius and earlier mass accretion. Besides the distinction between disc/direct fed accretion, combinations of accretor and donor masses control the magnitude of $\dot{f}$, where a larger accretor mass leads to a higher $\dot{f}$ for a given donor mass. Furthermore, the temperature of the donor star is

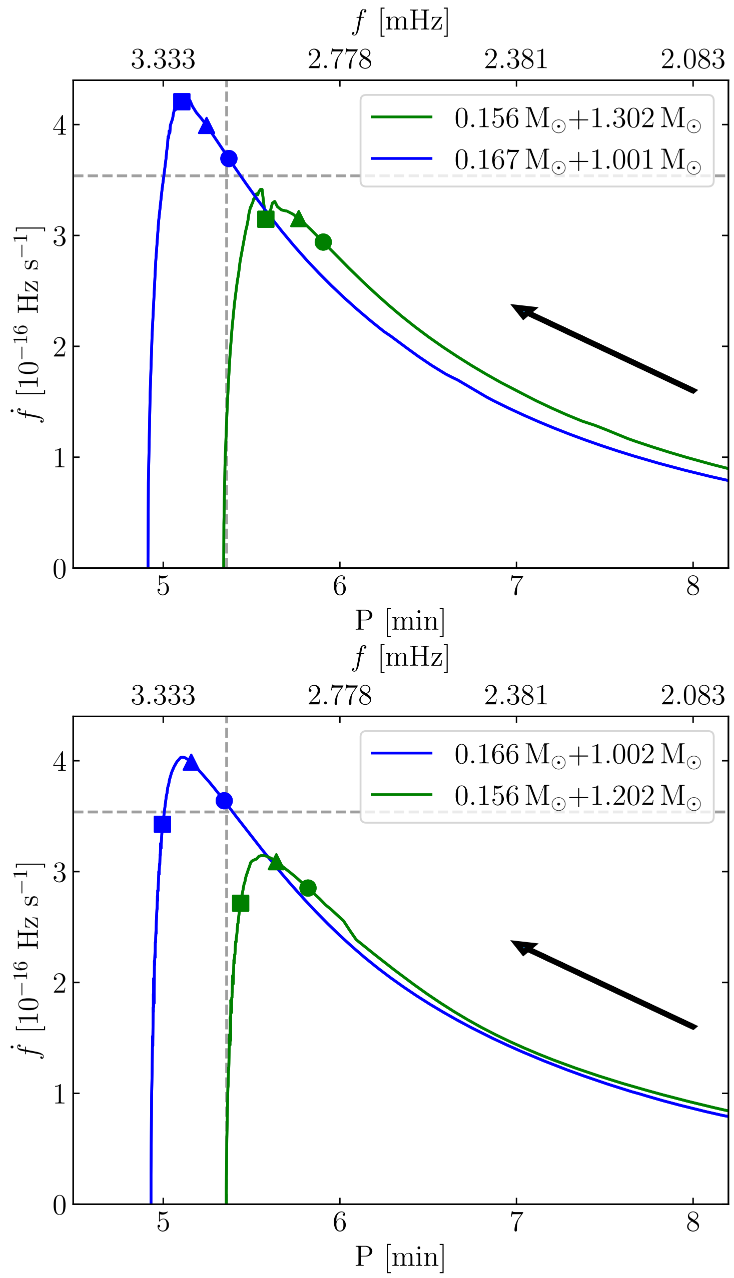

Figure 3.7: The best-fitting MESA results for HM Cnc. Counting from the top down, 1) $M_H = 0.1 \times 10^{-3}\,M_\odot$ 2) $M_H = 1.0 \times 10^{-3}\,M_\odot$ . . .

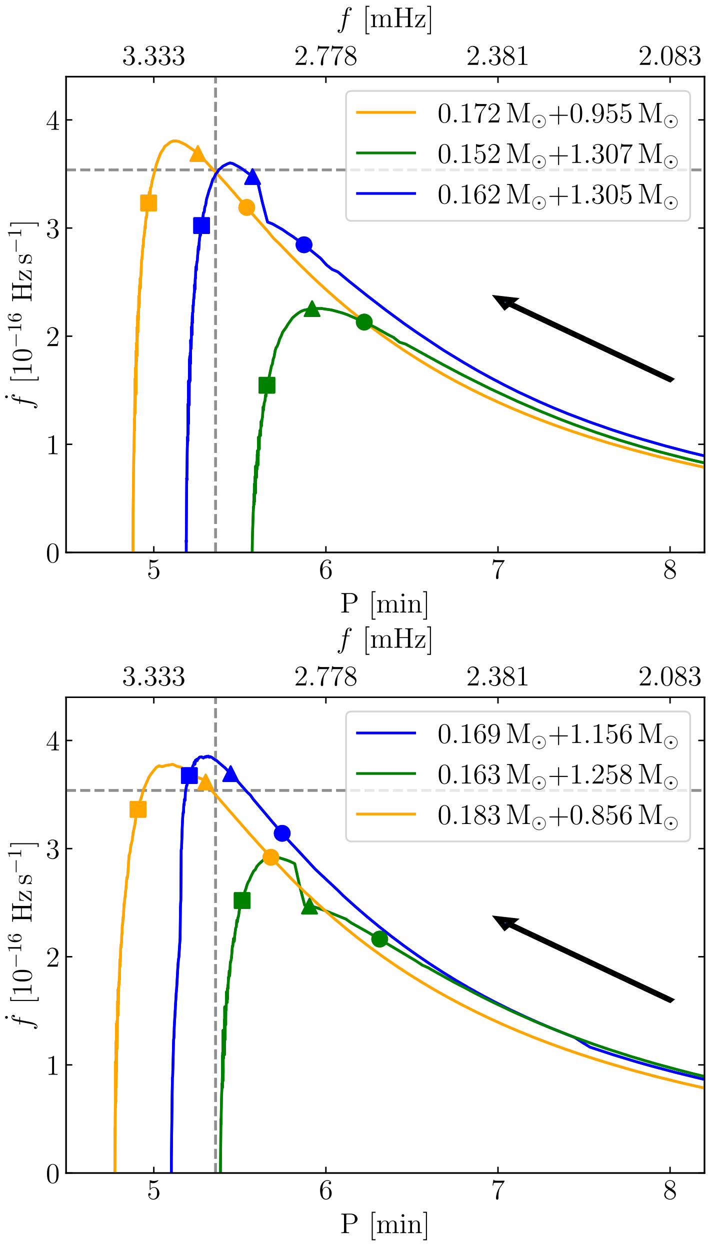

Figure 3.7: 3) $M_H = 3.0 \times 10^{-3}\,M_\odot$ 4) M_H of Istrate et al. [2016] models (see text in Section 3.6.1). Black arrows show the direction of evolution; increasing in time. Coloured circles, triangles and squares represent the moments at which the hydrogen envelope fraction of the donor, H/He (by number), equals 0.1, 0.05 and 0.01 respectively. The dashed grey crosshairs represent the observed f_0 and $\dot{f}_0$. The legend of each plot displays the predicted model masses of the donor and the accretor when the binary has a negative $\ddot{f}_0$. 'Kinks' in the direction of evolution occur due to a switch from disc to direct-impact accretion in certain cases. All models have a donor temperature in the range of 5.5–6.0 kK at present day. In each plot, the most massive donor models reach the largest maximum frequencies before turn-around.

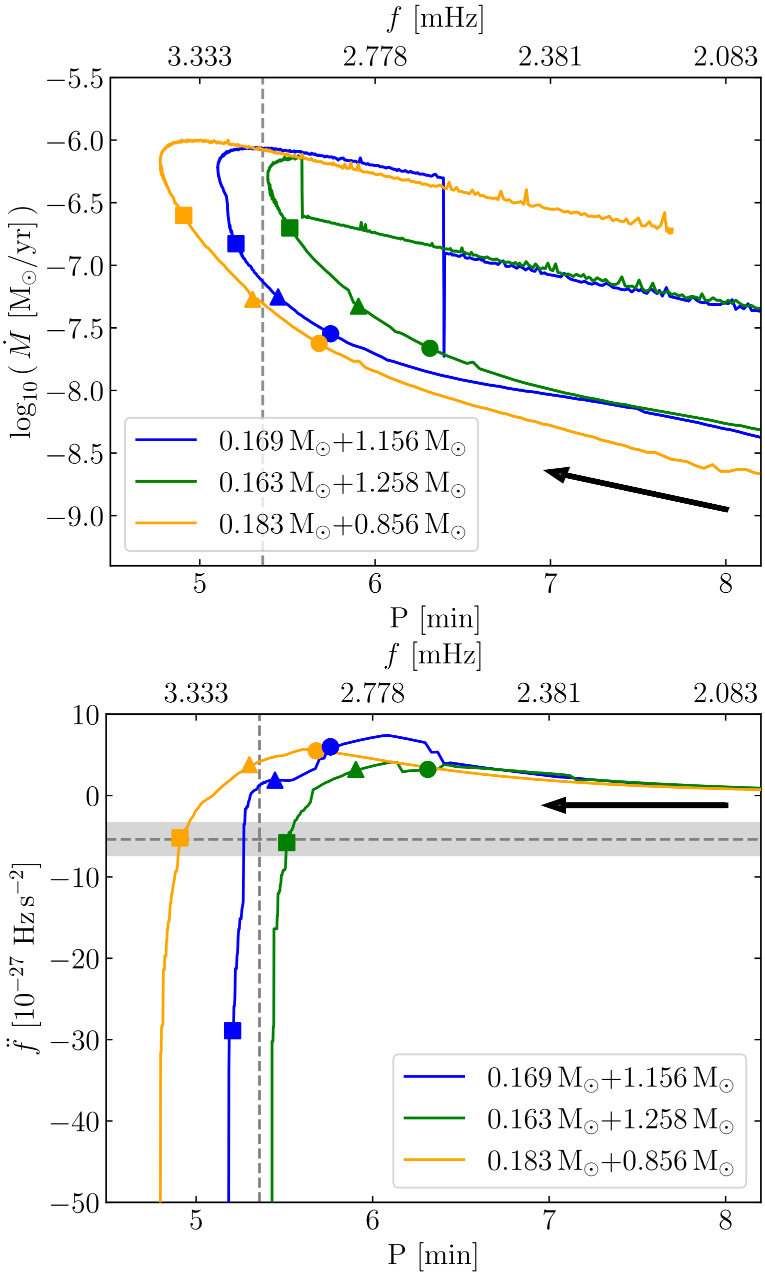

Figure 3.8: Models with evolved Istrate et al. [2016] donor stars shown in the fourth plot of Fig. 3.7 for the mass transfer rate (top) and $\ddot{f}$ (bottom). Black arrows show the direction of evolution, grey dashed lines are the present state of the system, the shaded grey represents the error on $\ddot{f}_0$ and the time of H/He = 0.1, 0.05 and 0.01 is included with circles, triangles and squares respectively. Kinks in the mass transfer figure are again due to a direct-fed/disc-fed accretion transition.

decisive in controlling the onset of mass transfer and the timing of a negative $\ddot{f}$, since a higher temperature WD results in a larger radius.

For my chosen selection of hydrogen envelopes, I performed an in-depth search of the full parameter space of Fig. 3.6 to determine which combinations of masses would lead to $\dot{f} \approx \dot{f}_0$ when $f = f_0$ at any stage of the system evolution before shortlisting to the best-agreeing candidate systems, those being where the sign of $\ddot{f}$ becomes negative near $f = f_0$. My best-fitting models are shown in Fig. 3.7, whereby in all cases $\ddot{f} \lessapprox 0$ at $f = f_0$. The exponential increase in $\dot{f}$ up to approximately 2.5 mHz is governed by an orbital trajectory dominated by gravitational wave radiation. The accreted material is pure hydrogen at lower frequencies and, at around 2.5 mHz in all cases, a diffused hydrogen-helium mixture is present at the surface. As the presence of hydrogen diminishes, the response of the donor is to expand, increasing the mass transfer rate, and causing resistance to inspiral.

I solely present the scenario where the donor star maintains an effective temperature of 5.5–6.0 kK. This is at odds with the donor temperature derived in Section 3.4.4, albeit a loose constraint. I attempted to investigate the scenario where the donor effective temperature is 16 kK and found that it becomes extremely difficult to maintain any hydrogen envelope for all combinations of permitted masses (Fig. 3.6) in MESA. Increasing the donor temperature requires a more massive (and with this a smaller radius) donor for the binary to reach f_0 before $\ddot{f} \lessapprox 0$ occurs. In the process, the binary reaches smaller orbital separations and a present-day mass transfer rate in excess of $10^{-6}\,\mathrm{M}_\odot\,\mathrm{yr}^{-1}$ in required, with the order of magnitude of $\ddot{f}$ to significantly increase over a few decades. Moreover, the total mass lost from a 16 kK donor for tested models exceeded $0.015\,\mathrm{M}_\odot$ leading up to present day, such that an extremely thick hydrogen envelope before any mass transfer begins would be required for hydrogen to be observed in the spectrum. My models therefore indicate a preference for cooler donor stars and smaller mass ratios.

I conclude from Fig. 3.7 that, if I consider the full selection of hydrogen envelope masses, the donor star has a mass in the range $\approx$0.16–0.17 $\mathrm{M}_\odot$ to observe a negative $\ddot{f}$ at $f = f_0$. This result agrees with the expectation from Kaplan et al. [2012], who suggest that the donor is an ELM WD. Additionally, I find that the accretor requires a minimum mass of $0.8\,\mathrm{M}_\odot$ to give rise to a sufficiently large $\dot{f}$ that matches the ephemeris with an ELM donor. These combinations of masses combined with the modelled separation indicate that the accretion stream would be close to the direct-disc mass transfer boundary, as is particularly noticeable by the kinks from the direct-to-disc accretion transition in Fig. 3.7 for some models. For these boundary-models in particular, direct impact occurs in the last few 10,000s of years only, although the present mass transfer mechanism for all combinations of star masses presented involve direct impact[7]. Furthermore, all models show that the

---

[7] I note that Barros et al. [2007] state the condition that direct impact can only occur in HM Cnc if

binary would not have deviated far from purely general-relativistic orbital decay, meaning that the true chirp mass of the system is comparable to the observed chirp mass of $0.3203 \pm 0.0001\,\mathrm{M}_{\odot}$.

I used the $0.169\,\mathrm{M}_{\odot}$ + $1.156\,\mathrm{M}_{\odot}$ and $0.183\,\mathrm{M}_{\odot}$ + $0.856\,\mathrm{M}_{\odot}$ Istrate et al. [2016] models presented in Figs. 3.7 and 3.8 to check for consistency with the relative phase difference between the optical and X-ray peak flux. Barros et al. [2007] discuss how the X-ray signal arrives $\approx$0.26 cycles later than the optical. My MESA models predict that the accretion stream directly impacts the accretor surface to produce a 0.35 and 0.30 cycle relative phase difference, respectively. This is approximately consistent with that observed, especially so as the accretor is likely to be at least partially inflated, acting to decrease the relative phase difference. For models with smaller initial hydrogen envelope masses, the relative phase differences are larger and show a worse accordance with the observations.

My models show a consistent hydrogen envelope fraction with the H/He $= 2.29 \pm 0.26\%$ derived in Section 3.4.4. We see from Figs. 3.7 and 3.8 that all models have a hydrogen number abundance ratio of less than 10% when $\ddot{f} = \ddot{f}_0$, and that for the more massive donor models presented the fraction is between 1% and 5%. While it may be possible for smaller starting mass hydrogen envelope models to match the hydrogen envelope fraction from our observations, I find a best agreement with the observations for higher starting envelope masses to be consistent with the location of the direct impact spot. A comparison of the full set of models does however show that a range of initial hydrogen envelope masses can produce DWD systems that reach the orbital period of HM Cnc, such that the evolutionary channel is not exclusive to a very narrow set of initial conditions. My models also show that the remaining hydrogen envelope of the donor will be almost entirely depleted by the time of maximum orbital frequency.

When I simulated a model similar to the $0.27\,\mathrm{M}_{\odot}$ donor and $0.55\,\mathrm{M}_{\odot}$ accretor predicted by Roelofs et al. [2010], I found that the sign of $\ddot{f}$ would be $positive$ at the observed period for the full range of hydrogen envelopes. To emphasise, this would be the case for a cool donor, whereas hotter donors may be able to reproduce the observed $\dot{f}_0$ and $\ddot{f}_0$ at f_0, although the aforementioned complications when modelling a 16 kK donor star make this difficult to explain. As well, analysis of $\ddot{f}$ indicates that it decreases much faster for a more massive donor, such that HM Cnc would spend only centuries in a turn-around phase. My models give a mass ratio $\approx$0.15–0.21, which disagrees with the mass ratio $0.27 \leq q \leq 0.79$ inferred by Roelofs et al. [2010]. I suspect that the uncertainty in the origin of light of helium emission lines [as discussed in Roelofs et al., 2010] and the choice of these lines to monitor the primary star makes it difficult to obtain absolute radial velocity measurements,

---

$0.6 < \mathrm{M}_1 < 0.9\,\mathrm{M}_{\odot}$, however this was deduced with a zero-temperature masses-radius relationship. The masses that I quote involve direct impact allowing for an accretor temperature $\mathrm{T}_{\mathrm{accretor}} = 42\,500\,\mathrm{K}$.

so that the observational constraint on the mass ratio might be misleading even though a radial velocity variability is apparent.

As shown in Fig. 3.8, the magnitude of $\ddot{f}$ increases dramatically on approach to the maximum orbital frequency. This indicates that the timing of the frequency maximum will actually be in less than 2100 ± 800 yrs and that deviations from a constant $\ddot{f}$ could become evident sooner than one might expect. The duration spent between orbital periods of 6–8 minutes is significantly longer, on the timescale of 100 000–200 000 years. It hence appears fortunate that HM Cnc has been detected just before the maximum orbital frequency, which may be consequential of a strong observational bias. Though from Fig. 3.8 I predict HM Cnc's luminosity to increase upon approach to the maximum orbital frequency, with the mass transfer rate suspected to increase by at least 10×, a clear observable difference is not expected in just 20 years (as suspected from Section 3.4.3).

The accretor MTRR radii in my best models for a 42 500 K accretor are 0.0055–0.0115 $\mathrm{R}_\odot$ for masses in the range 1.25–0.8 $\mathrm{M}_\odot$, respectively. In Section 3.4.4, I explained that a radius constraint and a minimised flux-scaling-factor to our spectrum can be used to gain a distance measurement. Including the range of radii from my MESA models with this technique, I estimate a distance to HM Cnc of D=1.05–2.24 kpc.

I followed a similar methodology to Strohmayer [2021] to compute the mass accretion rate with the observed X-ray luminosity. I assumed that the accretion luminosity is equal to the difference between the gravitational energy at the first Lagrangian point, ϕ_{L1}, and the surface of the accretor, ϕ_{R_a}, such that the accretion luminosity $\mathrm{L}_\mathrm{acc} = \dot{M}\,(\phi_{L1} - \phi_{R_\mathrm{a}})$, with ϕ_{L1} and ϕ_{R_a} calculable with the prescription of Han and Webbink [1999]. Taking donor and accretor masses of 0.17 $\mathrm{M}_\odot$ and 1.0 $\mathrm{M}_\odot$ with an accretor radius of 0.01 $\mathrm{R}_\odot$ and the X-ray luminosity to be $1.8{\times}10^{33}(\Delta\Omega/4\pi)D^2_\mathrm{kpc}\,\mathrm{erg\,s^{-1}}$ [Strohmayer, 2021], I find a mass transfer rate $\dot{M} = 1.84 \times 10^{-10} \times D^2_\mathrm{kpc}\,\mathrm{M}_\odot\,\mathrm{yr}^{-1}$. If a distance of 2 kpc is assumed, $\dot{M} = 10^{-9.1}\,\mathrm{M}_\odot\,\mathrm{yr}^{-1}$. As recognisable by Fig. 3.8, this would be a clear pitfall of my models, where we would be expecting $\dot{M} \approx 10^{-7.5}\,\mathrm{M}_\odot\,\mathrm{yr}^{-1}$. If the distance was instead 5 kpc, $\dot{M} = 10^{-8.3}\,\mathrm{M}_\odot\,\mathrm{yr}^{-1}$, such that assuming larger distances to the source would make my models consistent. An exception is that there could be a missing luminosity component in the extreme ultra-violet that we are not sensitive to with the X-ray nor our own observations, meaning that the X-ray luminosity under-predicts the mass accretion rate. For both the 5.5–6 kK and the 16 kK WD donors, and with the full grid of hydrogen models, I struggle to find a $\dot{M}$ consistent with $10^{-9} - 10^{-8}\,\mathrm{M}_\odot\,\mathrm{yr}^{-1}$ that would generate a negative $\ddot{f}_0$, since the higher mass accretion rates are associated with the timing of the turn-around phase.

As evident, there are still components of HM Cnc that remain unknown which make a precise characterisation of the system difficult. However, my models do show a good agreement with multiple observed properties, including the hydrogen fraction, the location of the impact spot and all components of the cubic ephemeris. My models favour larger initial hydrogen envelope masses and are consistent with the theory outlined by D'Antona et al. [2006] as an origin for HM Cnc and the ELM donor conclusion of Kaplan et al. [2012]. My models show that it is unlikely that HM Cnc had a hydrogen envelope thinner than $10^{-3}\,\mathrm{M}_{\odot}$ before the onset of mass transfer and require thicker initial hydrogen envelopes to be consistent with the location of the accretion impact spot. Better quantification of the donor temperature and an accurate distance measurement clearly remain the key to settle the nature of HM Cnc. If $D \approx 2\,\mathrm{kpc}$, my models would need to be tweaked to include a hotter donor temperature, a more massive initial hydrogen envelope or a mixture of the two to agree with the f_0, $\dot{f}_0$ and $\ddot{f}_0$ presented in this paper, since these components both permit larger mass donor stars and smaller mass accretors with an increased mass transfer rate.

3.7 Conclusions

I presented new timing measurements for HM Cnc following an optical observing campaign to monitor the binary over the last 20 years. I measured $\dot{f}_0$ precise to the 0.03% level while obtaining $\ddot{f}_0 = (-5.38 \pm 2.10) \times 10^{-27}\,\mathrm{Hz\,s^{-2}}$. The ephemeris affirms that the orbital frequency is still increasing, however the negative $\ddot{f}_0$ implies that HM Cnc may reach a maximum frequency within 2100 ± 800 yrs from now.

Then, I outlined a method whereby knowing $\ddot{f}_0$ provides a tight condition on the present state of the system. I used MESA to explore the DWD AM CVn configuration. Since the presence of hydrogen is directly witnessed in the HST spectra, I surveyed multiple masses of donor hydrogen envelopes with combinations of permitted donor and accretor masses. My best model for a cool and initially hydrogen-rich donor indicates system masses of $\mathrm{M_d} \approx 0.17\,\mathrm{M}_{\odot}$ and $\mathrm{M_a} \approx 1.0\,\mathrm{M}_{\odot}$. The model is able to reproduce the observed ephemeris, the hydrogen envelope fraction and the location of the direct impact spot, though suffers from finding a mass transfer rate higher than suggested from X-ray observations if a distance of less than 5 kpc is to be assumed. Furthermore, my model indicates that, after reaching a maximum frequency, the orbital frequency will decrease as the orbital separation increases, such that the binary is unlikely to merge unless an imminent helium-powered nova event [Shen, 2015] or a sub-Chandrasekhar mass type Ia supernova [e.g. Shen et al., 2018b] is to occur.

My MESA models predict that HM Cnc's $\dot{f}_0$ is close to that expected from the purely general relativistic orbital decay for two point masses. This means that the observed system chirp mass ($0.3203 \pm 0.0001\,\mathrm{M}_{\odot}$) is reflective of the true system chirp mass ($0.3347\,\mathrm{M}_{\odot}$ for a $0.17\,\mathrm{M}_{\odot}$ + $1.0\,\mathrm{M}_{\odot}$ combination) and predicts a characteristic strain of $2.67 \times 10^{-19}/D_{\mathrm{kpc}}$ after a 4 year observation time with LISA. Furthermore, a $0.17\,\mathrm{M}_{\odot}$ + $1.0\,\mathrm{M}_{\odot}$

star mass pairing, an inclination of ≈38° [Roelofs et al., 2010, although this could differ if the radial velocities are misleading, see Section 3.6.3] and a gravitational wave polarisation angle of 0° generate a LISA SNR of 147 after a 4 year mission for a distance of 5 kpc[8]. Even at 5 kpc, HM Cnc will be one of the highest SNR binary star systems detectable by the LISA spacecraft and is still an ideal reference source for the TianQin spacecraft.

---

[8] https://heasarc.gsfc.nasa.gov/lisa/lisatool/

3.8 Proper motion deduction

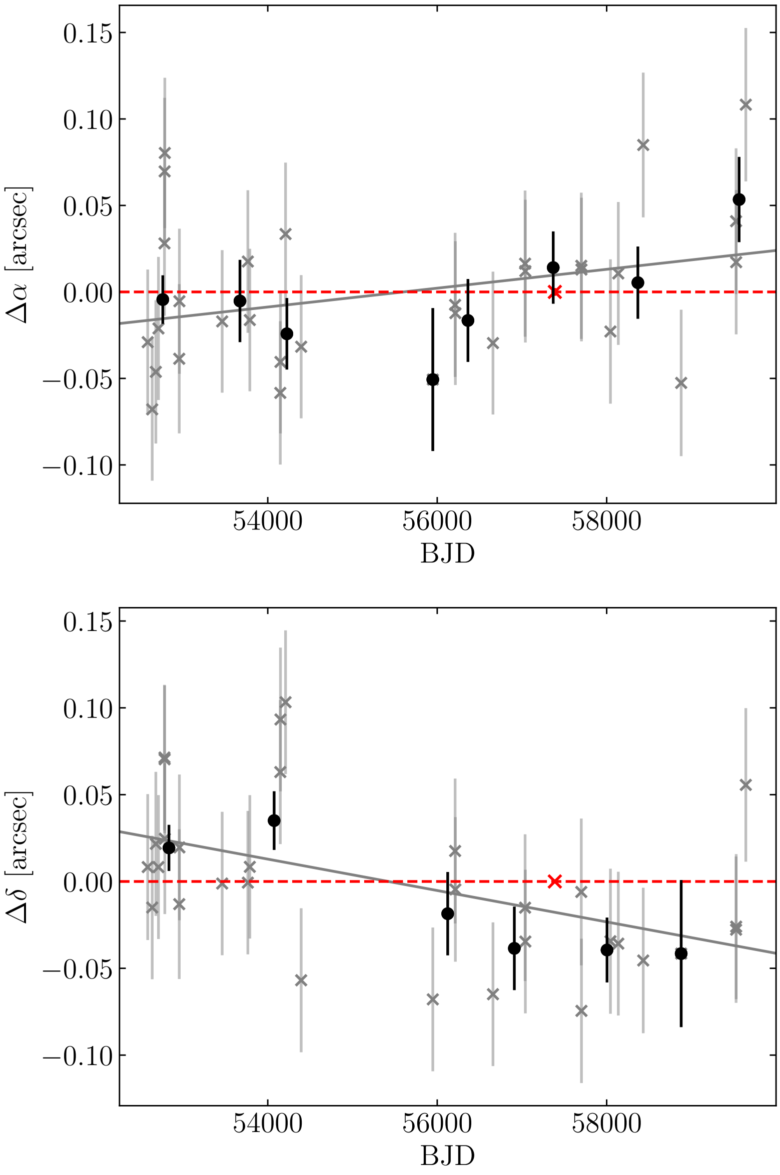

Figure 3.9: Individual measurements of the right ascension (α, top) and declination (δ, bottom), displayed as light grey crosses. Black circles are binned measurements in one thousand day intervals, starting at BJD=52500. The best-fit proper motions are displayed as a solid grey line, with upper proper motion limits constrained in Section 3.4.2. An artificial error has been added to the α/δ of all nights in quadrature, such that the reduced χ^2 of the best-fit proper motions is one. The single red point on each plot marks the Gaia DR3 coordinate of HM Cnc stated. These Gaia data points are not included in the proper motion fits since they are not impacted by atmospheric refraction. The majority of observations are from ULTRACAM, which has a pixel scale of $0.3''$ per pixel on all telescopes.

3.9 Timing solutions and observing log

Table 3.4: The full list of optical timing solutions addressed in this study. All solutions are raw extracted values for each individual filter; the phasing corrections of Table 3.3 and the 0.014 cycle ‘flickering error’ discussed in Section 3.5.4 were not applied to these presented values. A clear filter indicates that non-filtered white light was incident on the detector. In the instrument column, UCAM, USPEC and HCAM are abbreviations for ULTRACAM, ULTRASPEC and HiPERCAM. The time columns use the BMJD, TDB, UTC system.

Time	ΔTime	Telescope	Instrument	Filter
51634.033908	0.000067	ESO 3.6m	EFOSC	B
51911.047491	0.000026	TNG	DoLoReS	B
51911.103190	0.000052	TNG	DoLoReS	B
52225.293041	0.000032	VLT	FORS	R
52580.316805	0.000020	VLT	FORS	R
52583.230663	0.000023	TNG	DoLoReS	B
52619.187101	0.000034	VLT	FORS	R
52636.193912	0.000025	TNG	DoLoReS	V
52637.116848	0.000017	TNG	DoLoReS	B
52645.084430	0.000015	NOT	ALFOSC	Clear
52646.055759	0.000012	NOT	ALFOSC	Clear
52647.090283	0.000008	NOT	ALFOSC	Clear
52647.142372	0.000022	TNG	DoLoReS	B
52675.938780	0.000055	NOT	ALFOSC	Clear
52677.036455	0.000020	NOT	ALFOSC	Clear
52679.035021	0.000050	TNG	DoLoReS	B
52709.937606	0.000038	TNG	DoLoReS	B
52710.019443	0.000075	TNG	DoLoReS	V
52738.901426	0.000038	TNG	DoLoReS	B
52760.905962	0.000021	TNG	DoLoReS	B
52779.907568	0.000067	WHT	UCAM	g’
52780.897276	0.000072	WHT	UCAM	i’
52780.901042	0.000021	WHT	UCAM	g’
52780.901073	0.000051	WHT	UCAM	u’
52781.894725	0.000060	WHT	UCAM	u’
52781.894733	0.000084	WHT	UCAM	i’
52781.894763	0.000025	WHT	UCAM	g’
52782.892068	0.000062	WHT	UCAM	u’
52782.892226	0.000090	WHT	UCAM	i’
52782.899519	0.000034	WHT	UCAM	g’
52784.883031	0.000099	WHT	UCAM	u’
52784.883042	0.000034	WHT	UCAM	g’
52784.883089	0.000113	WHT	UCAM	i’
52955.260171	0.000070	WHT	UCAM	u’

Time	ΔTime	Telescope	Instrument	Filter
52955.260253	0.000057	WHT	UCAM	g’
52955.260287	0.000058	WHT	UCAM	i’
52957.191561	0.000039	WHT	UCAM	g’
52957.191619	0.000075	WHT	UCAM	u’
52957.195317	0.000112	WHT	UCAM	i’
52973.238365	0.000018	INT	WFC	Clear
53023.123751	0.000029	NOT	ALFOSC	Clear
53024.147096	0.000046	NOT	ALFOSC	Clear
53053.080944	0.000027	NOT	ALFOSC	Clear
53142.904373	0.000035	TNG	DoLoReS	B
53461.954123	0.000023	TNG	DoLoReS	V
53701.264987	0.000008	VLT	UCAM	g’
53701.264993	0.000016	VLT	UCAM	r’
53701.265027	0.000023	VLT	UCAM	u’
53702.232700	0.000027	VLT	UCAM	u’
53702.240109	0.000009	VLT	UCAM	g’
53702.243817	0.000016	VLT	UCAM	r’
53702.288476	0.000020	VLT	UCAM	u’
53702.292164	0.000014	VLT	UCAM	r’
53702.292206	0.000007	VLT	UCAM	g’
53702.329385	0.000013	VLT	UCAM	r’
53702.329398	0.000008	VLT	UCAM	g’
53702.329419	0.000023	VLT	UCAM	u’
53702.359121	0.000016	VLT	UCAM	r’
53702.359124	0.000011	VLT	UCAM	g’
53702.359171	0.000034	VLT	UCAM	u’
53703.244843	0.000026	VLT	UCAM	r’
53703.244848	0.000013	VLT	UCAM	g’
53703.244881	0.000062	VLT	UCAM	u’
53703.267148	0.000016	VLT	UCAM	r’
53703.267165	0.000009	VLT	UCAM	g’
53703.267165	0.000024	VLT	UCAM	u’
53703.296927	0.000013	VLT	UCAM	r’
53703.296960	0.000021	VLT	UCAM	u’
53703.300648	0.000008	VLT	UCAM	g’
53703.334140	0.000016	VLT	UCAM	r’
53703.334146	0.000008	VLT	UCAM	g’
53703.334180	0.000032	VLT	UCAM	u’
53703.356451	0.000013	VLT	UCAM	r’
53703.356470	0.000008	VLT	UCAM	g’
53703.360202	0.000024	VLT	UCAM	u’
53764.997223	0.000025	TNG	DoLoReS	V

Time	ΔTime	Telescope	Instrument	Filter
53765.983439	0.000018	TNG	DoLoReS	B
53788.136902	0.000030	TNG	DoLoReS	V
53797.015987	0.000019	TNG	DoLoReS	B
54149.909394	0.000040	TNG	DoLoReS	V
54149.957790	0.000044	TNG	DoLoReS	B
54209.968478	0.000032	TNG	DoLoReS	V
54394.235140	0.000012	WHT	UCAM	g’
54394.235166	0.000023	WHT	UCAM	r’
54394.235184	0.000029	WHT	UCAM	u’
55532.296391	0.000031	NTT	UCAM	u’
55532.300001	0.000040	NTT	UCAM	i’
55532.303745	0.000011	NTT	UCAM	g’
55947.917226	0.000026	WHT	UCAM	r’
55947.920928	0.000013	WHT	UCAM	g’
55947.920960	0.000027	WHT	UCAM	u’
56211.250500	0.000048	WHT	UCAM	u’
56211.250541	0.000027	WHT	UCAM	g’
56211.250555	0.000049	WHT	UCAM	r’
56214.168047	0.000047	WHT	UCAM	u’
56214.168116	0.000019	WHT	UCAM	g’
56214.168116	0.000034	WHT	UCAM	r’
56342.883367	0.000113	INT	WFC	Clear
56658.071653	0.000030	WHT	UCAM	r’
56658.071729	0.000028	WHT	UCAM	u’
56658.075349	0.000018	WHT	UCAM	g’
57037.085934	0.000034	WHT	UCAM	u’
57037.089626	0.000017	WHT	UCAM	g’
57040.181994	0.000026	WHT	UCAM	u’
57040.185668	0.000013	WHT	UCAM	g’
57040.185680	0.000024	WHT	UCAM	r’
57700.349106	0.000025	NTT	UCAM	g’
57700.349118	0.000049	NTT	UCAM	r’
57700.352702	0.000089	NTT	UCAM	u’
57702.347290	0.000019	NTT	UCAM	g’
57702.351091	0.000059	NTT	UCAM	u’
57702.354797	0.000039	NTT	UCAM	r’
58044.245911	0.000064	WHT	HCAM	i_s
58044.246005	0.000045	WHT	HCAM	r_s
58044.246034	0.000021	WHT	HCAM	g_s
58137.164798	0.000040	NTT	UCAM	u_s
58137.183422	0.000026	NTT	UCAM	r_s
58137.190855	0.000014	NTT	UCAM	g_s

Time	ΔTime	Telescope	Instrument	Filter
58431.326300	0.000015	NTT	UCAM	g_s
58431.326373	0.000058	NTT	UCAM	i_s
58431.330021	0.000040	NTT	UCAM	u_s
58494.047163	0.000015	GTC	HCAM	i_s
58494.047164	0.000008	GTC	HCAM	r_s
58494.047166	0.000006	GTC	HCAM	g_s
58494.047172	0.000039	GTC	HCAM	z_s
58494.047174	0.000015	GTC	HCAM	u_s
58879.239177	0.000051	NTT	UCAM	u_s
58879.246677	0.000019	NTT	UCAM	g_s
58879.250316	0.000078	NTT	UCAM	i_s
58880.746361	0.000037	TNO	USPEC	KG5
59259.711306	0.000032	TNO	USPEC	KG5
59281.643978	0.000046	TNO	USPEC	KG5
59526.333033	0.000020	NTT	UCAM	g_s
59526.336784	0.000050	NTT	UCAM	u_s
59527.319131	0.000044	NTT	UCAM	u_s
59527.319145	0.000017	NTT	UCAM	g_s
59527.319175	0.000057	NTT	UCAM	i_s
59528.346290	0.000045	NTT	UCAM	g_s
59528.346293	0.000075	NTT	UCAM	u_s
59528.346385	0.000079	NTT	UCAM	i_s
59642.131890	0.000019	NTT	UCAM	g_s
59642.131937	0.000046	NTT	UCAM	u_s
59642.132033	0.000102	NTT	UCAM	i_s

Table 3.5: An observing log of all HM Cnc observations acquired by us with HiPERCAM, ULTRACAM or ULTRSASPEC. Details of observations with archival data can be found at the appropriate studies cited in Section 3.4.1. Included in this table are the conditions for the data that we obtained. Unless mentioned in the comments, a night is not noticeably impacted by clouds. The duration represents the time that the telescope was on target after acquisition. $\mathrm{MJD_{mid}}$ is the MJD at the centre of the observing period. In the instrument column, UCAM, USPEC and HCAM are abbreviations for ULTRACAM, ULTRASPEC and HiPERCAM. Asterisked comments indicate data that were presented in Barros et al. [2007], though are reanalysed.

Night	$\mathrm{MJD_{mid}}$	Filters	Telescope	Instrument	Cadence (s)	Duration (min)	Comments
2003-05-20	52779.9	u' g' i'	WHT	UCAM	20.0	20.3	Seeing 1.5-2.0$''$
2003-05-21	52780.9	u' g' i'	WHT	UCAM	9.8	53.2	*Seeing 1.2$''$
2003-05-22	52781.9	u' g' i'	WHT	UCAM	9.8	57.9	*Seeing 1.0$''$
2003-05-23	52782.9	u' g' i'	WHT	UCAM	9.8	62.4	*Seeing 1.0$''$
2003-05-25	52784.9	u' g' i'	WHT	UCAM	9.8	41.2	*Seeing 1.3$''$
2003-11-11	52955.2	u' g' i'	WHT	UCAM	10.0	66.1	Seeing 1.0$''$
2003-11-13	52957.1	u' g' i'	WHT	UCAM	10.0	35.5	Seeing 1.0-1.3$''$
2005-11-26	53701.2	u' g' r'	VLT	UCAM	3.0	107.5	*Initially poor seeing, later 1.0-1.5$''$
2005-11-27	53702.3	u' g' r'	VLT	UCAM	1.5	215.5	*Seeing $< 1.0''$
2005-11-28	53703.3	u' g' r'	VLT	UCAM	1.5	195.9	*Seeing $< 1.0''$
2007-10-20	54394.2	u' g' r'	WHT	UCAM	9.7	102.2	Seeing 1.0–1.2$''$
2010-12-01	55532.3	u' g' i'	NTT	UCAM	19.7	193.6	Seeing 1.0-1.5$''$. Intermittent clouds
2012-01-21	55947.9	u' g' r'	WHT	UCAM	10.0	113.3	Seeing 1.0-1.5$''$
2012-10-10	56211.2	u' g' r'	WHT	UCAM	8.0	32.2	Seeing 1.0$''$
2012-10-13	56214.1	u' g' r'	WHT	UCAM	8.5	49.9	Seeing 1.4$''$
2013-12-31	56658.0	u' g' r'	WHT	UCAM	10.0	57.2	Seeing 1.5$''$
2015-01-14	57037.1	u' g' i'	WHT	UCAM	10.0	66.0	Flares in seeing; 1.0–3.0$''$

... continued

2015-01-17	57040.2	u' g' r'	WHT	UCAM	10.0	107.2	Seeing 1.0–1.4″
2016-11-07	57700.3	u' g' r'	NTT	UCAM	10.0	35.4	Seeing 1.5″
2016-11-09	57702.3	u' g' r'	NTT	UCAM	10.0	56.9	Seeing 1.2″
2018-01-18	58137.2	u_s g_s r_s	NTT	UCAM	20.0	141.1	Seeing 1.5″
2018-11-08	58431.3	u_s g_s i_s	NTT	UCAM	10.0	84.7	Seeing 1.3″
2020-01-30	58879.2	u_s g_s i_s	NTT	UCAM	10.0	147.8	Seeing 1.5″
2021-11-07	59526.3	u_s g_s i_s	NTT	UCAM	10.0	74.6	Focus issues. Good conditions.
2021-11-08	59527.3	u_s g_s i_s	NTT	UCAM	10.0	129.7	Seeing 1.0–1.2″
2021-11-09	59528.3	u_s g_s i_s	NTT	UCAM	10.0	20.4	Seeing 1.1″
2022-03-03	59642.1	u_s g_s i_s	NTT	UCAM	10.0	71.4	Seeing 1.2″
2017-10-17	58044.2	g_s r_s i_s z_s	WHT	HCAM	13.9	24.8	Seeing 1.2″
2019-01-10	58494.0	u_s g_s r_s i_s z_s	GTC	HCAM	10.0	43.3	Seeing 0.9″
2020-02-01	58880.7	KG5	TNO	USPEC	15.4	160.2	Seeing 1.5″
2021-02-14	59259.7	KG5	TNO	USPEC	14.2	96.7	Seeing 1.0–1.4″
2021-03-08	59281.6	KG5	TNO	USPEC	16.4	175.4	Seeing 0.9″

3.10 MESA input models

Table 3.6: The initial parameters of the MESA models presented in Fig. 3.7. The donor mass stated includes the mass of the diffused hydrogen envelope. The present day system mass is not the combination of the starting masses due to the mass loss mechanisms invoked, as discussed in Section 3.6.2.

M_{Donor} ($M_\odot$)	$M_{Accretor}$ ($M_\odot$)	H Envelope (10^{-3} $M_\odot$)	Fig. 3.7 Label
0.16	1.20	0.1	$0.156\,M_\odot + 1.202\,M_\odot$
0.16	1.30	0.1	$0.156\,M_\odot + 1.302\,M_\odot$
0.17	1.00	0.1	$0.167\,M_\odot + 1.001\,M_\odot$
0.16	1.20	1.0	$0.156\,M_\odot + 1.202\,M_\odot$
0.17	1.00	1.0	$0.166\,M_\odot + 1.002\,M_\odot$
0.17	1.20	3.0	$0.162\,M_\odot + 1.205\,M_\odot$
0.17	1.30	3.0	$0.162\,M_\odot + 1.305\,M_\odot$
0.18	0.95	3.0	$0.172\,M_\odot + 0.955\,M_\odot$
0.176	1.25	5.6	$0.163\,M_\odot + 1.258\,M_\odot$
0.179	1.15	5.3	$0.169\,M_\odot + 1.156\,M_\odot$
0.195	0.85	4.9	$0.183\,M_\odot + 0.856\,M_\odot$

Chapter 4

An eclipsing 47 min double white dwarf binary at 400 pc: WDJ022558.21-692025.38

James Munday, P.-E. Tremblay, J. J. Hermes, Brad Barlow, Ingrid Pelisoli, T. R. Marsh, Steven G. Parsons, David Jones, S. O. Kepler, Alex Brown, S. P. Littlefair, R. Hegedus, Andrzej Baran, Elmé Breedt, V. S. Dhillon, Martin J. Dyer, Matthew J. Green, Mark R. Kennedy, Paul Kerry, Isaac D. Lopez, Alejandra D. Romero, Dave Sahman, Hannah L. Worters

Contribution of co-authors

The source was discovered in a short-cadence search for rapid variability with the TESS spacecraft led by authors #3 and #9. Observations used in this study were obtained and/or reduced by all authors except #2 and #8. Author #2 performed spectral fitting to the stacked spectrum of the target presented in Section 4.2.2. Author #8 offered support to the PHOEBE package by activating a routine for Doppler beaming, that was necessary to include in this system. All authors contributed with comments on the manuscript during the submission/revision process by supplying key ideas to explore in creating the final version of the study. All other components and the leading of the study were performed by me.

Abstract

We present the discovery of the eclipsing double white dwarf (WD) binary WDJ $022558.21-692025.38$ that has an orbital period of 47.19 min. Following identification with the Transiting Exoplanet Survey Satellite, we obtained time-series ground based spectroscopy and high-speed multi-band ULTRACAM photometry which indicate a primary DA WD of mass $0.40 \pm 0.04\,\mathrm{M}_{\odot}$ and a $0.28 \pm 0.02\,\mathrm{M}_{\odot}$ mass secondary WD, which is likely of type DA as well. The system becomes the third-closest eclipsing double WD binary discovered with a distance of approximately 400 pc and will be a detectable source for upcoming gravitational wave detectors in the mHz frequency range. Its orbital decay will be measurable photometrically within 10 yrs to a precision of better than 1%. The fate of the binary is to merge in approximately 41 Myr, likely forming a single, more massive WD.

Table 4.1: Observed parameters of J0225−6920 taken from *Gaia* DR3 with reference epoch 2016-01-01. The quoted distance measurement is taken from the method described in Bailer-Jones et al. [2021].

Parameter	Constraint
RA	$36.492414189\,\mathrm{deg} \pm 0.035\,\mathrm{mas}$
Dec	$-69.34049573\,\mathrm{deg} \pm 0.035\,\mathrm{mas}$
PM RA	$-11.720 \pm 0.046\,\mathrm{mas\,yr^{-1}}$
PM Dec	$-25.500 \pm 0.049\,\mathrm{mas\,yr^{-1}}$
Parallax	$2.478 \pm 0.038\,\mathrm{mas}$
BP	$16.305 \pm 0.004\,\mathrm{mag}$
G	$16.398 \pm 0.001\,\mathrm{mag}$
RP	$16.600 \pm 0.007\,\mathrm{mag}$
Distance	$402.6^{+5.9}_{-6.8}\,\mathrm{pc}$
Source ID	4693541467955966848

4.1 Introduction to WDJ022558.21-692025.38

Eclipsing DWD binaries offer the most precise system characterisation and those with sub-hour orbital periods have the potential for their orbital decay to be measured observationally within decades. In this paper, we present the discovery of such a compact and eclipsing DWD binary with orbital period of 47.19 min. Its binarity was discovered using the Transiting Exoplanet Survey Satellite [TESS, Ricker et al., 2015], making it one of the shortest-period detached binary discovered by *TESS* to date. Compared to the characterised eclipsing DWD binary sample, WDJ 022558.21−692025.38 (hereafter J0225−6920) is located relatively nearby in the Galaxy at a distance of approximately 400 pc; at the time of writing, J0225−6920 becomes the third-closest eclipsing DWD discovered after NLTT 11748 [Steinfadt et al., 2010] and GALEX J1717+6757 [Vennes et al., 2011], both being of distance $\approx 180\,\mathrm{pc}$.

The observations are discussed in Section 4.2 followed by spectral modelling in Section 4.3. Then, I address light curve modelling and derived system parameters in Section 4.4. I close by discussing the projected orbital decay of J0225−6920 in Section 4.5.

4.2 Observations

4.2.1 Photometry

J0225−6920 was identified as a DA white dwarf by Kilkenny et al. [2015, EC02251-6933] and classified by Gentile Fusillo et al. [2019, 2021] as a high-probability white dwarf ($P_{\mathrm{WD}} > 0.95$). J0225−6920 was part of a 2 min cadence program with *TESS* in Sectors 27, 28, and 29 (program G03124, TIC 631238061). During this program, we saw clear eclipsing signatures in J0225$-$6920 that showed the system to be a DWD binary, although its orbital period was not immediately clear from boxed-least-squares periodogram aliases of 23.5 min and 47 min. To distinguish the orbital period, we initially obtained (white light) data from the 0.41 m PROMPT-1 telescope [Reichart et al., 2005], data from the 1.6 m Pico dos Dias Observatory (BG40 filter) and data from the South African Astronomical Observatory (SAAO) 1.0 m Lesedi telescope (white light). These revealed distinct primary and secondary eclipses for a 47 min orbital period.

Following identification, we then observed J0225$-$6920 with the high-speed photometer ULTRACAM [Dhillon et al., 2007] mounted on the ESO 3.5 m New Technology Telescope (NTT) during five nights in July 2021. Observations were simultaneously taken using the Super SDSS u_s, g_s and i_s filters [Dhillon et al., 2021]. We later observed with ULTRACAM on the NTT over three nights in September 2022 in the Super SDSS u_s, g_s and r_s filters. In total, we observed more than 15 hrs on target with ULTRACAM. A full observing log is supplied in Appendix 4.4.

All data were debiased and flat-fielded; the SAAO and PROMPT-1 data with custom scripts, and the ULTRACAM data using the HiPERCAM reduction pipeline [Dhillon et al., 2021]. Dark-current subtraction was additionally performed for the ULTRACAM data because of its hotter operational temperature. The flux of J0225$-$6920 was extracted through differential aperture photometry using a non-variable comparison star with *Gaia* DR3 source ID 4693540643322249216. I used a variable aperture size that reflected the seeing at the time of observation set to $1.8\times$ the full-width at half-maximum of the stellar profile. All mid-exposure time-stamps were placed on a Barycentric Modified Julian Date (BMJD) Barycentric Dynamical Time (TDB) time frame.

4.2.2 Spectroscopy

We obtained time-series long-slit spectra from the 4.1 m SOAR telescope with the SOAR Goodman spectrograph [Clemens et al., 2004] in October 2020. We observed with a 930 $1\,\mathrm{mm}^{-1}$ grating and a slit-width of $1''$, resulting in a resolution of $\lambda/\Delta\lambda \approx 1800$ with a wavelength coverage of 3600 –5275 Å. 43 consecutive spectra were obtained with exposure time 180 s and a 7 s readout time between adjacent exposures. FeAr arc lamp spectra were taken immediately before the first and immediately after the final spectrum. To avoid any possible drift to the wavelength solution extracted from FeAr arc lamps, we placed a second star (Gaia DR3 4693540643322249216) on the slit and calibrated the wavelength solution of each science exposure using the Balmer series of this comparison, i.e. the initial wavelength solution was obtained in the reference frame of the comparison star. The systemic velocity of the binary was measured from each set of calibrated spectra (see Section 4.3.2)

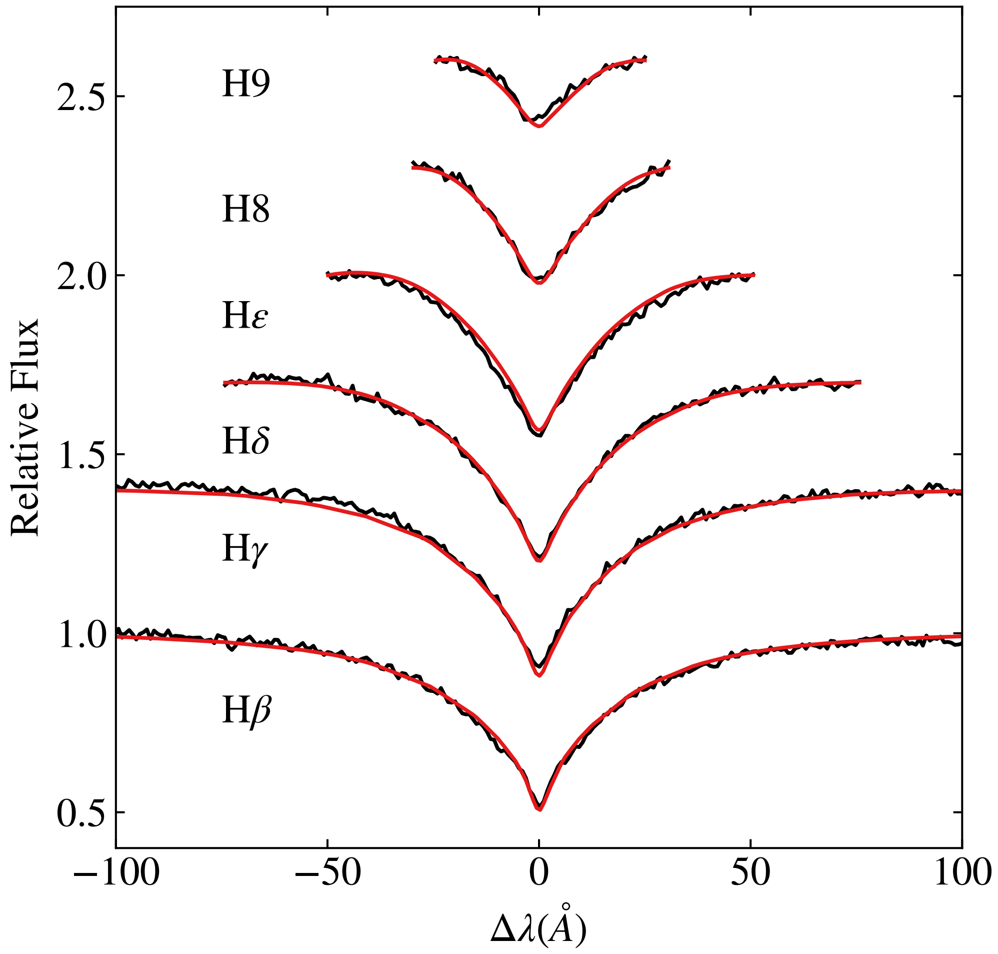

Figure 4.1: Normalised Balmer absorption line profiles from the combined SOAR/Goodman spectra, Hβ through H$_9$. The observations are displayed in black, with the best-fit model overplotted in red. Each profile is vertically offset for clarity. The displayed model has a primary star of $T_{\rm eff,1} = 25\,330$ K and $\log g_1 = 6.99$ dex combined with a secondary star of $T_{\rm eff,2} = 13\,750$ K and $\log g_2 = 7.60$ dex. The secondary star's effective temperature that is included here was derived from a single iteration of light curve fitting using the $T_{\rm eff,1}$ of a single-star fit to the co-added spectrum.

and the systemic velocity found through the FeAr lamp wavelength solution was used to convert from the reference frame of the comparison star to that of the barycentre, retaining the absolute wavelength calibration.

The signal-to-noise ratio (SNR) in each spectrum at the centre and wings of Hβ is approximately 15 and 23, respectively. These reveal clear Balmer absorption features indicating that the brighter component is a DA WD (see Fig. 4.1). Double-lined features in the spectrum were searched for, particularly at Hβ, but were not obviously apparent. No metals nor helium spectral lines were detected in the spectra.

4.3 Spectroscopic analysis

4.3.1 Atmospheric Parameters

The reduced spectra were co-added with a common rest wavelength. The normalised Balmer line profiles of the co-added spectrum were then fit with the DA WD models of Tremblay et al. [2011, 2015]. Fitting the spectrum with a single DA WD model to represent the primary star[1], we constrain the atmosphere of the brighter component[2] to have a surface gravity $\log g_1 = 7.07 \pm 0.04\,\mathrm{dex}$ and $T_{\mathrm{eff},1} = 24\,250 \pm 310\,\mathrm{K}$.

In an attempt to retrieve the surface gravity and temperature of the secondary star, and improve the accuracy of the primary star parameters, photometric flux measurements from wide-field surveys were utilised and used for fitting two unique WDs to the combined SED. At the time of finishing this study, *Gaia* DR3 and *SkyMAPPER* [Wolf et al., 2018] survey data were available, which were utilised to model the photometric and spectroscopic data simultaneously. The flux measurements were dereddened with an extinction constant of $A_V = 0.09$ [Gentile Fusillo et al., 2021] following the reddening prescription of Fitzpatrick and Massa [2007] with $R_V = 3.1$. The WD models require a conversion from an Eddington flux to a flux observed at Earth, so a posterior distribution on the fitted distance was enforced based on the *Gaia* DR3 parallax stated in Table 4.1. A single DA WD model to the dereddened *Gaia* photometric fluxes yields $T_{\mathrm{eff}} = 22\,500 \pm 910\,\mathrm{K}$ [Gentile Fusillo et al., 2021], which places a minimum temperature on the primary star since the flux contributed from the cooler companion weights a single star fit to cooler temperatures.

All dereddened photometric flux measurements and the normalised Balmer profiles were then simultaneously fit with a DA+DA model and enforced $T_{\mathrm{eff},2} = 13\,750\,\mathrm{K}$. This temperature measurement was guided by the results of my light curve fitting in Section 4.4

---

[1] I follow the convention in this paper that the primary star is the hotter and brighter WD.

[2] I present errors on the atmospheric constraints of the stars by combining in quadrature the statistical error from χ^2 fitting with an external error of 1.2% for $T_{\mathrm{eff},1}$ and 0.038 dex for $\log g_1$ [Liebert et al., 2005]. This is primarily to account for the error induced from flux calibration of spectra.

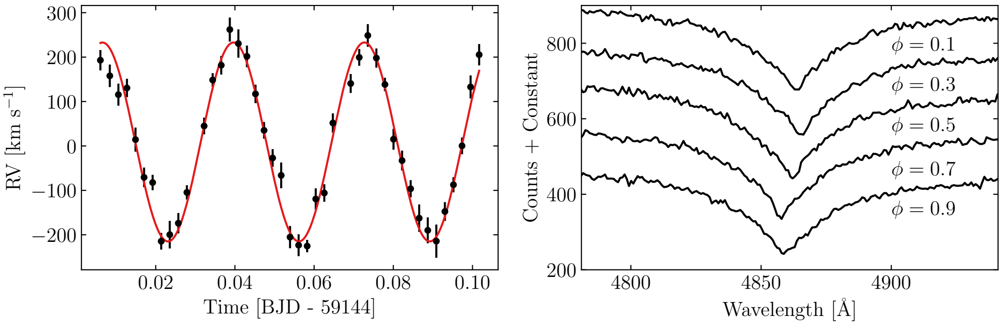

Figure 4.2: Left: Extracted radial velocity measurements of J0225−6920 with $K_1 = 224.0\,\mathrm{km\,s^{-1}}$ and $\gamma = 1.6\,\mathrm{km\,s^{-1}}$ overplot. Right: Stacked observations of J0225−6920 as a function of phase with bin widths of 0.2 cycles, magnified on Hβ. A trailed spectrogram is additionally provided in Appendix 4.8.

when using the measured $T_{\mathrm{eff},1}$ from a single star model to the co-added spectrum. The goals from fitting a DA+DA model were to improve the accuracy of the primary temperature by including the flux from a WD companion and to gain a measurement of the secondary's surface gravity. Pier-Emmanuel Tremblay obtained results of $T_{\mathrm{eff},1} = 25\,330 \pm 330\,\mathrm{K}$, with $\log g_1 = 6.99 \pm 0.04$ dex and $\log g_2 = 7.60 \pm 0.23$ dex (see Fig. 4.1). Interpolation of these parameters with WD atmosphere models indicate a primary mass of $M_1 = 0.35 \pm 0.01\,\mathrm{M}_\odot$ for a helium core [Althaus et al., 2013] and $M_1 = 0.27 \pm 0.01\,\mathrm{M}_\odot$ for a carbon-oxygen core [Bédard et al., 2020] WD. A hybrid carbon-oxygen/helium core composition is also possible, and predicted masses for this composition are similar to pure-helium masses at the primary temperature [Zenati et al., 2019]. Although both a carbon-oxygen and helium core WD would be possible core compositions for the primary depending on the evolutionary path of the system, carbon-oxygen-core WDs are not expected below roughly $0.33\,\mathrm{M}_\odot$ [Prada Moroni and Straniero, 2009], so I only consider solutions with a helium-core primary going forward. The core composition of the secondary is unclear from spectral analysis alone due to its large surface gravity error.

Lastly for atmospheric analysis, a DA+DBA WD spectral fit was performed with $T_{\mathrm{eff},2}$ again fixed at 13 750 K and two inconsistencies were found; this model significantly under-predicted the flux of the weakest Balmer transitions and a He I absorption feature (4471 Å) would be apparent, which is not in the observed spectrum. I consequently predict that the companion has a hydrogen rich atmosphere, perhaps of type DA also. This DA+DA WD prediction leads us to assume the spectroscopic results from the DA+DA model fit for the remainder of the paper, as listed in Table 4.2.

4.3.2 Radial Velocities

I then searched for any radial velocity variations in the normalised Hβ absorption-line profile by modelling the full set of spectra simultaneously following the methods outlined in Section 2.5.5. The line profiles themselves were fit with a 2-Gaussian component similar to all spectra, each having a standard deviation, $\sigma_{\mathrm{A,B}}$, an amplitude, $A_{\mathrm{A,B}}$ and a common central wavelength solved through equation 2.13. A negligible difference was found utilising a Gaussian, Lorentzian or Voigt line profile, or a combination of each to the measured radial velocities. One of these Gaussian components serves to model the broad local thermal equilibrium (LTE) component of Hβ, while the other models the non-LTE component which is well described by a Gaussian profile. Overall, this meant that γ, K, $\sigma_{\mathrm{A,B}}$ and $A_{\mathrm{A,B}}$ were all free parameters. To reach a solution, I iteratively trialed parameter combinations using a Markov Chain Monte Carlo (MCMC) algorithm with the Python package EMCEE [Foreman-Mackey et al., 2013], minimising the χ^2 between the model and the set of observed spectra. I chose this method to reduce the impact of the input absorption line model on the resultant measured semi-amplitude, where instead the shape of the Gaussian components are dynamically solved to when obtaining a best fit solution.

I measure $K_1 = 224.0 \pm 4.4\,\mathrm{km\,s^{-1}}$ and $\gamma = 1.6 \pm 4.1\,\mathrm{km\,s^{-1}}$. For clarity, I also extracted radial velocity measurements independently of orbital phase (as listed in Appendix 4.10) by keeping $\sigma_{A,B}$ and $A_{A,B}$ fixed from a best-fit to the stacked spectrum. Radial velocity errors are reported as the standard deviation of 1000 bootstrapping iterations. These measurements and the fit K_1 and γ are plotted in Fig. 4.2. It is important to note, however, that the measured radial velocity amplitude may be underestimated due to the contribution of light from the companion in anti-phase. Even though absorption lines from the companion are not obviously apparently (see Fig. 4.2), its contribution can be significant [e.g. Hallakoun et al., 2016]. To check if this has a significant impact in J0225$-$6920, I searched for a consistent radial velocity amplitude across all Balmer lines by measuring those of Hβ $-$ Hζ, finding them to be within 2σ of each other; Hβ being the largest. Light curve modelling to the photometry alone agreed best with the radial velocity at Hβ (see Section 4.4.2). As such, I report the radial velocity amplitude of Hβ as that of the system.

4.4 Binary Modelling

4.4.1 Ephemeris

To determine the orbital ephemeris, I simultaneously searched for an orbital period using the photometry from all detectors and filters using the multi-band Lomb-Scargle periodogram package of VanderPlas and Ivezić [2015]. By fitting individual eclipses with my best-fit

Table 4.2: Spectroscopically determined system parameters from the normalised Balmer line fit and the fit semi-amplitude to Hβ (following the method described in Section 4.3).

Parameter (Spectroscopy)	Value
Primary Temperature	$T_{\text{eff},1} = 25\,330 \pm 330\,\mathrm{K}$
Primary Surface Gravity	$\log g_1 = 6.99 \pm 0.04\,\mathrm{dex}$
Secondary Surface Gravity	$\log g_2 = 7.60 \pm 0.23\,\mathrm{dex}$
Systemic Velocity	$\gamma = 1.6 \pm 4.1\,\mathrm{km\,s^{-1}}$
Primary semi-amplitude	$K_1 = 224.0 \pm 4.4\,\mathrm{km\,s^{-1}}$

Table 4.3: J0225−6920 system parameters. All quoted measurements originate from a fit to K_1 and the ULTRACAM light curves only. Errors are quoted as the 16th and 84th percentiles of the post-burnin MCMC posteriors.

Parameter (Photometry)	Value
Period	0.03277099777(24) d
Primary mass	$M_1 = 0.40 \pm 0.04\,\mathrm{M}_\odot$
Primary temperature	$T_1 = 25\,550 \pm 200\,\mathrm{K}$
Primary radius	$R_1 = 0.0291 \pm 0.0010\,\mathrm{R}_\odot$
Secondary mass	$M_2 = 0.28 \pm 0.02\,\mathrm{M}_\odot$
Secondary temperature	$T_2 = 14\,350 \pm 100\,\mathrm{K}$
Secondary radius	$R_2 = 0.0244 \pm 0.0007\,\mathrm{R}_\odot$
Inclination	$i = 85.25 \pm 0.06\,\mathrm{deg}$
Primary surface gravity	$\log g_1 = 7.11 \pm 0.06\,\mathrm{dex}$
Secondary surface gravity	$\log g_2 = 7.11 \pm 0.04\,\mathrm{dex}$
Mass ratio	$q = M_2/M_1 = 0.70 \pm 0.09$
Relative squared radii	$(R_2/R_1)^2 = 0.70 \pm 0.06$
Primary semi-amplitude	$K_1 = 240.1 \pm 15.6\,\mathrm{km\,s^{-1}}$
Secondary semi-amplitude	$K_2 = 343.0 \pm 21.9\,\mathrm{km\,s^{-1}}$

synthetic light curves for the ULTRACAM data (see Section 4.4.2), I was able to refine the ephemeris to a higher precision. The orbital ephemeris that I obtain, centred on the primary mid-eclipse, is

$$\mathrm{BMJD_{TDB}} = 59403.299199(90) + 0.03277099777(24)E \tag{4.1}$$

4.4.2 PHOEBE

I modelled the ULTRACAM light curves using the PHOEBE package [Prša et al., 2016; Horvat et al., 2018; Jones et al., 2020; Conroy et al., 2020] to constrain the system components. I used blackbody spectra to compute the emergent flux[3]. Irradiation is treated using the 'Horvat' method outlined in Horvat et al. [2019] and a perfect reflection (an albedo of one) for both stars is assumed. The same Galactic reddening treatment as in Section 4.3.1 was applied, which has a small effect on the light curve morphology but is most impactful to the eclipse depths [e.g. Jones et al., 2020]. The synthetic light curves do not include the contribution of gravitational lensing, however, its impact on the emergent flux is suspected to be negligible for this system, amplifying the received flux by far less than 1% [Marsh, 2001].

Limb darkening and gravity darkening coefficients were interpolated uniquely for the two stars using tabulated values that are specific for the Super SDSS passbands. For limb darkening, I used a power-law prescription with its coefficients set according to the 3-dimensional WD models of Claret et al. [2020b], or the 1-dimensional WD models of Claret et al. [2020a] when the 3-dimensional grid boundaries were exceeded. Gravity darkening coefficients were interpolated from the tables of Claret et al. [2020a]. In each case, the interpolation was dependent on the effective temperature and the surface gravity of the respective star for a trial synthetic model.

I also reactivated the Doppler beaming functionality of PHOEBE 2.2 and pass beaming coefficients of Claret et al. [2020b][4]. The synthetic K_1 and K_2 are solved dynamically in PHOEBE as a function of phase (which is to say through Keplerian geometry) and incorporate the impact of gravitational redshift. The effect of smearing from a finite exposure time was corrected for assuming exposures of 9 s in the u_s-band and 3 s in the g_s, r_s and i_s bands (see Table 4.4).

To obtain a system solution, I implemented an MCMC algorithm using EMCEE

---

[3] WD model atmospheres are not currently available in PHOEBE. Since there is ambiguity on the secondary's contribution to the measured $T_{\mathrm{eff},1}$ (Section 4.3.1), the spectral energy distribution for WD atmospheres would not be exact neither, making a light-curve extracted $T_{\mathrm{eff},2}$ an approximation.

[4] In PHOEBE 2, this feature was disabled due to concerns of the accuracy of beaming factor computation from a non-implicit and fitted trend of the SED. In the Claret et al. [2020b] models, the beaming factor is calculated implicitly and integrated over the full SED. Therefore, the passed beaming constant is an accurate representation.

[Foreman-Mackey et al., 2013], where the goodness of fit was determined by minimisation of the χ^2 between the synthetic and observed light curves. I fit synthetic photometry to the ULTRACAM light curves simultaneously to improve the precision of the radii, masses and the inclination of the system. Since blackbody models are considered, the spectral energy distribution assumed for both stars in PHOEBE differs from that of a WD. The usage of blackbody models causes little issue to the g_s, r_s and i_s bands as the colour between each band for WD and blackbody spectra is small, whereas the $u_s - g_s$ colour deviates strongly. To overcome these issues, I modelled to the g_s, r_s and i_s bands only and I set a Gaussian prior for the primary star temperature based on the spectroscopic solution. With a final model, I then checked for consistency in the u_s band by allowing the temperature of the secondary to be a free parameter. The secondary temperature is identical for each of the other passbands.

I started by modelling independently of K_1 and found a good fit to the photometry where the synthetic K_1 was within the error of that measured, giving us confidence that the measured K_1 in Section 4.3.2 is reflective of the true value. Following this test, I introduced K_1 into the χ^2 minimisation. Overall, the mass, temperature and radius of the primary and secondary star and the inclination of the system were free parameters in the MCMC. Only $T_{\text{eff},1}$ included a Gaussian prior while all other parameters had no set prior.

4.4.3 Binary parameters

The post-burnin results of the MCMC are presented in Table 4.3, with the best-fitting binary model displayed in Fig. 4.3. A corner plot diagram is included in Appendix 4.6 showing the covariance between free parameters. A good model fit to the light curve is obtained about the eclipses and for K_1. Furthermore, the impact of Doppler beaming in quadrature (which causes the observed flux to be larger/smaller as a star moves towards/away from the observer) is well fit in the u_s-band; the band impacted most significantly [see e.g. Claret et al., 2020b].

From the light curve modelling, the primary star has an effective temperature of $25\,550 \pm 200$ K and for the secondary $14\,350 \pm 100$ K. Component masses and radii indicate that both stars likely have helium cores, falling closely on the evolutionary tracks of helium-core WD models [Althaus et al., 2013; Istrate et al., 2016], and that the system is detached. The primary star's Roche lobe is 12% filled and the secondary's is 18% filled. Interpolation of the masses and the temperatures of each WD with Istrate et al. [2016] cooling track models that feature rotational and diffusional physics indicate cooling ages for each star of $t_1 \approx 7$ Myr and $t_2 \approx 22$ Myr, such that the more massive primary star is the younger of the two. The primary mass determined from light curve fitting is consistent with the spectroscopically predicted mass of $M_1 = 0.35 \pm 0.01\,\mathrm{M}_\odot$ for a WD with a helium core (see

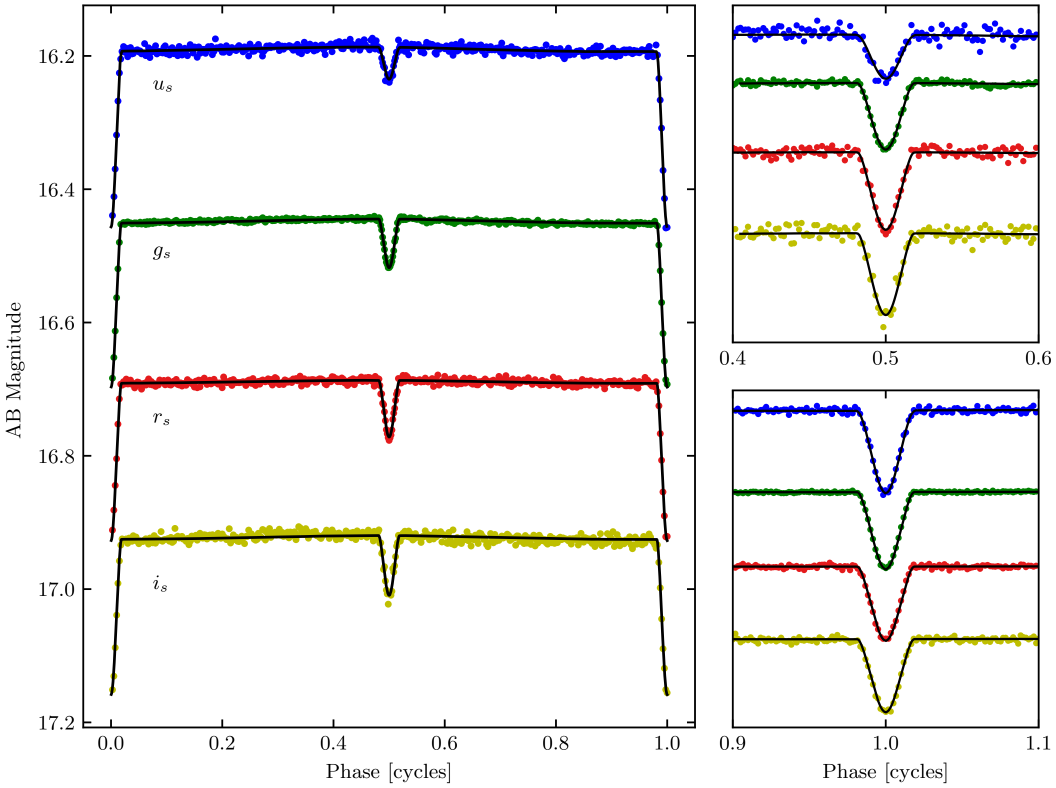

Figure 4.3: Left: The ULTRACAM photometry phase-folded on the orbital ephemeris of equation (4.1) and binned for clarity. PHOEBE synthetic light curves are overlaid in black. The AB magnitude is displayed on the vertical axes where all but the u_s-band are vertically offset by $g_s = 0.23\,\mathrm{mag}$, $r_s = 0.14\,\mathrm{mag}$ and $i_s = -0.16\,\mathrm{mag}$ for clarity. Top right/Bottom right: similar to the left-hand plot, but zoomed around the primary and secondary eclipses. Both right-hand-side plots are zoomed insets, where the light curves from each filter are manually offset in magnitude to enlarge the eclipses.

Section 4.3.1). While the $\log g_2 = 7.60 \pm 0.23$ dex for a two-star spectral fit shows a worse agreement to the light-curve inferred parameters, the measurements agree at approximately a 2σ level, where such a difference could have been influenced by the systematical errors such as smearing of the secondary star to the co-added spectrum. The modelled parameters indicate that the secondary is also likely a helium core WD.

4.4.4 Similarities with known systems

J0225$-$6920 bears a resemblance to the systems ZTF J1749+0924, ZTF J2029+1534 and ZTF J0722-1839 [Burdge et al., 2020b]. These systems are also detached DWD binaries with similar effective temperatures and masses to J0225$-$6920, each having a shorter orbital period. All of these systems likely exited a common-envelope phase under similar conditions and follow a similar evolutionary history. In each binary, both stars are likely helium-core WDs. The characterisation of these binaries has also been used in the study of Scherbak and Fuller [2023] to investigate the common envelope efficiency parameter, α, from a second mass transfer phase. Given the similarity of J0225$-$6920, my measurements are consistent with $\alpha \approx 0.2 - 0.4$, as inferred by these authors.

A further two compact systems that are comparable to J0225$-$6920, having similar star masses and temperatures, are SDSS J1152+0248 [Hallakoun et al., 2016; Parsons et al., 2020] and CSS 41177 [Bours et al., 2014, 2015]. These eclipsing DWD binaries have an orbital period of 144 min, and 167 min, respectively. J0225$-$6920 appears to bridge the period gap between all of these DWD binaries, which can be utilised in the future to study the impact of tides on orbital decay [e.g. Piro, 2019].

Lastly, J0225$-$6920 is much alike SDSS J232230.20+050942.06 in regards to the core composition, being the first double helium-core, DWD, LISA verification binary discovered [Brown et al., 2020a]. Systems such as these are vital gravitational wave sources for data quality verification of LISA when launched, given that the gravitational wave frequency and amplitude are solvable from the orbital parameters of the binary alone.

4.5 J0225$-$6920 as a gravitational wave source

The orbit of J0225$-$6920 will decay due to a loss of orbital angular momentum from gravitational wave radiation and tides. If one assumes that the decay is dominated by gravitational wave radiation, the inspiral will obey equation 1.9. Solving for the derived binary constraints in Section 4.4, this means that the predicted orbital frequency derivative is $\dot{f} = (1.03 \pm 0.15) \times 10^{-19}\,\mathrm{Hz\,s^{-1}}$, or, $\dot{P} = (-8.27 \pm 1.21) \times 10^{-13}\,\mathrm{s\,s^{-1}}$.

The orbital decay can be precisely measured with continued observations using the time of arrival of a given orbital phase, where a number of WD binaries have been characterised in this way through continued observations [Barros et al., 2007; Hermes et al., 2012; de Miguel et al., 2018; Burdge et al., 2019a,b, 2020a; Munday et al., 2023]. The deep eclipses of J0225$-$6920 make mid-eclipse timing the natural way to do so, where an earlier eclipse arrival time is explainable by an orbital decay. The deviation of the eclipse timing from a constant orbital period is dominated (to first order) by $\dot{P}t^2/2P$ for general relativistic effects, with t the length of time following the first eclipse. From the data presented in this paper, the arrival time difference from the full span of data is currently a mere second, however, the bright *Gaia* magnitude ($G = 16.4\,\mathrm{mag}$) and its $0.2\,\mathrm{mag}$ deep primary eclipses makes J0225$-$6920 an exemplar system for a measured $\dot{P}$ that can be utilised to probe non-gravitational wave induced orbital decay in the future. This may arise in J0225$-$6920 due to tidal dissipation [Benacquista, 2011; Piro, 2011; Fuller and Lai, 2012; Piro, 2019], in which orbital energy transferred into rotational energy of the stars is the cause of a faster orbital decay. Additionally, measurement of the orbital decay constrains the chirp mass, thus restricting the combinations of primary and secondary star masses for system modelling [e.g. Munday et al., 2023].

I find that timing of individual J0225$-$6920 primary and secondary eclipses in ideal conditions with ULTRACAM is accurate to $0.5\,\mathrm{s}$ and $2\,\mathrm{s}$, respectively. Considering this and the predicted orbital decay, I expect to obtain a period derivative precise to better than $\approx$5% after 5 yrs or $\approx$1% after 10 yrs; the precision scaling with t^2. The observed deviation of the centre of eclipse arrival time will be $\approx$4 s and $\approx$15 s after 5 yrs and 10 yrs. Furthermore, the compact binary is ideally situated in the *LISA* frequency band, as shown in Fig. 4.4. Its distance of $402.6^{+5.9}_{-6.8}\,\mathrm{pc}$ and derived orbital parameters generates a characteristic strain of $(4.5 \pm 0.7) \times 10^{-20}$, with a projected SNR of 1.3 ± 0.2 after a 4 yr *LISA* mission time, or 2.1 ± 0.4 after 10 yrs [Wagg et al., 2022b,a]. J0225$-$6920 is thus a detectable verification binary for LISA and will be the closest double helium core DWD verification binary known to date; which is a class that is expected to comprise 31% of all LISA detectable binaries [Lamberts et al., 2019]. For comparison, the second- and third-closest double helium-core DWD verification binaries are SDSS J063449.92+380352.2 at 435 pc and SMSS J033816.16$-$813929.9 at 533 pc [Kilic et al., 2021b].

In the future, J0225$-$6920 is expected to merge into a single WD, likely undergoing a hot subdwarf phase during which helium is burnt to form a carbon-oxygen core [Han et al., 2002]. For a circularised binary star system under purely general relativistic orbital decay, two stars will merge after a critical time calculable with equation 1.6I hence predict J0225$-$6920 to merge within $T_c(0.379\,R_{\odot}) = 41\,\mathrm{Myr}$.

---

[4] The data used to create Fig. 4.4 was obtained through https://gitlab.in2p3.fr/LISA/lisa-verification-binaries.

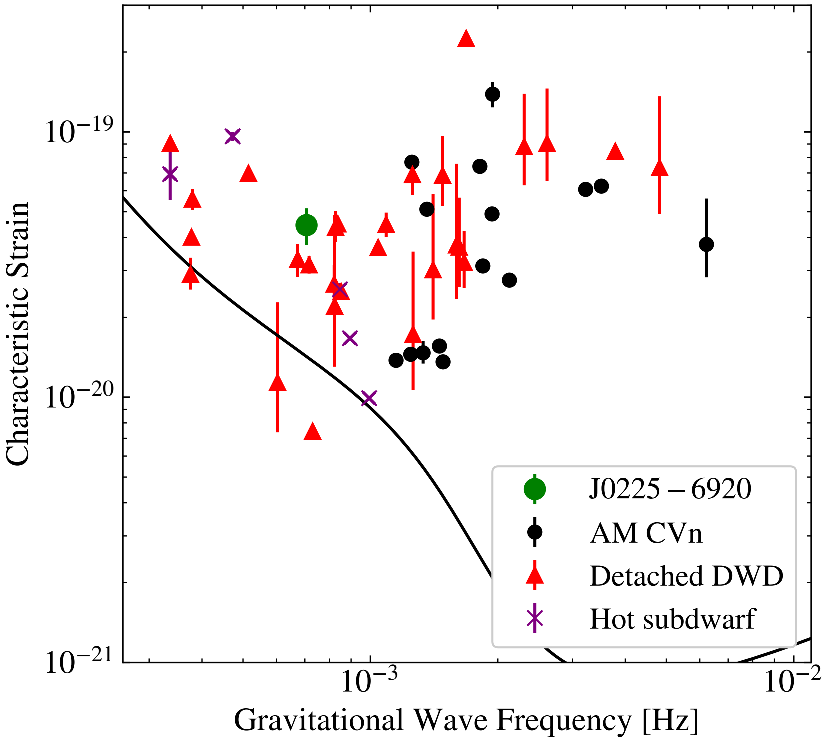

Figure 4.4: A plot of some of the currently known *LISA* verification binary star systems, with characteristic strains predicted from a 4 yr integration time. Systems that are listed in Kupfer et al. [2024, see references therein] are included[5]. These binaries are separated into the categories AM CVn, detached DWD or binaries comprising a hot subdwarf. The addition of J0225−6920 to these verification binaries is depicted. The curved black line represents the predicted detection threshold of *LISA* [Robson et al., 2019].

4.6 Conclusions

I have discovered that J0225$-$6920 is an eclipsing DWD binary with an orbital period of 47.19 min. Multi-band light curve modelling indicates that the system likely consists of two helium-core WDs, where the primary has a DA spectral type, having a pure hydrogen surface composition, and the secondary likely does too. Its relatively close distance and brightness makes the binary a prime candidate to measure the orbital period decay in the future, key to investigate deviations from purely general relativistic orbital decay due to tides. The binary will be a detectable source for the *LISA* spacecraft, and I believe it is the first such DWD verification binary discovered by the *TESS* mission. J0225$-$6920 joins a small sample of fully characterised DWD binaries which will merge within a Hubble time. It is the closest double-helium-core DWD verification binary known to date; a class that is expected to account for 31% of all LISA detectable DWDs [Lamberts et al., 2019].

4.7 Observation Log

Table 4.4: An observing log of all J0225−6920 observations acquired with ULTRACAM which were subsequently used for light-curve modelling. Nights were not noticeably impacted by clouds. The duration represents the time that the telescope was on target after acquisition. $\mathrm{MJD_{mid}}$ is the MJD at the centre of the observing period. All observations listed here were taken with ULTRACAM on the NTT. Observations in the u_s filter were 3× the cadence stated. ULTRACAM has a dead time of 24 ms between adjacent exposures.

Night	Filters	Cadence (s)	Duration (min)	Comments
2021-07-07	u_s g_s i_s	3.0	89.8	Seeing 1.2″
2021-07-08	u_s g_s i_s	3.0	21.9	Seeing 1.3″
2021-07-09	u_s g_s i_s	3.0	76.1	Seeing 1.1-1.5″
2021-07-15	u_s g_s i_s	3.0	44.5	Seeing 1.5″ to >2.0″
2021-07-16	u_s g_s i_s	3.2	35.6	Seeing 1.2″
2022-09-17	u_s g_s r_s	3.3	316.2	Seeing 1.8-2.2″
2022-09-18	u_s g_s r_s	3.7	201.6	Seeing 1.8-2.0″
2022-09-19	u_s g_s r_s	3.2	142.1	Seeing 2.2″, spikes

4.8 Trailed spectrogram

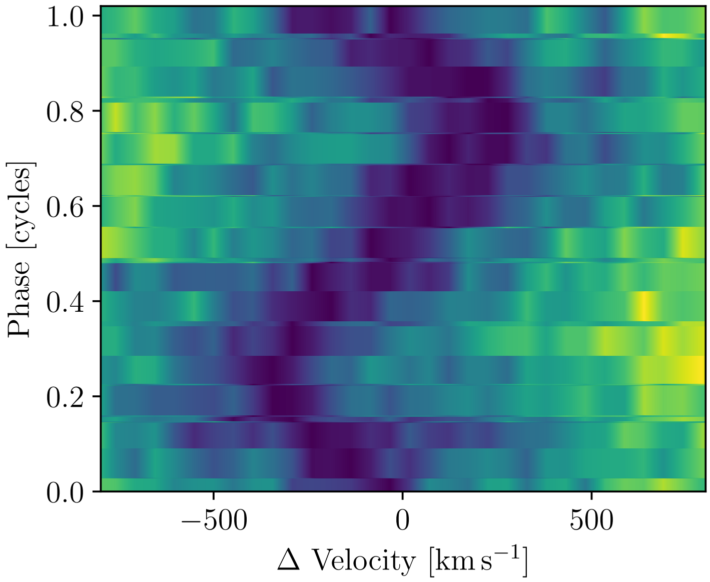

Figure 4.5: A trailed spectrogram of the Hβ line of J0225−6920 from the SOAR Goodman spectra. The centre velocity is set for a zero-velocity at wavelength 4861 Å.

4.9 Corner plot from Light Curve Fitting

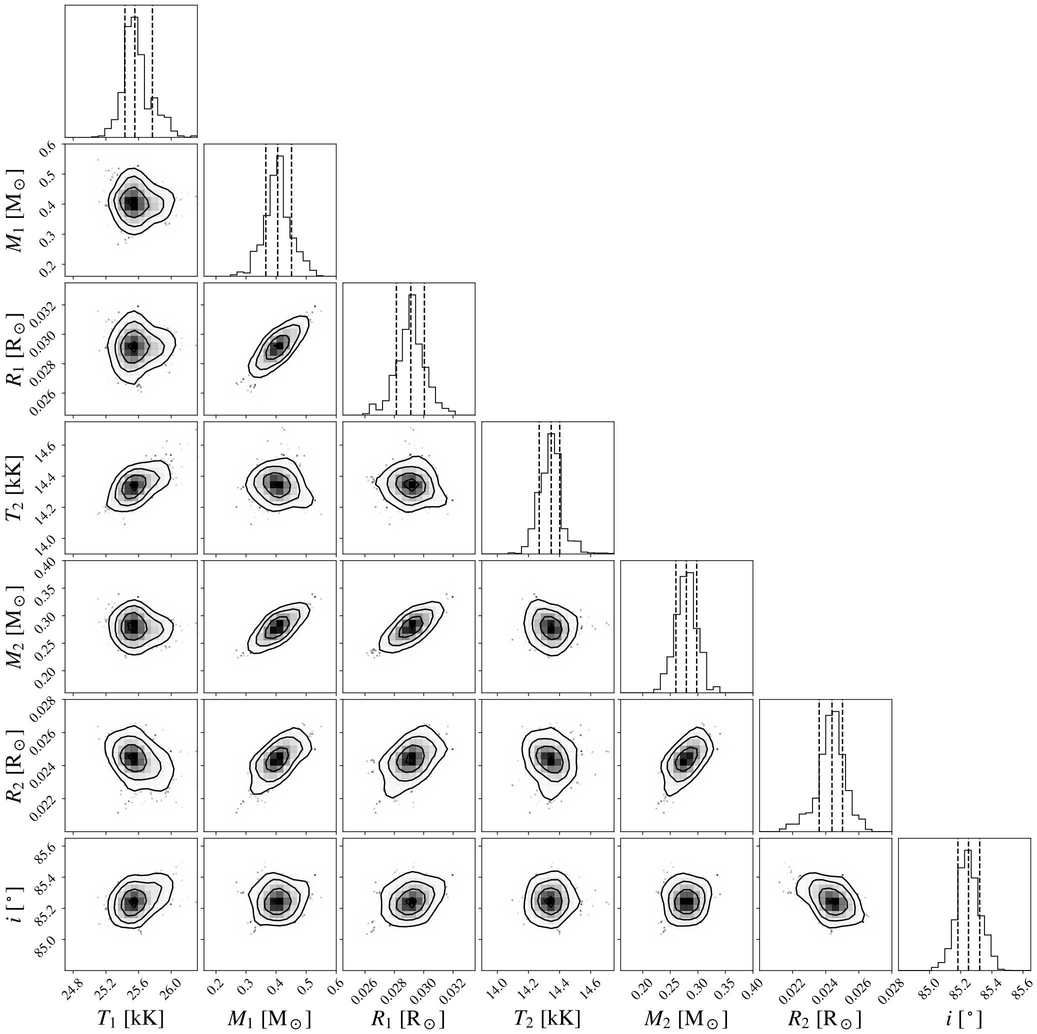

Figure 4.6: A corner plot diagram of the PHOEBE light-curve-modelling using an MCMC algorithm, showing the covariance of all free parameters.

4.10 Radial Velocities

Table 4.5: The extracted radial velocity measurements of J0225−6920 presented in Fig. 4.2. The time-stamps presented have been corrected to a barycentric reference frame (MBJD, TDB) and the velocities (V_b) have been corrected for a barycentric velocity also.

MBJD–59140	V_{bary} (km s^{-1})	MBJD–59140	V_{bary} (km s^{-1})
4.006026	185.6 ± 22.9	4.056087	-230.8 ± 24.6
4.008408	150.5 ± 25.3	4.05825	-232.7 ± 14.0
4.010571	108.1 ± 24.8	4.060413	-126.8 ± 24.0
4.012734	123.1 ± 20.8	4.062576	-113.3 ± 19.7
4.014897	6.9 ± 27.1	4.064739	44.2 ± 21.7
4.01706	-78.1 ± 22.0	4.069236	133.1 ± 21.3
4.019222	-89.7 ± 17.3	4.071399	192.0 ± 18.9
4.021386	-221.9 ± 18.9	4.073562	241.3 ± 25.5
4.023549	-207.1 ± 31.1	4.075725	190.5 ± 21.6
4.025712	-181.3 ± 23.0	4.077888	131.0 ± 15.1
4.027875	-112.0 ± 16.2	4.080051	7.7 ± 23.5
4.032223	37.6 ± 18.8	4.082214	-40.3 ± 22.4
4.034386	141.0 ± 15.5	4.084377	-103.7 ± 19.4
4.036549	174.3 ± 21.0	4.08654	-170.0 ± 30.9
4.038712	254.6 ± 27.1	4.088703	-197.4 ± 29.2
4.040875	223.1 ± 31.9	4.090866	-221.7 ± 37.4
4.043039	194.2 ± 24.4	4.093029	-154.9 ± 21.2
4.045201	109.7 ± 20.7	4.095192	-94.8 ± 17.0
4.047364	27.7 ± 18.8	4.097355	-7.1 ± 18.8
4.049527	-34.5 ± 19.9	4.099518	125.5 ± 25.9
4.05169	-73.6 ± 29.0	4.101681	198.0 ± 24.0
4.053924	-212.7 ± 25.0		

Chapter 5

The DBL Survey I: discovery of 34 double-lined double white dwarf binaries

James Munday, Ingrid Pelisoli, P.-E. Tremblay, T. R. Marsh, Gijs Nelemans, Antoine Bédard, Silvia Toonen, Elmé Breedt, Tim Cunningham, Mairi W. O'Brien, Harry Dawson

Contribution of co-authors

Observations used in this study were obtained by authors #4, #5, #7, and #8. All authors contributed with comments on the manuscript during the submission/revision process by supplying key ideas to explore in creating the final version of the study. Author #6 offered support in the creation of and verification of the results of my WD-BASS pipeline (see Section 5.4). Author #10 contributed by inspecting all spectra for interesting aspects and classification. Author #11 contributed by helping to test the function of the WD-BASS pipeline. All other components and the leading of the study were performed by me.

Abstract

We present the first discoveries of the double-lined double white dwarf (DBL) survey that targets over-luminous sources with respect to the canonical white dwarf cooling sequence according to a set of well-defined criteria. The primary goal of the DBL survey is to identify compact double white dwarf binary star systems from a unique spectral detection of both stars, which then enables a precise quantification of the atmospheric parameters and radial velocity variability of a system. Our search of 117 candidates that were randomly selected from a magnitude limited sample of 399 yielded a 29% detection efficiency with 34 systems exhibiting a double-lined signature. A further 38 systems show strong evidence of being single-lined or potentially-double-lined double white dwarf binaries and 7 single-lined sources from the full observed sample are radial velocity variable. The 45 remaining candidates appear as a single WD with no companion or a non-DA white dwarf, bringing the efficiency of detecting binaries to 62%. Atmospheric fitting of all double-lined systems reveals a large fraction that have two similar mass components that combine to a total mass of 1.0–1.3 $\mathrm{M}_{\odot}$ – a class of double white dwarf binaries that may undergo a sub-Chandrasekhar mass type Ia detonation or merge to form a massive O/Ne WD, although orbital periods are required to infer on which timescales. One double-lined system located 49 pc away, WDJ181058.67+311940.94, is super-Chandrasekhar mass, making it the second such double white dwarf binary to be discovered.

5.1 Motivation and introduction to the DBL survey project

Of the full confirmed and compact DWD sample at the time of this study being published, just 46 were known to be double-lined and 20 had a mass precision for both stars of $< 0.1\,\mathrm{M}_{\odot}$. Only with a large sample of precise constraints for both stars can we unravel the nuances of binary star evolution and effectively construct evolutionary models suitable for all initial conditions of two stars. In this pilot study, I introduce the double-lined double white dwarf (DBL) survey which aims to expand the double-lined and well-constrained sample of compact DWDs significantly, constructed with clearly defined selection cuts based on the position of candidate systems in the Hertzsprung-Russell (HR) diagram. As well, I strive to provide a well-constrained sample of compact DWDs surveying a range of orbital separations/periods to facilitate better mapping of post-common envelope binary stars. The undertaken search indicates an approximately one in three success rate of a candidate being double-lined, outlining a clear means to expand to an observable population of precisely constrained DWD binaries and especially so with the addition of phase-resolved spectroscopy (Munday et al, in prep).

5.2 The double-lined double white dwarf survey sample

5.2.1 Sample selection

Beginning the survey in 2018, we initiated the target selection of the DBL survey using the latest *Gaia* data release available at the time: *Gaia* DR2 [Gaia Collaboration et al., 2018]. We started with the full catalogue of 486 641 candidate WD sources presented in Gentile Fusillo et al. [2019], all of which assigned a probability of being a WD (PWD).

In search of double-lined DWD binaries, a few steps were considered. Firstly, it was considered that the majority of the population of WDs fall along a typical cooling track of a $0.6\,\mathrm{M}_{\odot}$ DA WD and use this as a baseline for the expected luminosity of a single star. As shown in Fig. 5.1, this track traverses the A-branch of WDs that is dominated by a population of hydrogen-rich atmosphere DA WDs [Jiménez-Esteban et al., 2023], implying that the majority of systems were expected to have Balmer absorption lines usable for RV extraction. Considering that double-lined DWDs were sought where the dimmer companion is not washed out of the spectrum by the brighter star, we aimed for the temperature of the brighter star to be less than 20 000 K. Such a $0.6\,\mathrm{M}_{\odot}$ WD has $G_{BP} - G_{RP} \approx -0.3\,\mathrm{mag}$, therefore, all targets in the selection required $G_{BP} - G_{RP} > -0.3\,\mathrm{mag}$.

Next, we required that the flux ratio between the companion and the brighter star is greater than a third to show a clear spectroscopic signature, meaning that a second star would cause the binary to be 0.31 mag above the single-star cooling track. Factoring in

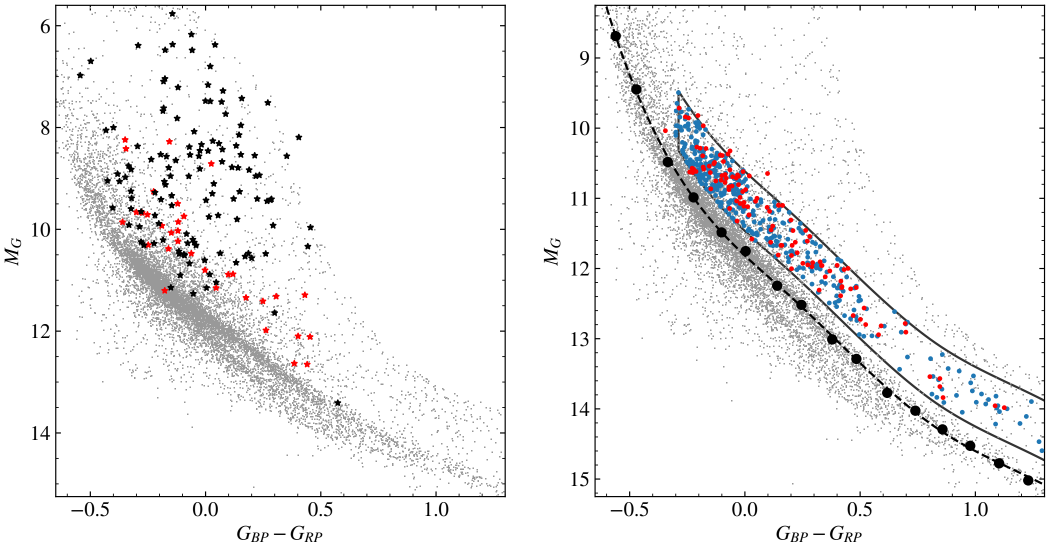

Figure 5.1: The sample selection cut on the HR diagram. Underplot on both graphs is the 100 pc sample of WDs from Gentile Fusillo et al. [2019] with PWD > 0.3, GMAG < 18, PARALLAX/PARALLAX_ERROR > 6. Left: the full sample of confirmed DWD binaries that were published before this work plotted on the HR diagram. Double-lined systems are denoted by red stars while single-lined systems are shown in black. Right: the 399 DWD candidate sources available for the WHT identification spectra with $G < 17$ mag and $\delta > -20^\circ$ in blue and in red the candidates that were observed. Both use an updated HR diagram location using *Gaia* DR3 astrometric solutions, which is why some of the observed candidates now fall slightly outside of the search box. In filled circles are evenly spaced colour bins with a dashed spline passing through, which were used to define the boxed space slightly above with step (2) of the selection criteria.

Table 5.1: The selection cuts applied to target DWD candidates along with the number of sources after each cut. Top: spline of the typical WD cooling sequence. Middle: selection of DWD candidates. Bottom: observable targets for the WHT.

Starting DR2 WD catalogue: 486 641 sources	
Selection for creating spline: (PWD > 0.3) AND (GMAG < 18) AND (PLX > 6.*E_PLX) 22 107 sources	
Sample 20 evenly spaced bins between BP_RP = −0.65 & 1.65, fit with a spline SPL_MG = f(BP_RP).	
Select for a ‘clean’ sample of candidate targets: (GMAG < 18.) AND (PLX > 10.*E_PLX) 22756 sources	(1)
(M_G < SPL_MG−0.35) AND (M_G > SPL_MG−1.2) 3494 sources	(2)
(BP_RP > −0.3) 2697 sources	(3)
Select for an observable sample on the WHT telescope: (GMAG < 17.) 625 sources	(4)
(DEDEG > −20) 399 sources	(5)

the uncertainty of a target’s *Gaia* HR diagram location from errors in the parallax and photometry, we slightly increase this minimum value and required the brightness of the binary to be 0.35 mag above the $0.6\,M_\odot$ WD cooling track to improve the search efficiency.

Going too far off of the cooling track would also contaminate the selection and its efficiency by introducing an abundance of WD–MS star candidates of the likes of cataclysmic variables [e.g. Abril et al., 2020], and with this in mind we limited the selection to systems with an absolute magnitude less than 1.2 mag brighter than the $0.6\,M_\odot$ WD cooling track. This upper boundary coincides with the typical cooling track for a helium-core WD of mass $0.3\,M_\odot$, hence excluded DWD binaries from this upper brightness limit are those with an approximately $0.35\,M_\odot$ or less massive component. The cuts applied to the Gentile Fusillo et al. [2019] catalogue conclude as written in Table 5.1.

After applying a selection cut of GMAG < 17 to select targets that would grant a signal-to-noise ratio (SNR) greater than 15 per spectral element at the centre of Hα in less than a 30 min exposure time with the 4.2 m William Herschel Telescope (WHT, see Section 5.3), 625 sources were left. Lastly, we selected targets that were visible on site for

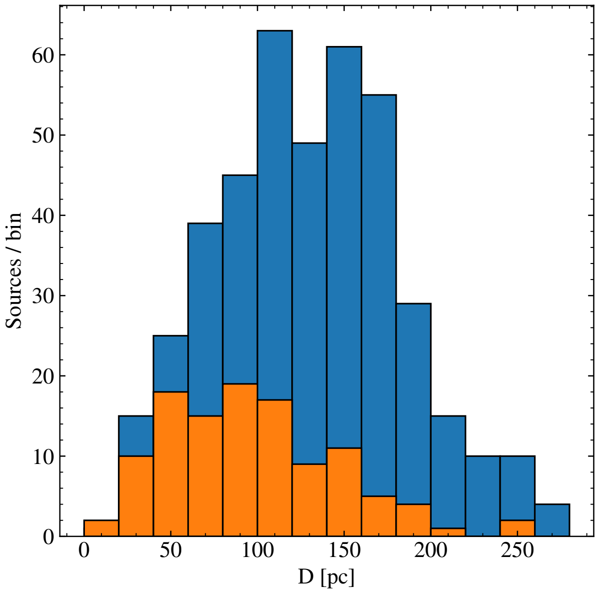

Figure 5.2: The distance distribution of the observable WD sample for the WHT identification sample, following steps (1) to (5) of the selection cuts mentioned in Section 5.2.1 when applied to the *Gaia* DR3 catalogue. Distances were obtained using *Gaia* DR3 parallaxes. Displayed in blue is the full DR3 candidate sample and in orange the sample that have now been observed.

prolonged durations ($\delta > -20°$) to arrive at a final sample that was suitable for identification spectra of 399 sources.

I note that after applying the same cuts to *Gaia* DR3, each step of the sample selection had the following number of sources utilising the same numbering scheme: 1) 26 616, 2) 3729, 3) 2862, 4) 695, 5) 451. The primary cause of the increase in size of the final sample stems from the improved parallax uncertainties in *Gaia* DR3.

5.2.2 Sample biases

The sample cuts outlined in steps (1) to (3) in Table 5.1 cause the sample to be slightly biased towards brighter systems owing to the fact that brighter systems have more precise astrometric solutions, hence smaller parallax uncertainties. This is particularly relevant given the initial *Gaia* DR2 selection of the candidate sample, but far less so for *Gaia* DR3. The fact that the selection relies on a 0.6 $M_\odot$ WD cooling track and that this is the median WD mass induces a natural bias towards at least one of the components being a WD of mass 0.6 $M_\odot$ ($\log g \approx 8$). This is primarily the case for wide binaries where the two stars evolve in near-isolated conditions. WDs with smaller masses have larger radii and are hence more luminous for all effective temperatures compared to a WD with higher mass. With this and the fact that the upper M_G selection cut of 1.2 mag above the 0.6 $\mathrm{M}_\odot$ cooling track coincides with that of a 0.3 $\mathrm{M}_\odot$ helium-core WD, no DWD binaries that host an extremely-low-mass WD are expected.

By applying a magnitude limit to the sample in steps (1) and (4), a strong bias towards the frequency of hotter systems in the sample is induced, which is clearly noticeable by the grouping of candidate systems with $\mathrm{M}_G < 12$ mag in Fig. 5.1. The magnitude limit imposed in the spline creation barely induces bias in the sample due to the large number of sources used in the spline fit, and the premise of introducing the magnitude limit in the step of creating the sample was to ensure good photometry across the BP-, RP- and G-bands.

The target selection, especially near the lining of the Milky Way and towards the Galactic bulge, is minorly biased towards brighter systems due to the impact of reddening since no reddening correction was applied to the sample selection. The most distant sources in the sample are found at 300 pc and the mean distance is $\approx$120 pc (Fig. 5.2), meaning that the impact of extinction is small and that even though the targets in our selection cuts will shift in colour to become bluer where some may lie slightly outside of the selection, the number that will is very small.

Limiting to a northern declination in step (5) is suspected to have negligible effects owing to the similarity between the results of volume-limited WD surveys in each hemisphere [McCleery et al., 2020; O'Brien et al., 2023]. A final bias in the results of the targets in this sample, which does not stem from the sample selection itself, are introduced by the detection efficiency in the observing strategy (see Section 5.3).

5.3 Observations

With the final candidate sample outlined in Section 5.2.1, we obtained identification spectra of 117 candidates; 27 were observed for a single epoch, 9 for two epochs, and 88 candidates for 3 or more. Typically, more than 3 identification epochs were taken if the candidate was immediately identified as a promising double-lined candidate from the first 3 spectra. The general observing strategy was to ensure that each candidate was observed on at least two separate nights spaced two nights apart; one of these nights with a single spectrum and the other night with two consecutive exposures to be sensitive to any ultra-compact systems with rapid RV variation. Generally speaking, compact DWDs have a median orbital period of approximately 1 day, meaning that the two day spacing granted sensitivity orbital periods up to a few days (Fig. 5.3), comprising over 90% of compact DWD systems [Nelemans et al., 2001c].

These identification spectra were taken with the Intermediate-dispersion Spectrograph and Imaging System (ISIS) mounted on the 4.2 m William Herschel Telescope (WHT)

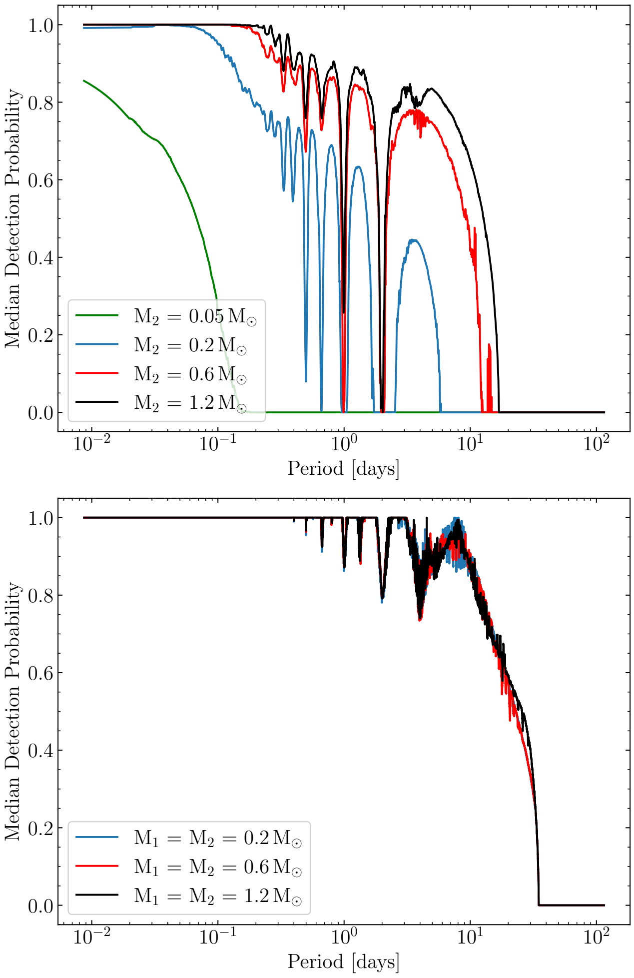

Figure 5.3: Left: The detection efficiency for a single-lined binary. Plotted is the detection probability for a $\geq 4\sigma$ significance of a non-constant RV over a range of orbital periods with the WHT observing strategy. A brighter $0.6\,M_\odot$ WD is assumed and the detection efficiency of a companion WD or brown dwarf with mass M_2 is plotted for $i = 60°$. The detection efficiency for a larger companion (e.g. a neutron star) is near identical to the efficiency for a $1.2\,M_\odot$ companion. The plotted detection probability is the median of all systems with three or more WHT identification epochs using the timestamps of the observations. Right: The same as the left, but for a double-lined DWD where the two stars have a similar flux contribution. Here, the difference between the RV of the two stars to be deemed separated at $R = 8\,000$ is $60\,\mathrm{km\,s^{-1}}$, and this requirement only needs satisfying on one epoch to result in a detection. Repeating dips are predominantly aliases of a $\approx$1 day period, arising due to the fact that ground-based observations are only possible at nighttime. There is likely a small difference in the detection efficiency dependent on the masses of the stars due to Hα being broader for larger values of surface gravity, which hence makes the double-lined signature less likely to be detected, but this is difficult to quantify and is unaccounted for since the surface gravity of the stars in the sample are suspected be in a narrow range of $\log\,g \approx 7.75$–8.25 dex (see also Fig. 5.14).

across 20 nights, being 28 August 2018 - 5 September 2018, 13-15 February 2019, 19 February 2019, 15-17 April 2019, 10 & 11 June 2019 and 6 & 7 July 2019. ISIS utilises a dichroic filter to be able to observe in a blue and a red arm simultaneously, where we used the R600B grism for the blue arm centred on 4400 Å giving a wavelength coverage of ≈3770–5030 Å and the R1200R grism for the red arm centred on 6562 Å giving a wavelength coverage of ≈6250–6870 Å. We used a 1.0″ slit width on all nights in 2018 and 1.1″ for the others, having a spectral resolution of 0.81 Å and 0.74 Å in the red arm and 2.2 Å and 2 Å in the blue arm, respectively. A CuNe+CuAr arc exposure was taken for each new telescope pointing after acquiring a target for wavelength calibration, where the error in wavelength calibration for each arc frame in the blue arm was approximately $3\,\mathrm{km\,s^{-1}}$ and $2\,\mathrm{km\,s^{-1}}$ in the red arm. The science exposure time was always maintained at under 30 min not to suffer greatly from orbital smearing and a SNR greater than 25 in the wings and 15 in the line core of Hα was sought after.

Bias frames and dome flats were taken at the beginning of each night and used in the data reduction. Spectrophotometric standard stars were also taken at the start or the end of each night to flux calibrate the science exposures and correct for the instrumental response function. When multiple arc frames were taken for a target, the arc closest in time to the science frame was used for wavelength calibration. All data were reduced using the MOLLY package [Marsh, 2019] and spectra were extracted using the method outlined in Marsh [1989].

The detection probability of a candidate being RV variable or double-lined, based off of the identification spectra alone, is displayed in Fig. 5.3. I determine a single-lined system to be RV variable if there is significant deviation from the mean velocity of all exposures (Section 5.5.2), while a double-lined system with two stars that contribute a similar flux is identifiable if the difference in velocity of the two stars is above $60\,\mathrm{km\,s^{-1}}$ for the resolution at Hα.

5.4 WD-BASS

I created a custom fitting code specialised for the analysis of RV variable WDs with time-series spectra and introduce it in this work to fit the full DBL I survey sample: the *White Dwarf Binary And Single Star* (WD-BASS) fitting package [Munday, 2024]. The code is specialised for DA, DB and DC WD fitting and is flexible to include any grid of synthetic spectra.

WD-BASS is divided into 4 primary branches: 1) one-star spectral line fitting, 2) two-star spectral line fitting, 3) simultaneous or independent photometric SED fitting, and 4) RV fitting with a fixed atmospheric solution. Each branch will now be explained.

Access to the code is public and a full description of the code's usage in its most recent version can be found on github[1].

5.4.1 One-star fitting

Single star fitting in WD-BASS is performed by normalising and fitting specific spectral lines of interest. The user specifies the sets of wavelength ranges on each edge of the line to be used for a linear normalisation and the wavelength range that is fitted. The resolution of the observations at the spectral line of choice is also user supplied. Multiple spectra can be fit simultaneously or independently. One has the capability to fix or vary an atmospheric solution, fix or vary the RV of a star for each spectrum or, if the system is in a binary and the user supplies an orbital period (P) and reference epoch (T_0), one can solve for a Keplerian orbit by varying the semi-amplitude (K) and/or the systemic velocity offset (V_γ). In the latter case, the eccentricity is assumed to be zero with a circularised orbit. Multiple spectral lines in a single spectrum can be fit independently or simultaneously with a fixed/varied RV for each line.

A Markov Chain Monte Carlo (MCMC) algorithm is employed in the code using the EMCEE python package [Foreman-Mackey et al., 2013] to probe a user-supplied parameter space and maximise the likelihood (which is equal to $-0.5\chi^2$) between the set of normalised observations and the normalised model fits sequentially. The interpolated spectrum for a trial solution is convolved to match the resolution of the observations with a Gaussian kernel.

5.4.2 Two-star fitting

The binary star fitting module of WD-BASS functions exactly the same as single star fitting but with the combination of two different model stars that can be of any spectral type, each star having a unique RV. Similar to before, any combination of the semi-amplitude of each star, K_1, K_2 or their velocity offset, $V_{\gamma,1}$, $V_{\gamma,2}$ can be input as fixed/fitted constraints (the velocity offset is not the same as the systemic velocity and is unique for the each star because of gravitational redshift).

Two stars in a binary have unique atmospheric parameters and radii, therefore in a normalised spectrum there is a relative flux scaling between the two. WD-BASS includes the options to fit for the relative flux scaling component, for it to be fixed, or for the scaling to be inferred through the radius of the two stars with $T_{\rm eff}$-log g-radius relationships. In its current version, the radius of a DA star is inferred using the evolutionary track models of Istrate et al. [2016] when $\rm M \leq 0.393\,M_\odot$, Althaus et al. [2013] when $0.393 < \rm M <$

---

[1] `https://github.com/JamesMunday98/WD-BASS`

$0.45\,\mathrm{M}_{\odot}$ and the hydrogen-rich evolutionary sequences of Bédard et al. [2020] otherwise, the assumption being that a star $< 0.45\,\mathrm{M}_{\odot}$ is likely a He-core WD and larger masses have a carbon-oxygen core. Hybrid carbon-oxygen/helium core composition WDs may exist in the mass range of ≈ 0.3–$0.6\,\mathrm{M}_{\odot}$ [Zenati et al., 2019], or the hydrogen envelope could be large in some cases [Romero et al., 2019], but a spectrum that is poorly fit in this mass range can be overcome by allowing the scaling factor to vary freely. That said, the scaling is always interpolated in this study as these issues never arose in the fitting, which has often been the case for detached systems [Parsons et al., 2017]. For helium-atmosphere DB/DC WDs, WD-BASS currently relies on a linear interpolation of the He-rich evolutionary sequences of Bédard et al. [2020] to predict the radius of the WD ($\mathrm{M_H}/\mathrm{M_{WD}} = 10^{-10}$).

The model Eddington flux is converted to a flux observed at Earth (F_{obs}) with the stellar radius (R, inferred from $\log g$–$\mathrm{T_{eff}}$–radius relationships) and the parallax, following

$$F_{\text{obs}}(\lambda) = \frac{4\pi}{D^2}\left(F_1(\lambda)R_1^2 + F_2(\lambda)R_2^2\right) \tag{5.1}$$

where $D = 1/\text{parallax}$, λ is the wavelength, $F(\lambda)$ is the flux and subscripts 1, 2 represent the brighter and dimmer star, respectively. The fluxes themselves are dependent on $\mathrm{T_{eff,1}}$, $\log g_1$, $\mathrm{T_{eff,2}}$, $\log g_2$.

5.4.3 Photometric SED fitting

In the advent of all-sky photometric surveys in the last decades, the astronomical community has a plethora of photometric magnitudes available in multiple wavebands that is publicly available and flux-calibrated. Yet, only recently have the parallaxes measured in the *Gaia* mission proved revolutionary in placing said stars distance scale [Gaia Collaboration et al., 2021, 2023]. For sources up to $G = 17\,\text{mag}$ in *Gaia* DR3 belonging to the 359 000 high-confidence WDs in the catalogue of Gentile Fusillo et al. [2021], 99.96% of the WDs have a PARALLAX/PARALLAX_ERROR greater than 10, such that there is now the opportunity to exploit simultaneous fitting of spectral lines with well-flux-calibrated photometry to grant more precise atmospheric parameters. This is highly advantageous not only in single-lined systems, but especially so for double-lined binaries where the unique signature of each star may be difficult to disentangle, also allowing a more accurate system solution [Bédard et al., 2017]. When handling photometry from satellite sources, air wavelengths in the model spectrum are converted to vacuum wavelengths.

To fit the photometry, synthetic spectra are created with equation 5.1 on an Eddington flux scale and can be reddened in WD-BASS with a supplied E(B-V) extinction constant and an assumed extinction curve with R_V=3.1, following the extinction curves of Gordon et al. [2023]. If fitting photometry simultaneously with spectroscopy, the same model is used for both datasets. The model is then integrated over the transmission spectrum of the respective filter to obtain the predicted observed flux in the bandpass. In the MCMC algorithm itself, a Gaussian prior on the parallax is applied and weighted by the supplied parallax error. The parallax, together with the radius inferred from $\log(g)$ and $\mathrm{T_{eff}}$, fixes the normalisation.

5.4.4 Improved radial velocity fitting

It is possible to determine RVs as discussed in the previous sub-sections and this is the standard procedure in WD-BASS. In case of a poor fit to the line core and specifically made for medium- to high-resolution data that includes Hα, where synthetic model spectra may struggle to reproduce the observed signature [Napiwotzki et al., 2020; Kilic et al., 2021a], WD-BASS also includes the option to take an atmospheric solution and fit an extra Gaussian component to the star(s) model spectrum (spectra). This process is performed by taking the same set of spectra that were used in the one-star (two-star) atmospheric fitting, fixing the temperature(s), $\log\ g$ (s) and RVs found in the previously determined solution and then minimising the χ^2 with an additional Gaussian solution for the star(s), having amplitude A_G and standard deviation σ_G. An upper limit of $\sigma_G < 5$ Å is enforced to solely improve the line core, rather than any correction to the shape of the wings of the Balmer lines. Although there is no improvement to the atmospheric fit in the optionally employable method, the purpose of this step is to grant an improved RV accuracy and precision when relevant.

5.5 Methods: Fitting the candidate sample

5.5.1 Atmospheric parameters

For the fitting of all WD atmospheric classifications, I performed a bilinear interpolation in the $\mathrm{T_{eff}}$ – $\log\ g$ space in trial solutions for DA WDs or trilinear in the $\mathrm{T_{eff}}$ – $\log\ g$–H/He space for DB WDs.

The observed spectra were normalised with a linear fit between the two wings of each spectral line and so were the model spectra (the spectral range for normalisation is different depending on the spectral type, detailed in Sections 5.5.1, 5.5.1). My method in choosing the spectral region for normalisation was proportional to the temperature of the WD, with cooler WDs having less-broadened absorption lines. All data within the region of normalisation was included in a χ^2 minimisation with a 4σ outlier rejection threshold. I probed trial solutions using the MCMC algorithm with WD-BASS, utilising 100 walkers, a burn-in and a post-burn-in phase. In the case of double-lined systems where multiple

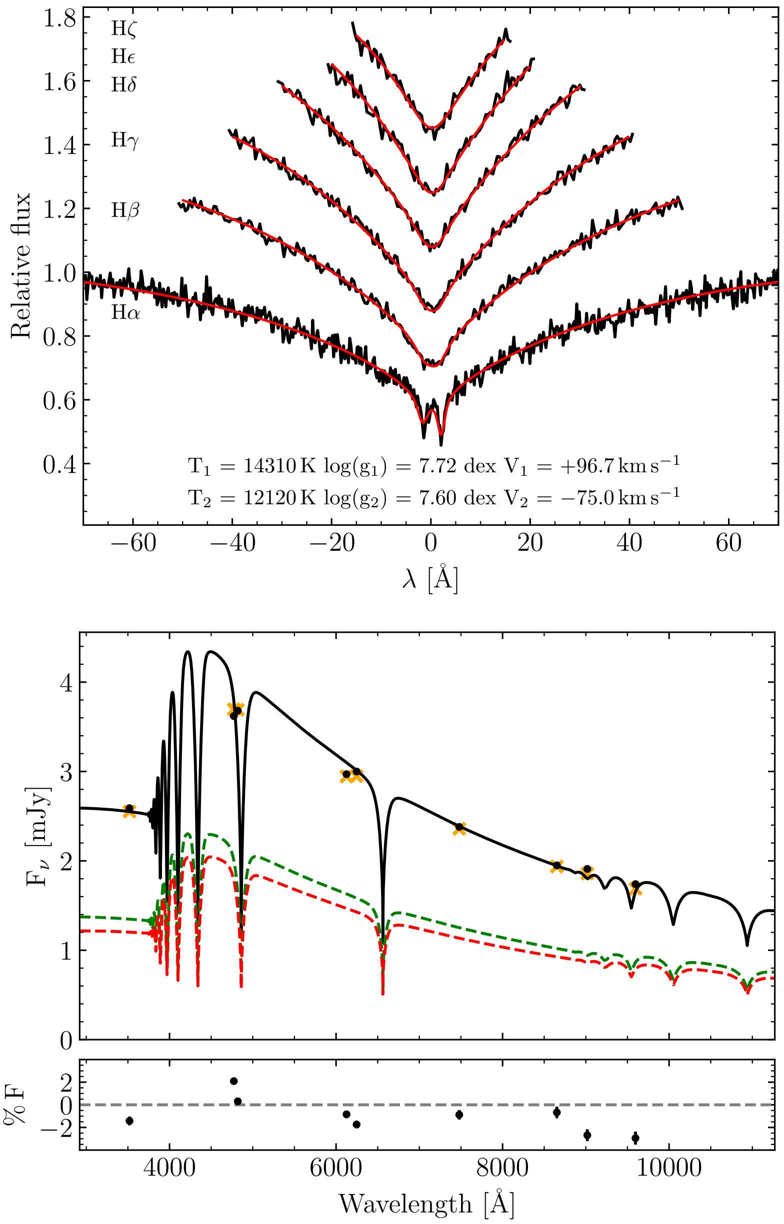

Figure 5.4: An example best-fit atmospheric solution for the double-lined system WDJ114446.16+364151.13 utilising simultaneous spectral (left) and photometric (right) fitting. On the left, the observed spectra is plotted in black and the model fit is over-plotted in red. The spectroscopic solution and the RVs of the epoch are written in text below Hα. On the right (top), the observed data is plotted in black circles, the integrated model flux in each filter in orange crosses, the combined model flux as a solid black line and the flux contributed from the individual stars in dashed red and dashed green. Below is the percentage difference of the observed flux to the model.

exposures of a target were taken, I omit data where both stars are not visible in the spectrum in the atmospheric fitting (originating from an unfavourable orbital phase). In single-lined sources, I model all WHT identification spectra.

Multiple studies have shown a systematic difference between atmospheric constraints predominantly from fitting single WDs photometrically and spectroscopically that varies from survey to survey [Tremblay et al., 2019; Genest-Beaulieu and Bergeron, 2019; Gentile Fusillo et al., 2021; Cukanovaite et al., 2021; Sahu et al., 2023; Izquierdo et al., 2023], stemming from a difference in flux calibration between the surveys and imperfect model atmospheres. However, even with the systematics, all targets within the initial selection criteria are over-luminous compared to the 0.6 $M_\odot$ WD cooling sequence and, in the vast majority of cases, the spectral features of one star dominate in the spectrum. I consider that the inclusion of photometry to reduce degeneracy in two-star atmospheric solutions outweighs the negatives induced from systematic effects in all cases. Therefore, I incorporate a hybrid fitting technique in WD-BASS of simultaneous spectroscopic and photometric fitting in all systems when available, whereby the combined χ^2 with no weighting for the two datasets is minimised to reach a final solution.

I chose to limit the sources of photometry to Pan-STARRS DR1 (grizy) [Chambers and Pan-STARRS Team, 2018] and SDSS DR16 (ugriz) [Ahumada et al., 2020] and I chose not to include *Gaia* photometry as the very broad filters of *Gaia* are not optimal for two star fitting, where any extra flux calibration offset between *Gaia* and the other surveys could hamper the validity of the atmospheric solution. In any case, *Gaia* was still the best starting point for candidate selection due to its increased photometric precision and all-sky coverage. The extinction coefficient, A_V, of each source was obtained through the reddening maps of Lallement et al. [2022] at a distance determined from the inverse of the *Gaia* DR3 parallax and was converted to E(B-V) $= A_V/3.1$ before reddening the synthetic spectrum. An example showcasing the quality of fit to Hα–H8 following all of these steps with simultaneous photometric and spectroscopic hybrid fitting is displayed in Fig. 5.4 for one double-lined DWD.

DA WDs

Over the course of this study, I fitted the full sample of DWD binary candidates with two primary grids of model spectra: the 3D local thermodynamic equilibrium (LTE) DA spectra of Tremblay et al. [2013a, 2015] and the 1D non-LTE (NLTE) DA spectra of Kilic et al. [2021a], which I will refer to as T15 and K21, respectively. Both grids rely on the line profiles of Tremblay and Bergeron [2009]. The NLTE grid of K21 was computed by performing NLTE spectral synthesis on the LTE atmospheric structures of Tremblay and Bergeron [2009] using a modified version of the SYNSPEC code (see Kilic et al. 2021a

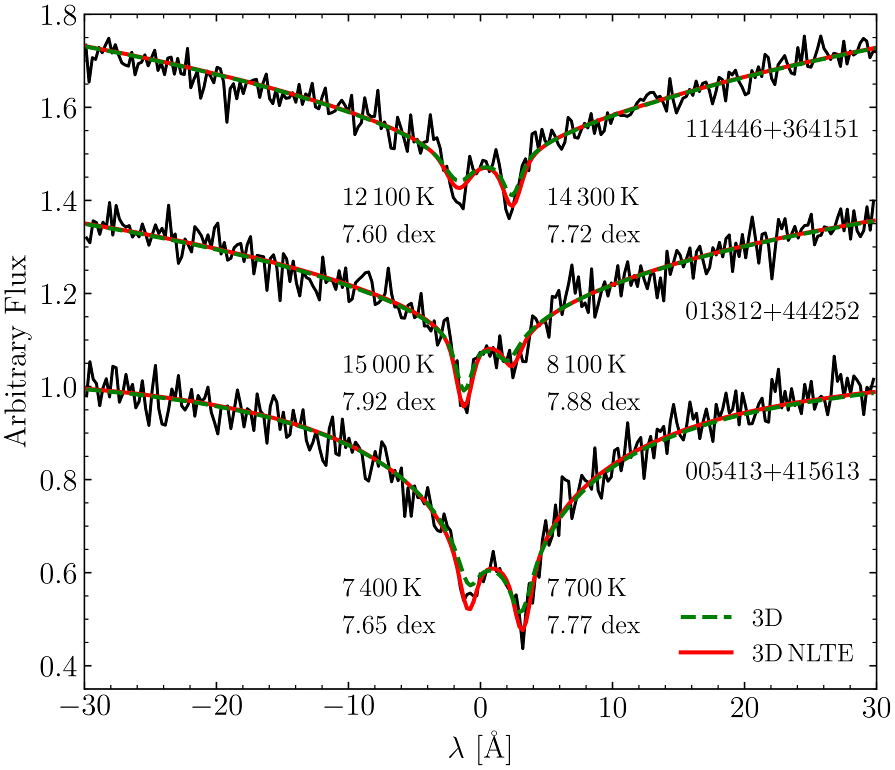

Figure 5.5: A comparison of the model fit to three double-lined systems with a variety of combinations of effective temperature. In red, the 3D+NLTE grid that was created in this work and used to fit all single- and double-lined systems (see Section 5.5). In dashed green, 3D effects only from T15. The lines Hα-H8 were fitted simultaneously in these systems, but Hα is shown alone in the figure since little difference is noticeable at the other Balmer lines because of the lower resolution of the data as well as the lesser impact of NLTE effects to the synthetic spectrum. The relative scaling between stars was included from the appropriate log g–T_{eff}–radius relationship (Section 5.4.2).

for details). NLTE effects are especially important in the atmosphere of hot WDs ($T_{\rm eff} \gtrsim$ 40 000 K; Napiwotzki 1997) but also remain non-negligible in the upper atmosphere of cooler objects, thus affecting the line cores [Heber et al., 1997; Koester et al., 1998]. In particular, they are noticeable in high-resolution Hα observations of cool WDs in double-lined binaries [Bergeron et al., 1989; Kilic et al., 2021a]. The same effect of a decreased model flux in the line cores is apparent for the 3D vs 1D and NLTE vs LTE grids; in the former case, because of the cooling effects that come with the inclusion of convective overshoot [Tremblay et al., 2013a] and in the latter because of an increased opacity (increased NLTE lower level population) in the upper atmosphere of a WD where the lines are formed.

I observe that NLTE effects on Hα line cores are noticeable at medium resolution for the full range of effective temperatures and surface gravities in the sample. Both the grids of K21 and T15 performed well for all other Balmer lines observed at lower resolution, where the line core impact diminishes due to the increased broadening from the response of the blue grating. That said and even with the use of NLTE physics in the models, the synthetic line cores were too shallow. While the poorer fit caused in this case may not be detrimental to or hardly noticeable in single star fitting of an isolated WD, the impact is amplified in spectra with two DA WD components as the stars are blended, such that the line cores are the only components where a unique signature of each star is prominent and hence significantly impact the validity of the fit.

I was therefore encouraged to create a new synthetic spectral grid that approximately include both the 3D and NLTE effects on the line cores; a hybrid "3D-NLTE" grid that was introduced for the first time in this work. I started by dividing the NLTE and LTE grids of K21, which include otherwise identical input physics, yielding a NLTE correction factor f $(\lambda, T_{\rm eff}, \log\, g)$. This factor was then interpolated onto the wavelength grid of T15 and applied to their 3D synthetic spectra. The final step was to broaden the product[2] with the velocity vector in figure 11 of Tremblay et al. [2013b] at optical depth $\log(\tau_R) = -4$. This generated a NLTE correction to a 3D grid with resulting synthetic spectra (that will herein be referred to as 3D-NLTE) that incorporate 3D and NLTE physics without a full computational effort to include both effects simultaneously.

A comparison of T15 with the 3D-NLTE grid including simultaneous photometric fitting for three double-lined systems in the sample is displayed in Fig. 5.5. In addition, I compared the T15, K21 and 3D-NLTE grids by fitting the full observed sample with each. I found that the difference in the reported atmospheric parameters of each double-lined system is small ($<$ 500 K, $<$ 0.05 dex for both stars) and smaller still for single-star fits to single-lined systems ($<$ 200 K, $<$ 0.03 dex), yet I found that the 3D-NLTE grid

---

[2] Convective (turbulent) velocity broadening is not included by default in the synthetic $\langle$3D$\rangle$ spectral grid in T15.

outperformed the others by better fitting the observed spectra, especially at Hα. For that reason, I have utilised the 3D-NLTE spectral grid to fit all sources presented in this study. I note that for a minority of double-lined systems and specifically in the temperature range 9 000–10 000 K and surface gravity range 7.6–8.0 dex, I witness that the 3D-NLTE synthetic spectra slightly under-predict the flux at Hα compared to the observations; the synthetic line cores become too deep instead of too shallow (see e.g. WDJ212935.23+001332.26 in Appendix 5.8). I accredit the flux under-prediction to either small imperfections in the T15 grid since 3D effects are strongest in this temperature regime, or to an artefact of not creating a grid with the inclusion of 3D and NLTE effects being modelled together instead of the multiplicative factor approach.

In the process of atmospheric fitting and in general for DAs, I chose to linearly normalise Balmer lines using data in the range of $\pm(4\,500 - 5\,000)\,\mathrm{km\,s^{-1}}$ around Hα, Hβ, Hγ, Hδ and $\pm(2\,000 - 2\,500)\,\mathrm{km\,s^{-1}}$ around Hϵ and H8 when $T_{\mathrm{eff}} \geq 8\,000\,\mathrm{K}$. In WDs cooler than 8 000 K, inferred from the temperature quoted in Gentile Fusillo et al. [2021] from the fitting of *Gaia* photometry, I reduced the normalisation range to be approximately $\pm(2\,250 - 2\,500)\,\mathrm{km\,s^{-1}}$ and $\pm(1\,750 - 2\,000)\,\mathrm{km\,s^{-1}}$, for the respective groups of Balmer lines. The narrower prescription for cooler WDs was chosen to restrict the contribution of the continuum to the fit. Fine tuning of a couple of angstroms either side of the absorption features was performed to improve the normalisation and spectroscopic fit if a flux-calibration artefact was within the normalisation range.

Two DA systems in the sample are unique from the rest in the way that their spectra show a sharp emission at Hα only originating from background emission in the galactic plane, not from the system itself. These are WDJ183442.33+170028.00 and WDJ193845.80+264751.85, and I mask the narrow hydrogen emission in both sources when performing the atmospheric fitting (see WDJ183442.33+170028.00 in Fig. 5.8). No photometric data is fitted for these sources.

Non-DA WDs

For the couple of DB WDs in the observed sample, I utilised synthetic spectra from Cukanovaite et al. [2021], incorporating 3D effects when possible. The observed and synthetic spectra were continuum normalised and all visible helium absorption features fitted. When including a helium-rich atmosphere DC WD component, I use the same synthetic spectra from Cukanovaite et al. [2021] but with a fixed H/He fraction of 10^{-5} [Bergeron et al., 2019; McCleery et al., 2020] and normalise spectra with a DC in the same way as for DA WDs. Hydrogen-rich atmosphere DC WDs exist below approximately 5 000 K and I continue using the T15 synthetic spectra to model hydrogen-rich DCs.

Some systems within the survey are not DA/DB/DC WDs (see Table 5.7). For the sample of interest, these systems are viewed as contaminants and as such I do not provide a full analysis of their atmospheric constraints in this paper. Notable targets of interest were 1) WDJ002215.19+423642.15 having a faint and shifted Hα towards the blue, perhaps indicative of a cool and magnetic star, 2) WDJ010343.47+555941.53 which could be an evolved CV or a subdwarf with an F/G/K star companion given the CH absorption band (G-band) at 4305Å (in *Gaia* DR3, this source has no parallax or proper motion, whereas it does in *Gaia* DR2). An analysis of time-series data is particularly encouraged for the last two systems.

Fitting single-lined DWD candidates

Irrelevant of the spectral type, the full observed sample is composed of DWD candidates. When I see unique signatures of both stars in the spectra and can identify individual spectral types, assigning the relevant atmosphere is simple. On the other hand, single-lined targets may still have an additional flux component that jeopardises the accuracy of a single-star solution.

To combat this dilemma, I perform two-star fits to all single-lined DA targets that show a missing flux component of a second WD, noticeable from overly shallow model fluxes in the line cores of the Balmer lines, a poor fit to the photometry or a fitted parallax outlier that deviates more than 3σ from the expected value. The vast majority of targets from the DBL survey show Balmer lines, and it is expected that in a poorly-fitting target for a single-star DA model that the missing component is another DA WD. Hence, I assume that the most common companion would be another star of type DA. The second option that I consider is that the companion is a DC WD with a helium-rich atmosphere[3] and a H/He fraction (by number) of 10^{-5} [Cukanovaite et al., 2021]. It is expected that a DC WD would have $\log(g) \approx 8.0$ dex and I fix the surface gravity of the DC to remove parameter degeneracy in the fitting, before comparing a DA+DA and DA+DC ($\log(g) = 8$) best-fit by eye. A visual comparison then allowed us to exclude a combination, if possible. As a last and separate check, I allowed the surface gravity of the DC to be free and comment on whether a DC WD with $\log(g)$ =7.5–9.0 would reproduce the observations and note if this is the case.

For any target where a single-star model fits well and I see little to no improvement in the χ^2 of the hybrid fitting when including a second star, I consider the situation entirely degenerate and report an atmospheric solution with just the one WD, but I advise that caution is taken when interpreting the solution. If these systems are binaries, the temperature of the brighter component will be slightly overestimated and the surface gravity slightly

---

[3] A hydrogen atmosphere DC companion is considered when fitting DA synthetic spectra when the temperature is less than approximately 5 000 K as DAs become DCs

underestimated.

5.5.2 Radial velocities

Fitting

To determine RVs, I fitted to Hα alone because of the much higher resolution in this spectral range for the observations, whereas the addition of data from the lower-resolution blue arm data would add confusion noise. Occasionally, and especially when the observing conditions worsened, the continuum SNR can be relatively low (SNR<20), leading to a poor spectrum normalisation. I use the best atmospheric fit rather than the data to calculate the normalisation factors for the observed spectrum and then minimise the χ^2 in the wavelength range within $40\,\text{Å}$ of Hα. Applying this re-normalisation slightly improved the accuracy and precision of the RVs in general and noticeably for the low SNR observations. Data within the $\pm 5 - 40\,\text{Å}$ range was sigma-clipped with a threshold of 4σ; excluding data near the line cores themselves. RVs and RV errors are reported from the median and standard deviation of 1000 bootstrapping iterations.

In double-lined DWD and single WD fitting, the model flux from each star is used in search for independent RVs. For the RVs of single-lined DWDs, a wide Gaussian component (to cover the broad wings of Hα) and a narrow Lorentizian component (to model the NLTE core) with a common RV were fit to all spectra to get a best model, and this model was then maintained fixed to search for independent RVs.

RV variability

From the identification spectra of double-lined systems, the atmospheric solution and the measured RV of each component can be used to assign each system a maximum orbital period. If we assume the unlikely case that the epoch of observation for all double-lined detection occurred when the stars were moving at a maximum orbital velocity and that the binary is angled edge-on ($i = 90°$), the binary mass function can be rearranged to be

$$P_{\text{max}} = \frac{2\pi G M_1^3}{K_{2,\text{min}}^3 (M_1 + M_2)^2} = \frac{2\pi G M_2^3}{K_{1,\text{min}}^3 (M_1 + M_2)^2} \tag{5.2}$$

where we can take a rudimentary assumption that $K_{1,\text{min}}$ and $K_{2,\text{min}}$ are half of the maximum RV difference of the two stars. With an atmospheric solution bringing photometric masses of M_1 and M_2, the maximum period can be solved for.

While spotting a double-lined signature is often obvious upon inspection of the data, a statistically significant RV variability for a single-lined system is not. To search for single-lined RV variability the mean of all extracted RVs for a source is taken and a null-hypothesis that the RV is a constant with respect to the mean is tested. I compute the χ^2 of all measurements compared to the mean and use the relevant χ^2-distribution for the number of degrees of freedom to calculate the probability that a source is not RV variable. For a system to be considered a candidate RV variable system, I require that it passes the 1% $(\log_{10} p_{\text{bin}} < -2)$ threshold and 0.01% $(\log_{10} p_{\text{bin}} < -4)$ to be considered as a WD binary with an unseen companion. All double-lined systems are naturally RV variable. All RV errors were propagated with an additional wavelength calibration error of $2\,\mathrm{km\,s^{-1}}$ in quadrature (Section 5.3).

5.6 Results

The best-fit atmospheric solutions are reported in Tables 5.2–5.6 as the 50th percentile of the post-burnin chains and errors as the 16th and 84th percentiles of this distribution. Within, subscripts 1 and 2 represent the hotter and cooler star, respectively.

34 systems are double-lined DWDs. Another 11 are double-lined DWD candidates as they show a small hint of a double-lined signature, however I can not confirm these as double-lined DWDs due to the SNR ratio of the data or perhaps an unfavourable orbital phase sampling. 27 single-lined DWDs were found where one star is visible in the spectrum but the source require an additional flux component for spectroscopic and photometric consistency, 38 sources appear as a single-lined DA WD with no companion present and 7 non-DA sources were found (Table 5.7). The location of these systems on the HR diagram separated by category is depicted in Fig. 5.6.

As the spectroscopic surface gravity of each star is largely defined by the relative depth of all Balmer lines compared to one another [Tremblay and Bergeron, 2009], I emphasise that care should be taken when interpreting the parameters of hybrid fits for stars with a temperature below approximately 5 500 K as the only Balmer lines visible in the data are Hα and at times Hβ; all other Balmer lines vanish at lower temperatures. Regardless, the temperatures of the stars are expected to be accurate given the inclusion to the fit of flux-calibrated photometry. The error on these stars stays relatively low because the surface gravity is also constrained with the photometric data.

5.6.1 Double-lined DA DWDs

The 34 targets listed in Table 5.2 were found to be double-lined, double-DA DWDs, signifying at least a 29% detection efficiency in the survey. A further 3 targets found in Table 5.3 are deemed to be likely double-lined DWDs but the SNR ratio of the data leads to a lack of certainty, and a further 8 targets show a faint hint of a double-lined signature. If all are

Table 5.2: The best-fitting parameters to the definite double-lined DWDs. Subscripts 1 and 2 represent the hotter and cooler star, respectively. Errors on the atmospheric constraints of the stars were obtained by combining in quadrature the statistical error from χ^2 fitting with an external error of 1.4% for $T_{\rm eff}$ and 0.042 dex for $\log g$ [Liebert et al., 2005], however this should be considered a minimum due to extra degeneracy in two-star fitting. I emphasise caution again on interpretation of the masses for stars with a temperature below 5 500 K. The rest of the sample including candidate double-lined DWDs are listed in Tables 5.3–5.7.

WDJ name	$T_{\rm eff,1}$ [kK]	$\log g_1$ [dex]	M_1 [$M_\odot$]	$T_{\rm eff,2}$ [kK]	$\log g_2$ [dex]	M_2 [$M_\odot$]
000319.54+022623.28	$18.2^{+0.3}_{-0.3}$	$7.69^{+0.05}_{-0.04}$	$0.47^{+0.02}_{-0.02}$	$7.5^{+0.3}_{-0.3}$	$7.48^{+0.06}_{-0.06}$	$0.38^{+0.02}_{-0.03}$
002602.29−103751.86	$10.7^{+0.2}_{-0.2}$	$7.74^{+0.04}_{-0.04}$	$0.47^{+0.02}_{-0.02}$	$5.8^{+0.1}_{-0.1}$	$7.60^{+0.04}_{-0.04}$	$0.42^{+0.01}_{-0.02}$
005413.14+415613.73	$7.7^{+0.2}_{-0.1}$	$7.69^{+0.10}_{-0.05}$	$0.43^{+0.05}_{-0.03}$	$7.4^{+0.2}_{-0.3}$	$7.73^{+0.05}_{-0.10}$	$0.45^{+0.03}_{-0.05}$
013446.42+282616.83	$13.1^{+0.2}_{-0.2}$	$7.60^{+0.04}_{-0.06}$	$0.41^{+0.02}_{-0.02}$	$9.3^{+0.2}_{-0.4}$	$7.72^{+0.05}_{-0.05}$	$0.45^{+0.03}_{-0.03}$
013812.93+444252.10	$15.0^{+0.2}_{-0.2}$	$7.92^{+0.04}_{-0.04}$	$0.57^{+0.02}_{-0.02}$	$8.0^{+0.1}_{-0.1}$	$7.88^{+0.05}_{-0.05}$	$0.53^{+0.03}_{-0.03}$
014202.72+262354.58	$12.2^{+0.2}_{-0.2}$	$7.86^{+0.06}_{-0.05}$	$0.53^{+0.03}_{-0.03}$	$8.3^{+0.2}_{-0.2}$	$7.72^{+0.07}_{-0.06}$	$0.45^{+0.03}_{-0.03}$
020119.40−050748.59	$8.3^{+0.1}_{-0.1}$	$7.80^{+0.05}_{-0.05}$	$0.49^{+0.03}_{-0.02}$	$6.7^{+0.1}_{-0.1}$	$7.91^{+0.06}_{-0.06}$	$0.54^{+0.03}_{-0.03}$
020847.22+251409.97	$21.2^{+0.3}_{-0.3}$	$7.86^{+0.04}_{-0.04}$	$0.55^{+0.02}_{-0.02}$	$11.6^{+0.2}_{-0.6}$	$8.21^{+0.04}_{-0.05}$	$0.74^{+0.03}_{-0.03}$
080856.79+461300.08	$14.0^{+0.2}_{-0.2}$	$7.99^{+0.05}_{-0.05}$	$0.60^{+0.03}_{-0.03}$	$10.1^{+0.2}_{-0.2}$	$7.76^{+0.05}_{-0.05}$	$0.47^{+0.02}_{-0.02}$
084457.81+453632.94	$9.8^{+0.2}_{-0.2}$	$7.97^{+0.06}_{-0.05}$	$0.58^{+0.04}_{-0.03}$	$5.9^{+0.1}_{-0.2}$	$7.71^{+0.06}_{-0.05}$	$0.43^{+0.03}_{-0.03}$
114446.16+364151.13	$13.3^{+0.2}_{-0.2}$	$7.63^{+0.05}_{-0.06}$	$0.42^{+0.02}_{-0.02}$	$13.0^{+0.2}_{-0.2}$	$7.69^{+0.12}_{-0.05}$	$0.45^{+0.06}_{-0.02}$
130014.82+181734.41	$10.9^{+0.2}_{-0.2}$	$8.13^{+0.05}_{-0.05}$	$0.68^{+0.03}_{-0.03}$	$6.7^{+0.1}_{-0.1}$	$7.75^{+0.06}_{-0.05}$	$0.46^{+0.03}_{-0.03}$
135342.35+165651.75	$9.6^{+0.2}_{-0.3}$	$7.76^{+0.05}_{-0.11}$	$0.47^{+0.03}_{-0.05}$	$7.6^{+0.2}_{-0.2}$	$7.70^{+0.13}_{-0.05}$	$0.43^{+0.07}_{-0.03}$
141625.94+311600.55	$13.3^{+0.3}_{-0.3}$	$7.74^{+0.06}_{-0.05}$	$0.47^{+0.03}_{-0.03}$	$12.8^{+0.2}_{-0.2}$	$7.62^{+0.05}_{-0.05}$	$0.42^{+0.02}_{-0.02}$
141632.84+111003.85	$10.5^{+0.2}_{-0.2}$	$7.76^{+0.06}_{-0.06}$	$0.47^{+0.03}_{-0.03}$	$7.5^{+0.2}_{-0.2}$	$7.60^{+0.05}_{-0.05}$	$0.42^{+0.02}_{-0.02}$
151109.90+404801.18	$9.1^{+0.1}_{-0.1}$	$8.12^{+0.05}_{-0.05}$	$0.67^{+0.03}_{-0.03}$	$7.6^{+0.1}_{-0.1}$	$7.71^{+0.05}_{-0.05}$	$0.44^{+0.02}_{-0.03}$
152038.37+390349.32	$9.6^{+0.1}_{-0.1}$	$8.02^{+0.04}_{-0.05}$	$0.61^{+0.03}_{-0.03}$	$5.4^{+0.1}_{-0.1}$	$7.35^{+0.05}_{-0.05}$	$0.32^{+0.03}_{-0.01}$
153615.83+501350.98	$9.6^{+0.1}_{-0.2}$	$7.73^{+0.05}_{-0.05}$	$0.46^{+0.02}_{-0.02}$	$7.3^{+0.2}_{-0.2}$	$7.79^{+0.06}_{-0.06}$	$0.48^{+0.03}_{-0.03}$
160822.19+420543.44	$14.0^{+0.2}_{-0.2}$	$7.89^{+0.05}_{-0.05}$	$0.55^{+0.03}_{-0.03}$	$11.0^{+0.2}_{-0.2}$	$7.76^{+0.04}_{-0.05}$	$0.47^{+0.02}_{-0.02}$
163441.85+173634.09	$11.4^{+0.2}_{-0.2}$	$7.69^{+0.04}_{-0.04}$	$0.44^{+0.02}_{-0.02}$	$8.1^{+0.1}_{-0.1}$	$7.80^{+0.05}_{-0.04}$	$0.48^{+0.03}_{-0.02}$
165935.59+620934.03	$13.0^{+0.2}_{-0.2}$	$7.80^{+0.04}_{-0.04}$	$0.50^{+0.02}_{-0.02}$	$8.2^{+0.3}_{-0.3}$	$8.17^{+0.07}_{-0.05}$	$0.70^{+0.04}_{-0.03}$
170120.99−191527.57	$20.5^{+0.3}_{-0.3}$	$8.08^{+0.05}_{-0.05}$	$0.67^{+0.03}_{-0.03}$	$13.5^{+0.2}_{-0.2}$	$7.75^{+0.05}_{-0.05}$	$0.48^{+0.02}_{-0.02}$
180115.37+721848.76	$18.0^{+0.3}_{-0.3}$	$7.88^{+0.04}_{-0.04}$	$0.55^{+0.02}_{-0.02}$	$11.2^{+0.2}_{-0.2}$	$8.02^{+0.05}_{-0.05}$	$0.62^{+0.03}_{-0.03}$
180150.89+103401.08	$22.0^{+0.3}_{-0.3}$	$7.92^{+0.04}_{-0.04}$	$0.59^{+0.02}_{-0.02}$	$8.3^{+0.2}_{-0.2}$	$7.89^{+0.05}_{-0.05}$	$0.53^{+0.03}_{-0.03}$
181058.67+311940.94	$20.0^{+0.3}_{-0.4}$	$8.16^{+0.04}_{-0.04}$	$0.72^{+0.03}_{-0.03}$	$16.7^{+0.3}_{-0.3}$	$8.35^{+0.04}_{-0.04}$	$0.83^{+0.03}_{-0.03}$
182606.04+482911.30	$14.4^{+0.3}_{-0.3}$	$7.72^{+0.12}_{-0.07}$	$0.47^{+0.06}_{-0.03}$	$11.3^{+0.8}_{-0.3}$	$7.89^{+0.09}_{-0.11}$	$0.54^{+0.05}_{-0.06}$
183442.33−170028.00	$8.2^{+0.1}_{-0.1}$	$7.59^{+0.05}_{-0.05}$	$0.42^{+0.02}_{-0.02}$	$7.0^{+0.2}_{-0.1}$	$7.76^{+0.06}_{-0.06}$	$0.46^{+0.03}_{-0.03}$
192002.51−184442.99	$20.4^{+0.4}_{-0.4}$	$8.17^{+0.08}_{-0.06}$	$0.73^{+0.05}_{-0.04}$	$12.0^{+0.3}_{-0.3}$	$8.08^{+0.07}_{-0.08}$	$0.65^{+0.04}_{-0.05}$
192420.74+070135.14	$16.7^{+0.4}_{-0.7}$	$7.96^{+0.07}_{-0.07}$	$0.59^{+0.04}_{-0.04}$	$14.1^{+0.7}_{-0.3}$	$8.03^{+0.08}_{-0.07}$	$0.63^{+0.05}_{-0.04}$
211327.98+720814.03	$11.1^{+0.2}_{-0.2}$	$7.63^{+0.05}_{-0.05}$	$0.42^{+0.02}_{-0.02}$	$7.0^{+0.2}_{-0.2}$	$7.50^{+0.05}_{-0.05}$	$0.38^{+0.02}_{-0.02}$
212935.23+001332.26	$9.2^{+0.4}_{-0.2}$	$7.69^{+0.08}_{-0.07}$	$0.44^{+0.04}_{-0.04}$	$7.9^{+0.6}_{-0.2}$	$7.64^{+0.09}_{-0.05}$	$0.44^{+0.02}_{-0.02}$
214323.95−175413.00	$14.2^{+0.2}_{-0.2}$	$8.05^{+0.05}_{-0.05}$	$0.64^{+0.03}_{-0.03}$	$14.0^{+0.2}_{-0.2}$	$8.04^{+0.05}_{-0.05}$	$0.64^{+0.03}_{-0.03}$
221209.01+612906.96	$8.1^{+0.1}_{-0.2}$	$7.90^{+0.06}_{-0.05}$	$0.54^{+0.03}_{-0.03}$	$7.0^{+0.2}_{-0.1}$	$7.93^{+0.06}_{-0.06}$	$0.55^{+0.04}_{-0.03}$
231404.30+552814.11	$14.0^{+0.2}_{-0.2}$	$8.08^{+0.05}_{-0.05}$	$0.66^{+0.03}_{-0.03}$	$8.6^{+0.1}_{-0.1}$	$7.50^{+0.05}_{-0.04}$	$0.38^{+0.03}_{-0.01}$

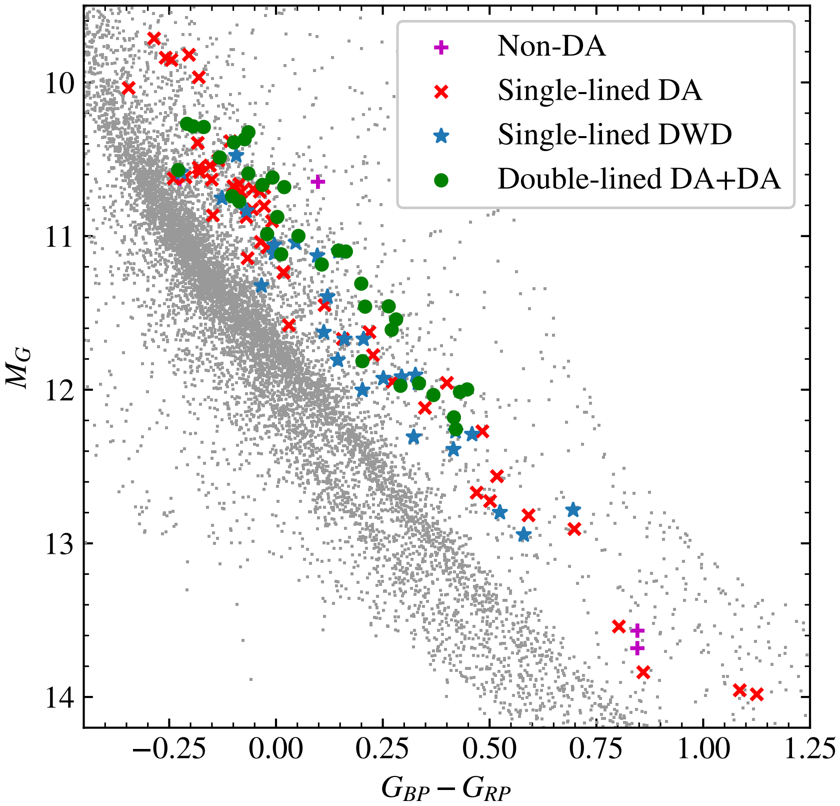

Figure 5.6: The same as Fig. 5.1, but further zoomed-in on the search selection area and with annotated object types of each target. Within are all double-lined DWDs (green circles), single-lined DWD binaries discovered from a poor spectroscopic or photometric solution with a single star model (blue stars), single-lined DA WDs that fit well for a single star model (red crosses) and non-DA WDs (purple pluses).

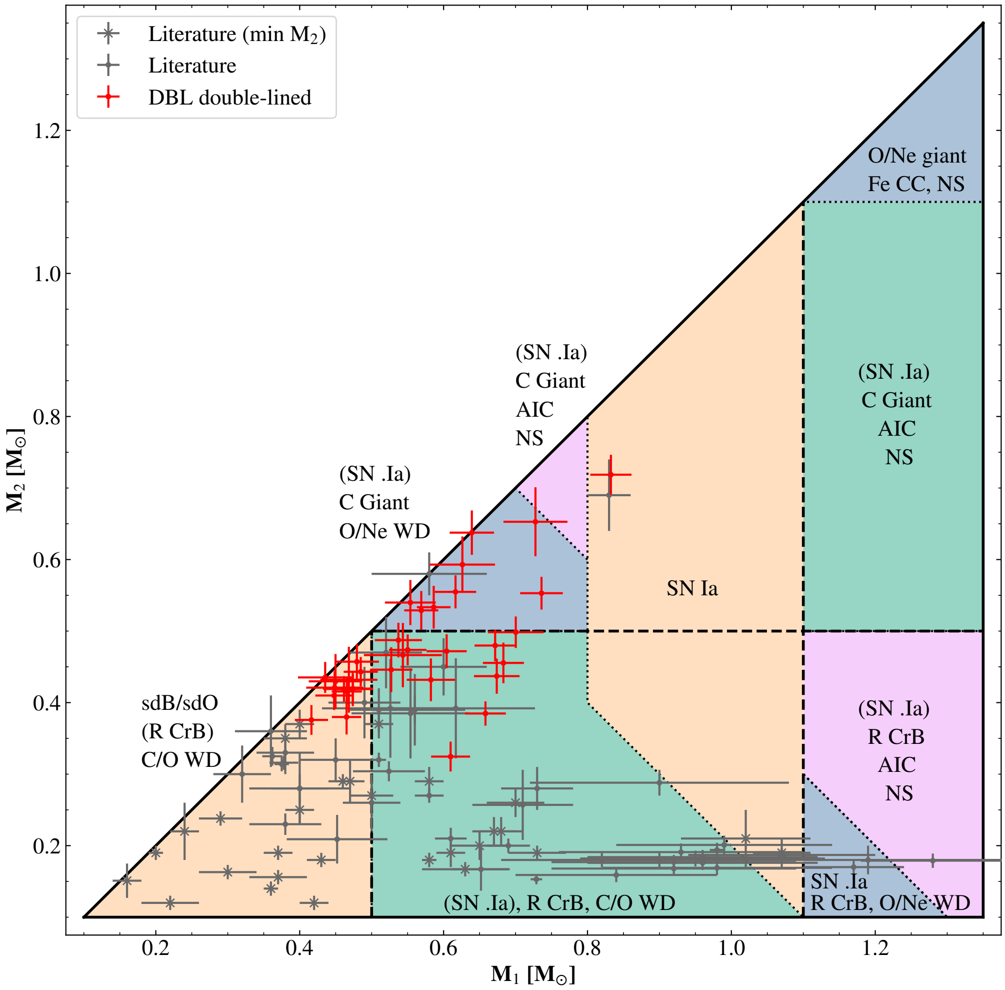

Figure 5.7: The mass distribution of compact DWD binaries where both star masses are quoted. The diagram is a reproduction of figure 3 of Shen [2015]. For this figure alone, M_1 is the larger mass of the two stars for each system and M_2 the smaller; all other mentions of star 1 or 2 in this study address indicate the hotter or cooler component, respectively. Systems plotted are DWDs in the literature where the mass of both components have an error better than 20% of the mass of the star (see the database upkept at github.com/JamesMunday98/CloseDWDbinaries for individual systems and references within). No filtering is applied on the orbital period for neither the literature sample nor the sample from the DBL survey, such that some objects will undergo the categorised events in over a Hubble time. The suggested evolutionary path for each category should be viewed as an approximate guideline only since stable mass transfer and AM CVn evolution are omitted. Acronyms first mentioned in the figure are as follows. sdB/sdO: hot subdwarf type B/O. R CrB: R Coronae Borealis. AIC: Accretion-induced collapse. NS: Neutron star. Fe CC: Iron core-collapse. SN: supernova.

double-lined DWDs, the detection efficiency of the survey rises to 32% and 38%, respectively. These detection efficiencies are minima given the fact that the inclusion of *Gaia* DR3 parallaxes and colours have removed some systems from the original sample selection criteria. In the case that these other 11 candidates are not double-lined DWDs, they would be single-lined DWD binaries owing to the photometric and spectroscopic fit requiring the flux of a second DA WD for a good Balmer line and/or photometric fit, which then could be compact or unresolved, wide binaries.

Since the initial identification spectra, a couple of systems have since been discovered by other authors and shown to be double-lined DWDs. WDJ153615.83+501350.98 was earlier noted to be a double-degenerate candidate by Zuckerman et al. [2003], but since has been independently confirmed and discovered by Kilic et al. [2021a, WD 1534+503] to be a double-lined DWD with much higher resolution observations at Hα. Using the WHT identification spectrum where the two stars are most separated (see Fig. 5.11), I obtain a 1σ consistent atmospheric solution with the solution in Kilic et al. [2021a] where my model reproduces Hβ–H8, the photometric SED and the *Gaia* parallax excellently and Hα well. Kilic et al. [2021a] do not fit to any data at Hα for atmospheric parameters and use Hβ–H8, nevertheless, I recommend the usage of the system parameters described in their study owing to a slightly better consistency with the orbital solution for the photometric masses derived. Published in the same study, WDJ163441.85+173634.09 was independently discovered by Kilic et al. [2021a, PG 1632+177] as a double-lined DWD and I again find 1σ-consistent atmospheric solution for both stars, where the fit in their study was also obtained using Hβ–H8. WDJ160822.19+420543.44 was independently discovered by Kilic et al. [2020a, WD 1606+422] and I find a near-identical atmospheric solution for both stars as well. Besides these 3 double-lined systems, I believe that all of the other 31 double-lined DWDs presented in this study are new discoveries.

While not a clear double-lined DWD discovery, WDJ181058.67+311940.94 was flagged by Sahu et al. [2023] as a strong double-degenerate candidate from a poor spectral fit to its Lyman-α profile. These authors do not extend their study to introduce two-star fits to the outliers in the data, meaning that the surface gravity of their single star solution is under-estimated and vastly different to my solution, but this is entirely expected due to the observed flux of the second star needing to be recovered by artificially inflating the radius in a single star fit. I have now confirmed the system as a DWD binary by detecting a double-lined feature at Hα.

My solutions for the confirmed double-lined systems report that the masses of the hotter component range from 0.4–$0.75\,\mathrm{M}_\odot$ with a median mass of $0.53\,\mathrm{M}_\odot$ and that the dimmer companion has a median mass of $0.45\,\mathrm{M}_\odot$. These measurements are slightly less than the $0.6\,\mathrm{M}_\odot$ canonical mass of a WD, but this is expected given that most if not all of these compact double-lined DWDs have underwent a phase of mass loss in the past from binary interactions.

WDJ183442.33−170028.00, which as noted in Section 5.5.1 shows a sharp hydrogen emission that does not originate from the system itself but from a background source in the galactic plane, is double-lined at the lower resolution Hβ in two exposures and is highly asymmetric at Hα after masking the hydrogen cloud emission. The observations of this DWD binary indicate a very large RV$_{\text{max}} = 294 \pm 12\,\text{km}\,\text{s}^{-1}$, which is the largest velocity difference detected amongst the full observed sample and the system is composed of two low-mass WDs of $0.42^{+0.04}_{-0.02}\,\text{M}_{\odot}$ and $0.38 \pm 0.03\,\text{M}_{\odot}$, giving rise to a maximum orbital period of 0.4 d. The second largest maximum RV difference was WDJ170120.99−191527.57, and the large total mass for this system of $1.31 \pm 0.04\,\text{M}_{\odot}$ leads to a maximum orbital period of 0.4 d, which is particularly interesting given the potential of a type Ia supernova in the astronomically soon future at 97.0 pc. It is possible that there are more compact systems than these in the observed sample based on the random phase sampling, and phase-resolved spectroscopy is the means to find out.

The new double-lined systems discovered seemingly show no preference for the cooler star being the more massive of the two. This challenges the scenario that the systems are formed via two common envelope phases that each led to significant shrinkage of the orbit, because in that case the more massive object would always have the largest cooling age. A feasible evolutionary path is instead that the less massive WD was first formed via stable mass transfer and cooled typically. Then, the other star evolved towards a WD, the system underwent a common envelope phase and exposed the star's core. The new WD has a larger mass than the old one, but is still hotter being fresh out of the envelope, while the older, less-massive WD is cooler.

An interesting feature of the DBL survey is that we see a build-up of double-lined DWDs that runs approximately 0.5 mag above and parallel to the 0.6 $\text{M}_{\odot}$ WD cooling track, as is prevalent in Fig. 5.6. The difference of 0.5 mag equates to roughly half of the flux, and so the natural conclusion is that double-lined DWD binaries are easiest to identify in the DBL survey for two stars of similar brightness. While this is an unavoidable detection bias, this emphasises a strength of the DBL survey and an important point for the future of double-lined DWD detection outside of the DBL survey: 10s to 100s of double-lined DWDs in this strip of the HR diagram are undetectable from RV variability in lower resolution data where the two stars are inseparable and the two signals average to a net zero velocity change; at higher resolution, these are easy to identify.

5.6.2 Single-lined DWDs

27 sources in Table 5.5 were found to be single-lined, but a poor fit to the photometric and/or spectroscopic solution indicates that they are likely DWD binaries. Together with the double-lined systems and the double-lined candidate systems, this means that 72 of the 117 systems surveyed in the initial search selection using the *Gaia* DR2 astrometric solution data show a noticeable spectroscopic and/or photometric contribution from a WD companion.

Three of the single-lined DWDs, WDJ024323.67−143957.37 ($\Delta\mathrm{RV}_{\mathrm{max}} = 67 \pm 7\,\mathrm{km\,s^{-1}}$), WDJ172740.51+102337.94 ($\Delta\mathrm{RV}_{\mathrm{max}} = 57 \pm 10\,\mathrm{km\,s^{-1}}$) and WDJ193833.62−092519.87 ($\Delta\mathrm{RV}_{\mathrm{max}} = 42 \pm 8\,\mathrm{km\,s^{-1}}$), show high RV variable log-probabilities of -99.0, -9.9 and -6.7, respectively. Further spectroscopic observations of these three DWDs to trace the RV of the brighter star are encouraged to search for an orbital period. WDJ231519.82-052900.27 is a candidate for being RV variable with a log-probability of -2.3. All other sources with multiple spectra are consistent with a non-variable RV and most if not all are expected to be binaries with an orbital period greater than 10 days, where the only prospects of finding an orbital period are from a larger time baseline of astrometric or spectroscopic observations. Some of the non-RV variable candidates could have periods that fall in the aliases that we are not sensitive to in this survey, which are predominantly aliases of 1 day (Fig. 5.3).

Overall in the sample of single- or double-lined DWDs, no system shows any signs of magnetism. If present, the spectra would be sensitive to detecting a magnetic field strength greater than approximately 50 kG with the identification spectra. The only DWD that has a strong magnetic field is NLTT 12758 [Kawka et al., 2017], and the dynamo theory proposed by Schreiber et al. [2021] has been shown to support the lack of magnetic DWD binaries in the observed population and can explain the apparently chance timing of detecting the magnetic WD in NLTT 12758 [Schreiber et al., 2022]. If true, a lack of magnetic DWDs in this survey is unsurprising, and the fact that we have specifically targeted systems with a $0.6\,\mathrm{M}_{\odot}$ star and a dimmer, likely more massive, companion [much like the $0.83{+}0.69\,\mathrm{M}_{\odot}$ pairing of NLTT 12758, Kawka et al., 2017] alludes that we may have been more sensitive to a magnetic component with the DBL survey's selection criteria, but none were found.

5.6.3 Single star DA WDs

38 targets in Table 5.6 appear as single-lined, DA WDs where a single-star model fits the photometric and spectroscopic data well. In many of these systems, the reason is likely that they are isolated, low mass WDs or that one star strongly outshines its companion, which is

highlighted by the grouping of single star DAs with $G_{\mathrm{mag}} \approx 10\,\mathrm{mag}$ in Fig. 5.6. Alternative reasons for identifying so many single star DA WDs in this region are that an additional unseen and red flux component makes the target appear redder and over-luminous, that the sources are indeed single WDs and a hybrid helium/carbon-oxygen core composition makes them appear over-luminous, that they are the product of an extremely-low-mass WD merger, or that some candidates are outliers in the *Gaia* database. Some of the sources classified as single DA WDs have crowded fields or issues with the *Gaia* DR3 parallax (see Table 5.6), meaning that they are spectroscopic fits instead of a hybrid. A few sources in Table 5.6 have M$\gtrsim$0.55 $\mathrm{M}_{\odot}$, and these are all cases where the location of the star on the HR diagram is on the lower edge of the search selection or when no photometry was fit. The minimum single star WD mass is approximately 0.3 $\mathrm{M}_{\odot}$, as was expected from the upper limit of the selection in Table 5.1. The median mass of the single star DA WDs in Table 5.6 is 0.43 $\mathrm{M}_{\odot}$.

I searched the single DA WDs for RV variations and a few targets displayed clear variability. The largest variation was in WDJ131913.72+450509.81 which exhibited an $75 \pm 5\,\mathrm{km\,s^{-1}}$ shift between two exposures, strongly indicating that this source has an unseen component and is a WD binary. WDJ031242.85+221828.36 is also a clear case where an unseen component is present, having a maximum shift of $70 \pm 10\,\mathrm{km\,s^{-1}}$. WDJ191927.69+395839.48 and WDJ230831.77+454212.19 exhibit a $30\,\mathrm{km\,s^{-1}}$ shift and both pass the threshold criteria of $\log_{10}(\mathrm{p_{bin}}) < -4$, making them RV variable systems. I promote follow-up observations of all to determine the orbital periods.

5.6.4 Gaia astrometric solutions

I cross-matched the *Gaia* non-single star catalogue [Halbwachs et al., 2023] with the full observed sample and I found that 5 in the observed sample have entries. One system that I flag as being a probable double-lined DWD but the SNR leads to a lack of clarity, WDJ225123.02+293944.49, has an astrometric period of $278.0 \pm 0.3\,\mathrm{d}$, indicative that it may be a triple star system. The same can be said for the candidate double-lined DWD WDJ211345.93+262133.27 which has an astrometric period of $219.7{\pm}0.2\,\mathrm{d}$. Three single-lined DWDs have detected astrometric periods, being WDJ023117.04+285939.88 ($103.9{\pm}0.07\,\mathrm{d}$), WDJ205650.56+062149.68 ($81.4{\pm}0.3\,\mathrm{d}$) and WDJ232519.87+140339.61 ($249.4 \pm 1.1\,\mathrm{d}$). The most likely situation for these three is that they are wide DWDs and it is hence unsurprising that no significant RV variability is witnessed. Finally, WDJ232519.87+140339.61, a source that I have categorised as a single-lined WD with no significant flux contribution from a companion, has an astrometric period of $249.4 \pm 1.1\,\mathrm{d}$.

5.7 The fate of the observed DWD sample

The end state of all of DWD binaries is largely dependent on the masses of the two constituents and core compositions. All compact WDs will gradually inspiral and initiate mass transfer from a loss of orbital angular momentum predominantly from the radiation of gravitational waves. The outcomes of a system are then a merger scenario, a detonation event or an orbital expansion following a brief period of mass transfer with a stripped companion. For a merger, exotic merger by-products such as the population of R CrB stars or hot subdwarfs [Schwab, 2018, 2019] in addition to the existence of some high-mass magnetic WDs [Kilic et al., 2023] are predicted to be at least partially explained by DWD mergers [Shen et al., 2012; Schwab et al., 2012]. The long suspected type Ia supernova detonation event, whereby mass accretion causes the carbon to ignite in degenerate conditions, either because the density increases due to mass accretion or due to shocks, can occur and in the last decade much interest has been sparked in the double-detonation sub-Chandrasekhar Supernova theory with .Ia supernovae [Bildsten et al., 2007]. Both have been observationally supported by the discovery of hyper-velocity runaway stars in the Milky Way [Shen et al., 2018a; El-Badry et al., 2023]. Yet, up to now, very few high-mass WDs in compact binaries have been found [Geier et al., 2007; Brown et al., 2016; Kawka et al., 2017; Pelisoli et al., 2021b; Adamane Pallathadka et al., 2024], drawing ambiguity on whether DWD binaries can replicate the observed rates of type Ia supernovae [Maoz and Mannucci, 2012]. Orbital expansion may happen when a system becomes an AM CVn [Solheim, 2010; Kupfer et al., 2024], although survival of a period minimum to produce an out-spiraling population of AM CVns remains unclear owing to the short lived period of time in this orbital phase and the large observational biases with the population.

The full series of photometric masses of double-lined DWD binaries identified in this work is plotted in Fig. 5.7, that shows the assessment of Shen [2015] of the most likely outcomes for mass combination but in many cases may be quite uncertain. Here and only in this figure, subscripts 1 and 2 are the more and less massive components, respectively. Single-lined DWDs are omitted since many could be wide binaries. As mentioned earlier, the vast majority of DWD binaries in the literature that constitute the observed population come in the form of low-mass WD binaries, which is far from reflective of the population as a whole [see e.g. Toonen et al., 2012]. An immediate change in the observed population of DWDs is now obvious from the newly uncovered sample, with the majority of these systems having larger combined total masses. None of the DBL survey sample falls into the low-mass regime and the majority of systems are dominated by a more massive star of approximately 0.55 $\mathrm{M}_{\odot}$.

One double-lined system in the observed sample exceeds the Chandrasekhar mass

Table 5.3: The same as Table 5.2, but double-lined DWD candidates where the lower SNR of the spectra of these targets is too difficult to conclude that they are double-lined definitively, although such a signature appears to be apparent. Continued observation and affirmation is encouraged. WDJ211927.07−030002.38 and WDJ225123.02+293944.49 had 1 exposure taken on one day followed by 2 on the other, and in both cases they appear double-lined in the first two exposures and slightly the third. The errors on the atmospheric constraints include an external error of 1.4% for $T_{\rm eff}$ and 0.042 dex for $\log g$ [Liebert et al., 2005], however this should be considered a minimum due to extra degeneracy in two-star fitting.

WDJ name	$T_{\rm eff,1}$ [kK]	$\log g_1$ [dex]	M_1 [$M_\odot$]	$T_{\rm eff,2}$ [kK]	$\log g_2$ [dex]	M_2 [$M_\odot$]
062538.73−162132.02	$14.0^{+0.2}_{-0.2}$	$7.99^{+0.07}_{-0.07}$	$0.60^{+0.04}_{-0.04}$	$11.3^{+0.2}_{-0.2}$	$7.87^{+0.06}_{-0.06}$	$0.53^{+0.03}_{-0.03}$
211927.07−030002.38	$11.1^{+0.2}_{-0.5}$	$8.31^{+0.06}_{-0.08}$	$0.80^{+0.04}_{-0.05}$	$6.5^{+0.2}_{-0.3}$	$7.56^{+0.10}_{-0.09}$	$0.40^{+0.04}_{-0.02}$
225123.02+293944.49	$6.3^{+0.1}_{-0.1}$	$8.56^{+0.07}_{-0.06}$	$0.95^{+0.04}_{-0.04}$	$5.1^{+0.1}_{-0.1}$	$7.79^{+0.05}_{-0.06}$	$0.46^{+0.03}_{-0.03}$

limit, being WDJ181058.67+311940.94 with a total mass of $1.55 \pm 0.04\,M_\odot$ and the maximum RV separation between the two stars indicates a maximum orbital period of 2.0 days. This represents the second super-Chandrasekhar mass DWD discovered to date after NLTT 12758 [Kawka et al., 2017]. Continued efforts to resolve the orbital period of WDJ181058.67+311940.94 may reveal a more compact nature and will provide a time estimate for the type Ia detonation. Furthermore, from the identification spectra alone, the maximum orbital periods confirm that some systems have orbital periods of less than $\approx$10 hrs signifying a merger time of less than a Hubble time. Continued work will strive to resolve the orbital dynamics of the sample (Munday et al, in prep).

Table 5.4: The same as Table 5.2, but candidate double-lined DWDs where the dimmer star is very slightly noticeable in the spectra, but could easily be confused with single-lined DWD binary. These double-lined candidates are much less probable than those in Table 5.3. High resolution and high SNR observations is again promoted to confirm/deny a double-lined state. The errors on the atmospheric constraints include an external error of 1.4% for $\mathrm{T_{eff}}$ and 0.042 dex for $\log g$ [Liebert et al., 2005], however this should be considered a minimum due to extra degeneracy in two-star fitting.

WDJ name	$\mathrm{T_{eff,1}}$ [kK]	$\log \mathrm{g_1}$ [dex]	$\mathrm{M_1}$ [$\mathrm{M_\odot}$]	$\mathrm{T_{eff,2}}$ [kK]	$\log \mathrm{g_2}$ [dex]	$\mathrm{M_2}$ [$\mathrm{M_\odot}$]
053316.88−075049.72	$11.1^{+0.5}_{-0.5}$	$7.22^{+0.09}_{-0.09}$	$0.32^{+0.05}_{-0.05}$	$7.7^{+0.4}_{-0.3}$	$7.16^{+0.12}_{-0.13}$	$0.29^{+0.03}_{-0.04}$
141354.17+153020.71	$15.2^{+0.3}_{-0.3}$	$7.61^{+0.04}_{-0.10}$	$0.42^{+0.02}_{-0.02}$	$12.1^{+0.5}_{-2.5}$	$8.36^{+0.29}_{-0.08}$	$0.83^{+0.18}_{-0.06}$
145011.93−191408.67	$8.1^{+0.1}_{-0.1}$	$7.66^{+0.05}_{-0.04}$	$0.42^{+0.02}_{-0.02}$	$5.3^{+0.3}_{-0.2}$	$7.78^{+0.08}_{-0.08}$	$0.46^{+0.05}_{-0.05}$
180600.36−002720.92	$25.0^{+0.4}_{-0.4}$	$7.60^{+0.04}_{-0.04}$	$0.45^{+0.02}_{-0.02}$	$11.2^{+0.5}_{-1.3}$	$7.94^{+0.07}_{-0.09}$	$0.57^{+0.04}_{-0.05}$
193642.54−054744.38	$10.2^{+0.2}_{-0.2}$	$7.83^{+0.05}_{-0.05}$	$0.51^{+0.03}_{-0.02}$	$7.1^{+0.3}_{-0.3}$	$7.98^{+0.06}_{-0.07}$	$0.58^{+0.03}_{-0.04}$
204922.92+262517.50	$16.9^{+0.3}_{-0.4}$	$7.83^{+0.05}_{-0.07}$	$0.53^{+0.02}_{-0.03}$	$14.6^{+0.3}_{-0.5}$	$8.06^{+0.06}_{-0.05}$	$0.65^{+0.04}_{-0.03}$
211345.93+262133.27	$8.6^{+0.1}_{-0.1}$	$7.79^{+0.04}_{-0.04}$	$0.48^{+0.02}_{-0.02}$	$5.8^{+0.1}_{-0.1}$	$7.83^{+0.08}_{-0.05}$	$0.49^{+0.04}_{-0.03}$
234929.57+102255.57	$14.4^{+0.2}_{-0.2}$	$7.82^{+0.04}_{-0.04}$	$0.51^{+0.02}_{-0.02}$	$7.4^{+0.2}_{-0.2}$	$7.96^{+0.06}_{-0.07}$	$0.57^{+0.04}_{-0.04}$

Table 5.5: The same as Table 5.2, but single-lined DWD binaries.References are provided if a study has performed a spectroscopic fit and obtained temperature estimates to both stars. Parameters subscripted by “AA” are for a DA+DA combination (or a $< 5000\,\mathrm{K}$ hydrogen-rich atmosphere DC) while parameters subscripted by “AC” are for a DA+DC where the DC has a helium-rich atmosphere and $\log(g_2) = 8.0\,\mathrm{dex}$ is assumed and fixed. Hyphens in the ‘AC’ columns represents that the fit to the photometry and/or spectroscopy with a DC model is poor and that the DA+DA solution should be adopted. An asterisk represents that a helium-rich atmosphere DC WD would fit the data only if the surface gravity is varied between $\log(g) = 7.5$–$9.0\,\mathrm{dex}$ (see Section 5.5.1). The errors on the atmospheric constraints include an external error of 1.4% for T_{eff} and 0.042 dex for $\log g$ [Liebert et al., 2005].p_{bin} was inferred from RVs that were obtained using the model flux of both stars with a common RV for the DA+DA stellar type combination.

WDJ name	$T_{1,AA}$ [kK]	$\log g_{1,AA}$ [dex]	$T_{2,AA}$ [kK]	$\log g_{2,AA}$ [dex]	$T_{1,AC}$ [kK]	$\log g_{1,AC}$ [dex]	$T_{2,AC}$ [kK]	D [pc]	Exp #	p_{bin} $\log_{10}$	Ref
001353.60+204852.65	$17.7^{+0.3}_{-0.4}$	$7.90^{+0.07}_{-0.06}$	$8.3^{+0.6}_{-0.3}$	$7.83^{+0.09}_{-0.11}$	$16.8^{+0.3}_{-0.3}$	$7.78^{+0.05}_{-0.05}$	$7.2^{+0.3}_{-0.3}$	291.0	3	-0.6	-
003045.78+273333.36	$16.1^{+0.2}_{-0.2}$	$7.86^{+0.04}_{-0.04}$	$7.6^{+0.2}_{-0.2}$	$7.74^{+0.05}_{-0.06}$	$14.6^{+0.2}_{-0.2}$	$7.70^{+0.04}_{-0.04}$	$*$	165.1	4	-0.2	-
014511.23+313243.56	$9.6^{+0.1}_{-0.1}$	$7.87^{+0.05}_{-0.05}$	$6.4^{+0.1}_{-0.1}$	$8.00^{+0.04}_{-0.04}$	$9.6^{+0.1}_{-0.2}$	$7.86^{+0.05}_{-0.05}$	$6.5^{+0.1}_{-0.1}$	36.7	1	-	1
023117.04+285939.88	$7.5^{+0.1}_{-0.1}$	$7.96^{+0.04}_{-0.04}$	$5.8^{+0.1}_{-0.1}$	$8.08^{+0.05}_{-0.04}$	$7.5^{+0.1}_{-0.1}$	$7.82^{+0.05}_{-0.05}$	$*$	27.9	5	-0.0	-
024323.67−143957.37	$9.2^{+0.3}_{-0.2}$	$7.72^{+0.06}_{-0.08}$	$5.1^{+0.2}_{-0.1}$	$7.61^{+0.13}_{-0.14}$	$9.1^{+0.7}_{-0.1}$	$7.70^{+0.06}_{-0.04}$	$*$	80.2	3	-99.0	-
080739.31+132110.65	$11.6^{+0.2}_{-0.2}$	$7.68^{+0.04}_{-0.05}$	$7.3^{+0.3}_{-0.3}$	$7.80^{+0.07}_{-0.07}$	$11.1^{+0.2}_{-0.2}$	$7.61^{+0.04}_{-0.05}$	$*$	115.0	1	-	-
084417.70+750008.79	$14.5^{+0.2}_{-0.2}$	$8.04^{+0.04}_{-0.04}$	$7.0^{+0.2}_{-0.2}$	$8.01^{+0.05}_{-0.06}$	$13.3^{+0.2}_{-0.2}$	$7.96^{+0.05}_{-0.04}$	$7.1^{+0.2}_{-0.1}$	102.4	4	-0.0	-
084634.41+194505.18	$10.9^{+0.3}_{-0.3}$	$7.65^{+0.09}_{-0.08}$	$7.7^{+0.3}_{-0.5}$	$7.61^{+0.08}_{-0.08}$	$10.1^{+0.2}_{-0.2}$	$7.44^{+0.04}_{-0.05}$	$*$	146.5	1	-	-
102459.83+044610.50	$12.4^{+0.6}_{-0.2}$	$7.62^{+0.04}_{-0.05}$	$5.7^{+0.3}_{-0.2}$	$7.64^{+0.35}_{-0.09}$	$12.1^{+0.2}_{-0.2}$	$7.60^{+0.04}_{-0.04}$	$*$	43.1	1	-	-
104709.19+345346.65	$9.2^{+0.1}_{-0.1}$	$7.70^{+0.05}_{-0.05}$	$5.4^{+0.1}_{-0.2}$	$7.69^{+0.05}_{-0.06}$	$9.0^{+0.2}_{-0.1}$	$7.63^{+0.04}_{-0.04}$	$*$	79.4	1	-	-
113100.20+493826.27	$11.6^{+0.2}_{-0.2}$	$7.91^{+0.04}_{-0.05}$	$6.9^{+0.1}_{-0.1}$	$7.71^{+0.06}_{-0.05}$	$10.7^{+0.3}_{-0.2}$	$7.72^{+0.04}_{-0.04}$	$7.3^{+0.1}_{-0.1}$	99.3	1	-	-
113347.81+624313.29	-	-	-	-	$6.4^{+0.1}_{-0.1}$	$7.92^{+0.04}_{-0.04}$	$6.0^{+0.1}_{-0.1}$	45.8	1	-	2
131257.90+580511.29	$11.6^{+0.2}_{-0.2}$	$8.01^{+0.04}_{-0.04}$	$6.7^{+0.1}_{-0.1}$	$8.12^{+0.05}_{-0.05}$	$11.2^{+0.2}_{-0.2}$	$7.93^{+0.04}_{-0.04}$	$6.4^{+0.1}_{-0.9}$	30.9	2	-0.0	-
135738.69−025819.41	$17.1^{+0.6}_{-0.4}$	$7.92^{+0.11}_{-0.08}$	$14.8^{+0.5}_{-1.1}$	$7.98^{+0.13}_{-0.12}$	$16.0^{+1.3}_{-1.3}$	$7.57^{+0.07}_{-0.05}$	$6.9^{+1.3}_{-0.8}$	137.2	2	-0.2	-
154214.21−034131.29	$11.5^{+0.2}_{-0.2}$	$8.07^{+0.05}_{-0.04}$	$7.9^{+0.2}_{-0.2}$	$8.07^{+0.04}_{-0.05}$	$10.8^{+0.2}_{-0.2}$	$7.89^{+0.07}_{-0.11}$	$5.5^{+1.0}_{-0.2}$	51.9	1	-	-

... continued

WDJ name	$T_{1,AA}$ [kK]	$\log g_{1,AA}$ [dex]	$T_{2,AA}$ [kK]	$\log g_{2,AA}$ [dex]	$T_{1,AC}$ [kK]	$\log g_{1,AC}$ [dex]	$T_{2,AC}$ [kK]	D [pc]	Exp #	p_{bin} $\log_{10}$	Ref
172740.51+102337.94	-	-	-	-	$10.5^{+0.2}_{-0.2}$	$8.23^{+0.04}_{-0.05}$	$7.8^{+0.2}_{-0.1}$	59.0	5	-9.9	-
191329.91+163822.12	$8.3^{+0.1}_{-0.1}$	$7.88^{+0.04}_{-0.05}$	$6.7^{+0.1}_{-0.1}$	$8.03^{+0.05}_{-0.05}$	$8.4^{+0.1}_{-0.1}$	$7.78^{+0.05}_{-0.04}$	*	77.0	5	-1.0	-
192359.24+214103.62	$9.4^{+0.1}_{-0.2}$	$7.81^{+0.05}_{-0.04}$	$6.1^{+0.2}_{-0.1}$	$7.81^{+0.05}_{-0.06}$	$9.5^{+0.1}_{-0.1}$	$7.80^{+0.04}_{-0.05}$	$6.4^{+0.1}_{-0.9}$	35.3	3	-0.0	-
193833.62−092519.87	$15.9^{+0.2}_{-0.2}$	$8.08^{+0.05}_{-0.04}$	$8.0^{+0.2}_{-0.1}$	$7.66^{+0.04}_{-0.04}$	$12.5^{+0.2}_{-0.2}$	$7.73^{+0.04}_{-0.04}$	$8.7^{+0.1}_{-0.1}$	114.8	3	-6.7	-
204517.85+810503.40	$8.7^{+0.1}_{-0.1}$	$8.19^{+0.06}_{-0.05}$	$7.8^{+0.1}_{-0.1}$	$8.01^{+0.05}_{-0.05}$	$8.9^{+0.1}_{-0.1}$	$7.93^{+0.04}_{-0.04}$	*	67.0	3	-1.7	1
205650.56+062149.68	$11.0^{+0.2}_{-0.2}$	$7.98^{+0.06}_{-0.05}$	$6.5^{+0.2}_{-0.2}$	$7.67^{+0.05}_{-0.07}$	$10.1^{+0.2}_{-0.1}$	$7.77^{+0.04}_{-0.04}$	$6.7^{+0.1}_{-0.1}$	95.0	3	-0.6	-
213616.39−131834.50	$10.3^{+0.1}_{-0.1}$	$7.85^{+0.04}_{-0.04}$	$5.0^{+0.1}_{-0.1}$	$8.03^{+0.04}_{-0.05}$	-	-	-	23.4	3	-0.1	-
214632.37+155039.08	$8.5^{+2.0}_{-0.3}$	$7.83^{+0.25}_{-0.14}$	$6.9^{+4.1}_{-0.3}$	$7.96^{+0.20}_{-0.52}$	$8.6^{+0.1}_{-0.1}$	$7.79^{+0.04}_{-0.05}$	*	74.5	3	-0.2	-
221052.87−045540.80	$7.9^{+0.1}_{-0.1}$	$7.84^{+0.04}_{-0.04}$	$6.9^{+0.1}_{-0.1}$	$7.90^{+0.05}_{-0.05}$	-	-	-	63.5	3	-0.1	-
231443.05−073417.85	$14.0^{+0.2}_{-0.2}$	$7.99^{+0.04}_{-0.04}$	$9.5^{+0.2}_{-0.2}$	$8.10^{+0.04}_{-0.05}$	-	-	-	75.1	3	-0.1	-
231519.82−052900.27	$6.5^{+0.1}_{-0.2}$	$7.65^{+0.21}_{-0.05}$	$5.9^{+0.1}_{-0.1}$	$7.88^{+0.07}_{-0.26}$	$6.3^{+0.1}_{-0.1}$	$7.48^{+0.04}_{-0.04}$	*	54.4	3	-2.3	-
233041.67+110206.43	$21.7^{+0.3}_{-0.3}$	$7.97^{+0.04}_{-0.04}$	$7.0^{+0.3}_{-0.3}$	$8.10^{+0.07}_{-0.07}$	$21.5^{+0.3}_{-0.3}$	$7.94^{+0.04}_{-0.04}$	$6.4^{+0.2}_{-0.6}$	99.2	1	-	-

5.8 Conclusions

I have presented a pilot study including the first results from the DBL survey based on 20 nights of observations with the WHT. A large sample of 117 DWD binary candidates that reside above the 0.6 $\mathrm{M}_{\odot}$ WD cooling track were surveyed through the exploitation of the *Gaia* DR2 HR diagram, randomly sampling candidates from a magnitude limited selection. Then, I fitted and obtained atmospheric solutions for the entire sample when all visible stars in the spectra were of spectral type DA, DB or DC with the custom-made fitting code WD-BASS that is designed for time-series spectroscopy of WDs and is publicly available for use.

The primary goal of the survey was to find double-lined DWDs which allow the obtention of precise masses for both stars in the binary through atmospheric fitting. The methods of the DBL survey demonstrate at least a 29% double-lined detection rate after a couple of observing epochs and that 73 of the 117 candidates show a separable spectroscopic/photometric flux contribution that must arise from a DWD configuration. A further 6 single-lined WDs are flagged for having an unseen companion based off RV variability. All double-lined DWDs are compact binaries, and the large RV difference between the two stars provides some insight to the orbital period distribution of the systems.

For the first time, I have been able to observationally identify a class of DWDs with system masses $M_T \geq 1.0\,\mathrm{M}_{\odot}$ that may undergo a type .Ia supernova or merge to become a massive WD. One system (WDJ181058.67+311940.94) located just 49 pc away hosts two relatively massive WDs of mass $0.72 \pm 0.03\,\mathrm{M}_{\odot}$ and $0.83 \pm 0.03\,\mathrm{M}_{\odot}$, making it the second DWD system confirmed as super-Chandrasekhar mass.

In continued work I will report orbital solutions of many of the double-lined DWDs in this study. Many more double-lined DWDs are waiting to be discovered within the search selection, where I will strive to obtain further completion of the 625 G_{mag}<17 mag double degenerate candidates.

5.9 All double-lined systems

All DWDs that exhibit a double-lined feature are displayed in Fig. 5.8 and all of the likely double-lined DWDs that should be confirmed with further observations are found in Figs. 5.11 and 5.12. While hybrid fitting was used to derive atmospheric parameters, which includes the simultaneous fitting of survey photometry and the WHT spectra, the data and model spectrum at Hα alone are shown in these figures to emphasise the double-lined nature of each system.

Table 5.6: The best fits to systems that appear as a single DA WD, where no/insufficient contribution of a second star is distinguishable in the spectroscopy and photometry. No photometric fitting was applied to underlined targets because they lie in a crowded field (hence only a spectroscopic fit was performed), and the distances underlined are instead obtained from the *Gaia* parallaxes. In the case of WDJ150402.99+345440.76, the *Gaia* solution reports a common proper motion pair at inconsistent distances to one another and neither are consistent with a photometrically fit parallax, and as such I ignore the *Gaia* parallax. The errors on the atmospheric constraints include an external error of 1.4% for $T_{\mathrm{eff},1}$ and 0.042 dex for $\log g_1$ [Liebert et al., 2005]. References are included when spectroscopic/hybrid fitting has been performed with the source within the last 5 years or the most recent study otherwise, under the assumption that there are common datasets between studies (e.g. SDSS). References: 1) Gianninas et al. [2011] 2) Kleinman et al. [2013] 3) Caron et al. [2023] 4) Blouin et al. [2019] 5) Kilic et al. [2020b] 6) Guo et al. [2015] 7) O'Brien et al. [2024] 8) McCleery et al. [2020].

WDJ name	T_{eff} [kK]	log g [$\mathrm{cm\,s^{-2}}$]	M [$M_\odot$]	D [pc]	p_{bin} $\log_{10}$	Ref
001321.07+282019.83	$26.2^{+0.4}_{-0.4}$	$7.84^{+0.04}_{-0.04}$	$0.56^{+0.02}_{-0.02}$	135.3	-0.5	1
003508.27+135045.32	$22.9^{+0.4}_{-0.7}$	$7.47^{+0.09}_{-0.06}$	$0.44^{+0.02}_{-0.02}$	246.8	-0.2	2
015437.45+374145.37	$12.9^{+0.2}_{-0.2}$	$7.53^{+0.04}_{-0.04}$	$0.42^{+0.01}_{-0.01}$	136.6	-0.1	-
022631.25+203106.04	$21.5^{+0.3}_{-0.3}$	$7.89^{+0.04}_{-0.04}$	$0.57^{+0.02}_{-0.02}$	164.9	-0.1	-
031242.85+221828.36	$6.3^{+0.1}_{-0.1}$	$7.36^{+0.04}_{-0.04}$	$0.33^{+0.03}_{-0.02}$	63.2	-99.0	3, 4
042127.88+701419.37	$12.4^{+0.2}_{-0.6}$	$7.60^{+0.04}_{-0.04}$	$0.41^{+0.02}_{-0.02}$	54.5	-	1
074837.63+004011.72	$15.5^{+1.2}_{-0.6}$	$7.57^{+0.06}_{-0.06}$	$0.40^{+0.03}_{-0.03}$	184.9	-0.8	-
081706.44+054954.62	$11.3^{+0.2}_{-0.2}$	$7.61^{+0.04}_{-0.04}$	$0.41^{+0.02}_{-0.02}$	133.3	-	-
091914.80+772350.79	$9.1^{+0.1}_{-0.1}$	$7.56^{+0.04}_{-0.04}$	$0.41^{+0.01}_{-0.01}$	46.5	-0.0	3
093709.98+650746.91	$18.1^{+0.4}_{-0.3}$	$7.92^{+0.04}_{-0.04}$	$0.58^{+0.02}_{-0.02}$	105.5	-0.3	-
101606.87−011917.14	$8.1^{+0.1}_{-0.1}$	$7.63^{+0.04}_{-0.04}$	$0.43^{+0.02}_{-0.02}$	$\underline{46.3}$	-	3, 5
114604.37+051401.54	$6.6^{+0.1}_{-0.1}$	$7.43^{+0.04}_{-0.04}$	$0.35^{+0.01}_{-0.01}$	62.3	-	3, 4, 5
130313.03−032323.92	$7.2^{+0.1}_{-0.1}$	$7.56^{+0.05}_{-0.04}$	$0.40^{+0.02}_{-0.02}$	64.6	-	3, 5
131913.72+450509.81	$13.1^{+0.2}_{-0.2}$	$7.43^{+0.04}_{-0.04}$	$0.40^{+0.01}_{-0.02}$	49.0	-99.0	5
134503.00−110434.10	$21.0^{+2.8}_{-0.8}$	$7.57^{+0.08}_{-0.12}$	$0.42^{+0.04}_{-0.04}$	246.6	-1.0	-
142047.04+465601.58	$10.2^{+0.5}_{-0.1}$	$7.58^{+0.05}_{-0.04}$	$0.42^{+0.02}_{-0.02}$	98.6	-0.1	3, 5
150402.99+345440.76	$18.8^{+0.3}_{-0.3}$	$8.07^{+0.04}_{-0.04}$	$0.66^{+0.03}_{-0.03}$	-	-0.2	1
152849.51−012853.74	$12.8^{+0.2}_{-0.2}$	$7.93^{+0.04}_{-0.04}$	$0.57^{+0.02}_{-0.02}$	52.4	-1.5	-
155840.22+162556.04	$12.3^{+0.2}_{-0.2}$	$7.47^{+0.05}_{-0.04}$	$0.40^{+0.01}_{-0.02}$	106.3	-	1
160647.76−152740.19	$31.9^{+0.8}_{-0.5}$	$7.98^{+0.06}_{-0.14}$	$0.64^{+0.03}_{-0.07}$	$\underline{194.4}$	-3.4	-
175644.61−020847.66	$16.1^{+1.4}_{-0.3}$	$7.52^{+0.09}_{-0.04}$	$0.43^{+0.01}_{-0.01}$	157.8	-0.0	-
181304.62+222449.79	$21.4^{+0.3}_{-0.3}$	$7.91^{+0.04}_{-0.04}$	$0.58^{+0.02}_{-0.02}$	209.3	-0.8	-
181339.31+255058.16	$19.1^{+1.1}_{-0.3}$	$7.53^{+0.05}_{-0.10}$	$0.40^{+0.02}_{-0.02}$	183.5	-0.5	-
182444.29+600159.40	$12.7^{+0.2}_{-0.2}$	$7.70^{+0.04}_{-0.04}$	$0.45^{+0.02}_{-0.02}$	96.2	-0.1	-
183752.49−125257.45	$37.8^{+0.6}_{-0.5}$	$8.21^{+0.04}_{-0.04}$	$0.78^{+0.03}_{-0.03}$	179.5	-0.2	-
185640.86+120844.61	$13.6^{+1.5}_{-0.4}$	$7.53^{+0.08}_{-0.05}$	$0.42^{+0.01}_{-0.01}$	156.3	-0.0	-
190401.01−102305.20	$16.2^{+0.2}_{-0.3}$	$7.92^{+0.04}_{-0.04}$	$0.57^{+0.02}_{-0.02}$	103.0	-0.1	-
191927.69+395839.48	$18.9^{+0.3}_{-0.3}$	$7.73^{+0.04}_{-0.04}$	$0.49^{+0.02}_{-0.02}$	105.8	-15.1	6

... continued

WDJ name	$T_{\rm eff}$ [kK]	log g [cm s^{-2}]	M [$M_{\odot}$]	D [pc]	$p_{\rm bin}$ $\log_{10}$	Ref
192817.81+354442.60	$20.5^{+0.3}_{-0.3}$	$7.92^{+0.04}_{-0.04}$	$0.58^{+0.02}_{-0.02}$	138.2	-	-
193845.80+264751.85	$22.2^{+0.4}_{-0.3}$	$7.93^{+0.04}_{-0.05}$	$0.59^{+0.02}_{-0.02}$	97.0	-0.2	-
195314.95−105417.89	$22.6^{+0.7}_{-0.6}$	$7.74^{+0.07}_{-0.08}$	$0.50^{+0.04}_{-0.03}$	145.0	-	-
195622.94+641359.19	$18.3^{+0.3}_{-0.3}$	$7.77^{+0.04}_{-0.04}$	$0.50^{+0.02}_{-0.02}$	85.5	-0.2	-
205020.65+263040.76	$5.2^{+0.1}_{-0.1}$	$8.54^{+0.04}_{-0.04}$	$0.94^{+0.03}_{-0.03}$	19.1	-	3, 4, 7, 8
230831.77+454212.19	$13.6^{+0.2}_{-0.2}$	$7.48^{+0.04}_{-0.04}$	$0.41^{+0.01}_{-0.02}$	103.1	-6.8	-
231406.68+233343.06	$7.1^{+0.1}_{-0.1}$	$7.45^{+0.04}_{-0.04}$	$0.36^{+0.02}_{-0.02}$	68.5	-0.2	3
232519.87+140339.61	$4.9^{+0.1}_{-0.1}$	$7.29^{+0.04}_{-0.04}$	$0.30^{+0.02}_{-0.02}$	23.5	-	3, 4, 7, 8
232557.82+255222.39	$5.6^{+0.1}_{-0.1}$	$7.49^{+0.04}_{-0.04}$	$0.38^{+0.03}_{-0.03}$	46.0	-0.0	3, 4
235313.18+205117.58	$7.4^{+0.1}_{-0.1}$	$7.64^{+0.04}_{-0.05}$	$0.43^{+0.02}_{-0.02}$	57.0	-0.2	3, 4

Table 5.7: Sources in the sample with no DA WD present. Spectral types of main sequence (MS) stars, cataclysmic variable (CV) systems and systems with a subdwarf (sd) are included. Underlined distances are obtained from a *Gaia* parallax (DR3 if available, otherwise DR2). The spectrum of WDJ010343.47+555941.53 is also plotted in Fig. 5.13.

WDJ name	D	SpT	Note
J002215.19+423642.15	34.5	DC	Perhaps Hα absorption at 6554Å.
J004502.15−040710.05	43.2	DQ	Swan bands
J010343.47+555941.53	26.1	-	Evolved CV or sd+F/G/K star
J021243.27−080216.23	119.7	MS	No WD signatures & blue object
J182138.99+144158.19	89.7	DB	$T_{\rm eff} = 21.3 \pm 0.3$ kK, $\log g = 8.02 \pm 0.04$ dex
J195513.90+222458.79	14.8	MS	No signature of WD
J201437.22+231607.23	29.8	MS	No signature of WD

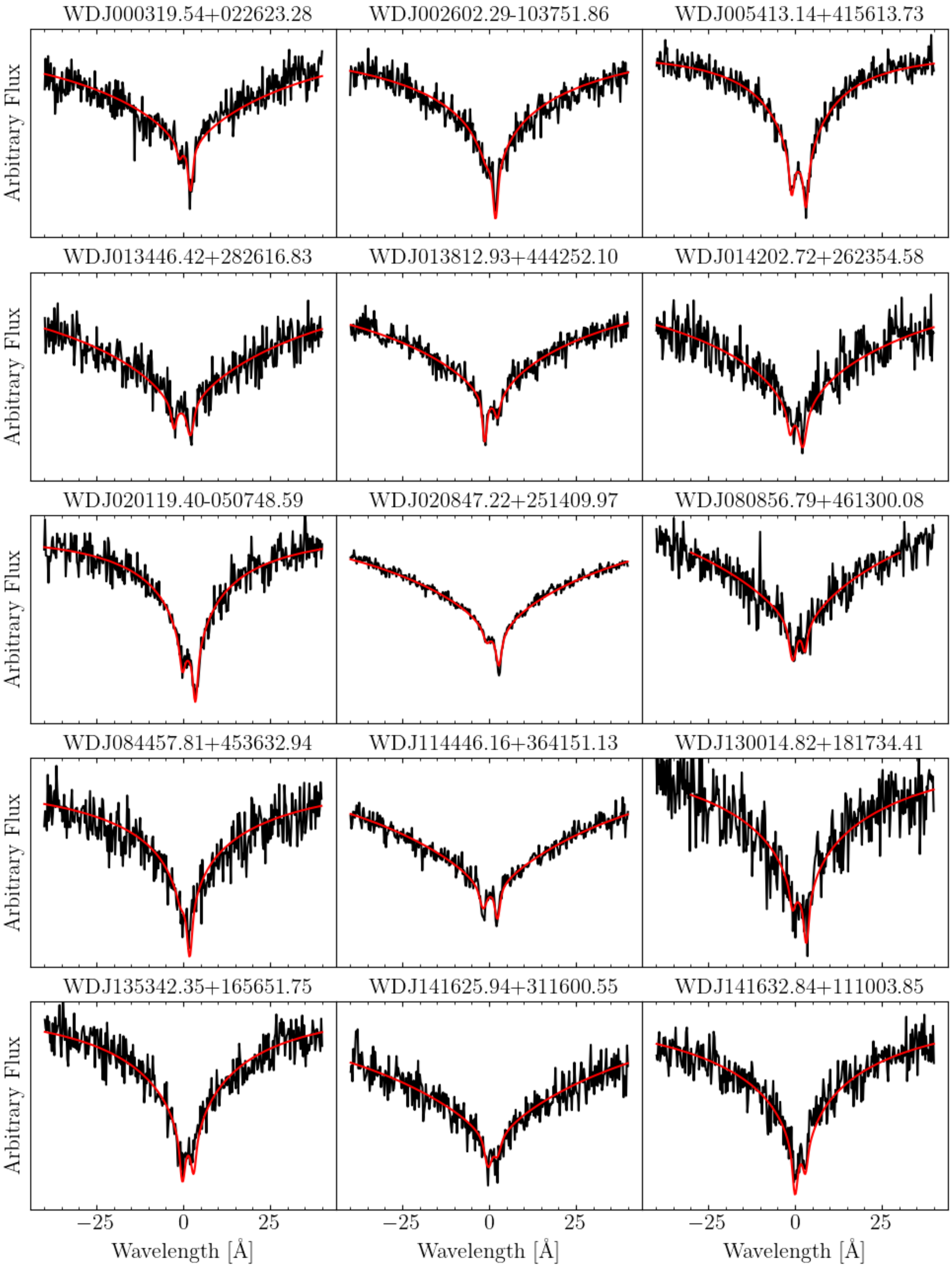

Figure 5.8: All model fits to the double-lined systems. Other Balmer lines and the photometry were fit simultaneously, but each spectrum is zoomed in at Hα.

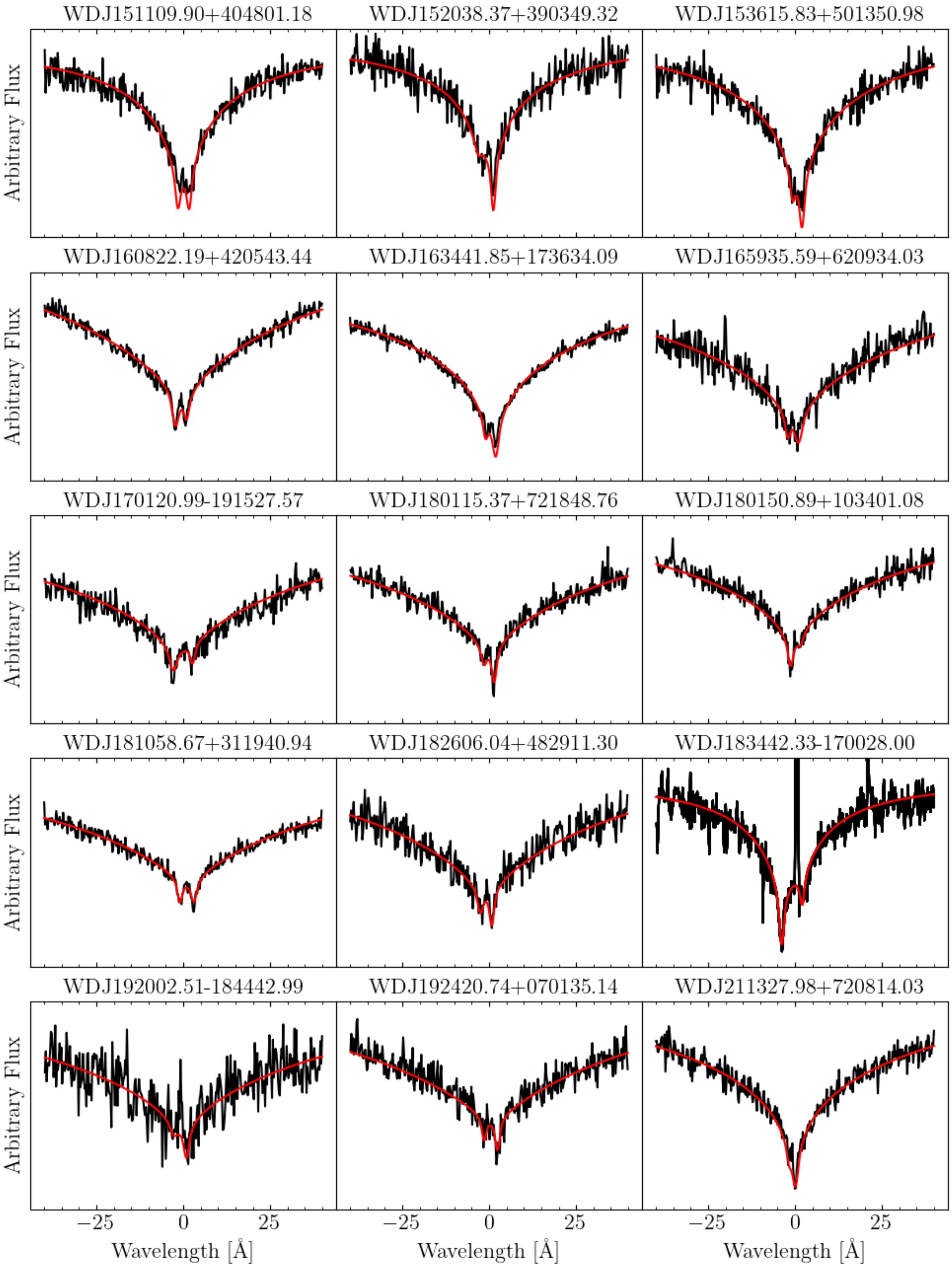

Figure 5.9: Continued. The spectrum of WDJ192002.51-184442.99 has a low SNR in the red arm, but it is also double-lined at Hβ with higher SNR data in the blue.

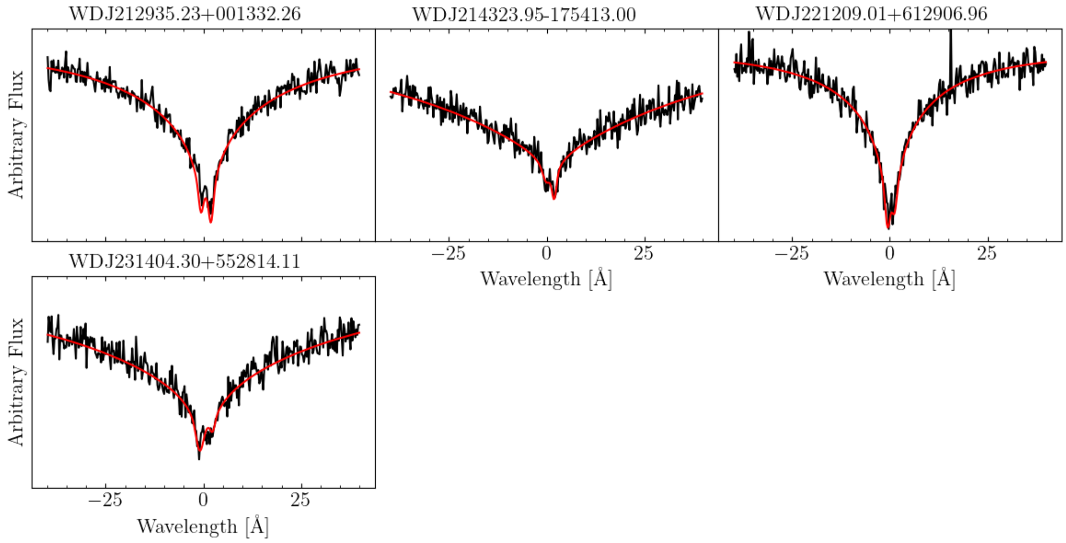

Figure 5.10: Continued...

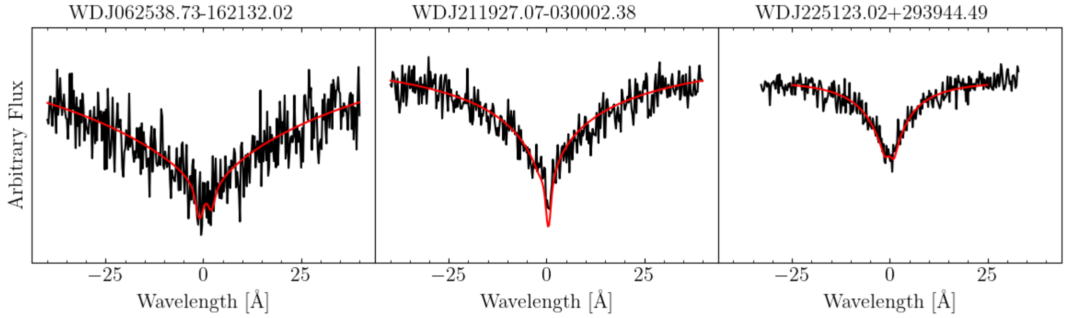

Figure 5.11: All model fits to likely double-lined systems that should be confirmed with higher SNR data. I note that even though the depth of Hα is shallow owing to the cool temperature of the two stars, in multiple exposures do the data and the best model fit hint at double-lined signature.

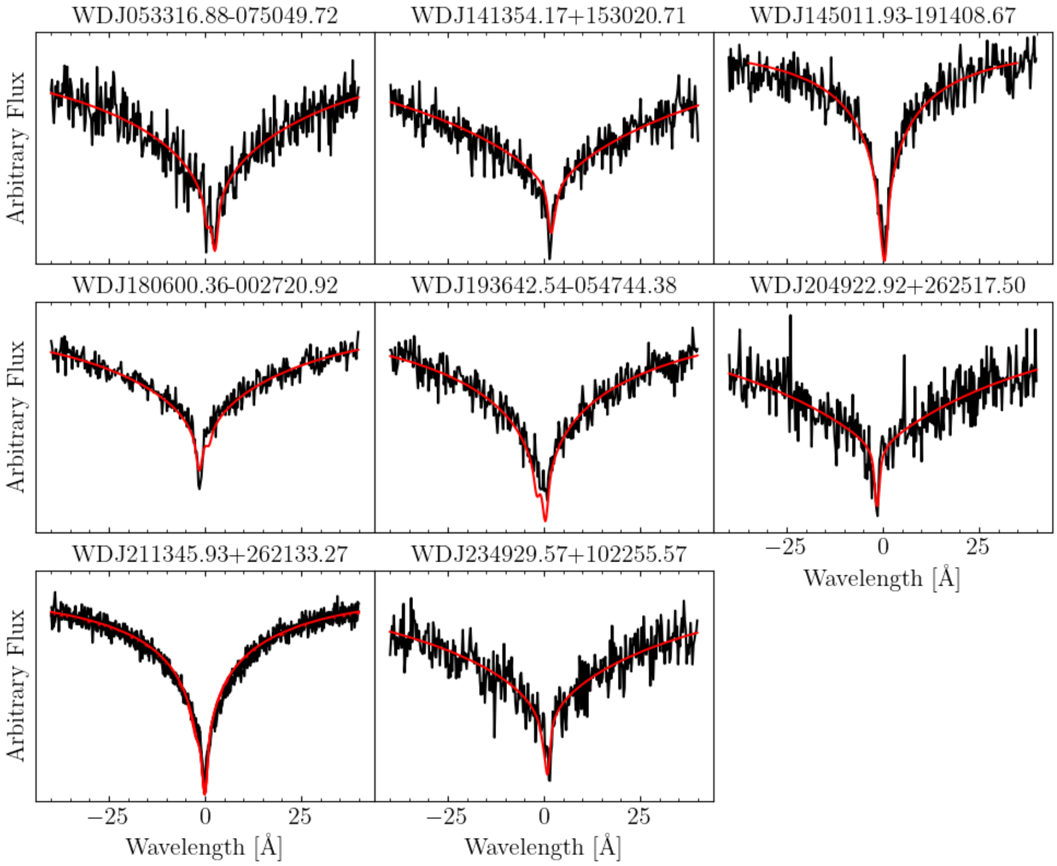

Figure 5.12: All model fits to the candidate double-lined systems that do not show a clear separation of the two stars but have asymmetric line profiles. Further observation is again encouraged to confirm if the sources are single- or double-lined. In the case that any are single-lined, the flux from an additional component is still required in the spectroscopic/photometric fit, and so these sources would be single-lined DWD binaries.

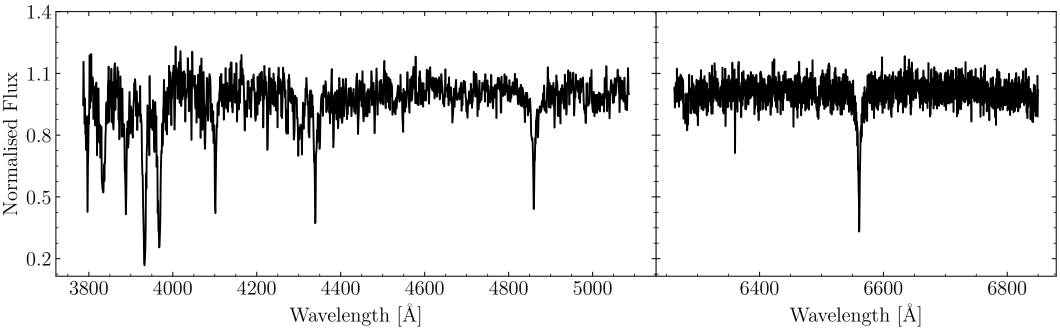

Figure 5.13: WDJ010343.47+555941.53, an evolved CV or a subdwarf with an F/G/K star companion.

5.10 Sensitivity to double-lined systems

The ability to detect a double-lined DWD is dependent on the relative flux contribution of the two stars, and hence there is a dependence on the stars' radii. I depict the impact of this effect in Fig. 5.14 to determine for which combinations of temperature and surface gravity would the companion contribute at least 25% of the flux at the centre of Hα in the WHT data. A minimum flux contribution of 25% was used to construct the selection criteria in Section 5.2.1, and below this threshold a second star is unlikely to be detectable at the signal-to-noise ratio of the WHT data.

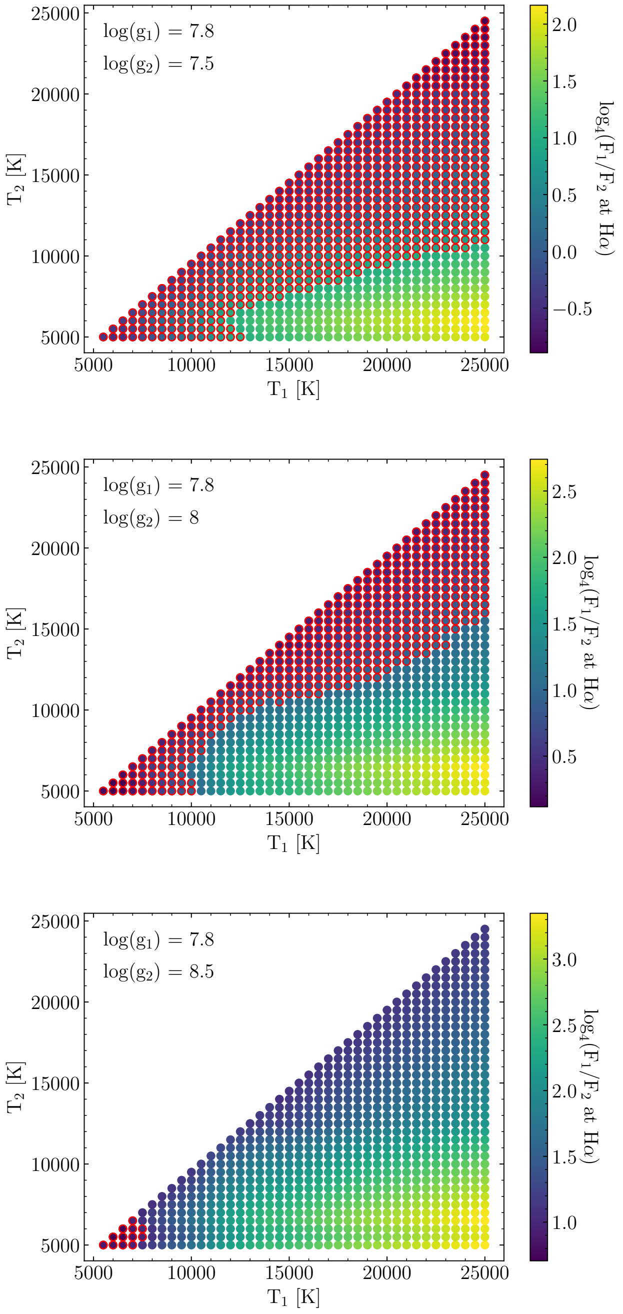

Figure 5.14: The sensitivity to double-lined systems for a given $\log(g_2)$. A $\log(g_1) = 7.8$ is maintained, which is approximately the median surface gravity of the brighter star in the double-lined sample (Table 5.2). Red circles around individual points indicate when the dimmer component contributes at least 25% of the flux ($\log_4$ $F_1/F_2 = 1$), as was desired in the selection criteria of the sample (Section 5.2.1). The temperatures of both stars are sampled in 500 K intervals and the scaling is included through interpolation of log(g)-temperature-radius relationships. The relative flux contribution was sampled at the centre of Hα and synthetic spectra were convolved to a spectral resolution of $R = 8\,000$.

Chapter 6

A super-Chandrasekhar mass type Ia supernova progenitor at 49 pc set to detonate in 23 Gyr

James Munday, Ruediger Pakmor, Ingrid Pelisoli, Snehaleta Sahu, David Jones, P.-E. Tremblay, Abinaya Swaruba Rajamuthukumar, Gijs Nelemans, Mark Magee, Silvia Toonen, Antoine Bédard, Tim Cunningham

Contribution of co-authors

Observations used in this study were obtained by author #5. Author #2 performed all components of the supernova fitting in Section 6.6 while author #7 contributed by supplying realistic stellar structure models of the WDs. Author #4 performed spectral fitting to the HST ultra-violet data of the target presented in Section 6.4.2. All authors contributed with comments on the manuscript during the submission/revision process by supplying key ideas to explore in creating the final version of the study. All other components and the leading of the study were performed by me.

Abstract

Double white dwarf binaries are a leading explanation to the origin of type Ia supernovae, but no system exceeding the Chandrasekhar mass limit ($1.4\,\mathrm{M}_\odot$) has been found that will explode anywhere close to a Hubble time. Here, we present the super-Chandrasekhar mass double white dwarf WDJ181058.67+311940.94 whose merger time ($22.6 \pm 1.0\,$Gyr) is of the same order as a Hubble time. The mass of the binary is large, combining to $1.555 \pm 0.044\,\mathrm{M}_\odot$, while being located only 49 pc away. We predict that the binary will explode dynamically via a double detonation destroying both stars just before they merge, appearing as a subluminous type Ia supernova with a peak apparent magnitude of about $m_V = -16$ (200 000 times brighter than Jupiter). The observationally-derived birthrate of super-Chandrasekhar mass double white dwarfs is now at least $6.0 \times 10^{-4}\,\mathrm{yr}^{-1}$ and the observed rate of type Ia supernovae in the Milky Way from such systems is approximately $4.4 \times 10^{-5}\,\mathrm{yr}^{-1}$, while the predicted type Ia supernova rate in the Milky Way from all progenitor channels is about sixty times larger. Hence, WDJ181058.67+311940.94 mitigates the observed deficit of massive double white dwarfs witnessed in volume-complete populations, but further evidence is required to determine the majority progenitors of type Ia supernovae.

6.1 Motivation

At the late stages of finishing off the DBL #1 project described in Chapter 5, the highest total mass system stood out above as a very exciting source. Especially at the close proximity of 49 pc, confirmation of a massive DWD and detection of its orbital period quickly became high priority. By chance, I already had some time-series spectra of the target that revealed evidence an orbital period around 6.5 hr, 9 hr, 13 hr or 26 hr, but the true period was not clear. The result warranted a paper on this single target for its cosmological importance, where the orbital and atmospheric analysis was mixed with a hydrodynamical simulation to model the final moments of its lifetime – the first time this has been done for the masses of a real DWD binary.

6.2 Introduction

In current synthetic models of the population, DWDs with total mass greater than the Chandrasekhar mass limit are indeed suspected to be scarce [Toonen et al., 2012; Rebassa-Mansergas et al., 2019; Li et al., 2023], but based on the models of Toonen et al. [2012] we still expect about 6 compact double white dwarf binaries to have total masses that exceed 1.5 $M_{\odot}$ within 100 pc. However, we have had no direct evidence that these systems exist in volume-complete populations [Toonen et al., 2017; Hollands et al., 2018; O'Brien et al., 2024], casting doubt on whether DWDs can account for a large percentage of the observed type Ia supernova rates [Maoz and Mannucci, 2012]. There has been only one super-Chandrasekhar mass DWD binary discovered [NLTT 12758, Kawka et al., 2017], but its 1.15 d period means that the two stars will come into contact in about 10 Hubble times. There are a handful of other high-mass, candidate subluminous type Ia progenitors that are DWDs [e.g. Maxted et al., 2002b; Karl et al., 2003; Nelemans et al., 2005; Rebassa-Mansergas et al., 2017; Munday et al., 2023, 2024], two WD+hot subdwarf systems that exceed 1.4 $\mathrm{M}_{\odot}$ and have an impending supernova fate [Pelisoli et al., 2021b; Luo et al., 2024] and one other WD+hot subdwarf that is also strong candidate [Maxted et al., 2000; Geier et al., 2007].

Type Ia supernovae initiated from the WD+hot subdwarf channel are observationally expected at a rate of at least $(1.5\text{–}7) \times 10^{-5}\,\mathrm{yr}^{-1}$ [Pelisoli et al., 2021b], while the rate of type Ia supernovae in the Galaxy from all progenitors is about $2.8 \pm 0.6 \times 10^{-3}\,\mathrm{yr}^{-1}$ [Li et al., 2011; Maoz et al., 2014; Li et al., 2023; Liu et al., 2023], inferred through observations of explosions in other galaxies of similar redshift. Multiple other evolutionary scenarios have been suggested as causes for normal and peculiar type Ia supernovae [see Liu et al., 2023] having different companion compositions, but the extent to which they contribute towards the missing fraction of type Ia supernovae is unclear. This ambiguity on the nature of type Ia progenitors is cosmologically problematic. A primary reason is that, until we confirm the leading progenitors of a type Ia, systematic errors to the distances derived to other galaxies could lead to inaccurate measurements, which is particularly troublesome for galaxies at high redshifts [Pan et al., 2012; Maoz et al., 2014]. In addition, the details of the ejecta velocity and its constituents are important for star formation [Lacchin et al., 2021] and the dynamics of gas in galaxies [Jiménez et al., 2015]. Massive DWDs are one of the most attractive channels for SNe Ia and, if the progenitor age is the predominant effect controlling SN luminosity, the WDs in a young galaxy will be massive ones as these have evolved more quickly. This hypothesis can be directly tested with massive DWDs in the Milky Way. Not only would the discovery of local, compact, super-Chandrasekhar mass DWDs have the ability to resolve the dearth of systems in the observed sample, but a sample of such systems has the power to reduce uncertainty of this cosmologically fundamental event.

In this study, I presented the first super-Chandrasekhar mass DWD to have a compact orbit (P $=$ $14.24\,$hr) which will likely explode as a subluminous type Ia supernova in $22.6 \pm 1.0\,$Gyr. The individual mass constituents are $0.834 \pm 0.039\,\mathrm{M}_{\odot}$ and $0.721 \pm 0.020\,\mathrm{M}_{\odot}$, making it the most massive DWD binary discovered to date, while being located on our Galactic doorstep at 49 pc.

6.3 Observations

WDJ181058.67+311940.94 was first discovered as part of the DBL survey [Munday et al., 2024] using medium-resolution spectra ($R = 8\,800$) on the 4.2 m William Herschel Telescope with the Intermediate-dispersion Spectrograph and Imaging System (ISIS). Two other ISIS exposures were taken on the nights 13 & 14 April 2019 using the R600B and R1200R gratings with $1.2''$ slit resulting in a resolution of $R = 3\,000$ at Hα and these spectra are included in the full orbital analysis of the DWD. The blue and red setups had a wavelength calibration accuracy of approximately $3\,\mathrm{km\,s^{-1}}$ and $2\,\mathrm{km\,s^{-1}}$, respectively.

I conducted a continued observational campaign to derive phase-resolved radial velocities (RVs) of the DWD binary. I utilised the 2.5 m Isaac Newton Telescope (INT) with the Intermediate Dispersion Spectrograph (IDS) over the nights 4-7 September 2019 (11 exposures, 1800 s each), and 24 September 2019 (4 exposures, 900 s each) with the Red+2 detector and a $1.2''$ slit width, resulting in a spectral resolution of $R = 6\,300$. Further phase-resolved spectra were taken with the INT telescope on the nights 25 & 26 August 2024 with the H1800V grating at a resolution of $R = 9\,400$ (20 exposures, 1500 s each). An arc lamp exposure was taken every 45 min of observing time and the science images were wavelength calibrated by interpolation of the nearest two arcs. The wavelength calibration accuracy per frame was approximately $2\,\mathrm{km\,s^{-1}}$.

Bias, flat field and spectrophotometric flux standard star images were taken on all nights and applied in the reduction. All data from the WHT and the INT were reduced using the MOLLY suite [Marsh, 2019], with the optimal extraction algorithm outlined in Marsh [1989].

I supplemented data from the INT and WHT with continued spectroscopic observations through 18 exposures of length 1 500 s on the 2.56 m Nordic Optical Telescope (NOT) using the FIbre-fed Echelle Spectrograph (FIES) in low-resolution mode. These granted full optical coverage at a resolution $R = 25\,000$ with a wavelength calibration accuracy of approximately $\pm 150\,\mathrm{m\,s^{-1}}$. Observations were obtained through a staff queue at random times, typically being two consecutive exposures, and through a NOT fast-track proposal. All FIES data were reduced using its automated data reduction pipeline – FIEStool[1]. I also obtained 5 exposures with the NOT Alhambra Faint Object Spectrograph and Camera (ALFOSC) with a $0.5''$ slit width, producing spectra at R=10 000 with wavelength range 6330-6870 Å. These were taken on 1 & 2 June 2024, and the data were reduced with the PYPEIT python package [Prochaska et al., 2020].

A continuous observing window of 4.5 hr was obtained through directors discretionary time on the 8.2 m Very Large Telescope (VLT) with the UV-Visual Echelle Spectrograph (UVES). Each exposure lasted for 730 s with a readout time between exposures of 45 s, totalling 20 exposures. I employed an observing setup of the dichroic 1 mode with central wavelengths of 3900 Å and 5640 Å for the blue and red arm, giving a wavelength range that covered the full visible spectrum besides gaps of 80 Å at 4580 Å and 5640 Å. A slit width of 1.0" and a 2×2 binning granted a spectral resolution $R = 20\,000$ and the wavelength calibration accuracy was approximately $200\,\mathrm{m\,s^{-1}}$ [Whitmore et al., 2010; Whitmore and Murphy, 2015].

In deriving final RVs for these data (Table 6.3), the wavelength calibration error was added in quadrature to the statistical error.

6.4 Spectral analysis

6.4.1 Atmospheric fitting of optical data

I used the package WD-BASS[2] [Munday, 2024] to fit atmospheric parameters to the spectra from VLT/UVES. For synthetic spectra, I utilised the 3D-NLTE model grid introduced in Munday et al. [2024], which was constructed using the 3D-LTE models of Tremblay et al.

---

[1] https://not.iac.es/instruments/fies/fiestool/FIEStool.html

[2] https://github.com/JamesMunday98/WD-BASS

[2015] with a further NLTE correction factor applied using the NLTE and LTE synthetic spectra described in Kilic et al. [2021a]. The two stars were scaled using temperature-log g-radius relationships with the evolutionary track models of Istrate et al. [2016] when $\mathrm{M} \leq 0.393\,\mathrm{M}_{\odot}$, Althaus et al. [2013] when $0.393 < \mathrm{M} < 0.45\,\mathrm{M}_{\odot}$ and the hydrogen-rich evolutionary sequences of Bédard et al. [2020] otherwise. The model spectra were converted from an Eddington flux to that observed at Earth and reddened with A(V) $=$ $0.0312\,$mag [Lallement et al., 2022], E(B-V) $=$ A(V)$/3.1$ using the reddening curves of Gordon et al. [2023].

I applied an atmospheric fitting technique that is very similar to that described in Munday et al. [2024], performing a hybrid fit with the UVES spectra and Pan-STARRS photometry [Chambers and Pan-STARRS Team, 2018] simultaneously. The differences were that, because of the improved signal-to-noise ratio of the data, I could fit bluer Balmer lines being all from Hα to H11. Then secondly, to give the photometric and spectroscopic data a similar overall weight, I applied an extra weighting ($\times$1000) to the photometric fit. Without this weighting, the spectra would have over-dominated the best-fit solution. Only spectra taken at the times where a distinct double-line splitting is evident at Hα were fit to avoid fitting degeneracies between the two stars, which were 10 of them (total of 20). In deriving errors, I individually fit each red-arm spectrum that reveals a double-lined Hα split along with the nearest-in-time blue-arm spectrum while weighting the photometry by $100\times$. Then, I took the standard deviation of all measurements to be the error in star's surface gravity and temperature. The new best-fit atmospheric parameters are stated in Table 6.1, which are entirely consistent with those found in Munday et al. [2024].

6.4.2 Atmospheric fitting of ultra-violet data

Author #4 performed an independent spectroscopic fit using the Hubble Space Telescope spectrum presented in Sahu et al. [2023]. WDJ181058.67+311940.94 was observed for a single 1 000 s exposure using the Cosmic Origins Spectrograph on the 19th February 2022 with the centre of exposure at 05:00 UT. The observation had a central wavelength of 1291 Å with the G130M grating, giving a resolution of $R = 12\,000$–$16\,000$ and a wavelength range of 1130–1430 Å with a gap at 1278–1288 Å due to the positioning of the two detector segments. Given the vastly different method and the fact that WDJ181058.67+311940.94 is not double-lined at Lyman-α in the ultra-violet data, no RVs were extracted, but the predicted RVs of the two stars at the centre of exposure ($-37.8\,\mathrm{km\,s^{-1}}$ for the more massive and $139.6\,\mathrm{km\,s^{-1}}$ for the less massive star, respectively) were fixed in the fitting procedure.

The spectral fitting method is identical to that presented in Sahu et al. [2023] with the only exceptions being that a second hydrogen-rich atmosphere WD is included in the

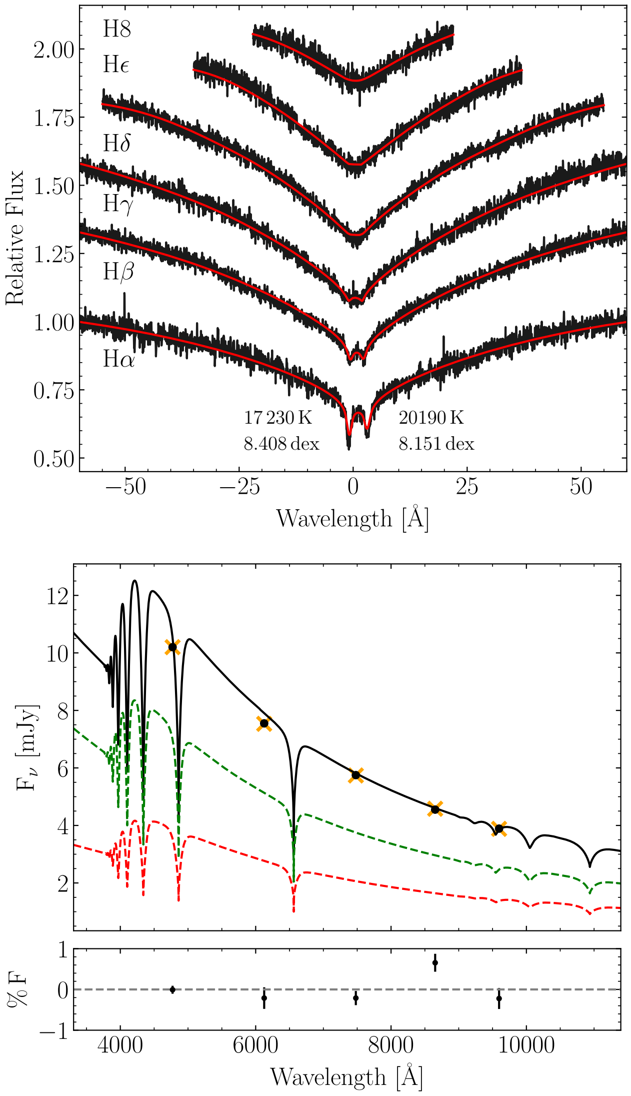

Figure 6.1: The results of a hybrid fit to the UVES spectra and the Pan-STARRS photometry. Left: A single UVES spectrum from Hα to H8 with the synthetic spectral model for atmospheric parameters $T_{\mathrm{eff},1} = 17\,230$ K, $\log(g_1) = 8.408$ dex, $T_{\mathrm{eff},2} = 20\,190$ K, $\log(g_2) = 8.151$ dex, overplotted in red. We remind that all Balmer lines up to H11 were fit but are omitted from the plot for clarity, and that all spectra with a split double-lined feature were fit simultaneously. Right: The observed fluxes in Pan-STARRS (black circles) and the synthetic photometry in each filter for the same atmospheric parameters (orange crosses). The percentage flux residual between the data and the combined flux is found below. The flux contributed from the more massive (dashed red) and less massive (dashed green) stars are included underneath.

Table 6.1: The atmospheric parameters for each spectroscopic data set. Hybrid fitting was performed in all cases using Pan-STARRS photometry. A systematic difference between the ultra-violet spectroscopy and the optical photometry was considered in the fitting (Section 6.4.2). Masses are inferred by interpolation of the evolutionary sequences in Bédard et al. [2020] and $\mathrm{M_T}$ is the total mass of the system. The final adopted values were obtained by concatenating the distributions obtained for each parameter to then quote the median and 68% confidence interval on the $\mathrm{T_{eff}}$ and $\log(g)$, while interpolating to find masses. The more/less massive star is labelled with subscript 1/2 respectively. The WHT/ISIS solution is quoted from the result of Munday et al. [2024].

	VLT/UVES	WHT/ISIS	HST/COS	Adopted
$\mathrm{T_{eff,1}}$	17230 ± 710	16500^{+400}_{-300}	18630 ± 80	17260^{+1380}_{-880}
$\log(\mathrm{g_1})$	8.408 ± 0.027	8.35 ± 0.05	8.307 ± 0.020	$8.350^{+0.066}_{-0.052}$
$\mathrm{M_1}$	0.871 ± 0.018	0.83 ± 0.03	0.810 ± 0.013	0.834 ± 0.039
$\mathrm{T_{eff,2}}$	20190 ± 280	20200 ± 300	18010 ± 70	20000^{+400}_{-2000}
$\log(\mathrm{g_2})$	8.151 ± 0.021	8.16 ± 0.04	8.178 ± 0.018	$8.164^{+0.027}_{-0.030}$
$\mathrm{M_2}$	0.713 ± 0.014	0.72 ± 0.03	0.727 ± 0.013	0.721 ± 0.020
$\mathrm{M_T}$	1.584 ± 0.022	1.55 ± 0.04	1.537 ± 0.018	1.555 ± 0.044

model, that A(V)=0.0312 mag was adopted and that the mid-exposure RV of the two stars is considered. A hybrid (spectroscopic and photometric) fit was performed with no extra error weighting applied, using the HST/COS spectrum and photometry from Pan-STARRS g, r, i, z, y [Chambers and Pan-STARRS Team, 2018], fixing the distance to *Gaia* DR3 parallax. Updated model atmospheres from Koester [2010] with a WD mass-radius relation extracted from Bédard et al. [2020] were used to fit the absolute fluxes. Additionally, strong absorption lines affecting the continuum were masked in the COS spectrum [Sahu et al., 2023]. To address the inconsistencies reported between ultra-violet and optical parameters [Sahu et al., 2023], a systematic offset of 1% in $\mathrm{T_{eff}}$ and 0.1 dex in $\log(\mathrm{g})$ were added to the ultra-violet values of both stars in the hybrid fitting, while trial values in the optical were unchanged. The best-fit model to the spectra are shown in Fig. 6.2, and the results of the atmospheric fitting in Table 6.1 with comparison to the optical solution. A total mass of $1.537 \pm 0.018\,\mathrm{M_\odot}$ was found through this analysis, which again is consistent with that stated in Munday et al. [2024].

To provide a final adopted value from the atmospheric fitting inclusive of the results from the optical and the ultra-violet datasets, I concatenated the distributions obtained for each parameter to then quote the median and 68% confidence interval on the $\mathrm{T_{eff}}$ and $\log(g)$, while interpolating these parameters to find obtain masses. The adopted values are quoted in Tables 6.2 and Table 6.1.

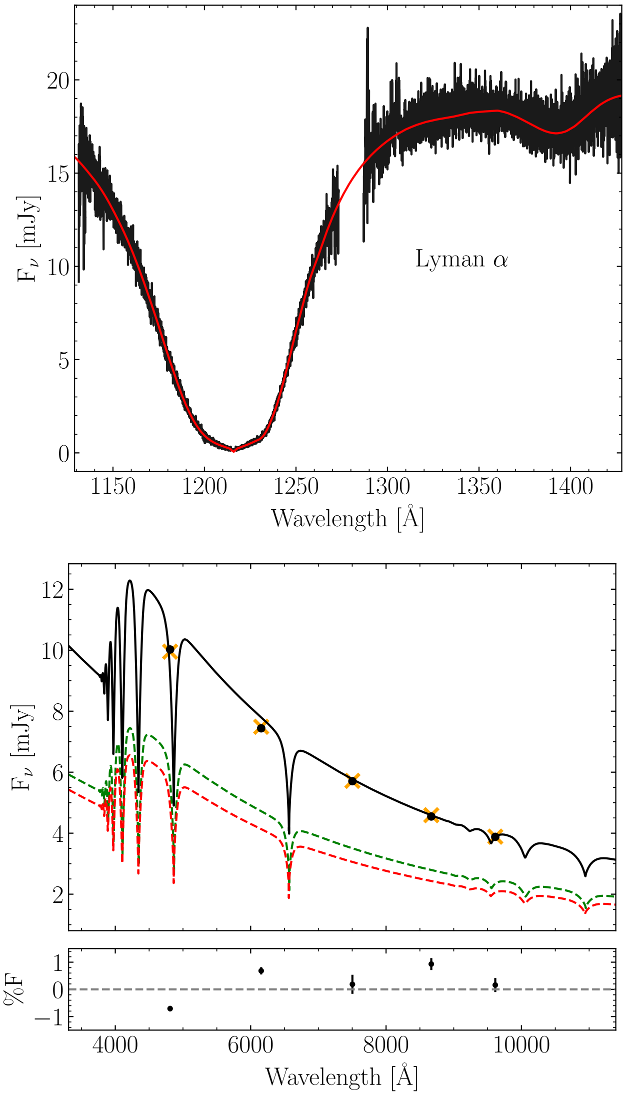

Figure 6.2: The results of a hybrid fit to the HST/COS ultra-violet spectrum with Pan-STARRS photometry for a two-star model. The synthetic spectra of DA WDs with atmospheric parameters $T_{\mathrm{eff},1} = 18\,630\,\mathrm{K}$, $\log(g_1) = 8.307\,\mathrm{dex}$, $T_{\mathrm{eff},2} = 18\,010\,\mathrm{K}$, $\log(g_2) = 8.178\,\mathrm{dex}$, are included. See Fig. 6.1 for further details.

Table 6.2: Positional, atmospheric and orbital parameters for WDJ181058.67+311940.94. The primary and secondary stars correspond to the more massive and less massive components, respectively. The temperatures, surface gravities and masses quoted are the adopted values from the spectroscopic fits, which were determined considering data from all sources (see Table 6.1).

Parameter	Unit	Value	Uncertainty
Right ascension	deg (2016)	272.744360834	± 0.000000005
Declination	deg (2016)	31.327961071	± 0.000000005
Reference epoch	HJD (UTC)	2458587.6663	± 0.0018
Orbital period	day	0.5931479	± 0.0000009
Gaia parallax	mas	20.438	± 0.023
Fitted parallax	mas	20.402	± 0.003
Primary temperature	K	17 260	$+1380/-880$
Secondary temperature	K	20 000	$+400/-2000$
Primary surface gravity	dex	8.350	$+0.066/-0.052$
Secondary surface gravity	dex	8.164	$+0.027/-0.030$
Primary mass	$M_\odot$	0.834	± 0.039
Secondary mass	$M_\odot$	0.721	± 0.020
System mass	$M_\odot$	1.555	± 0.044
Primary semi-amplitude	$\mathrm{km\,s^{-1}}$	93.9	± 2.0
Secondary semi-amplitude	$\mathrm{km\,s^{-1}}$	95.7	± 2.1
Primary velocity offset	$\mathrm{km\,s^{-1}}$	50.0	± 1.5
Secondary velocity offset	$\mathrm{km\,s^{-1}}$	53.5	± 1.6
Merger time	Gyr	22.6	± 1.0

6.4.3 Radial velocities and orbital parameters

WD-BASS was again used to obtain radial velocities (RVs) for all of the optical spectra. The best-fit synthetic spectrum agrees with the data extremely well (see Fig. 6.1), but even with the correction of NLTE effects to the model grid line cores, the synthetic model flux is over-predicted in the line cores of Hα. To obtain the most accurate template for RV extraction possible, I fit a Gaussian model to the Hα line cores of both stars combined with a 4-term polynomial to model the broader wings of Hα, all within 10 Å of the Hα centre. This method best modelled the shape of the spectral area around the line cores for the high signal-to-noise ratio and high resolution UVES spectra, but not for all other data sources. Instead, I took the result of the best-fit synthetic spectrum and added an extra Gaussian component at the line cores of Hα for both stars [following the method described in Section 4.4 of Munday et al., 2024], which improved the line-core shape significantly. The Gaussians were fit to all relevant spectra simultaneously and this final template spectrum was then used for RV extraction in WD-BASS. I started by fitting the RV of both stars to each spectrum by taking the median of 1000 bootstrapping iterations and taking errors as the standard deviation of this bootstrapped posterior distribution.

With the full set of 82 RV measurements (Appendix 6.8), I then searched for an orbital period, P, by minimising the χ^2 of equation 6.1 for trial semi-amplitudes (K_1, K_2) and velocity offsets (γ_1, γ_2) of each star using a least squares algorithm, where

$$\mathrm{PK}_{1,2}^3 = \frac{2\pi \mathrm{GM}_{2,1}^3 \sin(i)^3}{(\mathrm{M}_{1,2} + \mathrm{M}_{2,1})^2} \tag{6.1}$$

An upper bound on the semi-amplitude, $\mathrm{K}_{\mathrm{max},1}$ and $\mathrm{K}_{\mathrm{max},2}$ were set for a trial period set by applying an edge-on ($i = 90°$) inclination for a $1.4\,\mathrm{M}_\odot + 0.15\,\mathrm{M}_\odot$ DWD in a Keplerian orbit (the maximum and observed minimum mass of a WD, respectively). There is no indication of eccentricity from the RVs, so the orbit is assumed to be circularised ($e = 0$).

In the process, I noticed a deviation from Keplerian motion around conjunction which is caused by degeneracy in the fitted RVs as the stars spectrally overlap. This is unsurprising as the velocity resolution of the ALFOSC, ISIS and IDS data was around 30–40 $\mathrm{km\,s^{-1}}$, while in the higher resolution FIES spectra a lower signal-to-noise ratio of the spectra led to the same degeneracies. I decided to ignore these RVs when fitting the orbital motion by masking measurements which are within $15\,\mathrm{km\,s^{-1}}$ of the RV of each star at conjunction. All RVs from the UVES spectra within this range were utilised as its high signal-to-noise combined with twice the velocity resolution did not cause any noticeable deviation.

The phase-folded RV curve with the best-fit orbital solution is depicted in Fig. 6.3. The best-fitting orbital parameters are $P = 14.23557{\pm}0.00002\,\mathrm{hr}$, $\mathrm{K}_1 = 93.9{\pm}2.0\,\mathrm{km\,s^{-1}}$,

$K_2 = 95.7 \pm 2.1\,\mathrm{km\,s^{-1}}$, $\gamma_1 = 50.0 \pm 1.5\,\mathrm{km\,s^{-1}}$, $\gamma_2 = 53.5 \pm 1.6\,\mathrm{km\,s^{-1}}$. Being double-lined, the mass ratio is independently solvable without knowledge of the orbital inclination with $q = \mathrm{M_2/M_1} = \mathrm{K_1/K_2}$, such that the orbitally derived $q = 0.98 \pm 0.03$. This result is in best agreement with the star masses derived from the HST/COS spectrum, which was $q = 0.90 \pm 0.02$. The derived masses from the VLT/UVES spectra yield a lower $q = 0.82 \pm 0.02$, with the mass of the less massive star being near identical to the ultra-violet, and the adopted value taking into account all measurements indicates a mass ratio of $q = 0.86 \pm 0.04$. The surface gravity of the hotter, less massive star is near identical across fits to all datasets. This is unsurprising given that it contributes more flux than the dimmer WD, while its temperature difference between the ultra-violet and optical datasets primarily arises from the fitting of the slope of the spectral energy distribution across the ultra-violet. Forcing the orbitally-derived $q = 0.98 \pm 0.03$ in the atmospheric fit requires the surface gravity of the secondary to increase and the surface gravity of the primary to decrease to fit the broadness of the Balmer line profiles well. The secondary would thus be more massive, the primary less massive and as such, including for a mass ratio of approximately one, the binary is a super-Chandrasekhar mass DWD.

All evidence strongly points towards the total mass of WDJ181058.67+311940.94 being significantly above the Chandrasekhar mass limit and that the two have similar masses. Galactic population models predict that about half of super-Chandrasekhar mass systems contain similar mass stars within $0.2\,\mathrm{M_\odot}$ of each other [Toonen et al., 2012], as is the case also for NLTT 12758, where all systems with $q \gtrapprox 2/3$ are destined to undergo unstable mass transfer [Marsh et al., 2004]. Unstable mass transfer will hence occur in the future for WDJ181058.67+311940.94 as well.

Returning to equation 6.1 with mass constraints, we can solve for the orbital inclination, i. By taking into account all combinations of masses determined from the atmospheric analysis, I concluded that WDJ181058.67+311940.94 has an inclination $i \approx 35 - 45\,\mathrm{deg}$. I analysed the TESS [Ricker et al., 2015] light curve of WDJ181058.67+311940.94 in all cadences to search for any photometric signature of photometric variability with Lomb-Scargle [Lomb, 1976; Scargle, 1982] and boxed-least-squares periodograms but found no variation on the orbital period. For an eclipse to be witnessed in this system, the inclination would have to be above 89.64 deg and photometric variability from ellipsoidal modulation or irradiation is minute for a system with 14.24 hr orbital period. The Doppler beaming effect of the two stars is nullified by their opposing motion of near-identical RV amplitudes and a similar flux contribution [Hermes et al., 2014], hence non-eclipsing forms of variability are not expected.

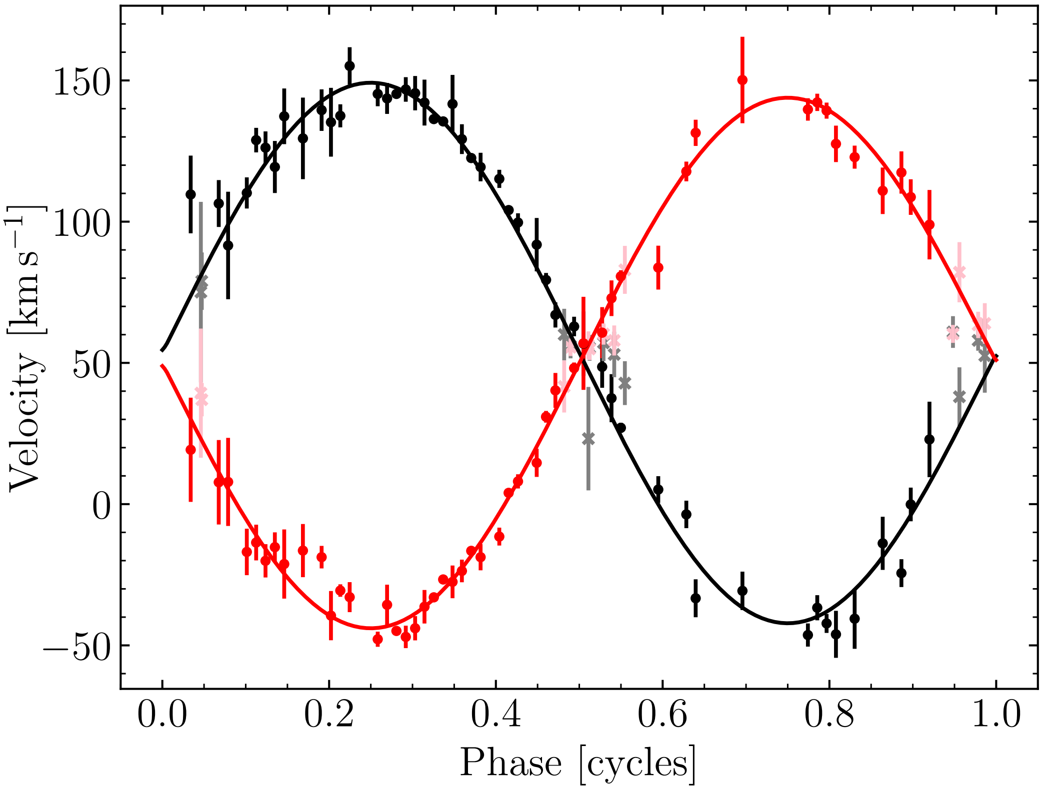

Figure 6.3: Left: The best-fit orbital solution phase-folded on the orbital period. In black points, the hotter star, and in red the cooler star. The RV curves are plotted showing the velocity of the two stars across a full orbit, binned into 80 evenly spaced phase bins. In faded colours and with crossed markers are the RVs that were masked in searching for an orbital solution (see Section 6.4.3 for details).

6.5 Merger time and population rate

The critical time at which the merger will occur is calculable using equation 1.8 and, for WDJ181058.67+311940.94, the present day semi-major axis is $a_0 = 0.01601 \pm 0.00015$ AU. This indicates that the type Ia supernova will occur in 22.6 ± 1.0 Gyr, while the less-massive component will begin Roche lobe overflow and initiate mass transfer approximately 100 yrs before the demise of binary.

We can use WDJ181058.67+311940.94 to observationally predict the number of super-Chandrasekhar mass DWDs in the Milky Way. If we assume that WDJ181058.67+311940.94 and NLTT 12758 are the only two within 49 pc and make the rudimentary assumption that DWDs are evenly scattered around the Milky Way, a cylindrical disk with radius $\mathrm{R_{max}} = 15$ kpc and scale height $\mathrm{h}_z = 300$ pc indicates approximately 861 000 systems in the Galaxy. Holberg et al. [2016] estimate a present WD birth rate of $\approx 1.4 \times 10^{-12}\,\mathrm{pc^{-3}\,yr^{-1}}$, there are 1076 WDs within the volume complete 40 pc sample [O'Brien et al., 2024] and extrapolated to 49 pc we would have 1978 WDs. This means that the birth rate of super-Chandrasekhar mass DWDs in the Galaxy becomes greater than approximately $6.0 \times 10^{-4}\,\mathrm{yr^{-1}}$.

Moreover, we can also calculate an observed rate of type Ia supernovae arising from super-Chandrasekhar mass double white dwarfs using WDJ181058.67+311940.94 ($T_c = 22.6 \pm 1.0$ Gyr) and NLTT 12758 ($T_c = 139 \pm 9$ Gyr). The frequency of the two events combined imply a supernova rate of about once every 19 Gyr within 49 pc, or $(4.37 \pm 0.17) \times 10^{-16}\,\mathrm{yr^{-1}\,pc^{-3}}$. When fully extrapolated with the cylindrical disk approximation, the observed rate of type Ia supernovae from super-Chandrasekhar mass double white dwarfs in the Milky Way hence becomes at least $(1.85 \pm 0.07) \times 10^{-4}\,\mathrm{yr^{-1}}$, though the quoted uncertainty does not account for uncertainties on the Galactic model. This result serves as a minimum based on the 49 pc population as it remains possible that other systems exists within the same radius.

Evidently, the magnitude of super-Chandrasekhar mass systems approaches the $(2.8 \pm 0.6) \times 10^{-3}\,\mathrm{yr^{-1}}$ rate predicted for all evolutionary channels leading to a type Ia [Li et al., 2011; Maoz et al., 2014; Liu et al., 2023], but we must recall that these two systems are set to come together in over a Hubble time and consider that the present observed supernova rate from these systems is about ten times smaller. Contribution to the double white dwarf type Ia rate from sub-Chandrasekhar mass limits detonation could at least be a partial solution to make up for the deficit, where a mass-period distribution of DWDs in a volume/magnitude limited sample serves as a means to put this to the test [Munday et al., 2024]. Ongoing efforts are crucial to properly quantify the number of massive DWD binaries in our local neighbourhood and the Milky Way, while deeper, volume-complete spectroscopic samples of WDs in all locations of the Hertzsprung-Russell diagram will become possible in the next decades through multi-object spectrograph surveys.

6.6 Modelling the fate of the binary system

To understand the fate of the binary system, author #2 simulated its interaction when just about to merge. They used the moving-mesh code AREPO [Springel, 2010; Pakmor et al., 2016; Weinberger et al., 2020] in a similar setup as in Pakmor et al. [2022]; Glanz et al. [2024]. Here we summarise the setup and simulation with an emphasis on improvements compared to Pakmor et al. [2022]. A detailed description and analysis will be presented as part of a large parameter study of WDs mergers in the near future, of which the simulation shown here is the forerunner.

Author #7 first created two white dwarfs from the pre-main sequence phase using the stellar evolution code MESA [Paxton et al., 2011, 2013, 2015, 2018, 2019; Jermyn et al., 2023], evolving them to carbon-oxygen white dwarfs of $0.87\,\mathrm{M}_\odot$ and $0.71\,\mathrm{M}_\odot$. These masses align with observations from VLT/UVES spectra fitting. Compared to previous merger simulations, using self-consistent models evolved in MESA allows us to start from realistic composition profiles. In particular, the two WDs have a helium shell of $8 \times 10^{-3}\,\mathrm{M}_\odot$ (for the $0.71\,\mathrm{M}_\odot$ WD) and $3 \times 10^{-3}\,\mathrm{M}_\odot$ (for the $0.87\,\mathrm{M}_\odot$ WD), respectively.

Author #2 then created two 3D WDs in hydrostatic equilibrium with the same masses and abundance profiles in AREPO. They resolved the WDs with cells with a roughly constant mass of $10^{-7}\,\mathrm{M}_\odot$ and used a passive scalar to resolve the helium shells of both WDs even better with a mass resolution of $10^{-8}\,\mathrm{M}_\odot$. They relaxed both WDs in isolation for 10 dynamical timescales, actively dampening any gas velocities for the first half of this time. The density and composition profiles of the relaxed WDs, in particular close to the surface, well resemble the initial 1D profiles obtained from MESA.

They put both WDs into a binary system in co-rotation with an initial period of $73\,\mathrm{s}$. At this period the separation is about 1.5 times larger than the separation where the secondary WD will fill its Roche-lobe. They applied an accelerated inspiral term that removes angular momentum in the same way as gravitational waves, but on a much faster timescale. This way we obtain a binary system in equilibrium when mass transfer starts on a scale that we can resolve in the simulation. At this time, the physical system will have transferred mass at a low rate for possibly thousands of years, but the total mass transferred is likely negligible. The secondary WD eventually starts filling and then overfilling its Roche-lobe, and they stopped the accelerated inspiral when the density at the inner Lagrange point between the WDs reaches $2 \times 10^4\,\mathrm{g\,cm^{-3}}$. Only then the density in the accretion stream becomes large enough to dynamically affect the surface of the primary WD [Guillochon et al., 2010; Pakmor et al., 2013, 2022].

The binary system has now shrunk to a separation of $0.03\,\mathrm{R}_\odot$ and an orbital period of $39\,\mathrm{s}$. Author #2 then continued to evolve the binary system conservatively and switch on a live nuclear reaction network with 55 isotopes [Pakmor et al., 2012a, 2022]. I show an overview of the dynamic evolution of the binary system in Fig. 6.4. After evolving the binary system conservatively for $55\,\mathrm{s}$ the interaction of the accretion stream with the surface of the primary WD ignites a helium detonation close to the point of interaction (second column of Fig. 6.4), consistent with previous simulations of more massive WD binaries [Pakmor et al., 2013, 2021, 2024]. As in the classic double detonation scenario where the helium detonation is caused by instabilities in a massive helium shell [Livne, 1990; Fink et al., 2010], the helium detonation wraps around the primary WD. It sends a shock wave into the core of the WD, that converges in a single point at a density of $9.6 \times 10^6\,\mathrm{g\,cm^{-3}}$. Because of a lack of numerical resolution, the simulation does not self-consistently ignite a carbon detonation there, but resolved ignition simulations indicate that at this density we expect a detonation to form at the convergence point [Seitenzahl et al., 2009; Shen and Bildsten, 2014]. To model the ignition of the detonation when the shock converges in the simulation, they set the temperature of 178 cells that contain $1.8 \times 10^{-5}\,M_\odot$ around the convergence point to $5 \times 10^9\,\mathrm{K}$. This injects $4.8 \times 10^{46}\,\mathrm{erg}$ (negligible compared to the energy release of the whole simulation) and ignites the detonation. The detonation completely destroys the primary WD. When the shock wave of its explosion hits the secondary WD, the double detonation mechanism repeats itself. The shock wave ignites a helium detonation that drives a shock wave into the core and converges at a density of $8.5 \times 10^6\,\mathrm{g\,cm^{-3}}$. In this case carbon burning even starts at the convergence point, but not strongly enough to start a detonation. They again ignited a detonation at the convergence point by setting the temperature of 708 cells that contain $6.9 \times 10^{-5}\,M_\odot$ to $6 \times 10^9\,\mathrm{K}$, which injects $8.2 \times 10^{47}\,\mathrm{erg}$ and is sufficient to ignite the detonation that then destroys the secondary WD as well.

There is no bound remnant and the ejecta of the explosion contain the full $1.58\,\mathrm{M}_\odot$ of the initial binary system, having a total explosion energy of $1.2 \times 10^{51}\,\mathrm{erg}$. The core of the secondary WD ignites $4.2\,\mathrm{s}$ after the core of the primary WD. At this time the ashes of the primary WD have already expanded far beyond the secondary WD. So when the latter explodes as well, its ejecta expand into and remain in the centre of the ejecta of the primary WD [Pakmor et al., 2022]. I show the structure and composition of the ejecta in Fig. 6.5. The outermost layers of ejecta are the ashes of the helium detonation of the primary WD. They consist mostly of intermediate mass elements, dominated by silicon, sulphur, and argon. Below them sit the ashes of the carbon-oxygen core of the primary WD. They again consist mostly of intermediate mass elements, but also contain $0.13\,\mathrm{M}_\odot$ of iron group elements, in particular $0.10\,\mathrm{M}_\odot$ of radioactive ^{56}Ni that will power the lightcurve. The centre of the ejecta consists of the ashes of the secondary WD, which contain $0.25\,\mathrm{M}_\odot$ of oxygen, $0.4\,\mathrm{M}_\odot$ of intermediate mass elements, and only $0.01\,\mathrm{M}_\odot$ of iron group elements with a roughly equal fraction of ^{56}Ni and ^{54}Fe.

Author #2 obtained preliminary synthetic light curves from spherically averaging the ejecta and computing light curves with the Monte-Carlo radiation transport code ARTIS [Kromer and Sim, 2009; Sim, 2007]. The resulting supernova has a maximum brightness in the B-band of $M_\mathrm{B} = -16.4$ ($m_B = -14.7$) and a maximum brightness in the V-band of $M_\mathrm{V} = -17.8$ ($m_V = -16.1$), consistent with traditional double detonation models of single WDs with a similar mass as the primary WD, because the secondary WD does not produce any significant amount of radioactive ^{56}Ni [Sim et al., 2010; Shen et al., 2021; Collins et al., 2022]. That said, the explosion likely avoids the imprint of thick helium shells on light curves and spectra [Kromer et al., 2010; Collins et al., 2022, 2023]. It will most likely appear as a sub-luminous type Ia supernova. However, the obvious large-scale asymmetries visible in Fig. 6.5 indicate that 3D synthetic observables will be needed to make any reliable statement about the expected display of this supernova [Collins et al., 2022; Pakmor et al., 2024]. They will be presented and discussed as part of a larger sample of merger simulations in the future. This new simulation also supports previous work which suggests that both stars will explode in massive DWD binaries that are about to merge [Pakmor et al., 2022; Boos et al., 2024; Shen et al., 2024].

6.7 Conclusions

I have presented the first confirmed to be compact, super-Chandrasekhar mass DWD binary which will merge in close to a Hubble time (23 Gyr), having an orbital period of 14.24 hr. With a total mass of $1.555 \pm 0.044\,\mathrm{M}_\odot$, WDJ181058.67+311940.94 is the most massive DWD binary confirmed to date, followed by one other super-Chandrasekhar mass DWD having a merger time of approximately 137 Gyr [Kawka et al., 2017]. I predict it to explode as a quadruple detonation and be destroyed completely. With all the mass ejected and a total explosion energy of 1.2×10^{51} erg, but only $0.1\,\mathrm{M}_\odot$ of ^{56}Ni in the ejecta, it will appear as a subluminous type Ia supernova with a peak apparent magnitude of approximately $m_B = -14.7$ and $m_V = -16.1$.

The lack of observational evidence of compact and massive DWD binaries has long troubled the theory that DWDs are the dominating evolutionary channel of type Ia detonations [Maoz and Mannucci, 2012]. WDJ181058.67+311940.94 provides tentative observational evidence that such systems with short merger times do exist in the Milky Way, and when combined with the close proximity of 49 pc the rate of super-Chandrasekhar mass DWDs born in the Milky Way is at least $6.0 \times 10^{-4}\,\mathrm{yr}^{-1}$. This draws closer the disparity

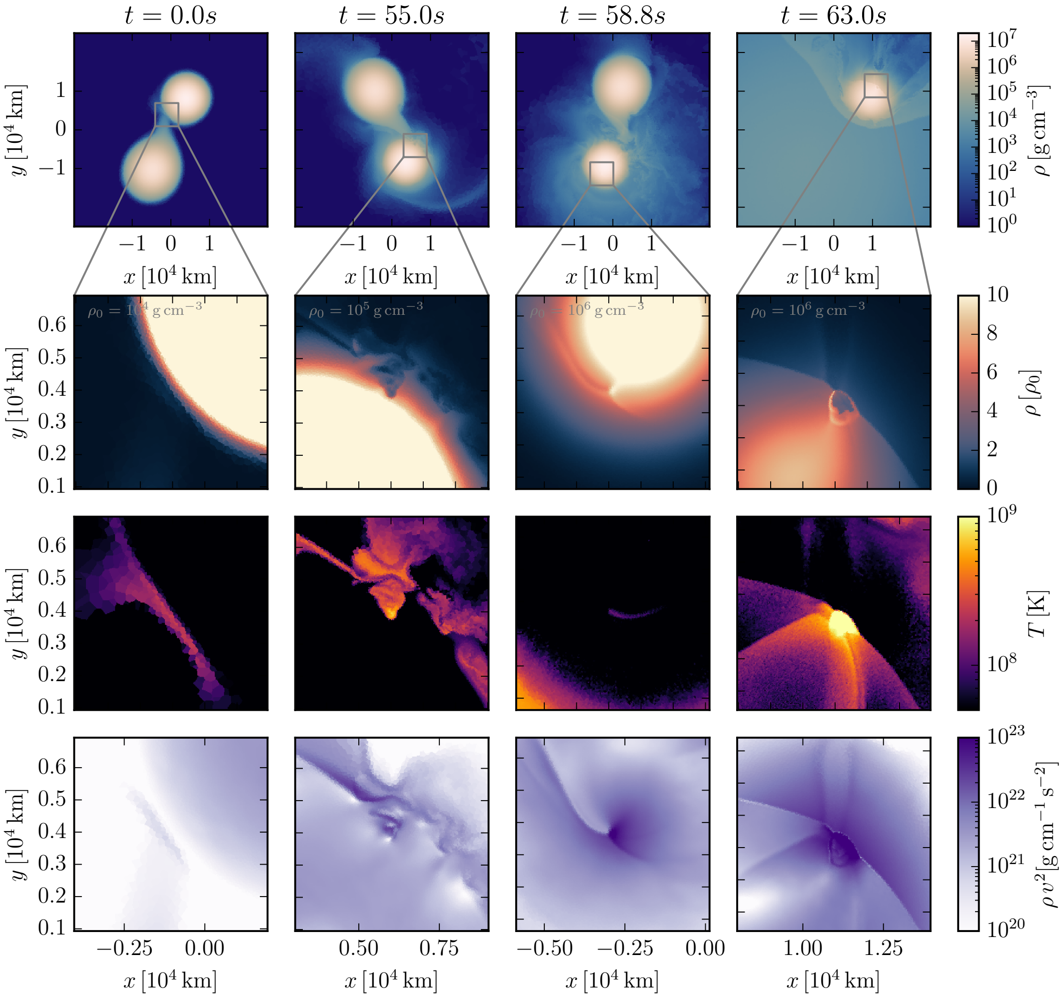

Figure 6.4: Time evolution in slices of the binary systems close to merger. The first column shows the time when we stop the accelerated inspiral and continue to evolve the binary system self-consistently. The second and third columns show the time when the helium detonation ignites on the surface of the primary WD, and the time when the shock wave that is driven into the core of the primary by the helium detonation converges in a single point. The fourth column shows the same shock convergence in the core of the secondary WD. The top row shows slices of density in the plane of rotation and the three below are zoomed insets at the point of interest. From top to bottom: density, temperature, and kinetic energy density. The qualitative evolution is very similar to the more massive binary system discussed in Pakmor et al. [2022]. The shock convergence points in both WDs occur at densities high enough to very likely ignite a carbon detonation and destroy the WD.

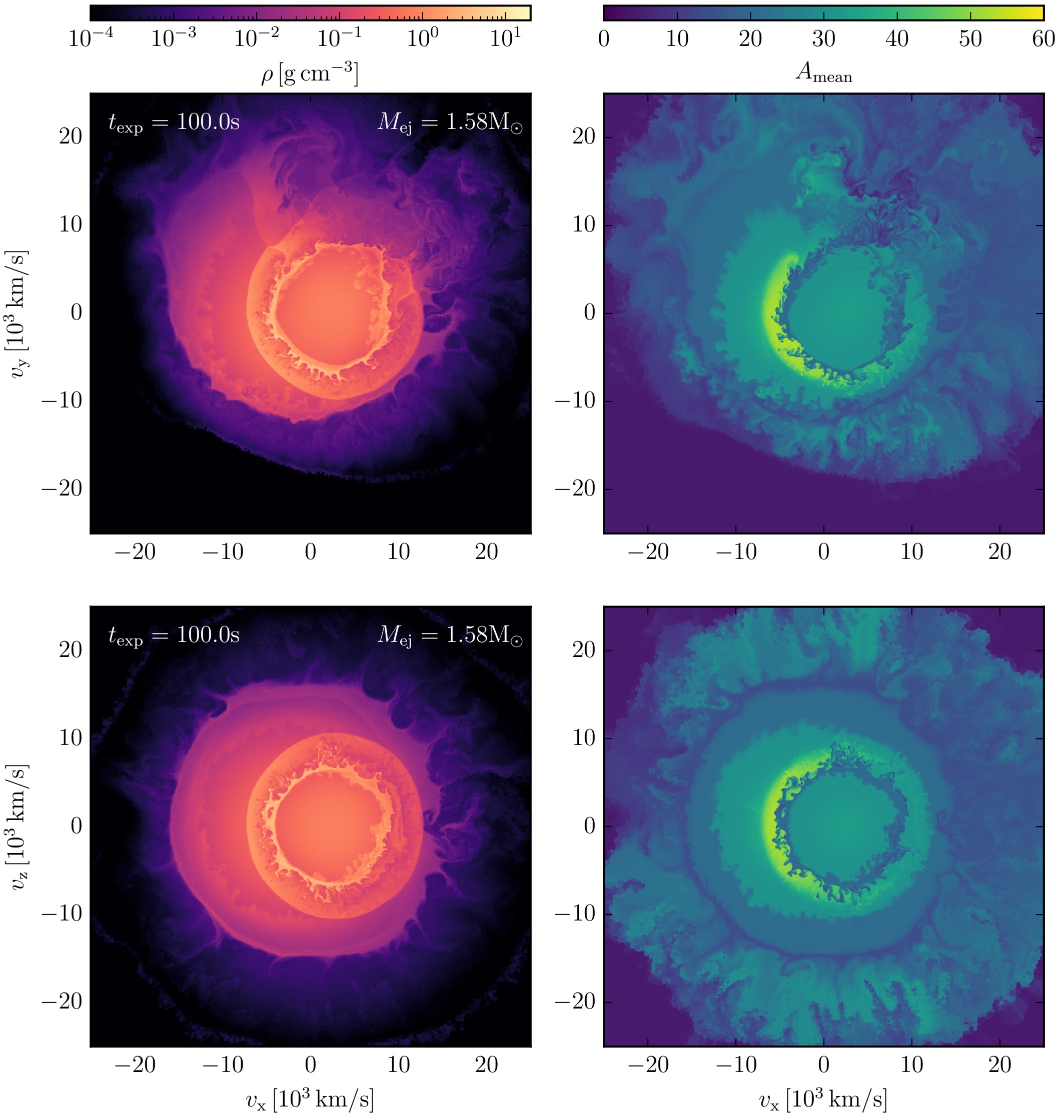

Figure 6.5: Slices of density (left column) and mean atomic weight (right column) of the supernova ejecta in homologous expansion 100 s after ignition of the first helium detonation. The top row shows slices in the original plane of rotation, the bottom row slices perpendicular to it. The outer layers are close to spherically symmetric, though significant deviations from spherical symmetry exist in the plane of rotation. The iron group elements (including ^{56}Ni) are essentially all produced in the explosion of the primary WD and form a half-sphere around the ejecta of the secondary WD.

between the observed and theoretical rates, though the observed is still approximately twice smaller.

Being discovered through a medium-resolution search of overluminous DWDs [Munday et al., 2024], which up to a magnitude limit of $G < 17$ is approximately 20% complete, it is entirely plausible that more super-Chandrasekhar mass DWDs reside in our Galactic neighbourhood and that we have the spectroscopic ability to resolve the formation channel of type Ia supernovae. Deeper completeness through photometric and spectroscopic surveys in the coming years, as well the inauguration of space-based gravitational wave detectors in the next decade, will be pivotal in detecting ultra-compact binaries on the cusp of detonation [Korol et al., 2017, 2024]. The combined efforts surveying type Ia progenitors across the full range of orbital periods will be the ultimate means to accurately quantify the contribution of double white dwarfs to type Ia supernovae.

6.8 Radial velocity measurements

Table 6.3: A table of all observed RVs (without relativistic correction) and the mid-exposure time-stamps. Wavelength calibration errors were propagated.

HJD−2450000 UTC	RV$_1$ [km s^{-1}]	ΔRV$_1$ [km s^{-1}]	RV$_2$ [km s^{-1}]	ΔRV$_2$ [km s^{-1}]	Source
8588.734699	−43.83	10.22	128.60	10.26	ISIS
8588.739403	−48.34	13.12	126.60	7.82	ISIS
8591.687642	−47.74	4.63	137.97	3.93	ISIS
8591.698183	−42.98	5.32	139.73	4.46	ISIS
8591.745818	−24.42	4.93	117.45	7.48	ISIS
8591.752887	−13.34	3.91	113.95	4.84	ISIS
8645.660736	−46.33	4.10	139.79	3.97	ISIS
8645.670120	−41.48	4.08	139.02	3.52	ISIS
8731.364001	149.73	9.28	−27.17	13.79	IDS
8732.411857	95.08	11.14	23.01	11.46	IDS
8732.432828	112.69	14.73	13.43	19.28	IDS
8732.460152	146.81	5.43	−24.69	8.03	IDS
8732.481127	137.36	9.86	−21.20	12.24	IDS
8732.506595	139.55	7.35	−18.77	3.99	IDS
8733.496923	−13.87	9.40	110.97	8.23	IDS
8733.517893	13.12	11.25	103.55	11.63	IDS
8734.382747	136.13	10.99	1.58	10.44	IDS
8751.390254	124.27	25.16	15.48	35.06	IDS
8751.400810	75.08	31.95	39.30	22.87	IDS
8751.411366	111.57	19.70	24.70	35.63	IDS
8751.421919	103.05	36.85	13.66	29.44	IDS
10385.714514	121.92	11.34	−48.04	5.86	FIES
10389.693347	95.12	3.91	−14.90	19.24	FIES
10389.711256	100.95	8.79	−19.22	14.96	FIES
10401.639249	137.53	4.08	−30.59	2.21	FIES
10401.675067	137.67	5.83	−44.11	3.54	FIES
10401.692976	149.54	12.12	−50.05	8.55	FIES
10402.602016	−40.56	10.65	122.89	4.08	FIES
10403.596407	23.18	18.31	56.32	4.86	FIES
10405.726945	119.48	6.67	−14.62	6.83	FIES
10412.657048	−25.61	7.60	146.64	4.69	FIES
10416.579027	123.96	6.33	−18.52	6.26	FIES
10426.543453	135.26	12.18	−39.47	8.71	IDS
10426.561527	155.21	6.64	−32.92	5.31	IDS
10426.579516	147.89	8.65	−51.49	5.29	IDS
10426.597579	150.34	8.63	−53.96	7.91	IDS
10426.615569	142.23	8.13	−36.32	5.93	IDS
10426.633728	141.73	10.30	−27.52	5.79	IDS
10426.651797	121.16	10.04	−22.66	9.27	IDS
10426.675840	104.72	6.37	3.20	4.94	IDS
10426.693911	99.42	18.86	10.39	9.92	IDS

continued...

HJD−2450000 UTC	RV_1 [km s^{-1}]	ΔRV_1 [km s^{-1}]	RV_2 [km s^{-1}]	ΔRV_2 [km s^{-1}]	Source
10426.711986	60.03	9.14	41.66	9.22	IDS
10426.730069	55.33	4.57	54.96	3.95	IDS
10427.568303	22.90	13.36	98.97	12.29	IDS
10427.586293	38.01	10.43	82.12	10.65	IDS
10427.604333	52.56	13.10	63.98	7.18	IDS
10427.640501	78.96	10.17	37.00	5.90	IDS
10427.658595	80.16	9.54	2.07	10.28	IDS
10427.677213	111.05	6.78	−2.50	9.76	IDS
10427.695279	119.40	9.22	−15.23	5.24	IDS
10427.713363	129.54	14.44	−16.45	9.41	IDS
10435.613760	56.04	4.41	55.55	3.10	FIES
10451.692321	5.16	4.73	83.75	7.77	FIES
10451.710229	−3.64	4.86	117.82	3.49	FIES
10462.684526	126.24	5.78	−20.07	5.89	ALFOSC
10463.515200	57.13	6.48	60.23	3.75	ALFOSC
10463.522815	53.00	8.06	57.95	5.32	ALFOSC
10463.530392	42.85	7.76	82.97	8.49	ALFOSC
10463.613866	−30.69	6.79	150.23	15.31	ALFOSC
10471.660727	142.69	1.09	−44.14	0.80	UVES
10471.669856	145.29	0.81	−44.88	0.94	UVES
10471.678957	143.42	1.04	−40.03	0.71	UVES
10471.688045	141.58	1.02	−37.81	0.75	UVES
10471.697140	136.39	1.12	−32.99	0.98	UVES
10471.706232	135.55	0.93	−26.67	0.93	UVES
10471.715322	129.76	1.02	−24.49	0.93	UVES
10471.724414	122.58	1.17	−16.54	0.89	UVES
10471.733505	117.61	1.09	−14.89	0.85	UVES
10471.742600	106.43	1.07	−4.46	0.97	UVES
10471.751691	104.14	1.27	3.99	0.94	UVES
10471.760789	94.76	1.39	12.92	0.94	UVES
10471.769880	84.35	1.31	18.86	0.92	UVES
10471.778969	79.40	2.45	30.92	2.07	UVES
10471.788065	67.00	4.46	40.27	6.17	UVES
10471.797156	62.90	3.46	48.17	1.98	UVES
10471.806251	56.81	11.41	56.94	16.47	UVES
10471.815355	48.61	7.41	60.71	9.05	UVES
10471.824448	37.51	8.51	72.91	6.31	UVES
10471.833536	27.02	1.78	80.67	2.15	UVES
10525.451278	60.95	5.62	60.27	3.17	FIES
10525.469185	57.98	3.66	63.47	4.66	FIES
10545.435565	−33.32	6.71	131.51	4.64	FIES

Chapter 7

The DBL Survey II: towards a mass-period distribution of double white dwarf binaries

James Munday, Ingrid Pelisoli, Pier-Emmanuel Tremblay, David Jones, Gijs Nelemans, Mukremin Kilic, Tim Cunningham, Silvia Toonen, Alejandro Santos-García, Harry Dawson, Viktoria Pinter, Benjamin Godson, Llanos Martinez, Jaya Chand, Ross Dobson, Kiran Jhass, Shravya Shenoy

Contribution of co-authors

Observations used in this study were obtained by authors #4, #6, #7, #9, #10, #11, #12, #13, #14, #15, #16, #17. All authors contributed with comments on the manuscript during the submission/revision process by supplying key ideas to explore in creating the final version of the study. All other components and the leading of the study were performed by me, with help and guidance from authors #2, #3, #4 and #5.

Abstract

Double white dwarf binaries are an important remnant of binary evolution as they are possible type Ia supernova progenitors and strong sources of gravitational waves in the low-frequency regime. The double-lined double white dwarf (DBL) survey searches for compact double white dwarfs where both stars are spectrally disentangleable. Candidates are identified by being overluminous compared to the cooling sequence of a typical mass, single white dwarf. In this second DBL survey instalment, we present full orbital solutions of 15 double white dwarf binaries from our ongoing campaign to accurately measure a magnitude-limited mass-period distribution. 12 of these systems are fully solved for the first time. A long-standing bias in the full population has been evident, favouring systems with orbital periods up to a few hours, with little exploration of the majority of the compact double white dwarf population, whose orbital period distribution centres at approximately 20 hr. The 15 systems in this study span the orbital period range $5 < P_{\mathrm{orb}} < 75\,$hr, significantly augmenting the number of well-characterised systems over these periods, and in general have two similar mass stars combining to $\approx 1.0\,\mathrm{M}_{\odot}$. We witness that the orbitally derived mass ratios generally show an excellent agreement with those deduced from atmospheric fits to double-lined spectra in previous work, emphasising the power of wide-scale spectroscopic surveys to efficiently locate the highest mass, double-lined double white dwarfs in the local Galaxy.

7.1 Motivation and introduction

The double-lined double white dwarf (DBL) survey was introduced in Munday et al. [2024] and a crucial aspect of the survey is to handle observational biases in the compact DWD population by characterising a magnitude-limited sample with well-defined and understood selection criteria. Without such a deliberate effort, biases are tricky to handle, hampering the accuracy of comparisons to synthetic population models and proving difficult to draw conclusions of the full population of DWDs. As part of this survey, identification spectra were obtained and atmospheric parameters fitted to all observed star systems, resulting in at least 73% of the 117 targets being DWD binaries of any kind. Specifically, the focus of the DBL survey is double-lined DWDs, being where a spectral signature from both stars is evident, for which at least a 29% success rate of a source being double lined was retained. An unveiled class of massive total mass DWD binaries was recovered which was poorly populated before, including multiple near- or super-Chandrasekhar total mass DWDs [Munday et al., 2024, 2025]. When brought into contact, the fate of the majority of detected systems is to initiate unstable mass transfer, resulting in the merger or pre-merger explosion of sources. The detection of double-lined sources is sensitive to mass ratios of $0.5 \lessapprox q \lessapprox 2$, with limits due to the fact that the dimmer star must contribute more than approximately 25% of the flux to be spectroscopically disentaglable.

Identification spectra of a large number of DWD candidates was the objective of this piloting work. What remained was phase-resolved spectroscopy of the systems to obtain the orbital periods and hence the underlying period distribution of the double-lined DWD binaries in the sample. Many of which I now present in this study. The follow-up observations that have been undertaken are supplied in Section 7.2, my fitting methods in extracting RVs and orbital solutions in Section 7.3, and in Section 7.4 the results of my work.

7.2 Observations

The purpose of the observations was to obtain phase-resolved spectra of the double-lined DA+DA DWDs discovered in Munday et al. [2024], where Balmer absorption lines of each star are spectrally disentanglable. As the orbital periods were largely unconstrained, having only the knowledge of a maximum orbital period, our observing strategy was to first obtain two series of 3 or 4 consecutive spectra with a gap of a couple of hours between them. Then, a third and fourth series of spectra would be taken in two of the following three nights to improve sensitivity to wider orbits. Together, this meant that I had a starting point of 12 to 15 spectra per target to resolve the orbital period. For systems where viable aliases were obtained in this time but the exact period alias was unclear, I obtained further observations at a later time with a targetted and dynamic strategy. For example, if strong period aliases appear at 10 hr and 20 hr, I would attempt to obtain spectra of the target with a gap of 5 hr. Stronger evidence of the true orbital period would then be ascertained due to the different orbital phase coverages.

Time-series spectra were obtained across 22 nights using the Intermediate Dispersion Spectrograph (IDS) on the 2.5 m Isaac Newton Telescope (INT). I used the R1200R grating centred on Hα with a $1.0''$ slit, covering the wavelength range of 6 000–7 130 Å with a spectral resolution of $R = 6310$ at the centre of Hα. Observations were carried out over the nights 27 August 2019 – 7 September 2019, 23 & 24 September 2019, 7 June 2020 – 14 June 2020. An arc frame was taken after acquisition of each targets. For an extended duration on target, arcs were taken every 45 min to correct for flexure. Later, after analysing the majority of these data, I obtained 9 nights on the INT from 25 April to 03 May 2024 to resolve the orbits of a few more systems and improve the solution of certain systems that had multiple viable period aliases. The first 4 nights utilised the H1800V grating with a $1.4''$ slit width (with a DIMM seeing of about $1.0''$), giving a spectral resolution of $R = 9400$, and the other 5 with the same R1200R grating setup mentioned before. Additional spectra were obtained with the INT across various nights in the years 2023 and 2024 using the R1200B grating, providing a spectral resolution of about $R = 4700$ at Hβ. These were reduced with the same method as the R1200R setup.

Bias frames and tungsten lamp flats were taken at the beginning of each night and used in the data reduction. Spectrophotometric standard stars were also observed at the start or the end of each night to flux calibrate the science exposures and correct for the instrumental response function. When multiple arc frames were taken of a target, the solution to the arcs was interpolated for the mid-exposure time of the science frame for wavelength calibration. All data were reduced using the MOLLY package [Marsh, 2019] and spectra were extracted using the method outlined in Marsh [1989]. Lastly, I utilise the spectra obtained from the William Herschel Telescope (WHT) of each target as was presented in Munday et al. [2024].

Once all of these data had been fully and thoroughly analysed, I decided to target orbital phases of three systems which were close to being solved using the Nordic Optical Telescope (NOT) across the nights 23–28 January 2025 and 21–25 May 2025. The employed instrument setup was ALFOSC with a g17 grating and a $0.75''$ slit width, giving wavelength coverage of Hα at a spectral resolution of $R = 7500$. An arc was taken before each exposure for wavelength calibration, and all data were reduced with the PYPEIT python package [Prochaska et al., 2020].

Finally, for the target WDJ231404.30+552814.11, nine spectra were taken with the Gemini Multi-Object Spectrograph (GMOS) on Gemini North as part of the queue program

GN-2022B-Q-103. Observations were taken over the period 3-8 August 2022 with the R831 grating and a $0.5''$ slit to give a spectral resolution of $R = 4396$. Each spectrum had an exposure time of 8 minutes. A CuAr lamp spectrum was taken after each exposure for wavelength calibration. The IRAF GMOS package was used by author #6 to reduce these data.

7.3 Methods

7.3.1 Synthetic spectra

To begin with, I used the atmospheric solution of both stars, derived in Munday et al. [2024], and maintained the solution fixed to create a synthetic spectrum of both stars. As a base model, I utilised the 3-dimensional (3D) non-local thermal equilibrium (NLTE) grid first introduced in Munday et al. [2024], which uses the 3D grids of Tremblay et al. [2013a, 2015] together with an NLTE correction that was presented in Kilic et al. [2021a]. The NLTE correction was shown to significantly improve the fit to higher resolution data at Hα.

The synthetic and observed spectra were normalised to facilitate the processing of ground-based flux-calibrated data. In general, when $\mathrm{T_{eff}} \approx 8\,000\,\mathrm{K}$, I chose to normalise Balmer lines using data between wavelengths that correspond to velocities of $\pm(4\,500 - 5\,000)\,\mathrm{km\,s^{-1}}$ for Hα, Hβ, Hγ and Hδ, and $\pm(2\,000 - 2\,500)\,\mathrm{km\,s^{-1}}$ for Hϵ and H8. In WDs cooler than 8 000 K, I halved the normalisation range to be $\approx \pm(2\,250 - 2\,500)\,\mathrm{km\,s^{-1}}$ and $\pm(1\,750 - 2\,000)\,\mathrm{km\,s^{-1}}$, for the respective groups of Balmer lines.

7.3.2 Improved atmospheric constraints on two systems

Since publishing the first DBL survey instalment, I obtained higher quality data of two systems presented in Munday et al. [2024]. The first is WDJ181058.67+311940.94, which at the time of writing has the largest total mass of any DWD binary ($1.555 \pm 0.044\,\mathrm{M_\odot}$) and a devoted investigation of the system was presented in Munday et al. [2025]. All data of WDJ181058.67+311940.94 obtained as part of the DBL follow-up were presented in that study, hence there is no change in the atmospheric or orbital solution system here. For completeness, the orbital parameters of the system are also presented in this study, as it is a member of the double-lined systems detected in the piloting campaign.

The second system with improved data quality is WDJ170120.99$-$191527.57. Early analysis of the RVs indicated an orbital period of a few hours, flagging the binary as one of particular interest due to the fast RV variability, hence the extra observation. Author #7 used the Magellan Echellette [MagE; Marshall et al., 2008] spectrograph on the 6.5 m Magellan Baade telescope at the Las Campanas Observatory to obtain two consecutive, 1200 s long, high signal-to-noise ratio (SNR) spectra at an orbital phase where the system was at quadrature. The observations were performed using the $0.85''$ slit, providing a wavelength coverage of 3700–9300Å at a resolving power of $R = 4800$. Three ThAr arc exposures were obtained immediately after our science exposures to generate an accurate wavelength solution. The spectroscopic data were reduced using `pypeit`. Author #7 also made use of the `merlin`[1] package which provides an end-to-end reduction pipeline based on `pypeit` v1.15.0 for MagE spectroscopic data. I hybrid fit these two spectra using an identical method to that presented in Munday et al. [2024] with the 3D-NLTE synthetic spectra grid and the spectral fit is supplied in Appendix 7.12. This indicates atmospheric parameters of $\mathrm{T}_1 = 19780 \pm 270\,\mathrm{K}$, $\log(\mathrm{g}_1) = 8.09 \pm 0.05\,\mathrm{dex}$, $\mathrm{T}_2 = 15490 \pm 260\,\mathrm{K}$, $\log(\mathrm{g}_2) = 7.87 \pm 0.05\,\mathrm{dex}$, which should be assumed in any continued analysis of the system. The quoted values include an external error of 1.4% for $\mathrm{T}_{\mathrm{eff}}$ and 0.042 dex for $\log g$ [Liebert et al., 2005] added in quadrature to the formal errors. The new star masses become $\mathrm{M}_1 = 0.673 \pm 0.024\,\mathrm{M}_{\odot}$ and $\mathrm{M}_2 = 0.544 \pm 0.022\,\mathrm{M}_{\odot}$, resulting in a slightly higher total mass ($1.217 \pm 0.032\,\mathrm{M}_{\odot}$) than previously reported.

7.3.3 Radial velocities

To determine radial velocities (RVs), I take the best-fit atmospheric solution and keep it fixed, convolve the model to the resolution of the observation, and perform a least-squares minimisation with the data in the range of ±20 Å of Hα. I chose to isolate this wavelength region so that the goodness of fit to the wings of Hα does not dominate, as the line core is the primary area of interest to fit RVs. Also, I fitted to Hα alone because of the much higher resolution in this spectral range for my observations and because the errors induced from imperfect wavelength calibration of data from the blue and red arms of ISIS exceed the benefits of its inclusion.

In a few cases (which are noted and commented on in Section 7.4), I found that the template spectrum used for RV extraction improves when I instead fit 2-Gaussian profiles to the line cores of each star (that is, two 2-Gaussian profiles, one pair for each star) at the centre of Hα, on top of a fourth-order polynomial to model the shape of the broad absorption line within 20 Å of its centre. This approach (or similar) has been frequently taken [e.g. Napiwotzki et al., 2002; Nelemans et al., 2005] as a 2-Gaussian model well approximates the shape of the centre of the Balmer absorption features, but the negative is that a fitted polynomial contains no physical information. I decided to employ this method for cases where the shape and depth of the synthetic line core profiles over- or under-fit the observed spectra across all instrumental setups. Doing so, I obtained a set of Gaussian parameters that

---

[1] https://github.com/vedantchandra/merlin/tree/main

are consistent to all spectra but smeared to the relevant spectral resolution[2]. A comparison of fits with synthetic spectra and the 2-Gaussian approach is plotted in Fig. 7.1.

Often, and in my INT data especially, when the site conditions worsened, the continuum SNR is relatively low (SNR < 20), leading to an imperfect spectrum normalisation. To optimise the normalisation, I minimised the residual between the data and the atmospheric fit within 20 Å of the centre of Hα. Data $\pm 5 - 20$ Å away from the centre of Hα was sigma-clipped with a threshold of 4σ; no data within 5Å of the centre was clipped. RVs and RV errors are reported from the median and standard deviation of 1000 bootstrapping iterations. To give an idea of the effect of this optimisation, I take the double-lined system WDJ114446.16+364151.13 that has spectra with a wide SNR range and a near-identical spectral signature for both stars at Hα. For a noisy spectrum that has SNR $= 15$ in the continuum and SNR $= 8$ at the line core centre, the RV errors with no optimising of the normalisation are $\pm 29.6\,\mathrm{km\,s^{-1}}$ and $\pm 20.1\,\mathrm{km\,s^{-1}}$, and with optimisation give errors of $\pm 22.6\,\mathrm{km\,s^{-1}}$ and $17.7\,\mathrm{km\,s^{-1}}$ for the two stars. Now, taking the same system but looking at data with SNR $= 40$ in the continuum and SNR $= 25$ at the line core centre, no optimising gives $\pm 4.8\,\mathrm{km\,s^{-1}}$ for both stars, while optimising gives $\pm 5.0\,\mathrm{km\,s^{-1}}$ for both stars. In the low SNR data case, the reported RV errors become appreciably better with optimisation, whereas the errors are nearly identical when the SNR is higher. Hence, applying this optimised normalisation method slightly improved the accuracy and precision of all RVs from low SNR data but made little difference to high SNR data. I furthermore note that the scatter in the residual of a sinusoidal fit to the RV curves (which is addressed in Section 7.3.4) decreased for an optimised normalisation, indicating an improved accuracy in the extracted RVs.

7.3.4 Orbital solutions

A couple of the candidate double-lined systems with time-series spectroscopy are indeed double-lined, but others turned out to be single-lined DWDs. In searching for single-lined RV variability, I invoked the same procedure as in Munday et al. [2024]. The mean of all extracted RVs for a source is taken and a null-hypothesis that the RV is a constant with respect to the mean is tested. I computed the χ^2 of all measurements compared to the mean and use the relevant χ^2-distribution for the number of degrees of freedom to calculate the probability that a source is not RV variable, setting a 4σ outlier threshold for variability, equivalent to a false positive probability of 0.62%.

---

[2] The reason for an imperfect atmospheric solution may lie with limitations in the input physics of synthetic grids, an inappropriately chosen mass-temperature-radius relation (carbon-oxygen core versus helium-core for WD masses ≈ 0.4–$0.6\,\mathrm{M_\odot}$), which would compromise the apparent-to-absolute-flux scaling factor when fitting photometric data, or a faint tertiary component contributing a small percentage of flux, all of which leading to a too deep/shallow synthetic line core signature

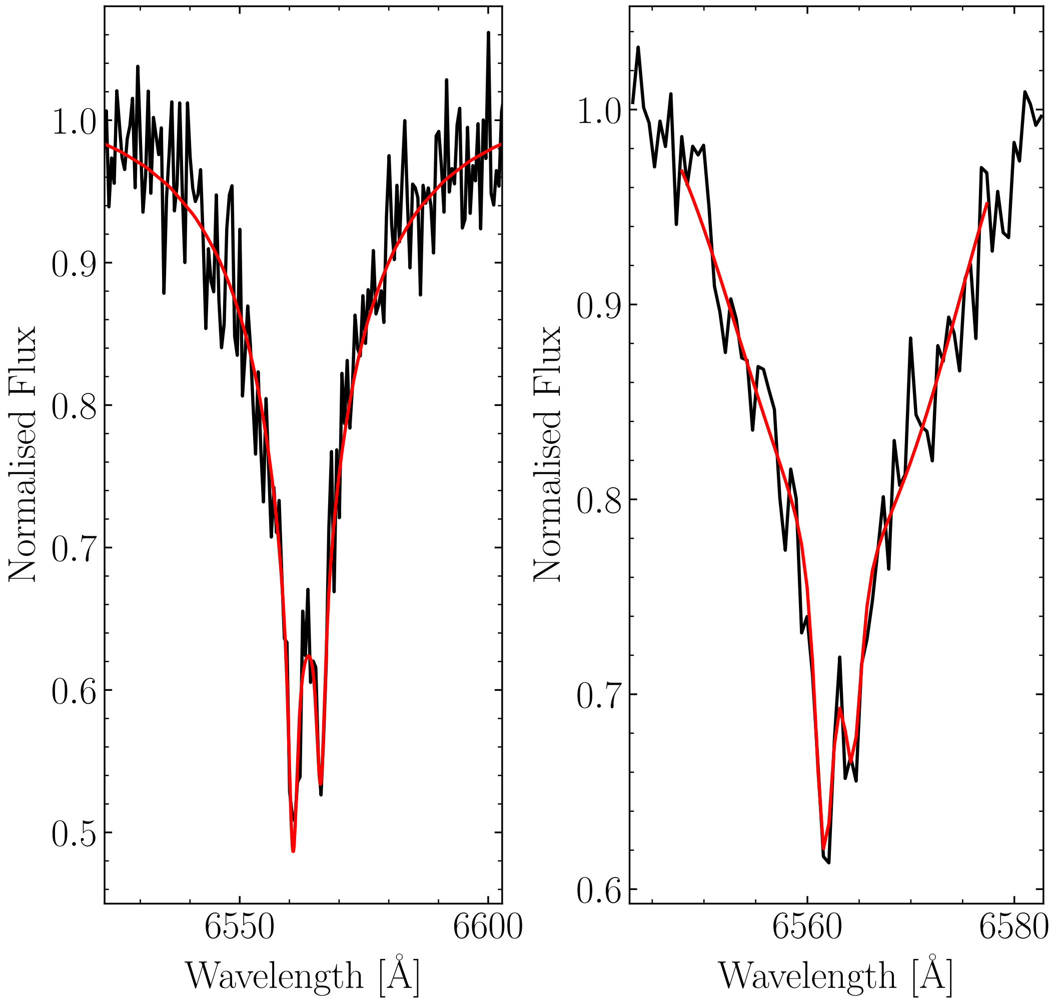

Figure 7.1: Example fits used to obtain RVs. The spectra are from the INT/IDS, reflecting the quality of the bulk of our data. *Left:* A best-fit synthetic spectrum of WDJ005413.14+415613.73 with our formerly presented solution. Both stars have a similar line-core signature and the statistical RV errors for the blueshifted and redshifted stars were 4.5 km s^{-1} and 6.1 km s^{-1}, respectively. *Right:* A case for WDJ163441.85+173634.09 where fitting with two 2-Gaussian components plus an underlying polynomial resulted in a better template to fit to the observations. The statistical RV errors of the blueshifted and redshifted stars were 4.6 km s^{-1} and 7.1 km s^{-1}, respectively. Generally, this approach slightly better fits the data but at the expense of losing spectral coverage, which becomes more important to utilise for lower ($\approx 10 - 15$ in continuum) signal-to-noise observations. The normalisation procedure in the two cases is different, as described in the text.

For all RV variable sources, double- or single-lined, I searched for a periodic signal when more than 5 spectra were taken. This was performed with a least-squares minimisation with trial orbital frequencies, f, spaced in a way that no more than 0.01 cycles are skipped over the full baseline of data. The χ^2 of each trial minimisation was analysed for a best-fit solution and the RVs (viewed at time T_{RV}) were modelled using equation 2.13 When analysing periodograms, I normalised the χ^2 of the best trial solution for each frequency to obtain a power spectrum following [Cumming, 2004]:

$$z_{\text{Kep}}(f) = \frac{N-5}{4}\frac{\chi_0^2 - \chi^2(f)}{\chi^2(f)} \tag{7.1}$$

with N the number of epochs, χ_0^2 the χ^2 with respect to the weighted mean of the RV measurements (whereas χ^2 is with the best Keplerian orbital fit). For double-lined fits, the RVs and weighted means from the two stars are handled separately and summed after. When the power z_{Kep} is maximised, the χ^2 is minimised.

I furthermore used physical insight of the system to limit the maximum constraint of $K_{1,2}$ for each trial frequency. From the binary mass function with the expectation that the stars are circularised, a minimum and maximum K_{max} can be inferred, using equation 2.15 with an inclination of 90° a maximum mass M_{max} on the numerator and the sum of a minimum mass M_{min} and M_{max} on the denominator. For a DWD system, a sub-Chandrasekhar mass limit $\text{M}_{\text{max}} = 1.4\,\text{M}_{\odot}$ and a minimum WD mass of $\text{M}_{\text{min}} \approx 0.15\,\text{M}_{\odot}$ [Istrate et al., 2016; Calcaferro et al., 2018] applies to put upper and lower limits on $K_{1,2}$, respectively. For single-lined WD binaries, the companion may be a neutron star with maximum mass of approximately $3.0\,\text{M}_{\odot}$ [e.g. Kalogera and Baym, 1996], hence M_{min}=$0.15\,\text{M}_{\odot}$ and M_{max}=$3.0\,\text{M}_{\odot}$ applies. Black hole companions to a WD are not expected in the sample due to their predicted much smaller number in the Galaxy [Nelemans et al., 2001b] and would only be applicable to systems that spectrally appear as a single WD (no excess flux). Additional restrictions can be applied to place limits on the orbital inclination, i, if photometric variability is or is not witnessed (Section 7.3.5), causing PK^3_{max} to alter. Similarly in this case, a constraint on PK^3_{min} could be applied.

I also limited the range of valid orbital solutions based on the details of the spectral fit using the gravitational redshifts and equation 2.18. with star radii predictable from mass-radius relationships. With this and the atmospheric solutions for each system, I decided to take the conservative approach of applying a flat prior on the relative gravitational redshift spanning 3σ from the median solution for both the masses and the radii of each star. The typical mass errors are $\pm 0.04\,\text{M}_{\odot}$ and, while I before assumed a thick hydrogen envelope consistent with single star evolutionary tracks to scale to an Eddington flux, the size of the hydrogen envelopes is largely unknown. With that in mind, 3σ errors on the interpolated radii were again appropriate to incorporate the uncertainty in the model fit. I note that this is an intentionally cautious approach and chosen as such in case of an incorrect atmospheric solution being found driven by a local minimum. The restriction on the difference of gravitational redshifts served to remove spurious periodogram solutions when finding a best-fit solution.

I calculated false alarm probabilities for each system to analyse the significance of each peak in the power spectrum. This was performed through a bootstrap approach by randomly shuffling the timestamps of observation, re-calculating Lomb-Scargle periodograms [Lomb, 1976; Scargle, 1982] over 50 iterations and taking quantiles of the full array of powers from these 50 iterations as the false alarm probability. I consider a trial period to be the true period of the system if there is a unique peak above a 4σ false alarm probability and 3σ for a peak to be considered an alias or the true period. Below those thresholds, the period is not completely solved but I assign limits on the maximum/orbital period based on the information currently extractable by taking the upper/lower boundaries where no period aliases fall above a 2σ false alarm probability. Here, further RV measurements would be required to fully solve the orbits. In cases where there are more than one peak above the 4σ or 3σ alarm probability, I inspected all individual peaks to look for a cause and assess if any of these solutions are suitable. When this happened, it often was an artifact of the wide time spacing between observations, but all cases where multiple are found above the threshold are commented in Section 7.4. An example periodogram for a solved system is found in Fig. 7.2.

7.3.5 Light curves

I analysed time-series archival photometry from the Transiting Exoplanet Survey Satellite [TESS, Ricker et al., 2015], Zwicky Transient Facility [Bellm et al., 2019], Catalina Real-time Transient Survey [Drake et al., 2009], *Gaia* [Gaia Collaboration et al., 2023] and Asteroid Terrestrial-impact Last Alert System [Tonry et al., 2018] to search for photometric variability amongst the full selection of DWDs[3]. The brightest of the sources saturate in some of these surveys and when they are saturating, time-series photometry is ignored. Sources in *Gaia* listed as variable have available photometric data for download as of data release 3 and in these cases the *Gaia* photometry is analysed. *TESS* light curves in the fast, short and long cadences are obtained when available from the MAST system and I extracted the photometry from *TESS* pixel frames when not available (typically for sources dimmer than 16th mag).

Finally, I note that *TESS* (all cadences) and *ZTF* (in filters g, r, i) photometry was inspected for all systems with solved periods by searching for variability within 2% of the

---

[3] https://github.com/JamesMunday98/AllSurveyPhotometry

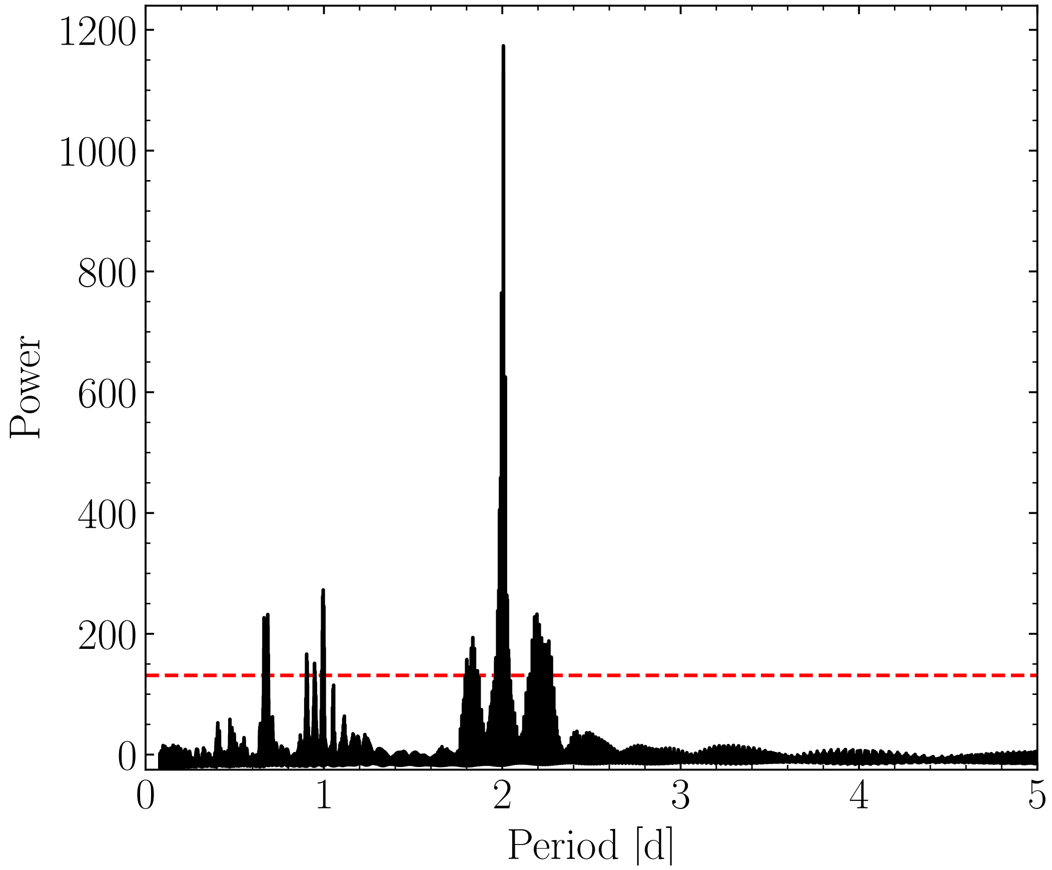

Figure 7.2: An example Lomb-Scargle periodogram showing that of WDJ020847.22+251409.97. The spacing between trial frequencies is chosen such that no more than 0.01 cycles are skipped across the full time baseline between adjacent solutions. The dashed red horizontal line shows the false alarm probability at a 4σ level. Multiple peaks lie above the 4σ level and are a consequence of the wide spacing of observation and certain aliases that better fit the RVs of just one of the stars. However, the non-highest peaks clearly show blocks of observations that lie off the sinusoidal trend upon visual inspection. This isolates the true orbital period of 2.008 d (48.1837 hr).

orbital period. The same was performed for all aliases of systems that have more than one above the false alarm probability, described in Section 7.4.2. In no case was a significant photometric signal observed for a 1-term Lomb-Scargle or a box least squares periodogram. Usage of a 1-term Lomb Scargle periodogram is most appropriate for identifying Doppler beaming, tidal deformation or irradiation, which will be the strongest orbitally-induced variability in all systems [Hermes et al., 2014], whereas a box least squares periodogram could reveal the unlikely event of eclipses, requiring an almost perfectly edge-on inclination for the typical DWD binary. Gravitational lensing is unlikely to occur or be detected [Marsh, 2001; Sajadian, 2025].

7.4 Results

I present here an overview of all systems that now have full atmospheric [Munday et al., 2024] and orbital solutions. This section speaks on newly presented results as well as ones obtained in prior work [4]. I particularly emphasise here that the full population of compact DWDs are expected to have a median period of about 20 hr, as found through synthetic binary population synthesis models [Nelemans et al., 2001c].

It should be noted that inter-night observations cause a decreased efficiency in solving orbital periods because of the consequent window function. For example, periods of 8 hr, 12 hr, 24 hr, 48 hr, etcetera, are more challenging to solve. Multiple day orbital periods are also more challenging to ascertain because our strategy of taking 3 consecutive spectra does not cover as large a range of orbital phase. The selection of systems from the 34 double-lined systems we found in Munday et al. [2024] is largely random, with the only restriction being the visibility for the scheduled telescope nights and the need for both stars to be separable at a spectral resolution of $R = 6310$. Lastly, there is sensitivity to the full range of orbital periods above 2 hr (with this minimum set because of orbital smearing across 30 min exposure times) and orbital periods are sampled up to 10 d.

7.4.1 Solved periods

The list of fully solved systems are as follows, with comments on the validity of the results when comparing the atmospheric and orbital solutions. The RV curves for each are plotted in Fig. 7.3 and Fig. 7.4. Merger times are mentioned when the orbital period is below 15 hr using Peters' equation [Peters, 1964] for a circular orbit. The double-lined systems here are

---

[4] In Munday et al. [2025], I noted that the RVs of spectra with spectral resolution $R < 10\,000$ were slightly inaccurate ($5 - 10\,\mathrm{km\,s^{-1}}$) when spectral lines perfectly overlap at the time of observation and were removed when solving for the orbital solution. Here however, I chose not to disregard any RVs that fall into this category since, with approximately 15–20 RVs per system, the information gained by including them in settling period aliases is far beneficial. One should consider their removal if more RVs are obtained in future work.

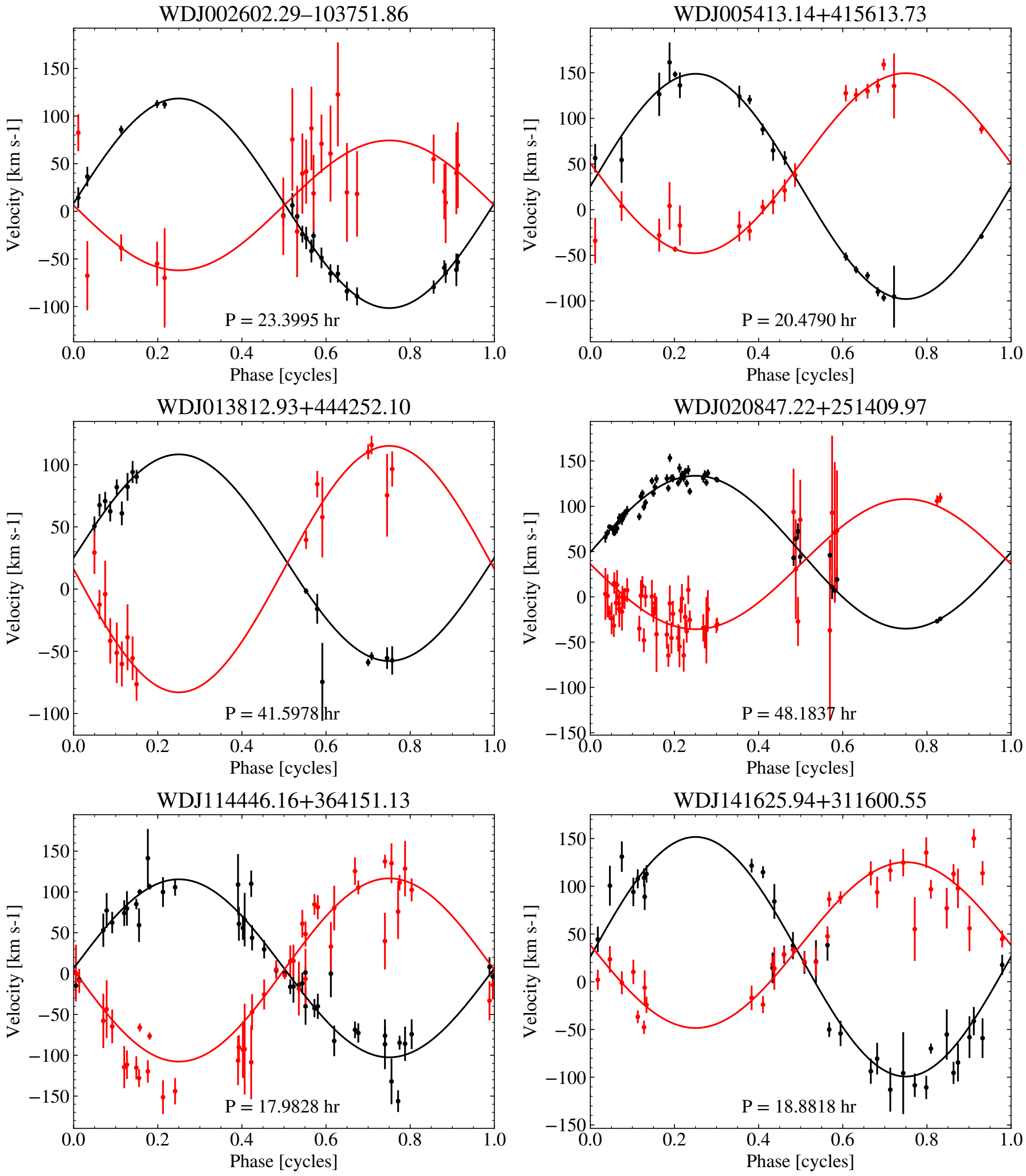

Figure 7.3: RV curves of all double-lined systems with orbital solutions presented in this study. The data points and the curves in black represent the hotter star and those in red are for the cooler star. The details of each solution is given and described in text. Titles above each plot show the system that each curve corresponds to, while the orbital period is mentioned at the bottom of each plot for convenience. The velocity for each point here has been corrected for relativistic effects and therefore is not an observed velocity.

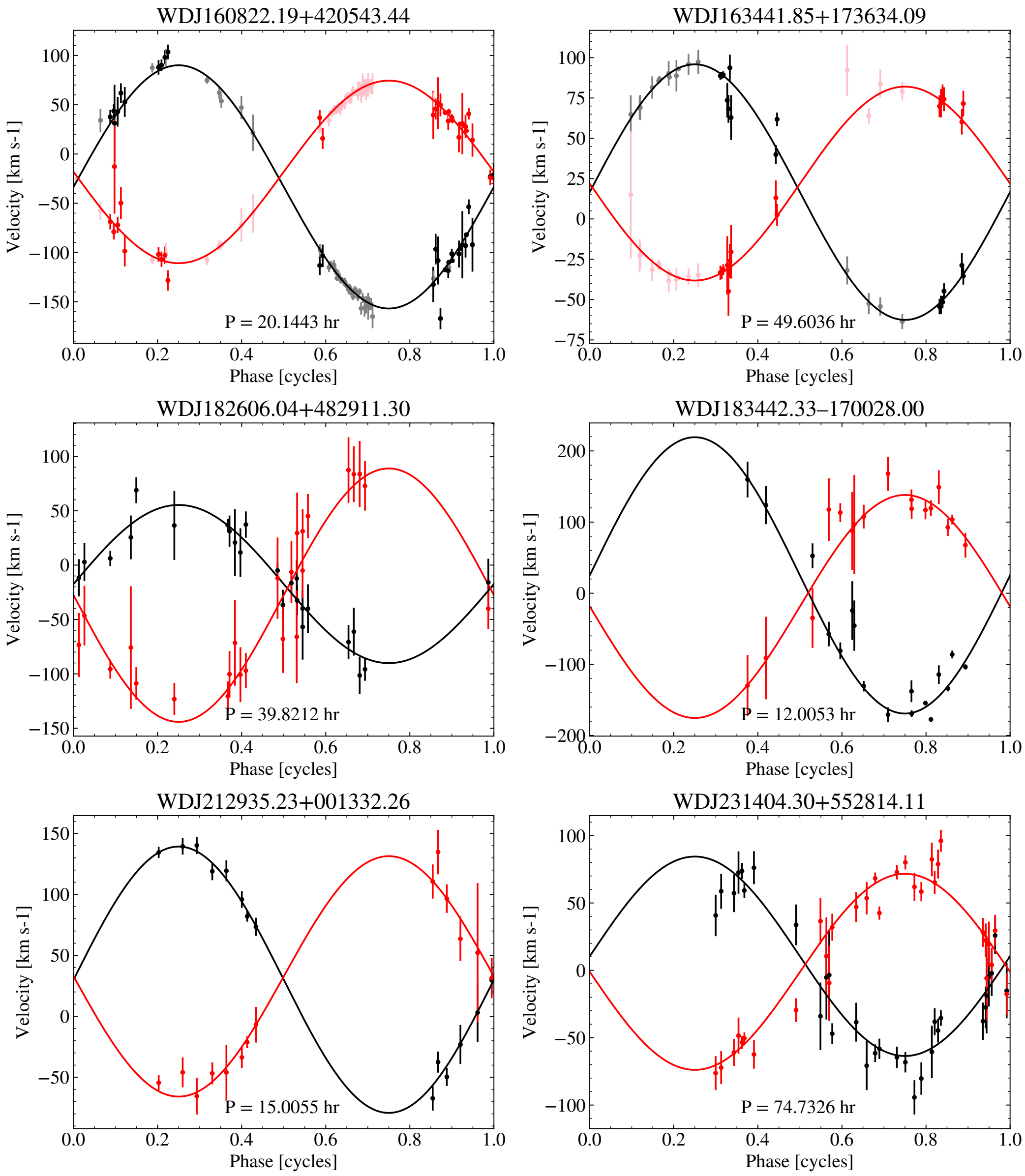

Figure 7.4: RV curves of the other six systems presented in this work, continuing from Fig. 7.3. The data for the hotter star of the binary is plotted black, and the cooler star in red. WDJ153615.83+501350.98 is omitted from the plots as we only had two further RV measurements to add to those in Kilic et al. [2021a], whereas for WDJ160822.19+420543.44 and WDJ163441.85+173634.09 I were able to recover the same orbital solutions in this work with a much larger number of RVs to add. The RVs presented in Kilic et al. [2020a] and Kilic et al. [2021a] for these two systems were incorporated into my analysis, plotted in light red/black shades. The system WDJ151109.90+404801.18 is also omitted given its unclear orbital solution, even though the correct period alias has been identified.

15 of the 34 presented in Munday et al. [2024], while the first discovery of 3 of them was in other studies.

WDJ002602.29$-$103751.86 has one peak above 4σ and one other close to this threshold, lying at 23.40 hr and 7.91 hr respectively. The first of these clearly best fits the RVs of the brighter star and has a near-zero difference in gravitational redshift, while the other solution slightly better fits RVs for the dimmer star and has a gravitational redshift difference of 10–20 $\mathrm{km\,s^{-1}}$. I strongly expect that the true period is 23.40 hr because of the better fit and accordance with the atmospheric solution, and hence adopt this value. This leads to the system having an orbitally derived mass ratio of $q = K_2/K_1 = 0.62 \pm 0.27$, while the atmospheric mass ratio is $q = M_1/M_2 = 1.12 \pm 0.07$, which is significantly different. This difference cannot be resolved by forcing a carbon-oxygen or helium core mass-radius relationship in the atmospheric fit, as this still leads to a poor match to the observations for all combinations. The detection of the dimmer star is marginal at Hα and the fractional flux contributed in other wavelengths is small – further RVs are encouraged to improve the accuracy of K_2 and perhaps higher signal to noise observations at quadrature with Hα. A double Gaussian plus polynomial fit proved advantageous for more precise RVs due to the slight detection of the cooler WD in this system.

WDJ005413.14+415613.73 has an orbital period of 20.48 hr, with an orbitally derived mass ratio $q = K_2/K_1 = 0.78 \pm 0.08$ and the atmospheric solution represents $q = 0.96 \pm 0.12$.

WDJ013812.93+444252.10 has an orbital period of 41.60 hr, with an orbitally derived mass ratio $q = K_2/K_1 = 1.19 \pm 0.27$ and the atmospheric solution represents $q = 1.08 \pm 0.07$.

WDJ020847.22+251409.97 is the closest new double-lined DWD in the DBL survey located at 39 pc, formerly identified as a double degenerate candidate in the 40 pc survey of WDs [McCleery et al., 2020]. I find that it has an orbital period of 48.18 hr, the atmospheric solution represents $q = M_1/M_2 = 0.74 \pm 0.04$ and the orbital solution $q = K_2/K_1 = 0.85 \pm 0.11$. A double Gaussian plus polynomial fit was used to extract RVs, again because of the slight detection of the cooler WD.

WDJ114446.16+364151.13 has an orbital period of 17.98 hr, with an orbitally derived mass ratio $q = K_1/K_2 = 1.03 \pm 0.15$ and the atmospheric solution represents $q = 0.93 \pm 0.09$.

WDJ141625.94+311600.55 has an orbital period of 18.88 hr with an orbitally derived mass ratio $q = K_2/K_1 = 0.69 \pm 0.12$ and the mass ratio from the atmospheric solution is $q = 1.23 \pm 0.10$. The two stars are near identical in terms of their atmospheric parameters and their spectral signature, where if I switch the hotter star to have the RVs of the previously thought-to-be cooler one's RV assignments, I get atmospheric parameters of $T_{1,\mathrm{eff}} = 13\,460 \pm 400\,\mathrm{K}$, $T_{2,\mathrm{eff}} = 12\,740 \pm 250\,\mathrm{K}$, $\log(g_1) = 7.66 \pm 0.16\,\mathrm{dex}$, $\log(g_2) = 7.70 \pm 0.15\,\mathrm{dex}$, $M_1 = 0.44 \pm 0.05\,\mathrm{M}_\odot$ and $M_2 = 0.45 \pm 0.05_\odot$. This generates an atmospheric mass ratio of $q = 0.98 \pm 0.16$ which far better aligns with the orbital solution, hence I assume these new atmospheric parameters going forward.

WDJ151109.90+404801.18 is an interesting case where, for 5 of the 23 spectra (3 on one night, 2 on another), I am not able to determine which star is which in the double-lined spectra even when trialling every valid combination of RV assignments. The reason for this is that the spectral signature from both stars at Hα is very similar. However, what is common to all trial combinations is that an orbital period of approximately 23.3–23.6 hr is clearly the highest and the only high in power peak, making an orbital period in this range the correct solution for this binary. The short-term RV variability of a group of six spectra on the same night covering a 4.8 hr observing window affirms that the near 1 day orbital period is a true detection. At times and depending on the assignment of the unclear RVs, another peak at half of this period emerges, but this well fits the RVs of only one of the stars. For the 23.3–23.6 hr period aliases, I find that $q = K_2/K_1 \approx 1.0$–1.5 in all cases, but the error on q is approximately ± 0.4–0.5 and so it is largely unconstrained. The high percentage error stems from the poor phase coverage given the near 1 d orbital period, though, because of the similar spectral signature from both stars, conclusively resolving the orbital parameters of this binary would be very challenging unless devoting entire telescope nights to its observation. The atmospheric solution for this system gives $q = 1.52 \pm 0.11$, which is in the general vicinity of the orbital solution. Two Gaussians plus a polynomial were fit to measure RVs since the template fit to the line core shapes was improved for these stars with a similar line core signature.

WDJ153615.83+501350.98, or **WD 1534+503**, was discovered and published before completion of this work [Kilic et al., 2021a], and I only have 2 additional RV measurements from the identification spectra for this system which I obtained using the double Gaussian plus polynomial method. Combining datasets, I find $P_{\mathrm{orb}} = 17.02\,\mathrm{hr}$. This orbital period has a greatly improved precision to previously published work given the extra year time baseline of the new RV measurements. I next quote my orbital solution, though emphasise that differences in the fitting procedure between their work and ours, and the instrumental setups/data reduction, could lead to systematic errors in the results. I find $K_1 = 135.08 \pm 4.27\,\mathrm{km\,s^{-1}}$, $K_2 = 89.15 \pm 9.88\,\mathrm{km\,s^{-1}}$, $\gamma_1 = 23.22 \pm 3.22\,\mathrm{km\,s^{-1}}$, $\gamma_2 = 44.45 \pm 7.00\,\mathrm{km\,s^{-1}}$. The orbital solution hence indicates $q = K_2/K_1 = 0.660 \pm 0.076$. This remains in good agreement with the atmospheric solution presented in Kilic et al. [2021a], which was $q = M_1/M_2 = 0.64 \pm 0.15$ and less so with that of Munday et al. [2024], which was $q = M_1/M_2 = 0.96 \pm 0.07$. The difference likely stems from the choice in mass-radius relationships employed, in such a way that the lower mass star's radius does not align well with a helium-core WD model. It may be a carbon-oxygen or a hybrid core, and the orbital solution hence encourages adoption of the atmospheric solution in Kilic et al. [2021a].

WDJ160822.19+420543.44, or **WD 1606+422**, was independently discovered and published before completion of this work [Kilic et al., 2020a]. To verify the orbital solution found by these authors with a unique dataset, I used my 30 RV measurements of the binary and found a consistent solution with their results. Maintaining the same convention that star 1 is the hotter star and given the excellent agreement, I decided to merge the datasets to improve the orbital solution further. Overall, I arrive at a solution of a 20.14 hr orbital period with $K_1 = 92.60 \pm 2.45\,\mathrm{km\,s^{-1}}$, $K_2 = 127.24 \pm 2.30\,\mathrm{km\,s^{-1}}$, $\gamma_1 = -18.04 \pm 1.65\,\mathrm{km\,s^{-1}}$, $\gamma_2 = -31.40 \pm 1.57\,\mathrm{km\,s^{-1}}$. With this, the newfound mass ratio from the orbital solution is $q = K_2/K_1 = 1.37 \pm 0.04$. My atmospheric solution suggests $q = M_1/M_2 = 1.17 \pm 0.08$, and with this all results are consistent.

WDJ163441.85+173634.09, or **PG 1632+177**, was also independently discovered and published by Kilic et al. [2021a] and again I find consistency between my atmospheric solution and theirs. Given a non-ideal atmospheric fit to the Hα line cores for this binary, I decided to fit the RVs with a quartic polynomial plus two Gaussian functions, one for each star. The orbital solution to the RVs from both studies with my additional 14 RV measurements gives an orbital period of 49.60 hr, $K_1 = 79.63 \pm 1.73\,\mathrm{km\,s^{-1}}$, $K_2 = -60.59 \pm 1.74\,\mathrm{km\,s^{-1}}$, $\gamma_1 = 16.21 \pm 1.79\,\mathrm{km\,s^{-1}}$, $\gamma_2 = 22.38 \pm 1.44\,\mathrm{km\,s^{-1}}$. This system is another case where the mass of one of the stars is on the boundary of that considered for a CO-/He-core WD, and this shows with the larger discrepancy between M_1/M_2 and K_2/K_1. The solution presented in Kilic et al. [2021a] better fits the data for which the lower mass WD with $M_1 = 0.392^{+0.069}_{-0.059}\,\mathrm{M_\odot}$ has a hybrid He/CO or a CO core and the larger mass WD has a mass $M_2 = 0.526^{+0.095}_{-0.082}\,\mathrm{M_\odot}$. I continue to encourage usage of this result, making the atmospheric $q = M_1/M_2 = 0.75 \pm 0.18$ and the newly-found orbital with an improved precision on the orbital period $q = K_2/K_1 = 0.761 \pm 0.027$.

WDJ181058.67+311940.94, as presented in Munday et al. [2025], has an orbital period of 14.24 hr, with an orbitally derived mass ratio $q = K_2/K_1 = 0.98 \pm 0.03$ and the updated atmospheric solution represents $q = 0.86 \pm 0.04$. Its merger time is 22.6 ± 1.0 Gyr.

WDJ182606.04+482911.30 has an orbital period of 39.82 hr, with an orbitally derived mass ratio $q = K_2/K_1 = 1.60 \pm 0.29$ and the atmospheric solution represents $q = 0.87 \pm 0.12$. In this case, I found 3 periodogram peaks above the 4σ false alarm probability threshold, but inspection of the RV curve for the 2 lower aliases shows a largely spurious result with only the RVs of the brighter star being well fit, and so they can be rejected. This just leaves the 39.82 hr peak as a valid solution. The spectral fit for the atmospheric solution appears very good with a slightly over-predicted synthetic photometry in the blue. *Gaia* photometry alone was used as there are two entries of the same source in PanSTARRS with reported magnitudes that slightly conflict, but when fitting just the spectra I obtain a very similar best-fit atmospheric solution. The reason for this large discrepancy in mass ratios alludes us, and it is hoped that future photometric/astrometric survey data releases or an improved precision on the orbital solution will aid in finding consistency in the future.

WDJ183442.33$-$170028.00 had 3 solutions above the 4σ false alarm probability. All well fit the RVs from the hotter star, but only the highest power peak well fits the RVs from the cooler WD, leaving one unique and valid solution. The source has an orbital period of 12.01 hr, with an orbitally derived mass ratio $q = K_2/K_1 = 0.807 \pm 0.468$ and the atmospheric solution represents $q = M_1/M_2 = 0.91 \pm 0.07$. The system is a unique case amongst the current DBL survey sample, having strong emission at Hα which is not RV variable and likely originates from an unrelated hydrogen cloud given the location of the field. This severely jeopardises the precision of RVs from the secondary, leading to the high uncertainty on the orbital mass ratio. However, the found orbital solution is consistent with the atmospheric, and so I continue with the assumption that the atmospherically deduced masses of both WDs are accurate. At approximately 0.4 $\mathrm{M}_\odot$ each, both stars are relatively low mass compared to the rest of the double-lined sample, and the merger time is $43{\pm}4$ Gyr.

WDJ212935.23+001332.26 has an orbital period of 15.01 hr, with an orbitally derived mass ratio $q = K_1/K_2 = 0.90 \pm 0.11$ and the atmospheric solution represents $q = 1.00 \pm 0.10$. The two Gaussian plus a polynomial was better and used here to extract RVs because of an inadequate atmospheric fit to the Hα line cores.

WDJ231404.30+552814.11 has an orbital period of 74.73 hr, making it the largest orbital period of all system solutions presented in this work. The orbital mass ratio is $q = K_2/K_1 = 0.99 \pm 0.13$ while the atmospheric solution gives $q = 1.74 \pm 0.12$ – a striking discrepancy. With this, I decided to refit the atmospheric solution with a forced carbon-oxygen core relation for both stars, yet no combination of synthetic spectra agree with the orbital solution while performing hybrid fitting to the photometry, parallax and spectroscopy of the source. If I fit to the spectroscopy only and with a forced carbon-oxygen mass radius relationship, the fit appreciably improves in all Balmer lines besides Hα and I am able to find an improved agreement with the orbital solution. The parameters I find are $T_1 = 13770 \pm 210\,$K, $T_2 = 8260 \pm 190\,$K, $\log(g_1) = 7.86 \pm 0.05\,$dex, $\log(g_2) = 7.64 \pm 0.04\,$dex, making $M_1 = 0.53 \pm 0.03\,\mathrm{M}_\odot$ and $M_2 = 0.44 \pm 0.01\,\mathrm{M}_\odot$. With this atmospheric solution, the mass ratio becomes $q = M_1/M_2 = 1.20 \pm 0.07$ and I find consistency between the atmospheric and orbital solutions. With that in mind, I encourage usage of this atmospheric solution which ignores the photometry and parallax of the source. In measuring RVs, I used a two Gaussian plus polynomial model as it resulted in an improved accuracy and is independent of the best-fit synthetic spectra.

7.4.2 Systems with period aliases and constraints

Similar to before, here I address the systems where my RVs restrict the valid orbital solution of the binary by describing potential aliases. Presented are a further 5 of the 34 double-lined systems that I identified, plus details of a sixth source which was formerly considered a candidate double-lined and is now verified as double-lined.

WDJ000319.54+022623.28 has 17 RV measurements of each star recorded and has two peaks above the 4σ false alarm probability, where it is difficult to separate which is correct. The peak of highest power is at a 14.55 hr orbital period and the other at a 37.06 hr orbital period. The relative flux difference between the Hα line cores is large, meaning that, with approximately 3–5 more RV measurements closely separated in time, the true solution would be easily solvable in future work. Relatively uneven RV phase coverage leads to a large orbitally derived mass ratio of about $q = K_2/K_1 \approx 1.9$ in both cases, but I promote more observations before drawing any further conclusion and solely state these two period aliases.

WDJ080856.79+461300.08 has one unique peak above the 4σ false alarm probability that poorly covers the orbital phase space, with an orbital period of 21.93 hr. But, there is another, relatively high in power peak of 19.48 hr that appears suitable, leading us to categorise this as a system with aliases. Further smaller and similar height peaks exist in the periodogram in the range of 60–110 hr, but they do not account for the short-term RV variability that is clearly noticed, with the peaks likely appearing because of the window function of the widely spaced observations. An orbital period of about 20 hr seems the most likely solution, where the 21.93 hr alias has $q = K_2/K_1 = 1.17 \pm 0.20$ and 19.48 hr has $q = 1.15 \pm 0.33$, both consistent with that indicated from the atmospheric solution which is $q = 1.28 \pm 0.08$. The 2-Gaussian plus polynomial method was used in obtaining RVs as the line core fit was significantly better.

WDJ170120.99$-$191527.57 reveals the most compact orbital period of all systems presented in this work, but its true orbital period is not clear. Good orbital solutions are obtained above the 4σ alarm probability for 4.95 hr, 6.24 hr and 4.10 hr orbital periods, in order of periodogram peak power. A few out of phase points are witnessed in the RV curve for an 8.43 hr period, having about a third of the power as the other three peaks, but it is still significant. All of these solutions have an orbital mass ratio of $q \approx 0.85$–0.9, while the atmospheric masses were found to be $0.673 \pm 0.024\,\mathrm{M}_\odot$ and $0.544 \pm 0.022\,\mathrm{M}_\odot$ (Section 7.3.2), and with this the atmospheric $q = M_1/M_2 = 1.24 \pm 0.07$. For all of these orbital period aliases, the merger time of the system must be within a few gigayears.

WDJ180115.37+721848.76 has 10 RV measurements in total, which are relatively few to solve an orbit and with the periodogram is inconclusive. The true alias of the DWD would be easy to resolve with just a couple more measurements even with a long time spacing given the clear shape of the Hα line cores at a spectral resolution of $R = 6310$. The atmospheric solution gives $q = 0.89 \pm 0.05$ which aligns with the semi-amplitude ratio for the highest-power aliases, but for now I can only conclude that the orbital period is very likely between 6–40 hr.

WDJ221209.01+612906.96 has 9 RVs for each star. The spectral signature of each star is very similar, making it challenging to correctly assign to the hotter or cooler star at each epoch too. I tried all combinations of assignments possible, but without clear periodogram aliases appearing in all cases. Little can be said except that the orbital period is more than 3 hr and the maximum possible period based on the binary mass function and the maximum perceived RV split between the stars is 13.5 d. With the lack of certainty around the correct star at each epoch, I choose not to present the measured RVs for these systems.

WDJ234929.57+102255.57 was originally categorised as a candidate double-lined DWD in Munday et al. [2024]. Further spectra clearly indicate a double-lined DWD, affirming the presumption. The periodogram of my 7 RV measurements give strong evidence in favour of an orbital period above 24 hr, with prominent aliases of 27.49 hr, 53.81 hr, and 61.01 hr. The latter two solutions have an orbital mass $q \approx 1$, which would align well with the atmospheric solution, but the small number of spectra at hand are insufficient to draw a robust conclusion.

Table 7.1: The measured orbital parameters for each system. For WDJ151109.90+404801.18, the period alias is resolved but some RV measurements are unclear, leading us not to present detailed orbital parameters or T_0.

Name	Period d	$T_0 - 2450000$ HJD, UTC	K_1 $\mathrm{km\,s^{-1}}$	K_2 $\mathrm{km\,s^{-1}}$	γ_1 $\mathrm{km\,s^{-1}}$	γ_2 $\mathrm{km\,s^{-1}}$
WDJ002602.29−103751.86	0.9749777(58)	8358.5743(60)	110.1 ± 5.8	68.3 ± 29.4	8.4 ± 3.4	6.2 ± 15.7
WDJ005413.14+415613.73	0.853294(70)	8358.232(58)	127.4 ± 5.0	99.0 ± 8.9	26.3 ± 3.1	51.0 ± 6.1
WDJ013812.93+444252.10	1.73324(13)	8357.016(21)	81.9 ± 9.7	97.5 ± 18.9	25.1 ± 3.6	17.4 ± 9.8
WDJ020847.22+251409.97	2.007653(28)	8357.064(13)	84.4 ± 3.3	71.9 ± 9.0	49.1 ± 3.3	36.2 ± 6.9
WDJ114446.16+364151.13	0.7492851(65)	8645.273(12)	108.6 ± 10.8	111.7 ± 12.4	6.5 ± 6.0	4.5 ± 9.2
WDJ141625.94+311600.55	0.7867420(15)	8589.519(25)	125.5 ± 12.4	86.9 ± 13.1	26.0 ± 9.2	38.3 ± 8.4
WDJ151109.90+404801.18	≈ 0.97–0.99	-	-	-	-	-
WDJ153615.83+501350.98	0.709254(48)	8287.808(29)	135.1 ± 4.3	89.2 ± 9.9	23.2 ± 3.2	44.5 ± 7.0
WDJ160822.19+420543.44	0.8393438(36)	8281.5690(18)	92.6 ± 2.5	127.24 ± 2.30	-18.0 ± 1.7	-31.4 ± 1.6
WDJ163441.85+173634.09	2.066817(44)	8281.2062(80)	79.6 ± 1.7	60.6 ± 1.7	16.2 ± 1.8	22.4 ± 1.4
WDJ181058.67+311940.94	0.5931479(9)	8587.6663(18)	93.9 ± 2.0	95.7 ± 2.1	50.0 ± 1.5	53.5 ± 1.6
WDJ182606.04+482911.30	1.659219(28)	8358.620(25)	72.7 ± 9.3	116.6 ± 14.9	-17.3 ± 6.4	-27.5 ± 10.2
WDJ183442.33−170028.00	0.5002200(39)	8359.9874(54)	194.2 ± 29.1	156.7 ± 87.8	25.1 ± 25.2	-18.6 ± 73.2
WDJ212935.23+001332.26	0.6252288(96)	8359.3171(76)	108.2 ± 6.9	97.5 ± 10.0	31.4 ± 4.6	32.6 ± 6.9
WDJ231404.30+552814.11	3.11386(15)	8358.422(48)	74.1 ± 7.8	73.2 ± 6.1	10.9 ± 6.4	-1.7 ± 5.7

7.4.3 Follow-up of candidate double-lined DWDs and single-lined systems

Further observations of a couple of single-lined targets were taken to probe RV variability when no other good targets were able to be observed at the time and conditions of the observations, but all of them resulted in no firm detection of binarity. These consist of three spectra of WDJ185640.86+120844.61 and ten spectra of WDJ192817.81+354442.60.

7.5 Discussion

With many new orbital solutions presented, I turn our attention towards making comparisons with the full sample of published DWD binaries[5]. I emphasise again that the choice of which double-lined systems were followed up for time-series RVs was purely based upon which were observable for the allocated telescope nights and for systems where both stars would be separable at the slightly lower spectral resolution of the INT observations. Hence, the sampling of systems from the full list of double-lined DWDs in the DBL survey is relatively random, including the outlier in total mass WDJ181058.67+311940.94 which was the highest total mass system discovered.

Fig. 7.5 shows the orbital period and mass ratio distribution of the observed sample. As is clear from the previous section and Fig. 7.5, these DWD binaries group around an orbital mass ratio of $q = 1$. This is an unsurprising observational bias of the survey, given that two similar stars are easiest to detect as a double-lined source DWD. The newly discovered systems populate a period space that before was sparsely sampled. Their range of periods aligns well with predictions from recent synthetic populations, which forecast an abundance of $q \approx 1$ DWDs at certain periods [Ge et al., 2010; Toonen et al., 2012; Ge et al., 2015, 2020; Li et al., 2023]. In the vast majority of cases, the orbital and atmospheric mass ratios agree well (Figs. 7.5 and 7.6), emphasising the general accuracy of the masses of double-lined DWDs obtained from identification spectra alone when fitting full-visible spectroscopy in combination with absolute photometry and precise parallaxes, although the discrepancy varies on a case by case basis. This discrepancy is especially relevant for systems where at least one star has a mass close to 0.45 $M_{\odot}$, being the mass I used to transition from a carbon-oxygen or helium core mass radius relationship in the atmospheric parameter fitting.

With the selection of DWDs having similar masses for both stars, the total mass of the DBL systems characterised in this work mostly fall around $1.0\,M_{\odot}$, shown in Fig. 7.7. In comparison to other double-lined or eclipsing systems in the literature (which, generally speaking, are those with accurate masses for both components), the systems investigated

---

[5] https://github.com/JamesMunday98/CloseDWDbinaries [Munday et al., 2024]

in this paper double the number of compact DWDs with an orbital period above 10 hr. This much better reflects the expectations of synthetic populations. All of these newly-characterised systems will merge in more than a Hubble time, with the one notable outlier being WDJ170120.99−191527.57, having an unclear orbital solution. With a mass ratio close to one, unstable mass transfer will likely cause a merger as the end-state for these binaries leading to a R CrB star or larger mass, single WD. I show how close each system is to the boundary of stable and unstable mass transfer in Fig. 7.8. WDJ181058.67+311940.94 will also initiate unstable mass transfer, but its total mass significantly exceeds the Chandrasekhar mass limit, inevitably giving rise to a type Ia supernova explosion before the event of merger [Munday et al., 2025].

Fig. 7.9 again shows the orbital periods of the samples, but compared with the mass of the brighter star, while Fig. 7.10 depicts the mass of the dimmer star. A trend of an increasing mass of the brighter star with an increasing orbital period is slightly evident for the presented DBL survey sources (besides the one case of WDJ181058.67+311940.94). This likely appears because mass transfer initiated later for the systems showing longer orbital periods after the common envelope phase, allowing the WD progenitor to grow to higher core masses. The trend here can be a powerful tool in constraining an empirical relationship for the final separation of DWDs exiting the common envelope phase and with this a correlation with the core mass of the former giant star, but it is difficult to draw strong conclusions with the sample size.

Additionally, a graphical representation of the masses of the brighter and dimmer stars in the orbitally solved binaries from this paper can be found in Fig. 7.11. A concentration of systems can be seen following the trend $\mathrm{M_{bright}/M_{dim}} = 1.25$. Overall, about one-quarter of the 34 double-lined systems give a brighter star that is more massive, where this situation can arise from the “formation reversal channel” [Toonen et al., 2012] in which the first mass transfer phase initially forms a helium star that then cools to become a WD, thus delaying the star’s arrival to the cooling sequence and making it appear younger than the later-formed companion WD. The large fraction of these systems could be an artifact of the magnitude limit employed in the DBL survey, rather than being reflective of the full DWD population, since the first-formed WD remains brighter for longer in this evolutionary channel.

7.6 Conclusions

I have presented a continuation on the DBL survey supplying orbital solutions for 15 double-lined DWD binaries and have narrowed down the viable period aliases for a further 6 DWDs to a couple of good solutions. These systems cover a wide range of orbital periods

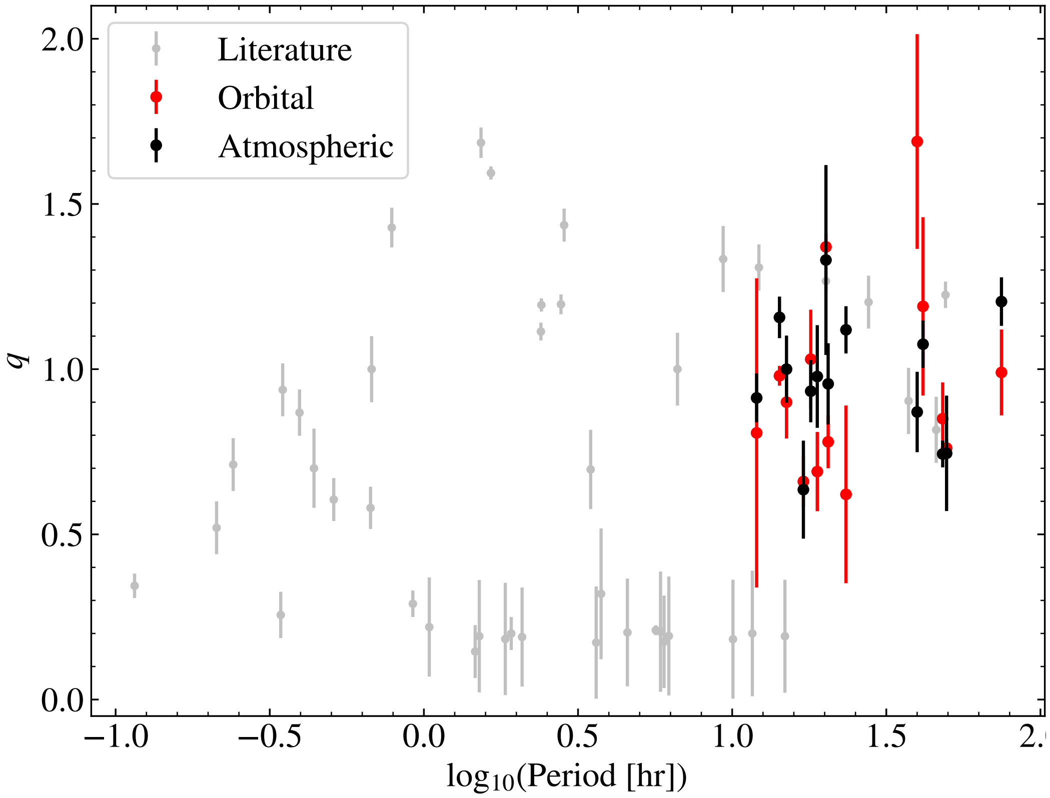

Figure 7.5: A comparison of the orbital and atmospheric mass ratios against the orbital period. The mass ratios of other previously studied DWDs are included in grey to show the overall observed mass ratio versus period distribution of DWDs. Mass ratios of the double-lined DWDs found in the DBL survey are limited to approximately $q = 0.5$–2.0.

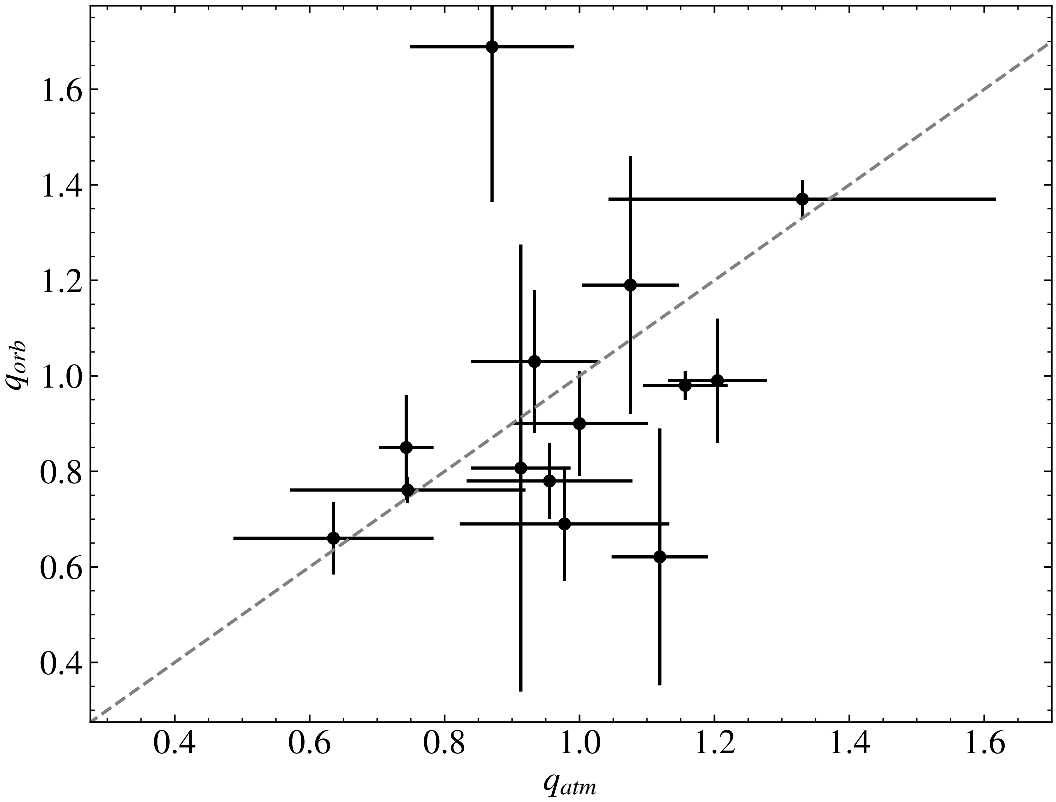

Figure 7.6: A comparison of the mass ratios deduced from the orbital solution and the fitting of synthetic spectra to obtain atmospherically determined masses. The dashed line represents $q_{\rm orb} = q_{\rm atm}$.

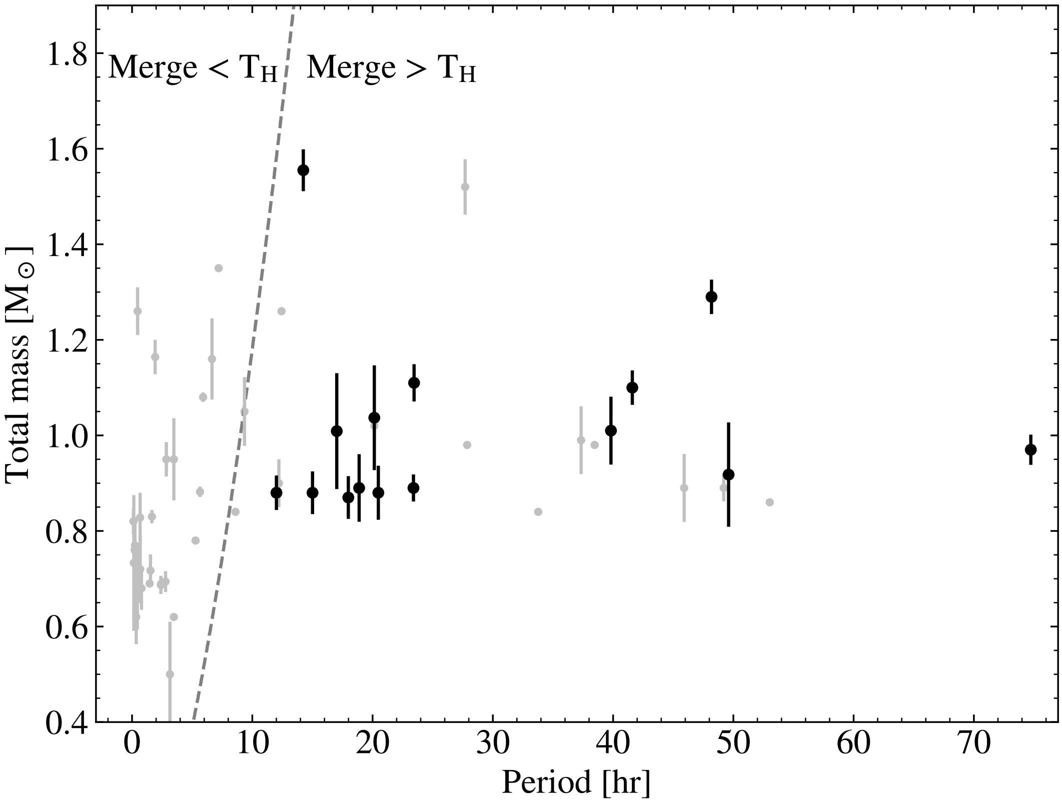

Figure 7.7: The total mass versus orbital period distribution of the observed sample of DWDs. The points in gray circles are systems in the literature that are eclipsing or double-lined, whereas the black crosses are systems systems with orbital solutions reported in this work. The dashed grey line is, for two stars of equal mass, the boundary for a binary merging within a Hubble time (T_H). One double-lined DWD [PG1115+166, Bergeron and Liebert, 2002] is not plotted for clarity because of its approximately 30 d orbital period [Maxted et al., 2002a]. The total masses of the targets that fall in the DBL survey are restricted to approximately 0.8–2.0 $M_\odot$ because of the Hertzsprung-Russell diagram cuts imposed.

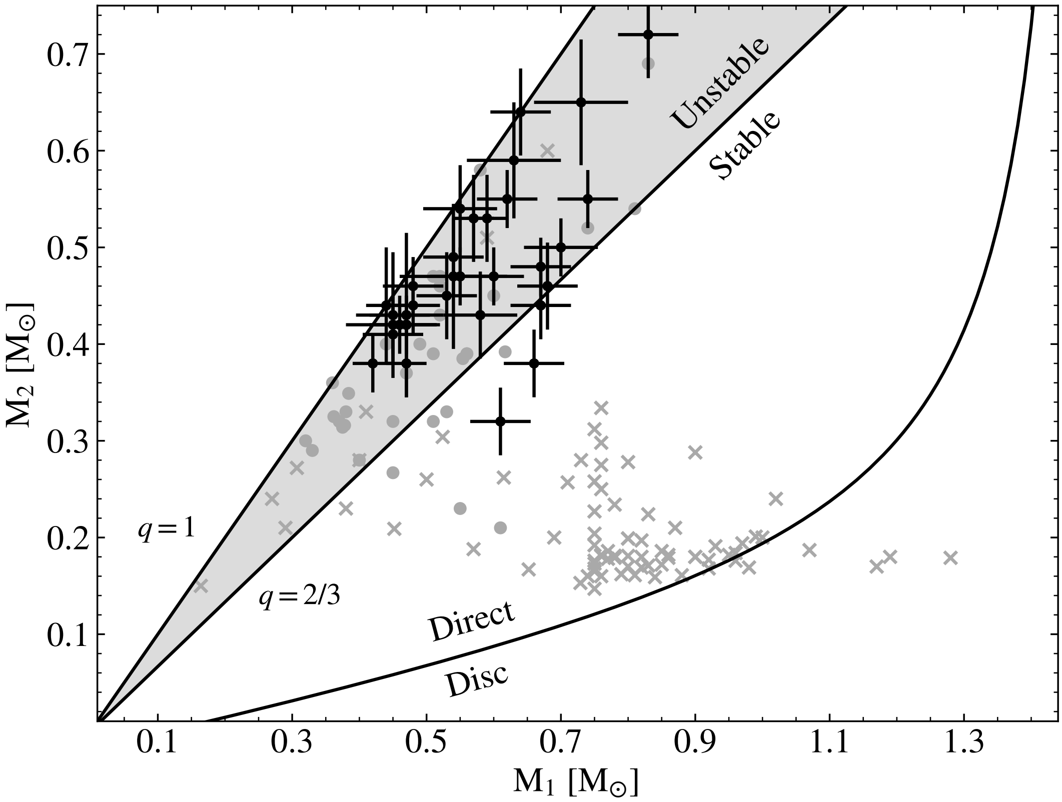

Figure 7.8: The location of all DBL survey double-lined systems (black) versus other systems in the literature (grey) when comparing a future stable versus unstable mass transfer scenario and whether disc or direct accretion will eventually take place. The literature points in circles are double-lined DWDs and those in crosses are single-lined DWDs. Direct impact accretion occurs when the trajectory of the accretion stream collides with the surface of the accretor, serving as an angular momentum sink that speeds up the inspiral of a binary, and observationally recognised by strong electromagnetic pulses on the orbital period.

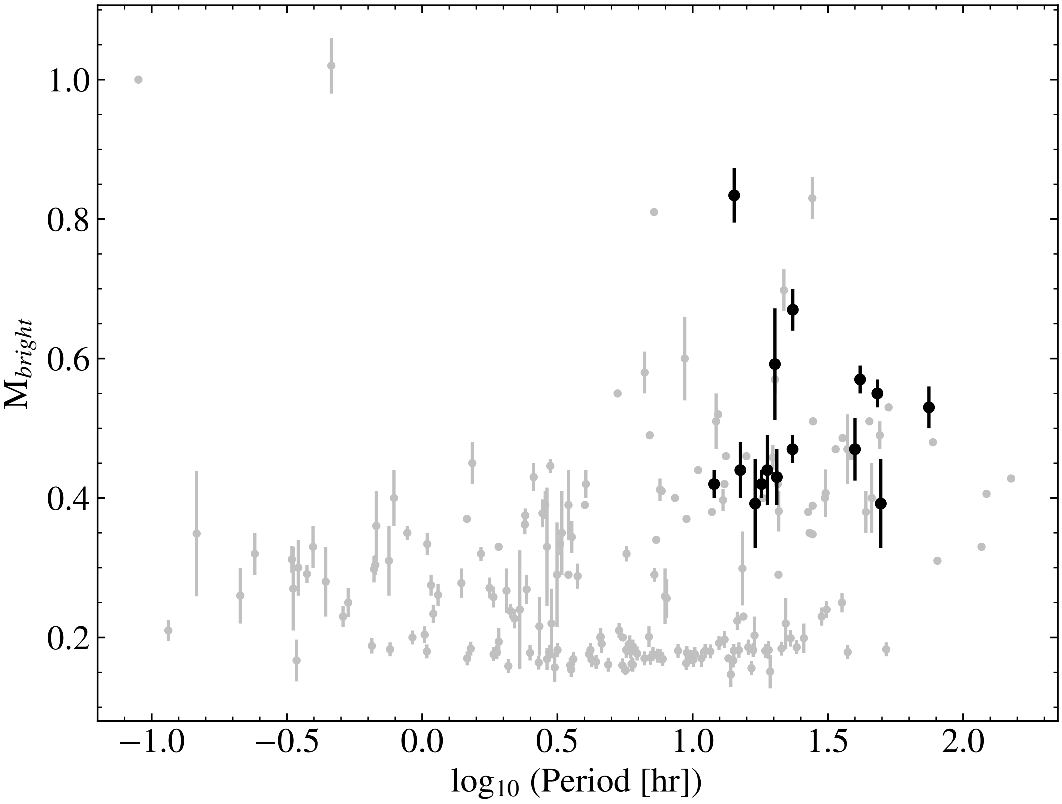

Figure 7.9: The mass of the brighter star in DWD binaries compared with the orbital period. The clumping of systems with $M_{\rm bright} = 0.2\,M_\odot$ are ELM binaries that are confirmed to be DWDs stemming largely from the ELM survey [Brown et al., 2020b; Kosakowski et al., 2023] which primarily form from the mass transfer sequence of a common envelope followed by stable Roche lobe overflow. The brightest absolute magnitude possible for a target found in the DBL survey is similar to a $0.4\,M_\odot$ DA WD evolutionary sequence for a helium core mass-radius relationship, making 0.35–$0.4\,M_\odot$ the minimum mass of the brighter component.

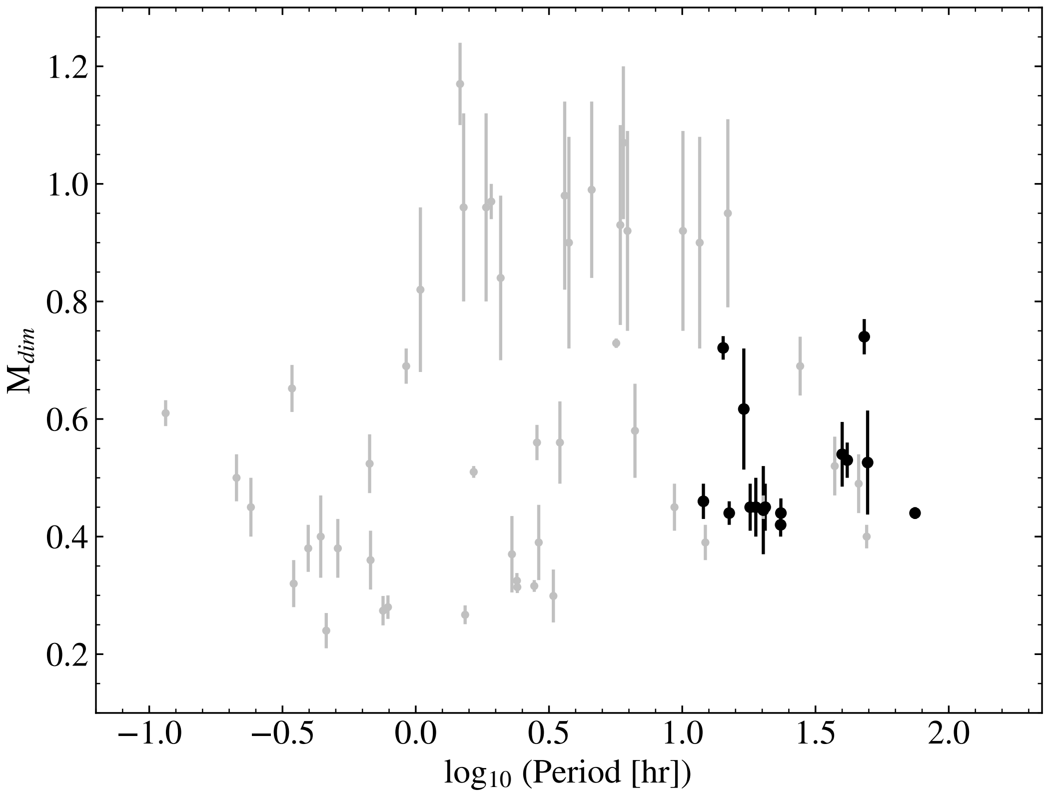

Figure 7.10: The same as Fig. 7.9, but for the dimmer star of the binary ($M_{\rm dim}$). I limit plotting of the literature systems where the fractional error of the mass of the dimmer star is below 20% for the purpose of clarity, which appreciably removes cases around 0.8–1.0 $M_\odot$.

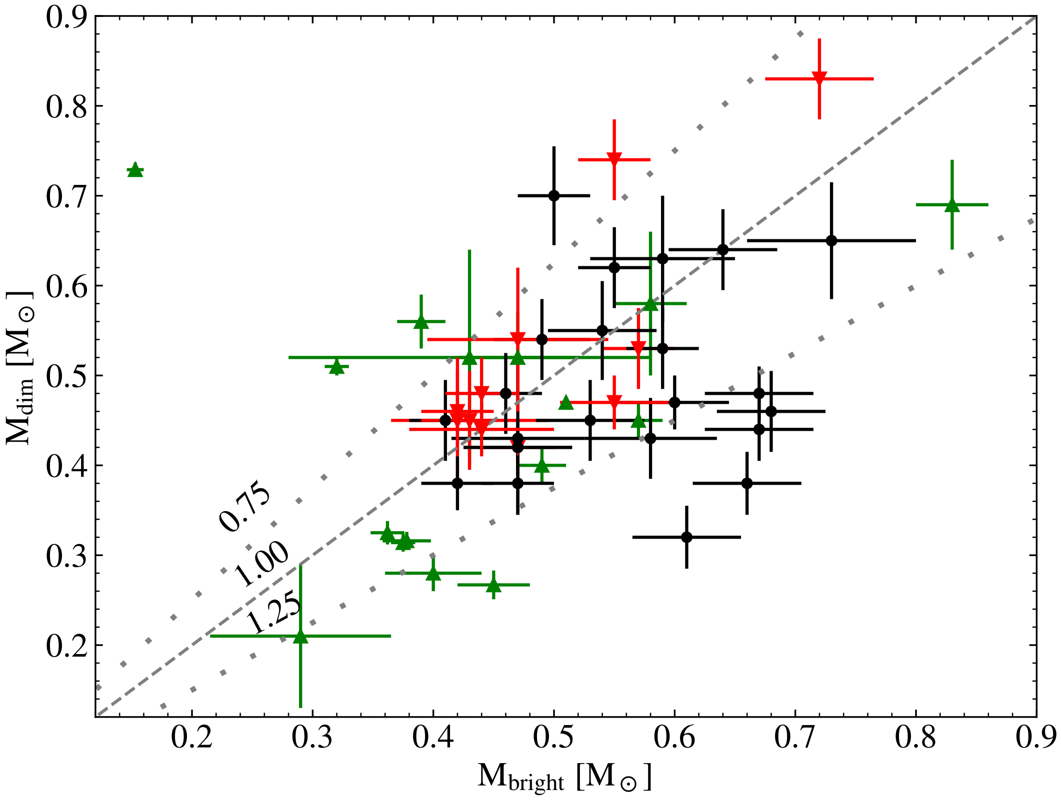

Figure 7.11: A comparison of the mass of the brighter (more luminous) and dimmer component for well-characterised DWDs. The downward facing and red triangles are the systems with complete orbital solutions discussed in Section 7.4.1. Black points are all other systems presented in the DBL I study. The upward facing green triangles are other eclipsing or double-lined systems found in the literature. In dotted lines are ratios of $M_{\mathrm{bright}}/M_{\mathrm{dim}} = 0.75$, 1.00 and 1.25.

for compact DWD binaries, spreading between $P = 5$–$75\,$hr. I directly analysed the compatibility of the mass ratio derived from the orbital solutions with the mass ratio determined from spectral fitting, finding a good agreement with the values deduced from identification spectra alone. This hence emphasises the potential power of hybrid (combined photometric and spectroscopic) fitting in deducing a mass distribution of double-lined DWDs in wide-scale searches through medium resolution spectra.

Ultimately, I have taken the first steps in obtaining a mass-period distribution of double-lined DWDs that lie within the selection criteria of the DBL survey, outlined in Munday et al. [2024]. This will be a powerful tool to calibrate synthetic population models of DWDs when exploring systems where the mass of the brighter WD exceeds approximately $0.4\,\mathrm{M}_{\odot}$. Future work will aspire to build a larger and more robust sample towards this goal, both in terms of orbital characterisation and of identification of new double-lined DWDs.

7.7 Spectroscopic fit to WDJ170120.99−191527.57

With the new and higher quality data described in Section 7.3.2, I present in Fig. 7.12 the atmospheric fit to this double-lined DWD.

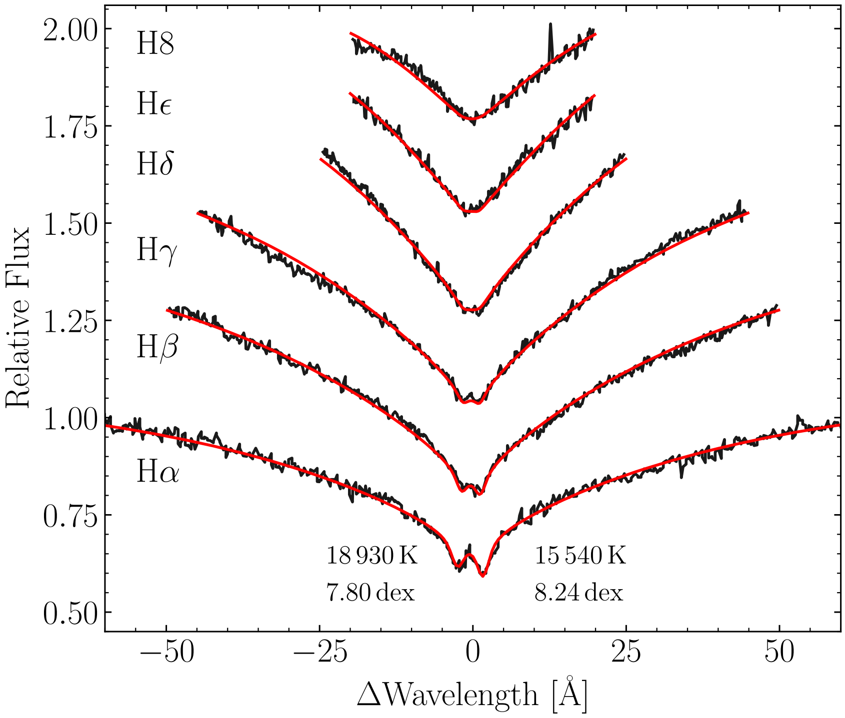

Figure 7.12: The spectroscopic fit (red) overlaid on a Magellan/MagE spectrum (black) of WDJ170120.99−191527.57 from the Balmer lines Hα to H8. The atmospheric parameters for the two stars are labelled, where here the blue-shifted star is hotter and less massive.

Chapter 8

Conclusion and outlook

I have presented a thesis focused around close DWD binary star systems, performing analyses of targets ranging from the most compact of orbital periods on the timescale of minutes to unresolved, wide binaries with periods on the timescale of tens of days.

8.1 Implications for ultra-compact binaries and the gravitational wave sky

I have presented the analysis of a multi-decade campaign timing the shortest period binary star system known to date. Uniquely as of yet for any system, I optically discovered the acceleration of orbital decay and, incredibly, witnessed a resistance of orbital inspiral due to the high mass transfer rate of the system with the orbit desiring to restabilise. Even more remarkably is how HM Cnc has been detected a mere 2000 yr before period minimum, assuming there is no catastrophic demise to the system, which could lead on to be an outspiraling AM CVn binary star systems; a still poorly understood population in terms of space density and contribution from which progenitor channels. The chance timing of the event so close to period minimum creates an open question... are we lucky? The distance to HM Cancri is still unclear with maximum estimates pushing out to 10 kpc, which is to say that in this space volume, should we have been sensitive to more outspiraling systems that maintain a high mass transfer rate for a longer period time if they exist? Are we limited to ES Ceti alone? Observing bias must play a part in answering this question, but without a precise knowledge of the final moments of the lifetime of the system, the contribution of observing biases biases and the frequency of outspiraling AM CVn systems remain unsolved issues for the future of the field.

I then presented a bright system that is the shortest-period eclipsing source discovered by *TESS* and marks the first case of a detectable gravitational wave source discovered by the space mission. Bright eclipsing binaries are ideal for timing measurements and the suspected double-lined feature of this source would make for very precise system masses too, such that with continued eclipse timings the chirp mass of the source will be measured with minute error, which can be included as a constraint in light/RV curve modelling. In the next decades, continued timing of systems eclipsing, ultra-compact binaries across the full sub-hour period range will be crucial in exploring the role of tidal effects in binary star systems, which up to now has been explored purely theoretically.

Precisely constraining the orbital decay of a system is of top importance in modelling the gravitational wave background from DWDs residing in the Milky Way. Better exploration of the fraction of systems that can survive inspiral (hence contributing to the gravitational wave background on outspiral as well) is crucial in modelling the noise background, particularly at the upper range of frequencies detectable by space-based missions focused on the mHz regime [Korol et al., 2017]. This is only possible through devoted analyses of exemplar systems and the hunt for many more that are yet to be discovered.

8.2 The role of double white dwarfs as exotic phenomena and the investigation of binary evolution

I have discovered a large class of massive DWD binaries that approach the Chandrasekhar mass limit through a dedicated search collectively named the DBL survey. One of the discovered systems surpasses the Chandrasekhar mass limit and will undoubtedly detonate as a type Ia supernova in the absence of third body interference. This discovery inches towards a more complete overview of the likely progenitors of type Ia supernovae, for which its dominant progenitors are a present and longstanding ambiguity.

The fact that the DBL survey was performed with clear, well-defined and well-understood selection biases makes future efforts in obtaining volume complete and magnitude samples within the declared selection cuts of the Hertzsprung-Russell diagram trivial. The method is perfect to directly compare the outputs of binary population syntheses to observations, hence granting a precise calibration tool for models. In coming years, these DWDs should give rise to a leap in the accuracy of binary evolutionary channels that form DWDs, such as the prescriptions of stable mass transfer and common envelope evolution [Nelemans et al., 2000, 2001a,c; van der Sluys et al., 2006; Woods et al., 2012; Toonen et al., 2012; Temmink et al., 2023; Li et al., 2023]. Earlier stages of binary evolution will also benefit for comparison with the recent works exploring post-common envelope binaries and significantly augmenting the observed sample [Boffin and Jones, 2019; Yamaguchi et al., 2024; Garbutt et al., 2024, and references therein]. Together, all efforts strive towards a complete picture of binary stars' role in Galactic evolution, transient events and the local population of stars in the Milky Way, unifyingly unraveling our origin.

I have described in Chapters 1, 5 and 6 how the lack of discoveries of massive DWD binaries in the last few decades has been troublesome not only for the expectation of binary population synthesis models but also from the need to the origins of type Ia supernovae. Following from the work presented in this thesis, we now have convincing evidence of many sub-Chandrasekhar mass detonation candidates where, if a detonation does occur, they would likely lead on to be subluminous supernovae. Further exploration is hence required to separate the nuances of type Ia ejecta energy and morphologies to finally explain the contribution of various single or double degenerate evolutionary channels to the full population of type Ia supernovae. Looking at Fig. 5.7, the primary-secondary mass distribution is still vacant for total system masses $> 1.6\,\mathrm{M}_\odot$ which raises the intriguing open question: if they do exist, where are the highest mass DWD binaries? Accretion induced collapses have been explained by the collapse of a WD into a neutron star, so, are there candidate DWDs which could lead to such an event in the Galaxy? Where are they? More investigation is required in the coming years which should be aided by technological advancements and the capabilities of modern instrumentation.

In Chapter 7, I have provided full orbital solutions for many of the double-lined DWDs discovered in the DBL survey, making some of the first steps in creating a mass-period distribution of DWD binaries from a sample with minimal observational biases. With orbital periods ranging 5–75 hr, this work doubles the number of compact DWDs with an orbital period 10 hr, building towards the overarching goal of a robust sample for model comparison. I verified that the stellar masses obtained through hybrid fitting DWD data are in good accordance with the orbital mass ratios determined through Keplerian motion. For future discoveries of double-lined DWDs, this indicates that, across a large sample of systems, a DWD mass distribution could efficiently be deduced from sets of identification spectra alone, while randomly chosen candidates with precise orbital period information can guide the details of stable Roche lobe overflow and common envelope evolution in the production of compact DWD binaries.

8.3 My research goals for the near future

I will stay in academia for the foreseeable future and have many aspirations that are in line with the theme of this thesis. Firstly, I am continuing to build the DBL survey sample in both the northern and southern hemispheres to hunt for many more double-lined DWDs. While the DBL survey was introduced as a magnitude limited sample, I want to add a 100 pc volume completeness to the selection cuts. Plenty of new spectra have already obtained for this mission. Not having a volume completeness is often detrimental to many model comparisons, or limits the depth of interpretation of population statistics, motivating the cut. Moreover, for many more of the set of 34 double-lined DWDs presented in Chapter 5, I am pursuing phase-resolved spectroscopy of sources to expand the mass-period distribution.

Towards the end of my PhD, I have spent much time with teams of DWD population modelling experts to begin model calibration with the DBL sample. In my opinion, the biggest issue in DWD population modelling is that the best-fitting method to the observations is to apply an artificial angular momentum loss to the orbital evolution of systems after the first, second or both mass transfer phases to recreate populations that well reflect observed samples. The method [introduced in Nelemans et al., 2000] continues to outperform physical models [Nelemans et al., 2025], but its lack of physical meaning highlights the ambiguity of our understanding of binary star mass transfer. A reason for this may be that earlier-evolutionary-stage orbits lack eccentricity in models in comparison to the Galactic population, which in turn alters the orbital trajectory, the timing of Roche lobe overflow from the donor and hence the giant star core masses. However, this still a vibrant area of modern research. I will lead, or be closely involved in, population analysis studies in future years with updated DBL survey samples to try and shed light on this important research issue.

With the discovery of the highest total mass DWD at $1.55\,\mathrm{M}_\odot$, I want to keep pushing this maximum further. I plan to exploit data from MOS surveys to find the highest total mass and RV variable systems, characterise them and discover the most energetic type Ia supernova progenitors. The ambitious goal is to ascertain whether DWD binaries are responsible for being the majority contributors of type Ia supernovae through spectroscopic surveys. If enough massive and highly RV variable systems are found that can recover the galactic type Ia supernova rate, this would indicate DWDs as the majority contributors. Or, if none or few are found, I hope to show compelling evidence that the single-degenerate evolutionary channel in the formation of type Ia supernovae is far more significant than models predict. Furthermore, synthetic models predict total mass DWDs in excess of $2\,\mathrm{M}_\odot$, so I also want to be the first person to identify DWDs that one day may become accretion-induced collapse events, forming a neutron star.

I am continuing to research ultra-compact DWDs, both in the form of direct impacting AM CVn like HM Cnc and detached DWDs with sub-20 min orbital periods that reveal clear period derivatives on the timescale of decades. I am conducting a devoted investigation on V407 Vul to separate the WD component from the G-type star that outshines the system and well quantifying the orbital decay, perhaps making V407 Vul first ultra-compact DWD in a triple system. As spoken about in Section 1.2.2, eRASSU J060839.5-704014 gives hints of being a direct impact accretor given its X-ray pulses that are near identical to those of HM Cnc. I am obtaining observations to settle this through time-series spectroscopy and to map the possible accretion spot location through precise time-series photometry. The motivation for both of these is to best characterise the 'brightest' LISA verification sources as well as the systems closest to the end of the final stage of binary star evolution. For the same reasons, I have been monitoring J0651+2844 for multiple years to obtain a second period derivative method, as was done for HM Cnc in Chapter 3. Being detached and eclipsing, this offers the first observational opportunity to separate tidal effects from gravitational wave induced orbital decay in DWD binaries. Furthermore, once the impact of tidal interactions can be identified, this element can be accurately accounted for in the angular orbital momentum transfer of the system and hence gives the first opportunity to measure tidal synchronisation timescales in ultra-compact accreting DWD binaries, starting with HM Cnc – the prevalent component in the survivability of a DWD through period minimum into an outspiraling AM CVn.

In continuation of the work in Chapter 4, I also obtained time-series medium-resolution spectra of WDJ022558.21-692025.38 from X-Shooter on the VLT which show faint signs of the dimmer WD in the spectra at system quadrature. I am continuing to monitor the target with ULTRACAM to time eclipse arrival times. Together, all data will be one of the tightest mass constraints of any DWD owing to the 47 min orbital period being too large to be impacted by non-general relativistic angular momentum loss mechanisms yet small enough to measure the Chirp mass through the period derivative. As a double-lined and eclipsing system too, providing an independent method in obtaining system masses, all components can be simultaneously modelled to an unprecedented precision. This marks the system as a perfect individual to function as an anchor in calibrating LISA populations.

8.4 Future missions and predictions

As emphasised in Fig. 1.11, we are experiencing a boom in the exponential increase of such systems by the invent of ground-based all sky surveys monitoring changes in the night sky every couple of days. Popularity has increased in this method of exploring the universe and, with the many similar projects currently under construction and in particularly the Legacy Survey of Space and Time mission, one can expect many more fascinating binaries to appear in coming years at magnitude depths never before possible.

We are inching towards a unifying solution for the final moments of a binary's lifetime and the future of the field in 10 years will be unrecognisable from the present. The developments of new analysis methods of ultra-compact binaries will be revolutionary with the triangulation potential of LISA, indicating where to search for phenomenal binaries in even the most crowded of fields towards the Galactic bulge. Not only this, but, with gravitational waves able to traverse through material in the Galaxy, we will have a unique probe of the Galactic potential, its structure [Breivik et al., 2020], the Chirp mass-period distribution of ultra-compact DWDs and hence their contribution towards Galactic type Ia supernovae [Korol et al., 2024]. Recent estimates suggest that about 10 000 new DWDs are detectable with LISA alone [Lamberts et al., 2019; Amaro-Seoane et al., 2022]. Many DWDs in hierarchal triple star systems should become identifiable with epoch astrometry in the upcoming *Gaia* data releases 4 and 5, which could put a close to the lack of ultra-compact binaries found as a part of verification triple star systems. All of these new and old methods to characterise and identify DWDs in harmony will grant unprecedented developments in the field.

I believe that the next couple of years of DWD research will revolve around MOS survey analysis. In the field of DWD research, I foresee plenty of insight on the population to come about through accurately measuring the Galactic binary fraction in a similar way to that performed by Maoz et al. [2012]; Badenes and Maoz [2012]; Maoz and Hallakoun [2017]; Maoz et al. [2018] and I expect plenty of compact RV variable sources to arise due to mission overlaps between the likes of SDSS, DESI, 4MOST and WEAVE. Even with the likes of deeper all-sky, high cadence photometric campaigns, I believe that MOS surveys will be the primary means to identify new compact, not edge-on DWDs across all orbital periods. I also expect many more hidden companions to be revealed through randomly sampled RV variability, like WD plus M-dwarf binaries which could be the explanation for the abundance of single WDs found in Chapter 5.

As well, automated detection methods of WD binaries through machine learning algorithms are needed to quickly handle thousands or hundreds of spectra without the need for manual human vetting. This is crucial with the continued upscaling of data sources in astronomy. With machine learning being newly implemented in the field over the course of my PhD, there is some application to single WD research [Vincent et al., 2023] or a handful of cases where it has been used for white dwarf binary classification [Inight et al., 2025], but I expect that machine learning will be an essential element of many studies in the next 5 years. On top of its use to MOS spectra and general data analysis, I believe that machine learning will be at the core of many data reduction pipelines in a similar way to image enhancement on modern cameras, or even the programming of telescope observations and proposal marking.

Looking towards the beginning of the 2030s, I predict that the DWD field will take another strong turn in focus to gravitational wave research with the looming launch of LISA. Tens of papers are already centred around DWDs and LISA each year, and LISA will bring many more job opportunities with responsibilities related to data handling and analysis. I am particularly excited in the distribution of sub-20 min orbital period systems that will be discovered in all parts of the Galaxy, and I hope to see a large number of negative Chirp mass, outspiraling systems that are valuable tools for determining the evolutionary scenarios required for DWDs to survive period minimum, just like ES Ceti.

We truly are at the dawn of a series of exciting revelations and capabilities in multi-messenger astronomy.

Bibliography

C. Abate, O. R. Pols, R. G. Izzard, S. S. Mohamed, and S. E. de Mink. Wind Roche-lobe overflow: Application to carbon-enhanced metal-poor stars. *Astron. Astrophys.*, 552: A26, April 2013. doi: 10.1051/0004-6361/201220007.

Javier Abril, Linda Schmidtobreick, Alessandro Ederoclite, and Carlos López-Sanjuan. Disentangling cataclysmic variables in Gaia's HR diagram. *Mon. Not. R. Astron. Soc.*, 492(1):L40–L44, February 2020. doi: 10.1093/mnrasl/slz181.

Gautham Adamane Pallathadka, Vedant Chandra, Nadia L. Zakamska, Hsiang-Chih Hwang, Yossef Zenati, J. J. Hermes, Kareem El-Badry, Boris T. Gänsicke, Sean Morrison, Nicole R. Crumpler, and Stefan Arseneau. Discovery of a Proto–White Dwarf with a Massive Unseen Companion. *Astrophys. J.*, 968(1):42, June 2024. doi: 10.3847/1538-4357/ad3e86.

Romina Ahumada, Carlos Allende Prieto, Andrés Almeida, Friedrich Anders, Scott F. Anderson, Brett H. Andrews, Borja Anguiano, Riccardo Arcodia, Eric Armengaud, Marie Aubert, Santiago Avila, Vladimir Avila-Reese, Carles Badenes, Christophe Balland, Kat Barger, Jorge K. Barrera-Ballesteros, Sarbani Basu, Julian Bautista, Rachael L. Beaton, Timothy C. Beers, B. Izamar T. Benavides, Chad F. Bender, Mariangela Bernardi, Matthew Bershady, Florian Beutler, Christian Moni Bidin, Jonathan Bird, Dmitry Bizyaev, Guillermo A. Blanc, Michael R. Blanton, Médéric Boquien, Jura Borissova, Jo Bovy, W. N. Brandt, Jonathan Brinkmann, Joel R. Brownstein, Kevin Bundy, Martin Bureau, Adam Burgasser, Etienne Burtin, Mariana Cano-Díaz, Raffaella Capasso, Michele Cappellari, Ricardo Carrera, Solène Chabanier, William Chaplin, Michael Chapman, Brian Cherinka, Cristina Chiappini, Peter Doohyun Choi, S. Drew Chojnowski, Haeun Chung, Nicolas Clerc, Damien Coffey, Julia M. Comerford, Johan Comparat, Luiz da Costa, Marie-Claude Cousinou, Kevin Covey, Jeffrey D. Crane, Katia Cunha, Gabriele da Silva Ilha, Yu Sophia Dai, Sanna B. Damsted, Jeremy Darling, Jr. Davidson, James W., Roger Davies, Kyle Dawson, Nikhil De, Axel de la Macorra, Nathan De Lee, Anna Bárbara de Andrade Queiroz, Alice Deconto Machado, Sylvain de la

Torre, Flavia Dell'Agli, Hélion du Mas des Bourboux, Aleksandar M. Diamond-Stanic, Sean Dillon, John Donor, Niv Drory, Chris Duckworth, Tom Dwelly, Garrett Ebelke, Sarah Eftekharzadeh, Arthur Davis Eigenbrot, Yvonne P. Elsworth, Mike Eracleous, Ghazaleh Erfanianfar, Stephanie Escoffier, Xiaohui Fan, Emily Farr, José G. Fernández-Trincado, Diane Feuillet, Alexis Finoguenov, Patricia Fofie, Amelia Fraser-McKelvie, Peter M. Frinchaboy, Sebastien Fromenteau, Hai Fu, Lluís Galbany, Rafael A. Garcia, D. A. García-Hernández, Luis Alberto Garma Oehmichen, Junqiang Ge, Marcio Antonio Geimba Maia, Doug Geisler, Joseph Gelfand, Julian Goddy, Violeta Gonzalez-Perez, Kathleen Grabowski, Paul Green, Catherine J. Grier, Hong Guo, Julien Guy, Paul Harding, Sten Hasselquist, Adam James Hawken, Christian R. Hayes, Fred Hearty, S. Hekker, David W. Hogg, Jon A. Holtzman, Danny Horta, Jiamin Hou, Bau-Ching Hsieh, Daniel Huber, Jason A. S. Hunt, J. Ider Chitham, Julie Imig, Mariana Jaber, Camilo Eduardo Jimenez Angel, Jennifer A. Johnson, Amy M. Jones, Henrik Jönsson, Eric Jullo, Yerim Kim, Karen Kinemuchi, IV Kirkpatrick, Charles C., George W. Kite, Mark Klaene, Jean-Paul Kneib, Juna A. Kollmeier, Hui Kong, Marina Kounkel, Dhanesh Krishnarao, Ivan Lacerna, Ting-Wen Lan, Richard R. Lane, David R. Law, Jean-Marc Le Goff, Henry W. Leung, Hannah Lewis, Cheng Li, Jianhui Lian, Lihwai Lin, Dan Long, Penélope Longa-Peña, Britt Lundgren, Brad W. Lyke, J. Ted Mackereth, Chelsea L. MacLeod, Steven R. Majewski, Arturo Manchado, Claudia Maraston, Paul Martini, Thomas Masseron, Karen L. Masters, Savita Mathur, Richard M. McDermid, Andrea Merloni, Michael Merrifield, Szabolcs Mészáros, Andrea Miglio, Dante Minniti, Rebecca Minsley, Takamitsu Miyaji, Faizan Gohar Mohammad, Benoit Mosser, Eva-Maria Mueller, Demitri Muna, Andrea Muñoz-Gutiérrez, Adam D. Myers, Seshadri Nadathur, Preethi Nair, Kirpal Nandra, Janaina Correa do Nascimento, Rebecca Jean Nevin, Jeffrey A. Newman, David L. Nidever, Christian Nitschelm, Pasquier Noterdaeme, Julia E. O'Connell, Matthew D. Olmstead, Daniel Oravetz, Audrey Oravetz, Yeisson Osorio, Zachary J. Pace, Nelson Padilla, Nathalie Palanque-Delabrouille, Pedro A. Palicio, Hsi-An Pan, Kaike Pan, James Parker, Romain Paviot, Sebastien Peirani, Karla Peña Ramŕez, Samantha Penny, Will J. Percival, Ismael Perez-Fournon, Ignasi Pérez-Ràfols, Patrick Petitjean, Matthew M. Pieri, Marc Pinsonneault, Vijith Jacob Poovelil, Joshua Tyler Povick, Abhishek Prakash, Adrian M. Price-Whelan, M. Jordan Raddick, Anand Raichoor, Amy Ray, Sandro Barboza Rembold, Mehdi Rezaie, Rogemar A. Riffel, Rogério Riffel, Hans-Walter Rix, Annie C. Robin, A. Roman-Lopes, Carlos Román-Zúñiga, Benjamin Rose, Ashley J. Ross, Graziano Rossi, Kate Rowlands, Kate H. R. Rubin, Mara Salvato, Ariel G. Sánchez, Laura Sánchez-Menguiano, José R. Sánchez-Gallego, Conor Sayres, Adam Schaefer, Ricardo P. Schiavon, Jaderson S. Schimoia, Edward Schlafly, David Schlegel, Donald P. Schneider, Mathias Schultheis, Axel Schwope, Hee-Jong

Seo, Aldo Serenelli, Arman Shafieloo, Shoaib Jamal Shamsi, Zhengyi Shao, Shiyin Shen, Matthew Shetrone, Raphael Shirley, Víctor Silva Aguirre, Joshua D. Simon, M. F. Skrutskie, Anže Slosar, Rebecca Smethurst, Jennifer Sobeck, Bernardo Cervantes Sodi, Diogo Souto, David V. Stark, Keivan G. Stassun, Matthias Steinmetz, Dennis Stello, Julianna Stermer, Thaisa Storchi-Bergmann, Alina Streblyanska, Guy S. Stringfellow, Amelia Stutz, Genaro Suárez, Jing Sun, Manuchehr Taghizadeh-Popp, Michael S. Talbot, Jamie Tayar, Aniruddha R. Thakar, Riley Theriault, Daniel Thomas, Zak C. Thomas, Jeremy Tinker, Rita Tojeiro, Hector Hernandez Toledo, Christy A. Tremonti, Nicholas W. Troup, Sarah Tuttle, Eduardo Unda-Sanzana, Marica Valentini, Jaime Vargas-González, Mariana Vargas-Magaña, Jose Antonio Vázquez-Mata, M. Vivek, David Wake, Yuting Wang, Benjamin Alan Weaver, Anne-Marie Weijmans, Vivienne Wild, John C. Wilson, Robert F. Wilson, Nathan Wolthuis, W. M. Wood-Vasey, Renbin Yan, Meng Yang, Christophe Yèche, Olga Zamora, Pauline Zarrouk, Gail Zasowski, Kai Zhang, Cheng Zhao, Gongbo Zhao, Zheng Zheng, Zheng Zheng, Guangtun Zhu, and Hu Zou. The 16th Data Release of the Sloan Digital Sky Surveys: First Release from the APOGEE-2 Southern Survey and Full Release of eBOSS Spectra. *Astrophys. J. Suppl. Ser.*, 249(1): 3, July 2020. doi: 10.3847/1538-4365/ab929e.

Leandro G. Althaus, Alejandro H. Córsico, Jordi Isern, and Enrique García-Berro. Evolutionary and pulsational properties of white dwarf stars. *Astron. Astrophys. Rev.*, 18(4): 471–566, October 2010. doi: 10.1007/s00159-010-0033-1.

Leandro G. Althaus, Marcelo M. Miller Bertolami, and Alejandro H. Córsico. New evolutionary sequences for extremely low-mass white dwarfs. Homogeneous mass and age determinations and asteroseismic prospects. *Astron. Astrophys.*, 557:A19, September 2013. doi: 10.1051/0004-6361/201321868.

Pau Amaro-Seoane, Heather Audley, Stanislav Babak, John Baker, Enrico Barausse, Peter Bender, Emanuele Berti, Pierre Binetruy, Michael Born, Daniele Bortoluzzi, Jordan Camp, Chiara Caprini, Vitor Cardoso, Monica Colpi, John Conklin, Neil Cornish, Curt Cutler, Karsten Danzmann, Rita Dolesi, Luigi Ferraioli, Valerio Ferroni, Ewan Fitzsimons, Jonathan Gair, Lluis Gesa Bote, Domenico Giardini, Ferran Gibert, Catia Grimani, Hubert Halloin, Gerhard Heinzel, Thomas Hertog, Martin Hewitson, Kelly Holley-Bockelmann, Daniel Hollington, Mauro Hueller, Henri Inchauspe, Philippe Jetzer, Nikos Karnesis, Christian Killow, Antoine Klein, Bill Klipstein, Natalia Korsakova, Shane L Larson, Jeffrey Livas, Ivan Lloro, Nary Man, Davor Mance, Joseph Martino, Ignacio Mateos, Kirk McKenzie, Sean T McWilliams, Cole Miller, Guido Mueller, Germano Nardini, Gijs Nelemans, Miquel Nofrarias, Antoine Petiteau, Paolo Pivato, Eric Plagnol, Ed Porter, Jens Reiche, David Robertson, Norna Robertson, Elena Rossi, Giuliana Russano, Bernard Schutz, Alberto Sesana, David Shoemaker, Jacob Slutsky, Carlos F. Sopuerta, Tim Sumner, Nicola Tamanini, Ira Thorpe, Michael Troebs, Michele Vallisneri, Alberto Vecchio, Daniele Vetrugno, Stefano Vitale, Marta Volonteri, Gudrun Wanner, Harry Ward, Peter Wass, William Weber, John Ziemer, and Peter Zweifel. Laser Interferometer Space Antenna. *arXiv e-prints*, art. arXiv:1702.00786, February 2017.

Pau Amaro-Seoane, Jeff Andrews, Manuel Arca Sedda, Abbas Askar, Razvan Balasov, Imre Bartos, Simone S. Bavera, Jillian Bellovary, Christopher P. L. Berry, Emanuele Berti, Stefano Bianchi, Laura Blecha, Stéphane Blondin, Tamara Bogdanović, Samuel Boissier, Matteo Bonetti, Silvia Bonoli, Elisa Bortolas, Katie Breivik, Pedro R. Capelo, Laurentiu Caramete, Federico Catorini, Maria Charisi, Sylvain Chaty, Xian Chen, Martyna Chruślińska, Alvin J. K. Chua, Ross Church, Monica Colpi, Daniela D'Orazio, Camilla Danielski, Melvyn B. Davies, Pratika Dayal, Alessandra De Rosa, Andrea Derdzinski, Kyriakos Destounis, Massimo Dotti, Ioana Duţan, Irina Dvorkin, Gaia Fabj, Thierry Foglizzo, Saavik Ford, Jean-Baptiste Fouvry, Tassos Fragkos, Chris Fryer, Massimo Gaspari, Davide Gerosa, Luca Graziani, Paul J. Groot, Melanie Habouzit, Daryl Haggard, Zoltan Haiman, Wen-Biao Han, Alina Istrate, Peter H. Johansson, Fazeel Mahmood Khan, Tomas Kimpson, Kostas Kokkotas, Albert Kong, Valeriya Korol, Kyle Kremer, Thomas Kupfer, Astrid Lamberts, Shane Larson, Mike Lau, Dongliang Liu, Nicole Lloyd-Ronning, Giuseppe Lodato, Alessandro Lupi, Chung-Pei Ma, Tomas Maccarone, Ilya Mandel, Alberto Mangiagli, Michela Mapelli, Stefan Mathis, Lucio Mayer, Sean McGee, Berry McKernan, M. Coleman Miller, David F. Mota, Matthew Mumpower, Syeda S. Nasim, Gijs Nelemans, Scott Noble, Fabio Pacucci, Francesca Panessa, Vasileios Paschalidis, Hugo Pfister, Delphine Porquet, John Quenby, Fritz Röpke, John Regan, Stephan Rosswog, Ashley Ruiter, Milton Ruiz, Jessie Runnoe, Rafaella Schneider, Jeremy Schnittman, Amy Secunda, Alberto Sesana, Naoki Seto, Lijing Shao, Stuart Shapiro, Carlos Sopuerta, Nick Stone, Arthur Suvorov, Nicola Tamanini, Tomas Tamfal, Thomas Tauris, Karel Temmink, John Tomsick, Silvia Toonen, Alejandro Torres-Orjuela, Martina Toscani, Antonios Tsokaros, Caner Unal, Verónica Vázquez-Aceves, Rosa Valiante, Maurice van Putten, Jan van Roestel, Christian Vignali, Marta Volonteri, Kinwah Wu, Ziri Younsi, Shenghua Yu, Silvia Zane, Lorenz Zwick, Fabio Antonini, Vishal Baibhav, Enrico Barausse, Alexander Bonilla Rivera, Marica Branchesi, Graziella Branduardi-Raymont, Kevin Burdge, Srija Chakraborty, Jorge Cuadra, Kristen Dage, Benjamin Davis, Selma E. de Mink, Roberto Decarli, Daniela Doneva, Stephanie Escoffier, Poshak Gandhi, Francesco Haardt, Carlos O. Lousto, Samaya Nissanke, Jason Nordhaus, Richard O'Shaughnessy, Simon Portegies Zwart, Adam Pound, Fabian Schussler, Olga Sergijenko, Alessandro Spallicci, Daniele Vernieri, and Alejandro Vigna-Gómez. Astrophysics with the Laser Interferometer Space Antenna. *arXiv e-prints*, art.

arXiv:2203.06016, March 2022.

Pau Amaro-Seoane, Jeff Andrews, Manuel Arca Sedda, Abbas Askar, Quentin Baghi, Razvan Balasov, Imre Bartos, Simone S. Bavera, Jillian Bellovary, Christopher P. L. Berry, Emanuele Berti, Stefano Bianchi, Laura Blecha, Stéphane Blondin, Tamara Bogdanović, Samuel Boissier, Matteo Bonetti, Silvia Bonoli, Elisa Bortolas, Katelyn Breivik, Pedro R. Capelo, Laurentiu Caramete, Federico Cattorini, Maria Charisi, Sylvain Chaty, Xian Chen, Martyna Chruślińska, Alvin J. K. Chua, Ross Church, Monica Colpi, Daniel D'Orazio, Camilla Danielski, Melvyn B. Davies, Pratika Dayal, Alessandra De Rosa, Andrea Derdzinski, Kyriakos Destounis, Massimo Dotti, Ioana Dutan, Irina Dvorkin, Gaia Fabj, Thierry Foglizzo, Saavik Ford, Jean-Baptiste Fouvry, Alessia Franchini, Tassos Fragos, Chris Fryer, Massimo Gaspari, Davide Gerosa, Luca Graziani, Paul Groot, Melanie Habouzit, Daryl Haggard, Zoltan Haiman, Wen-Biao Han, Alina Istrate, Peter H. Johansson, Fazeel Mahmood Khan, Tomas Kimpson, Kostas Kokkotas, Albert Kong, Valeriya Korol, Kyle Kremer, Thomas Kupfer, Astrid Lamberts, Shane Larson, Mike Lau, Dongliang Liu, Nicole Lloyd-Ronning, Giuseppe Lodato, Alessandro Lupi, Chung-Pei Ma, Tomas Maccarone, Ilya Mandel, Alberto Mangiagli, Michela Mapelli, Stéphane Mathis, Lucio Mayer, Sean McGee, Barry McKernan, M. Coleman Miller, David F. Mota, Matthew Mumpower, Syeda S. Nasim, Gijs Nelemans, Scott Noble, Fabio Pacucci, Francesca Panessa, Vasileios Paschalidis, Hugo Pfister, Delphine Porquet, John Quenby, Angelo Ricarte, Friedrich K. Röpke, John Regan, Stephan Rosswog, Ashley Ruiter, Milton Ruiz, Jessie Runnoe, Raffaella Schneider, Jeremy Schnittman, Amy Secunda, Alberto Sesana, Naoki Seto, Lijing Shao, Stuart Shapiro, Carlos Sopuerta, Nicholas C. Stone, Arthur Suvorov, Nicola Tamanini, Tomas Tamfal, Thomas Tauris, Karel Temmink, John Tomsick, Silvia Toonen, Alejandro Torres-Orjuela, Martina Toscani, Antonios Tsokaros, Caner Unal, Verónica Vázquez-Aceves, Rosa Valiante, Maurice van Putten, Jan van Roestel, Christian Vignali, Marta Volonteri, Kinwah Wu, Ziri Younsi, Shenghua Yu, Silvia Zane, Lorenz Zwick, Fabio Antonini, Vishal Baibhav, Enrico Barausse, Alexander Bonilla Rivera, Marica Branchesi, Graziella Branduardi-Raymont, Kevin Burdge, Srija Chakraborty, Jorge Cuadra, Kristen Dage, Benjamin Davis, Selma E. de Mink, Roberto Decarli, Daniela Doneva, Stephanie Escoffier, Poshak Gandhi, Francesco Haardt, Carlos O. Lousto, Samaya Nissanke, Jason Nordhaus, Richard O'Shaughnessy, Simon Portegies Zwart, Adam Pound, Fabian Schussler, Olga Sergijenko, Alessandro Spallicci, Daniele Vernieri, and Alejandro Vigna-Gómez. Astrophysics with the Laser Interferometer Space Antenna. *Living Reviews in Relativity*, 26(1):2, December 2023. doi: 10.1007/s41114-022-00041-y.

I. Appenzeller, K. Fricke, W. Fürtig, W. Gässler, R. Häfner, R. Harke, H. J. Hess, W. Hummel, P. Jürgens, R. P. Kudritzki, K. H. Mantel, W. Meisl, B. Muschielok, H. Nicklas, G. Rupprecht, W. Seifert, O. Stahl, T. Szeifert, and K. Tarantik. Successful commissioning of FORS1 - the first optical instrument on the VLT. *The Messenger*, 94:1–6, December 1998.

Carles Badenes and Dan Maoz. The Merger Rate of Binary White Dwarfs in the Galactic Disk. *Astrophys. J. Lett.*, 749(1):L11, April 2012. doi: 10.1088/2041-8205/749/1/L11.

Stefano Bagnulo and John D. Landstreet. Multiple Channels for the Onset of Magnetism in Isolated White Dwarfs. *Astrophys. J. Lett.*, 935(1):L12, August 2022. doi: 10.3847/2041-8213/ac84d3.

C. A. L. Bailer-Jones, J. Rybizki, M. Fouesneau, M. Demleitner, and R. Andrae. Estimating Distances from Parallaxes. V. Geometric and Photogeometric Distances to 1.47 Billion Stars in Gaia Early Data Release 3. *Astron. J.*, 161(3):147, March 2021. doi: 10.3847/1538-3881/abd806.

S. C. C. Barros, T. R. Marsh, V. S. Dhillon, P. J. Groot, S. Littlefair, G. Nelemans, G. Roelofs, D. Steeghs, and P. J. Wheatley. ULTRACAM photometry of the ultracompact binaries V407 Vul and HM Cnc. *Mon. Not. R. Astron. Soc.*, 374(4):1334–1346, February 2007. doi: 10.1111/j.1365-2966.2006.11244.x.

A. Bédard, P. Bergeron, and G. Fontaine. Measurements of Physical Parameters of White Dwarfs: A Test of the Mass-Radius Relation. *Astrophys. J.*, 848(1):11, October 2017. doi: 10.3847/1538-4357/aa8bb6.

A. Bédard, P. Bergeron, P. Brassard, and G. Fontaine. On the Spectral Evolution of Hot White Dwarf Stars. I. A Detailed Model Atmosphere Analysis of Hot White Dwarfs from SDSS DR12. *Astrophys. J.*, 901(2):93, October 2020. doi: 10.3847/1538-4357/abafbe.

Eric C. Bellm, Shrinivas R. Kulkarni, Matthew J. Graham, Richard Dekany, Roger M. Smith, Reed Riddle, Frank J. Masci, George Helou, Thomas A. Prince, Scott M. Adams, C. Barbarino, Tom Barlow, James Bauer, Ron Beck, Justin Belicki, Rahul Biswas, Nadejda Blagorodnova, Dennis Bodewits, Bryce Bolin, Valery Brinnel, Tim Brooke, Brian Bue, Mattia Bulla, Rick Burruss, S. Bradley Cenko, Chan-Kao Chang, Andrew Connolly, Michael Coughlin, John Cromer, Virginia Cunningham, Kishalay De, Alex Delacroix, Vandana Desai, Dmitry A. Duev, Gwendolyn Eadie, Tony L. Farnham, Michael Feeney, Ulrich Feindt, David Flynn, Anna Franckowiak, S. Frederick, C. Fremling, Avishay Gal-Yam, Suvi Gezari, Matteo Giomi, Daniel A. Goldstein, V. Zach Golkhou, Ariel Goobar, Steven Groom, Eugean Hacopians, David Hale, John Henning, Anna Y. Q. Ho, David Hover, Justin Howell, Tiara Hung, Daniela Huppenkothen, David Imel, Wing-Huen Ip, Željko Ivezić, Edward Jackson, Lynne Jones, Mario Juric, Mansi M. Kasliwal, S. Kaspi, Stephen Kaye, Michael S. P. Kelley, Marek Kowalski, Emily Kramer, Thomas Kupfer, Walter Landry, Russ R. Laher, Chien-De Lee, Hsing Wen Lin, Zhong-Yi Lin, Ragnhild Lunnan, Matteo Giomi, Ashish Mahabal, Peter Mao, Adam A. Miller, Serge Monkewitz, Patrick Murphy, Chow-Choong Ngeow, Jakob Nordin, Peter Nugent, Eran Ofek, Maria T. Patterson, Bryan Penprase, Michael Porter, Ludwig Rauch, Umaa Rebbapragada, Dan Reiley, Mickael Rigault, Hector Rodriguez, Jan van Roestel, Ben Rusholme, Jakob van Santen, S. Schulze, David L. Shupe, Leo P. Singer, Maayane T. Soumagnac, Robert Stein, Jason Surace, Jesper Sollerman, Paula Szkody, F. Taddia, Scott Terek, Angela Van Sistine, Sjoert van Velzen, W. Thomas Vestrand, Richard Walters, Charlotte Ward, Quan-Zhi Ye, Po-Chieh Yu, Lin Yan, and Jeffry Zolkower. The Zwicky Transient Facility: System Overview, Performance, and First Results. *Publ. Astron. Soc. Pac.*, 131 (995):018002, January 2019. doi: 10.1088/1538-3873/aaecbe.

Vasily Belokurov, Zephyr Penoyre, Semyeong Oh, Giuliano Iorio, Simon Hodgkin, N. Wyn Evans, Andrew Everall, Sergey E. Koposov, Christopher A. Tout, Robert Izzard, Cathie J. Clarke, and Anthony G. A. Brown. Unresolved stellar companions with Gaia DR2 astrometry. *Mon. Not. R. Astron. Soc.*, 496(2):1922–1940, August 2020. doi: 10.1093/mnras/staa1522.

Matthew J. Benacquista. Tidal Perturbations to the Gravitational Inspiral of J0651+2844. *Astrophys. J. Lett.*, 740(2):L54, October 2011. doi: 10.1088/2041-8205/740/2/L54.

P. Bergeron and James Liebert. Spectroscopic Analysis of the DAB White Dwarf PG 1115+166: An Unresolved DA+DB Degenerate Binary. *Astrophys. J.*, 566(2):1091–1094, February 2002. doi: 10.1086/338279.

P. Bergeron, F. Wesemael, James Liebert, and G. Fontaine. Determination of the Atmospheric Parameters of the Binary DA White Dwarf L870-2 (EG 11). *Astrophys. J. Lett.*, 345:L91, October 1989. doi: 10.1086/185560.

P. Bergeron, Rex A. Saffer, and James Liebert. A Spectroscopic Determination of the Mass Distribution of DA White Dwarfs. *Astrophys. J.*, 394:228, July 1992. doi: 10.1086/171575.

P. Bergeron, P. Dufour, G. Fontaine, S. Coutu, S. Blouin, C. Genest-Beaulieu, A. Bédard, and B. Rolland. On the Measurement of Fundamental Parameters of White Dwarfs in the Gaia Era. *Astrophys. J.*, 876(1):67, May 2019. doi: 10.3847/1538-4357/ab153a.

Lars Bildsten, Ken J. Shen, Nevin N. Weinberg, and Gijs Nelemans. Faint Thermonuclear

Supernovae from AM Canum Venaticorum Binaries. *Astrophys. J. Lett.*, 662(2):L95–L98, June 2007. doi: 10.1086/519489.

K. Bąkowska, T. R. Marsh, D. Steeghs, G. Nelemans, and P. J. Groot. Spectroscopy of the helium-rich binary ES Ceti reveals accretion via a disc and evidence of eclipses. *Astron. Astrophys.*, 645:A114, January 2021. doi: 10.1051/0004-6361/202039266.

S. Blouin, P. Dufour, C. Thibeault, and N. F. Allard. A New Generation of Cool White Dwarf Atmosphere Models. IV. Revisiting the Spectral Evolution of Cool White Dwarfs. *Astrophys. J.*, 878(1):63, June 2019. doi: 10.3847/1538-4357/ab1f82.

Henri M. J. Boffin and David Jones. *The Importance of Binaries in the Formation and Evolution of Planetary Nebulae*. Springer, 2019. doi: 10.1007/978-3-030-25059-1.

A. Bonsor, A. J. Mustill, and M. C. Wyatt. Dynamical effects of stellar mass-loss on a Kuiper-like belt. *Mon. Not. R. Astron. Soc.*, 414(2):930–939, June 2011. doi: 10.1111/j.1365-2966.2011.18524.x.

Samuel J. Boos, Dean M. Townsley, Ken J. Shen, Spencer Caldwell, and Broxton J. Miles. Multidimensional Parameter Study of Double Detonation Type Ia Supernovae Originating from Thin Helium Shell White Dwarfs. *Astrophys. J.*, 919(2):126, October 2021. doi: 10.3847/1538-4357/ac07a2.

Samuel J. Boos, Dean M. Townsley, and Ken J. Shen. Type Ia Supernovae Can Arise from the Detonations of Both Stars in a Double Degenerate Binary. *Astrophys. J.*, 972(2):200, September 2024. doi: 10.3847/1538-4357/ad5da2.

M. C. P. Bours, S. Toonen, and G. Nelemans. Single degenerate supernova type Ia progenitors. Studying the influence of different mass retention efficiencies. *Astron. Astrophys.*, 552:A24, April 2013. doi: 10.1051/0004-6361/201220692.

M. C. P. Bours, T. R. Marsh, S. G. Parsons, C. M. Copperwheat, V. S. Dhillon, S. P. Littlefair, B. T. Gänsicke, A. Gianninas, and P. E. Tremblay. Precise parameters for both white dwarfs in the eclipsing binary CSS 41177. *Mon. Not. R. Astron. Soc.*, 438(4):3399–3408, March 2014. doi: 10.1093/mnras/stt2453.

M. C. P. Bours, T. R. Marsh, B. T. Gänsicke, and S. G. Parsons. HST+COS spectra of the double white dwarf CSS 41177 place the secondary inside the pulsational instability strip. *Mon. Not. R. Astron. Soc.*, 448(1):601–605, March 2015. doi: 10.1093/mnras/stv021.

Angela Bragaglia, Laura Greggio, Alvio Renzini, and Sandro D'Odorico. Double Degenerates among DA White Dwarfs. *Astrophys. J. Lett.*, 365:L13, December 1990. doi: 10.1086/185877.

E. Breedt, D. Steeghs, T. R. Marsh, N. P. Gentile Fusillo, P. E. Tremblay, M. Green, S. De Pasquale, J. J. Hermes, B. T. Gänsicke, S. G. Parsons, M. C. P. Bours, P. Longa-Peña, and A. Rebassa-Mansergas. Using large spectroscopic surveys to test the double degenerate model for Type Ia supernovae. *Mon. Not. R. Astron. Soc.*, 468(3):2910–2922, July 2017. doi: 10.1093/mnras/stx430.

Katelyn Breivik, Chiara M. F. Mingarelli, and Shane L. Larson. Constraining Galactic Structure with the LISA White Dwarf Foreground. *Astrophys. J.*, 901(1):4, September 2020. doi: 10.3847/1538-4357/abab99.

Warren R. Brown, Mukremin Kilic, Scott J. Kenyon, and A. Gianninas. Most Double Degenerate Low-mass White Dwarf Binaries Merge. *Astrophys. J.*, 824(1):46, June 2016. doi: 10.3847/0004-637X/824/1/46.

Warren R. Brown, Mukremin Kilic, A. Bédard, Alekzander Kosakowski, and P. Bergeron. A 1201 s Orbital Period Detached Binary: The First Double Helium Core White Dwarf LISA Verification Binary. *Astrophys. J. Lett.*, 892(2):L35, April 2020a. doi: 10.3847/2041-8213/ab8228.

Warren R. Brown, Mukremin Kilic, Alekzander Kosakowski, Jeff J. Andrews, Craig O. Heinke, Marcel A. Agüeros, Fernando Camilo, A. Gianninas, J. J. Hermes, and Scott J. Kenyon. The ELM Survey. VIII. Ninety-eight Double White Dwarf Binaries. *Astrophys. J.*, 889(1):49, January 2020b. doi: 10.3847/1538-4357/ab63cd.

Warren R. Brown, Mukremin Kilic, Alekzander Kosakowski, and A. Gianninas. The ELM Survey. IX. A Complete Sample of Low-mass White Dwarf Binaries in the SDSS Footprint. *Astrophys. J.*, 933(1):94, July 2022. doi: 10.3847/1538-4357/ac72ac.

Kevin B. Burdge, Michael W. Coughlin, Jim Fuller, Thomas Kupfer, Eric C. Bellm, Lars Bildsten, Matthew J. Graham, David L. Kaplan, Jan van Roestel, Richard G. Dekany, Dmitry A. Duev, Michael Feeney, Matteo Giomi, George Helou, Stephen Kaye, Russ R. Laher, Ashish A. Mahabal, Frank J. Masci, Reed Riddle, David L. Shupe, Maayane T. Soumagnac, Roger M. Smith, Paula Szkody, Richard Walters, S. R. Kulkarni, and Thomas A. Prince. General relativistic orbital decay in a seven-minute-orbital-period eclipsing binary system. *Nature*, 571(7766):528–531, July 2019a. doi: 10.1038/s41586-019-1403-0.

Kevin B. Burdge, Jim Fuller, E. Sterl Phinney, Jan van Roestel, Antonio Claret, Elena Cukanovaite, Nicola Pietro Gentile Fusillo, Michael W. Coughlin, David L. Kaplan, Thomas Kupfer, Pier-Emmanuel Tremblay, Richard G. Dekany, Dmitry A. Duev, Michael Feeney, Reed Riddle, S. R. Kulkarni, and Thomas A. Prince. Orbital Decay in a 20 Minute Orbital Period Detached Binary with a Hydrogen-poor Low-mass White Dwarf. *Astrophys. J. Lett.*, 886(1):L12, November 2019b. doi: 10.3847/2041-8213/ab53e5.

Kevin B. Burdge, Michael W. Coughlin, Jim Fuller, David L. Kaplan, S. R. Kulkarni, Thomas R. Marsh, Eric C. Bellm, Richard G. Dekany, Dmitry A. Duev, Matthew J. Graham, Ashish A. Mahabal, Frank J. Masci, Russ R. Laher, Reed Riddle, Maayane T. Soumagnac, and Thomas A. Prince. An 8.8 Minute Orbital Period Eclipsing Detached Double White Dwarf Binary. *Astrophys. J. Lett.*, 905(1):L7, December 2020a. doi: 10.3847/2041-8213/abca91.

Kevin B. Burdge, Thomas A. Prince, Jim Fuller, David L. Kaplan, Thomas R. Marsh, Pier-Emmanuel Tremblay, Zhuyun Zhuang, Eric C. Bellm, Ilaria Caiazzo, Michael W. Coughlin, Vik S. Dhillon, Boris Gaensicke, Pablo Rodríguez-Gil, Matthew J. Graham, JJ Hermes, Thomas Kupfer, S. P. Littlefair, Przemek Mróz, E. S. Phinney, Jan van Roestel, Yuhan Yao, Richard G. Dekany, Andrew J. Drake, Dmitry A. Duev, David Hale, Michael Feeney, George Helou, Stephen Kaye, Ashish. A. Mahabal, Frank J. Masci, Reed Riddle, Roger Smith, Maayane T. Soumagnac, and S. R. Kulkarni. A Systematic Search of Zwicky Transient Facility Data for Ultracompact Binary LISA-detectable Gravitational-wave Sources. *Astrophys. J.*, 905(1):32, December 2020b. doi: 10.3847/1538-4357/abc261.

B. Buzzoni, B. Delabre, H. Dekker, S. Dodorico, D. Enard, P. Focardi, B. Gustafsson, W. Nees, J. Paureau, and R. Reiss. The ESO Faint Object Spectrograph and Camera / EFOSC. *The Messenger*, 38:9, December 1984.

Leila M. Calcaferro, Leandro G. Althaus, and Alejandro H. Córsico. The coolest extremely low-mass white dwarfs. *Astron. Astrophys.*, 614:A49, June 2018. doi: 10.1051/0004-6361/201732551.

M. Camisassa, J. R. Fuentes, M. R. Schreiber, A. Rebassa-Mansergas, S. Torres, R. Raddi, and I. Dominguez. Main sequence dynamo magnetic fields emerging in the white dwarf phase. *Astron. Astrophys.*, 691:L21, November 2024. doi: 10.1051/0004-6361/202452539.

Alexandre Caron, P. Bergeron, Simon Blouin, and S. K. Leggett. A spectrophotometric analysis of cool white dwarfs in the Gaia and pan-STARRS footprint. *Mon. Not. R. Astron. Soc.*, 519(3):4529–4549, March 2023. doi: 10.1093/mnras/stac3733.

Kenneth Chambers and Pan-STARRS Team. The Pan-STARRS1 Surveys. In *American*

Astronomical Society Meeting Abstracts #231, volume 231 of *American Astronomical Society Meeting Abstracts*, page 102.01, January 2018.

Vedant Chandra, Hsiang-Chih Hwang, Nadia L. Zakamska, Boris T. Gänsicke, J. J. Hermes, Axel Schwope, Carles Badenes, Gagik Tovmassian, Evan B. Bauer, Dan Maoz, Matthias R. Schreiber, Odette F. Toloza, Keith P. Inight, Hans-Walter Rix, and Warren R. Brown. A 99 minute Double-lined White Dwarf Binary from SDSS-V. *Astrophys. J.*, 921(2):160, November 2021. doi: 10.3847/1538-4357/ac2145.

S. Chandrasekhar. The highly collapsed configurations of a stellar mass. *Mon. Not. R. Astron. Soc.*, 91:456–466, March 1931. doi: 10.1093/mnras/91.5.456.

S. Chandrasekhar. The highly collapsed configurations of a stellar mass (Second paper). *Mon. Not. R. Astron. Soc.*, 95:207–225, January 1935. doi: 10.1093/mnras/95.3.207.

Hai-Liang Chen, Xuefei Chen, and Zhanwen Han. Evolution of AM CVn binaries with WD donors. *arXiv e-prints*, art. arXiv:2207.04592, July 2022.

Sihao Cheng, Jeffrey D. Cummings, and Brice Ménard. A Cooling Anomaly of High-mass White Dwarfs. *Astrophys. J.*, 886(2):100, December 2019. doi: 10.3847/1538-4357/ab4989.

R. Chini, V. H. Hoffmeister, A. Nasseri, O. Stahl, and H. Zinnecker. A spectroscopic survey on the multiplicity of high-mass stars. *Mon. Not. R. Astron. Soc.*, 424(3):1925–1929, August 2012. doi: 10.1111/j.1365-2966.2012.21317.x.

A. Claret, E. Cukanovaite, K. Burdge, P. E. Tremblay, S. Parsons, and T. R. Marsh. Gravity and limb-darkening coefficients for compact stars: DA, DB, and DBA eclipsing white dwarfs. *Astron. Astrophys.*, 634:A93, February 2020a. doi: 10.1051/0004-6361/201937326.

A. Claret, E. Cukanovaite, K. Burdge, P. E. Tremblay, S. Parsons, and T. R. Marsh. Doppler beaming factors for white dwarfs, main sequence stars, and giant stars. Limb-darkening coefficients for 3D (DA and DB) white dwarf models. *Astron. Astrophys.*, 641:A157, September 2020b. doi: 10.1051/0004-6361/202038436.

J. Christopher Clemens, J. Adam Crain, and Robert Anderson. The Goodman spectrograph. In Alan F. M. Moorwood and Masanori Iye, editors, *Ground-based Instrumentation for Astronomy*, volume 5492 of *Society of Photo-Optical Instrumentation Engineers (SPIE) Conference Series*, pages 331–340, September 2004. doi: 10.1117/12.550069.

Christine E. Collins, Sabrina Gronow, Stuart A. Sim, and Friedrich K. Röpke. Double detonations: variations in Type Ia supernovae due to different core and He shell masses - II. Synthetic observables. *Mon. Not. R. Astron. Soc.*, 517(4):5289–5302, December 2022. doi: 10.1093/mnras/stac2665.

Christine E. Collins, Stuart A. Sim, Luke J. Shingles, Sabrina Gronow, Friedrich K. Röpke, Rüdiger Pakmor, Ivo R. Seitenzahl, and Markus Kromer. Helium as a signature of the double detonation in Type Ia supernovae. *Mon. Not. R. Astron. Soc.*, 524(3):4447–4454, September 2023. doi: 10.1093/mnras/stad2170.

Kyle E. Conroy, Angela Kochoska, Daniel Hey, Herbert Pablo, Kelly M. Hambleton, David Jones, Joseph Giammarco, Michael Abdul-Masih, and Andrej Prša. Physics of Eclipsing Binaries. V. General Framework for Solving the Inverse Problem. *Astrophys. J. Suppl. Ser.*, 250(2):34, October 2020. doi: 10.3847/1538-4365/abb4e2.

Elena Cukanovaite, Pier-Emmanuel Tremblay, Pierre Bergeron, Bernd Freytag, Hans-Günter Ludwig, and Matthias Steffen. 3D spectroscopic analysis of helium-line white dwarfs. *Mon. Not. R. Astron. Soc.*, 501(4):5274–5293, March 2021. doi: 10.1093/mnras/staa3684.

Andrew Cumming. Detectability of extrasolar planets in radial velocity surveys. *Mon. Not. R. Astron. Soc.*, 354(4):1165–1176, November 2004. doi: 10.1111/j.1365-2966.2004.08275.x.

Jeffrey D. Cummings, Jason S. Kalirai, P. E. Tremblay, Enrico Ramirez-Ruiz, and Jieun Choi. The White Dwarf Initial-Final Mass Relation for Progenitor Stars from 0.85 to 7.5 M $_\odot$. *Astrophys. J.*, 866(1):21, October 2018. doi: 10.3847/1538-4357/aadfd6.

S. Dall'Osso, G. L. Israel, and L. Stella. Astrophysical unipolar inductors powered by GW emission. *Astron. Astrophys.*, 447(3):785–796, March 2006. doi: 10.1051/0004-6361:20052843.

S. Dall'Osso, G. L. Israel, and L. Stella. Unipolar inductor model coupled to GW emission: energy budget and model application to RX J0806+15 and RX J1914+24. *Astron. Astrophys.*, 464(2):417–427, March 2007. doi: 10.1051/0004-6361:20064862.

F. D'Antona, P. Ventura, L. Burderi, and A. Teodorescu. Modeling the Closest Double Degenerate System RX J0806.3+1527 and Its Decreasing Period. *Astrophys. J.*, 653(2):1429–1434, December 2006. doi: 10.1086/507408.

Enrique de Miguel, Joseph Patterson, Jonathan Kemp, Gordon Myers, Robert Rea, Thomas Krajci, Berto Monard, and Lewis M. Cook. Orbital Period Increase in ES Ceti. *Astrophys. J.*, 852(1):19, January 2018. doi: 10.3847/1538-4357/aa9ed6.

Christopher J. Deloye and Ronald E. Taam. The Turn-On of Mass Transfer in AM CVn Binaries: Implications for RX J0806+1527 and RX J1914+2456. *Astrophys. J. Lett.*, 649 (2):L99–L102, October 2006. doi: 10.1086/508372.

V. S. Dhillon, T. R. Marsh, M. J. Stevenson, D. C. Atkinson, P. Kerry, P. T. Peacocke, A. J. A. Vick, S. M. Beard, D. J. Ives, D. W. Lunney, S. A. McLay, C. J. Tierney, J. Kelly, S. P. Littlefair, R. Nicholson, R. Pashley, E. T. Harlaftis, and K. O'Brien. ULTRACAM: an ultrafast, triple-beam CCD camera for high-speed astrophysics. *Mon. Not. R. Astron. Soc.*, 378(3):825–840, July 2007. doi: 10.1111/j.1365-2966.2007.11881.x.

V. S. Dhillon, T. R. Marsh, D. C. Atkinson, N. Bezawada, M. C. P. Bours, C. M. Copperwheat, T. Gamble, L. K. Hardy, R. D. H. Hickman, P. Irawati, D. J. Ives, P. Kerry, A. Leckngam, S. P. Littlefair, S. A. McLay, K. O'Brien, P. T. Peacocke, S. Poshyachinda, A. Richichi, B. Soonthornthum, and A. Vick. ULTRASPEC: a high-speed imaging photometer on the 2.4-m Thai National Telescope. *Mon. Not. R. Astron. Soc.*, 444(4):4009–4021, November 2014. doi: 10.1093/mnras/stu1660.

V. S. Dhillon, N. Bezawada, M. Black, S. D. Dixon, T. Gamble, X. Gao, D. M. Henry, P. Kerry, S. P. Littlefair, D. W. Lunney, T. R. Marsh, C. Miller, S. G. Parsons, R. P. Ashley, E. Breedt, A. Brown, M. J. Dyer, M. J. Green, I. Pelisoli, D. I. Sahman, J. Wild, D. J. Ives, L. Mehrgan, J. Stegmeier, C. M. Dubbeldam, T. J. Morris, J. Osborn, R. W. Wilson, J. Casares, T. Muñoz-Darias, E. Pallé, P. Rodríguez-Gil, T. Shahbaz, M. A. P. Torres, A. de Ugarte Postigo, A. Cabrera-Lavers, R. L. M. Corradi, R. D. Domínguez, and D. García-Alvarez. HiPERCAM: a quintuple-beam, high-speed optical imager on the 10.4-m Gran Telescopio Canarias. *Mon. Not. R. Astron. Soc.*, 507(1):350–366, October 2021. doi: 10.1093/mnras/stab2130.

Vik Dhillon, Simon Dixon, Trevor Gamble, Paul Kerry, Stuart Littlefair, Steven Parsons, Thomas Marsh, Naidu Bezawada, Martin Black, Xiaofeng Gao, David Henry, David Lunney, Christopher Miller, Marc Dubbeldam, Timothy Morris, James Osborn, Richard Wilson, Jorge Casares, Teo Muñoz-Darias, Enric Pallé, Pablo Rodriguez-Gil, Tariq Shahbaz, and Antonio de Ugarte Postigo. First light with HiPERCAM on the GTC. In Christopher J. Evans, Luc Simard, and Hideki Takami, editors, *Ground-based and Airborne Instrumentation for Astronomy VII*, volume 10702 of *Society of Photo-Optical Instrumentation Engineers (SPIE) Conference Series*, page 107020L, July 2018. doi: 10.1117/12.2312041.

Vikram S. Dhillon, Thomas R. Marsh, Naidu Bezawada, Martin Black, Simon Dixon, Trevor Gamble, David Henry, Paul Kerry, Stuart Littlefair, David W. Lunney, Timothy Morris, James Osborn, and Richard W. Wilson. HiPERCAM: a high-speed quintuple-beam CCD camera for the study of rapid variability in the universe. In Christopher J. Evans, Luc Simard, and Hideki Takami, editors, *Ground-based and Airborne Instrumentation for Astronomy VI*, volume 9908 of *Society of Photo-Optical Instrumentation Engineers (SPIE) Conference Series*, page 99080Y, August 2016. doi: 10.1117/12.2229055.

Ronald A. Downes and Michael M. Shara. A Catalog of Cataclysmic Variables. *Publ. Astron. Soc. Pac.*, 105:127, February 1993. doi: 10.1086/133139.

Alexandra E. Doyle, Beth L. Klein, Patrick Dufour, Carl Melis, B. Zuckerman, Siyi Xu, Alycia J. Weinberger, Isabella L. Trierweiler, Nathaniel N. Monson, Michael A. Jura, and Edward D. Young. New Chondritic Bodies Identified in Eight Oxygen-bearing White Dwarfs. *Astrophys. J.*, 950(2):93, June 2023. doi: 10.3847/1538-4357/acbd44.

A. J. Drake, S. G. Djorgovski, A. Mahabal, E. Beshore, S. Larson, M. J. Graham, R. Williams, E. Christensen, M. Catelan, A. Boattini, A. Gibbs, R. Hill, and R. Kowalski. First Results from the Catalina Real-Time Transient Survey. *Astrophys. J.*, 696(1): 870–884, May 2009. doi: 10.1088/0004-637X/696/1/870.

Reza Ebadi, Vladimir Strokov, Erwin H. Tanin, Emanuele Berti, and Ronald L. Walsworth. LISA double white dwarf binaries as Galactic accelerometers. *arXiv e-prints*, art. arXiv:2405.13109, May 2024. doi: 10.48550/arXiv.2405.13109.

P. P. Eggleton. Aproximations to the radii of Roche lobes. *Astrophys. J.*, 268:368–369, May 1983. doi: 10.1086/160960.

Kareem El-Badry and Hans-Walter Rix. Imprints of white dwarf recoil in the separation distribution of Gaia wide binaries. *Mon. Not. R. Astron. Soc.*, 480(4):4884–4902, November 2018. doi: 10.1093/mnras/sty2186.

Kareem El-Badry, Hans-Walter Rix, and Tyler M. Heintz. A million binaries from Gaia eDR3: sample selection and validation of Gaia parallax uncertainties. *Mon. Not. R. Astron. Soc.*, 506(2):2269–2295, September 2021a. doi: 10.1093/mnras/stab323.

Kareem El-Badry, Hans-Walter Rix, Eliot Quataert, Thomas Kupfer, and Ken J. Shen. Birth of the ELMs: a ZTF survey for evolved cataclysmic variables turning into extremely low-mass white dwarfs. *Mon. Not. R. Astron. Soc.*, 508(3):4106–4139, December 2021b. doi: 10.1093/mnras/stab2583.

Kareem El-Badry, Charlie Conroy, Jim Fuller, Rocio Kiman, Jan van Roestel, Antonio C. Rodriguez, and Kevin B. Burdge. Magnetic braking saturates: evidence from the orbital period distribution of low-mass detached eclipsing binaries from ZTF. *Mon. Not. R. Astron. Soc.*, 517(4):4916–4939, December 2022. doi: 10.1093/mnras/stac2945.

Kareem El-Badry, Ken J. Shen, Vedant Chandra, Evan B. Bauer, Jim Fuller, Jay Strader, Laura Chomiuk, Rohan P. Naidu, Ilaria Caiazzo, Antonio C. Rodriguez, Pranav Nagarajan, Natsuko Yamaguchi, Zachary P. Vanderbosch, Benjamin R. Roulston, Boris Gänsicke, Jiwon Jesse Han, Kevin B. Burdge, Alexei V. Filippenko, Thomas G. Brink, and WeiKang Zheng. The fastest stars in the Galaxy. *The Open Journal of Astrophysics*, 6: 28, July 2023. doi: 10.21105/astro.2306.03914.

Paolo Esposito, Gian Luca Israel, Simone Dall'Osso, and Stefano Covino. Swift X-ray and ultraviolet observations of the shortest orbital period double-degenerate system RX J0806.3+1527 (HM Cnc). *Astron. Astrophys.*, 561:A117, January 2014. doi: 10.1051/0004-6361/201322719.

M. Fink, F. K. Röpke, W. Hillebrandt, I. R. Seitenzahl, S. A. Sim, and M. Kromer. Double-detonation sub-Chandrasekhar supernovae: can minimum helium shell masses detonate the core? *Astron. Astrophys.*, 514:A53, May 2010. doi: 10.1051/0004-6361/200913892.

E. L. Fitzpatrick and D. Massa. An Analysis of the Shapes of Interstellar Extinction Curves. V. The IR-through-UV Curve Morphology. *Astrophys. J.*, 663(1):320–341, July 2007. doi: 10.1086/518158.

Edward L. Fitzpatrick. Correcting for the Effects of Interstellar Extinction. *Publ. Astron. Soc. Pac.*, 111(755):63–75, January 1999. doi: 10.1086/316293.

Daniel Foreman-Mackey, David W. Hogg, Dustin Lang, and Jonathan Goodman. emcee: The MCMC Hammer. *Publ. Astron. Soc. Pac.*, 125(925):306, March 2013. doi: 10.1086/670067.

Diana Foss, Richard A. Wade, and Richard F. Green. Limits on the Space Density of Double Degenerates as Type IA Supernova Progenitors. *Astrophys. J.*, 374:281, June 1991. doi: 10.1086/170116.

Jim Fuller and Dong Lai. Dynamical tides in compact white dwarf binaries: tidal synchronization and dissipation. *Mon. Not. R. Astron. Soc.*, 421(1):426–445, March 2012. doi: 10.1111/j.1365-2966.2011.20320.x.

Gaia Collaboration, A. G. A. Brown, A. Vallenari, T. Prusti, J. H. J. de Bruijne, F. Mignard, R. Drimmel, C. Babusiaux, C. A. L. Bailer-Jones, U. Bastian, M. Biermann, D. W.

Evans, L. Eyer, F. Jansen, C. Jordi, D. Katz, S. A. Klioner, U. Lammers, L. Lindegren, X. Luri, W. O'Mullane, C. Panem, D. Pourbaix, S. Randich, P. Sartoretti, H. I. Siddiqui, C. Soubiran, V. Valette, F. van Leeuwen, N. A. Walton, C. Aerts, F. Arenou, M. Cropper, E. Høg, M. G. Lattanzi, E. K. Grebel, A. D. Holland, C. Huc, X. Passot, M. Perryman, L. Bramante, C. Cacciari, J. Castañeda, L. Chaoul, N. Cheek, F. De Angeli, C. Fabricius, R. Guerra, J. Hernández, A. Jean-Antoine-Piccolo, E. Masana, R. Messineo, N. Mowlavi, K. Nienartowicz, D. Ordóñez-Blanco, P. Panuzzo, J. Portell, P. J. Richards, M. Riello, G. M. Seabroke, P. Tanga, F. Thévenin, J. Torra, S. G. Els, G. Gracia-Abril, G. Comoretto, M. Garcia-Reinaldos, T. Lock, E. Mercier, M. Altmann, R. Andrae, T. L. Astraatmadja, I. Bellas-Velidis, K. Benson, J. Berthier, R. Blomme, G. Busso, B. Carry, A. Cellino, G. Clementini, S. Cowell, O. Creevey, J. Cuypers, M. Davidson, J. De Ridder, A. de Torres, L. Delchambre, A. Dell'Oro, C. Ducourant, Y. Frémat, M. García-Torres, E. Gosset, J. L. Halbwachs, N. C. Hambly, D. L. Harrison, M. Hauser, D. Hestroffer, S. T. Hodgkin, H. E. Huckle, A. Hutton, G. Jasniewicz, S. Jordan, M. Kontizas, A. J. Korn, A. C. Lanzafame, M. Manteiga, A. Moitinho, K. Muinonen, J. Osinde, E. Pancino, T. Pauwels, J. M. Petit, A. Recio-Blanco, A. C. Robin, L. M. Sarro, C. Siopis, M. Smith, K. W. Smith, A. Sozzetti, W. Thuillot, W. van Reeven, Y. Viala, U. Abbas, A. Abreu Aramburu, S. Accart, J. J. Aguado, P. M. Allan, W. Allasia, G. Altavilla, M. A. Álvarez, J. Alves, R. I. Anderson, A. H. Andrei, E. Anglada Varela, E. Antiche, T. Antoja, S. Antón, B. Arcay, N. Bach, S. G. Baker, L. Balaguer-Núñez, C. Barache, C. Barata, A. Barbier, F. Barblan, D. Barrado y Navascués, M. Barros, M. A. Barstow, U. Becciani, M. Bellazzini, A. Bello García, V. Belokurov, P. Bendjoya, A. Berihuete, L. Bianchi, O. Bienaymé, F. Billebaud, N. Blagorodnova, S. Blanco-Cuaresma, T. Boch, A. Bombrun, R. Borrachero, S. Bouquillon, G. Bourda, H. Bouy, A. Bragaglia, M. A. Breddels, N. Brouillet, T. Brüsemeister, B. Bucciarelli, P. Burgess, R. Burgon, A. Burlacu, D. Busonero, R. Buzzi, E. Caffau, J. Cambras, H. Campbell, R. Cancelliere, T. Cantat-Gaudin, T. Carlucci, J. M. Carrasco, M. Castellani, P. Charlot, J. Charnas, A. Chiavassa, M. Clotet, G. Cocozza, R. S. Collins, G. Costigan, F. Crifo, N. J. G. Cross, M. Crosta, C. Crowley, C. Dafonte, Y. Damerdji, A. Dapergolas, P. David, M. David, P. De Cat, F. de Felice, P. de Laverny, F. De Luise, R. De March, D. de Martino, R. de Souza, J. Debosscher, E. del Pozo, M. Delbo, A. Delgado, H. E. Delgado, P. Di Matteo, S. Diakite, E. Distefano, C. Dolding, S. Dos Anjos, P. Drazinos, J. Duran, Y. Dzigan, B. Edvardsson, H. Enke, N. W. Evans, G. Eynard Bontemps, C. Fabre, M. Fabrizio, S. Faigler, A. J. Falcão, M. Farràs Casas, L. Federici, G. Fedorets, J. Fernández-Hernández, P. Fernique, A. Fienga, F. Figueras, F. Filippi, K. Findeisen, A. Fonti, M. Fouesneau, E. Fraile, M. Fraser, J. Fuchs, M. Gai, S. Galleti, L. Galluccio, D. Garabato, F. García-Sedano, A. Garofalo, N. Garralda, P. Gavras, J. Gerssen, R. Geyer, G. Gilmore, S. Girona,

G. Giuffrida, M. Gomes, A. González-Marcos, J. González-Núñez, J. J. González-Vidal, M. Granvik, A. Guerrier, P. Guillout, J. Guiraud, A. Gúrpide, R. Gutiérrez-Sánchez, L. P. Guy, R. Haigron, D. Hatzidimitriou, M. Haywood, U. Heiter, A. Helmi, D. Hobbs, W. Hofmann, B. Holl, G. Holland, J. A. S. Hunt, A. Hypki, V. Icardi, M. Irwin, G. Jevardat de Fombelle, P. Jofré, P. G. Jonker, A. Jorissen, F. Julbe, A. Karampelas, A. Kochoska, R. Kohley, K. Kolenberg, E. Kontizas, S. E. Koposov, G. Kordopatis, P. Koubsky, A. Krone-Martins, M. Kudryashova, I. Kull, R. K. Bachchan, F. Lacoste-Seris, A. F. Lanza, J. B. Lavigne, C. Le Poncin-Lafitte, Y. Lebreton, T. Lebzelter, S. Leccia, N. Leclerc, I. Lecoeur-Taibi, V. Lemaitre, H. Lenhardt, F. Leroux, S. Liao, E. Licata, H. E. P. Lindstrøm, T. A. Lister, E. Livanou, A. Lobel, W. Löffler, M. López, D. Lorenz, I. MacDonald, T. Magalhães Fernandes, S. Managau, R. G. Mann, G. Mantelet, O. Marchal, J. M. Marchant, M. Marconi, S. Marinoni, P. M. Marrese, G. Marschalkó, D. J. Marshall, J. M. Martín-Fleitas, M. Martino, N. Mary, G. Matijevič, T. Mazeh, P. J. McMillan, S. Messina, D. Michalik, N. R. Millar, B. M. H. Miranda, D. Molina, R. Molinaro, M. Molinaro, L. Molnár, M. Moniez, P. Montegriffo, R. Mor, A. Mora, R. Morbidelli, T. Morel, S. Morgenthaler, D. Morris, A. F. Mulone, T. Muraveva, I. Musella, J. Narbonne, G. Nelemans, L. Nicastro, L. Noval, C. Ordénovic, J. Ordieres-Meré, P. Osborne, C. Pagani, I. Pagano, F. Pailler, H. Palacin, L. Palaversa, P. Parsons, M. Pecoraro, R. Pedrosa, H. Pentikäinen, B. Pichon, A. M. Piersimoni, F. X. Pineau, E. Plachy, G. Plum, E. Poujoulet, A. Prša, L. Pulone, S. Ragaini, S. Rago, N. Rambaux, M. Ramos-Lerate, P. Ranalli, G. Rauw, A. Read, S. Regibo, C. Reylé, R. A. Ribeiro, L. Rimoldini, V. Ripepi, A. Riva, G. Rixon, M. Roelens, M. Romero-Gómez, N. Rowell, F. Royer, L. Ruiz-Dern, G. Sadowski, T. Sagristà Sellés, J. Sahlmann, J. Salgado, E. Salguero, M. Sarasso, H. Savietto, M. Schultheis, E. Sciacca, M. Segol, J. C. Segovia, D. Segransan, I. C. Shih, R. Smareglia, R. L. Smart, E. Solano, F. Solitro, R. Sordo, S. Soria Nieto, J. Souchay, A. Spagna, F. Spoto, U. Stampa, I. A. Steele, H. Steidelmüller, C. A. Stephenson, H. Stoev, F. F. Suess, M. Süveges, J. Surdej, L. Szabados, E. Szegedi-Elek, D. Tapiador, F. Taris, G. Tauran, M. B. Taylor, R. Teixeira, D. Terrett, B. Tingley, S. C. Trager, C. Turon, A. Ulla, E. Utrilla, G. Valentini, A. van Elteren, E. Van Hemelryck, M. van Leeuwen, M. Varadi, A. Vecchiato, J. Veljanoski, T. Via, D. Vicente, S. Vogt, H. Voss, V. Votruba, S. Voutsinas, G. Walmsley, M. Weiler, K. Weingrill, T. Wevers, Ł. Wyrzykowski, A. Yoldas, M. Žerjal, S. Zucker, C. Zurbach, T. Zwitter, A. Alecu, M. Allen, C. Allende Prieto, A. Amorim, G. Anglada-Escudé, V. Arsenijevic, S. Azaz, P. Balm, M. Beck, H. H. Bernstein, L. Bigot, A. Bijaoui, C. Blasco, M. Bonfigli, G. Bono, S. Boudreault, A. Bressan, S. Brown, P. M. Brunet, P. Bunclark, R. Buonanno, A. G. Butkevich, C. Carret, C. Carrion, L. Chemin, F. Chéreau, L. Corcione, E. Darmigny, K. S. de Boer, P. de Teodoro, P. T. de Zeeuw, C. Delle Luche, C. D. Domingues,

P. Dubath, F. Fodor, B. Frézouls, A. Fries, D. Fustes, D. Fyfe, E. Gallardo, J. Gallegos, D. Gardiol, M. Gebran, A. Gomboc, A. Gómez, E. Grux, A. Gueguen, A. Heyrovsky, J. Hoar, G. Iannicola, Y. Isasi Parache, A. M. Janotto, E. Joliet, A. Jonckheere, R. Keil, D. W. Kim, P. Klagyivik, J. Klar, J. Knude, O. Kochukhov, I. Kolka, J. Kos, A. Kutka, V. Lainey, D. LeBouquin, C. Liu, D. Loreggia, V. V. Makarov, M. G. Marseille, C. Martayan, O. Martinez-Rubi, B. Massart, F. Meynadier, S. Mignot, U. Munari, A. T. Nguyen, T. Nordlander, P. Ocvirk, K. S. O'Flaherty, A. Olias Sanz, P. Ortiz, J. Osorio, D. Oszkiewicz, A. Ouzounis, M. Palmer, P. Park, E. Pasquato, C. Peltzer, J. Peralta, F. Péturaud, T. Pieniluoma, E. Pigozzi, J. Poels, G. Prat, T. Prod'homme, F. Raison, J. M. Rebordao, D. Risquez, B. Rocca-Volmerange, S. Rosen, M. I. Ruiz-Fuertes, F. Russo, S. Sembay, I. Serraller Vizcaino, A. Short, A. Siebert, H. Silva, D. Sinachopoulos, E. Slezak, M. Soffel, D. Sosnowska, V. Straižys, M. ter Linden, D. Terrell, S. Theil, C. Tiede, L. Troisi, P. Tsalmantza, D. Tur, M. Vaccari, F. Vachier, P. Valles, W. Van Hamme, L. Veltz, J. Virtanen, J. M. Wallut, R. Wichmann, M. I. Wilkinson, H. Ziaeepour, and S. Zschocke. Gaia Data Release 1. Summary of the astrometric, photometric, and survey properties. *Astron. Astrophys.*, 595:A2, November 2016a. doi: 10.1051/0004-6361/201629512.

Gaia Collaboration, T. Prusti, J. H. J. de Bruijne, A. G. A. Brown, A. Vallenari, C. Babusiaux, C. A. L. Bailer-Jones, U. Bastian, M. Biermann, D. W. Evans, L. Eyer, F. Jansen, C. Jordi, S. A. Klioner, U. Lammers, L. Lindegren, X. Luri, F. Mignard, D. J. Milligan, C. Panem, V. Poinsignon, D. Pourbaix, S. Randich, G. Sarri, P. Sartoretti, H. I. Siddiqui, C. Soubiran, V. Valette, F. van Leeuwen, N. A. Walton, C. Aerts, F. Arenou, M. Cropper, R. Drimmel, E. Høg, D. Katz, M. G. Lattanzi, W. O'Mullane, E. K. Grebel, A. D. Holland, C. Huc, X. Passot, L. Bramante, C. Cacciari, J. Castañeda, L. Chaoul, N. Cheek, F. De Angeli, C. Fabricius, R. Guerra, J. Hernández, A. Jean-Antoine-Piccolo, E. Masana, R. Messineo, N. Mowlavi, K. Nienartowicz, D. Ordóñez-Blanco, P. Panuzzo, J. Portell, P. J. Richards, M. Riello, G. M. Seabroke, P. Tanga, F. Thévenin, J. Torra, S. G. Els, G. Gracia-Abril, G. Comoretto, M. Garcia-Reinaldos, T. Lock, E. Mercier, M. Altmann, R. Andrae, T. L. Astraatmadja, I. Bellas-Velidis, K. Benson, J. Berthier, R. Blomme, G. Busso, B. Carry, A. Cellino, G. Clementini, S. Cowell, O. Creevey, J. Cuypers, M. Davidson, J. De Ridder, A. de Torres, L. Delchambre, A. Dell'Oro, C. Ducourant, Y. Frémat, M. García-Torres, E. Gosset, J. L. Halbwachs, N. C. Hambly, D. L. Harrison, M. Hauser, D. Hestroffer, S. T. Hodgkin, H. E. Huckle, A. Hutton, G. Jasniewicz, S. Jordan, M. Kontizas, A. J. Korn, A. C. Lanzafame, M. Manteiga, A. Moitinho, K. Muinonen, J. Osinde, E. Pancino, T. Pauwels, J. M. Petit, A. Recio-Blanco, A. C. Robin, L. M. Sarro, C. Siopis, M. Smith, K. W. Smith, A. Sozzetti, W. Thuillot, W. van Reeven, Y. Viala, U. Abbas, A. Abreu Aramburu, S. Accart, J. J.

Aguado, P. M. Allan, W. Allasia, G. Altavilla, M. A. Álvarez, J. Alves, R. I. Anderson, A. H. Andrei, E. Anglada Varela, E. Antiche, T. Antoja, S. Antón, B. Arcay, A. Atzei, L. Ayache, N. Bach, S. G. Baker, L. Balaguer-Núñez, C. Barache, C. Barata, A. Barbier, F. Barblan, M. Baroni, D. Barrado y Navascués, M. Barros, M. A. Barstow, U. Becciani, M. Bellazzini, G. Bellei, A. Bello García, V. Belokurov, P. Bendjoya, A. Berihuete, L. Bianchi, O. Bienaymé, F. Billebaud, N. Blagorodnova, S. Blanco-Cuaresma, T. Boch, A. Bombrun, R. Borrachero, S. Bouquillon, G. Bourda, H. Bouy, A. Bragaglia, M. A. Breddels, N. Brouillet, T. Brüsemeister, B. Bucciarelli, F. Budnik, P. Burgess, R. Burgon, A. Burlacu, D. Busonero, R. Buzzi, E. Caffau, J. Cambras, H. Campbell, R. Cancelliere, T. Cantat-Gaudin, T. Carlucci, J. M. Carrasco, M. Castellani, P. Charlot, J. Charnas, P. Charvet, F. Chassat, A. Chiavassa, M. Clotet, G. Cocozza, R. S. Collins, P. Collins, G. Costigan, F. Crifo, N. J. G. Cross, M. Crosta, C. Crowley, C. Dafonte, Y. Damerdji, A. Dapergolas, P. David, M. David, P. De Cat, F. de Felice, P. de Laverny, F. De Luise, R. De March, D. de Martino, R. de Souza, J. Debosscher, E. del Pozo, M. Delbo, A. Delgado, H. E. Delgado, F. di Marco, P. Di Matteo, S. Diakite, E. Distefano, C. Dolding, S. Dos Anjos, P. Drazinos, J. Durán, Y. Dzigan, E. Ecale, B. Edvardsson, H. Enke, M. Erdmann, D. Escolar, M. Espina, N. W. Evans, G. Eynard Bontemps, C. Fabre, M. Fabrizio, S. Faigler, A. J. Falcão, M. Farràs Casas, F. Faye, L. Federici, G. Fedorets, J. Fernández-Hernández, P. Fernique, A. Fienga, F. Figueras, F. Filippi, K. Findeisen, A. Fonti, M. Fouesneau, E. Fraile, M. Fraser, J. Fuchs, R. Furnell, M. Gai, S. Galleti, L. Galluccio, D. Garabato, F. García-Sedano, P. Garé, A. Garofalo, N. Garralda, P. Gavras, J. Gerssen, R. Geyer, G. Gilmore, S. Girona, G. Giuffrida, M. Gomes, A. González-Marcos, J. González-Núñez, J. J. González-Vidal, M. Granvik, A. Guerrier, P. Guillout, J. Guiraud, A. Gúrpide, R. Gutiérrez-Sánchez, L. P. Guy, R. Haigron, D. Hatzidimitriou, M. Haywood, U. Heiter, A. Helmi, D. Hobbs, W. Hofmann, B. Holl, G. Holland, J. A. S. Hunt, A. Hypki, V. Icardi, M. Irwin, G. Jevardat de Fombelle, P. Jofré, P. G. Jonker, A. Jorissen, F. Julbe, A. Karampelas, A. Kochoska, R. Kohley, K. Kolenberg, E. Kontizas, S. E. Koposov, G. Kordopatis, P. Koubsky, A. Kowalczyk, A. Krone-Martins, M. Kudryashova, I. Kull, R. K. Bachchan, F. Lacoste-Seris, A. F. Lanza, J. B. Lavigne, C. Le Poncin-Lafitte, Y. Lebreton, T. Lebzelter, S. Leccia, N. Leclerc, I. Lecoeur-Taibi, V. Lemaitre, H. Lenhardt, F. Leroux, S. Liao, E. Licata, H. E. P. Lindstrøm, T. A. Lister, E. Livanou, A. Lobel, W. Löffler, M. López, A. Lopez-Lozano, D. Lorenz, T. Loureiro, I. MacDonald, T. Magalhães Fernandes, S. Managau, R. G. Mann, G. Mantelet, O. Marchal, J. M. Marchant, M. Marconi, J. Marie, S. Marinoni, P. M. Marrese, G. Marschalkó, D. J. Marshall, J. M. Martín-Fleitas, M. Martino, N. Mary, G. Matijevič, T. Mazeh, P. J. McMillan, S. Messina, A. Mestre, D. Michalik, N. R. Millar, B. M. H. Miranda, D. Molina, R. Molinaro, M. Molinaro, L. Molnár,

M. Moniez, P. Montegriffo, D. Monteiro, R. Mor, A. Mora, R. Morbidelli, T. Morel, S. Morgenthaler, T. Morley, D. Morris, A. F. Mulone, T. Muraveva, I. Musella, J. Narbonne, G. Nelemans, L. Nicastro, L. Noval, C. Ordénovic, J. Ordieres-Meré, P. Osborne, C. Pagani, I. Pagano, F. Pailler, H. Palacin, L. Palaversa, P. Parsons, T. Paulsen, M. Pecoraro, R. Pedrosa, H. Pentikäinen, J. Pereira, B. Pichon, A. M. Piersimoni, F. X. Pineau, E. Plachy, G. Plum, E. Poujoulet, A. Prša, L. Pulone, S. Ragaini, S. Rago, N. Rambaux, M. Ramos-Lerate, P. Ranalli, G. Rauw, A. Read, S. Regibo, F. Renk, C. Reylé, R. A. Ribeiro, L. Rimoldini, V. Ripepi, A. Riva, G. Rixon, M. Roelens, M. Romero-Gómez, N. Rowell, F. Royer, A. Rudolph, L. Ruiz-Dern, G. Sadowski, T. Sagristà Sellés, J. Sahlmann, J. Salgado, E. Salguero, M. Sarasso, H. Savietto, A. Schnorhk, M. Schultheis, E. Sciacca, M. Segol, J. C. Segovia, D. Segransan, E. Serpell, I. C. Shih, R. Smareglia, R. L. Smart, C. Smith, E. Solano, F. Solitro, R. Sordo, S. Soria Nieto, J. Souchay, A. Spagna, F. Spoto, U. Stampa, I. A. Steele, H. Steidelmüller, C. A. Stephenson, H. Stoev, F. F. Suess, M. Süveges, J. Surdej, L. Szabados, E. Szegedi-Elek, D. Tapiador, F. Taris, G. Tauran, M. B. Taylor, R. Teixeira, D. Terrett, B. Tingley, S. C. Trager, C. Turon, A. Ulla, E. Utrilla, G. Valentini, A. van Elteren, E. Van Hemelryck, M. van Leeuwen, M. Varadi, A. Vecchiato, J. Veljanoski, T. Via, D. Vicente, S. Vogt, H. Voss, V. Votruba, S. Voutsinas, G. Walmsley, M. Weiler, K. Weingrill, D. Werner, T. Wevers, G. Whitehead, Ł. Wyrzykowski, A. Yoldas, M. Žerjal, S. Zucker, C. Zurbach, T. Zwitter, A. Alecu, M. Allen, C. Allende Prieto, A. Amorim, G. Anglada-Escudé, V. Arsenijevic, S. Azaz, P. Balm, M. Beck, H. H. Bernstein, L. Bigot, A. Bijaoui, C. Blasco, M. Bonfigli, G. Bono, S. Boudreault, A. Bressan, S. Brown, P. M. Brunet, P. Bunclark, R. Buonanno, A. G. Butkevich, C. Carret, C. Carrion, L. Chemin, F. Chéreau, L. Corcione, E. Darmigny, K. S. de Boer, P. de Teodoro, P. T. de Zeeuw, C. Delle Luche, C. D. Domingues, P. Dubath, F. Fodor, B. Frézouls, A. Fries, D. Fustes, D. Fyfe, E. Gallardo, J. Gallegos, D. Gardiol, M. Gebran, A. Gomboc, A. Gómez, E. Grux, A. Gueguen, A. Heyrovsky, J. Hoar, G. Iannicola, Y. Isasi Parache, A. M. Janotto, E. Joliet, A. Jonckheere, R. Keil, D. W. Kim, P. Klagyivik, J. Klar, J. Knude, O. Kochukhov, I. Kolka, J. Kos, A. Kutka, V. Lainey, D. LeBouquin, C. Liu, D. Loreggia, V. V. Makarov, M. G. Marseille, C. Martayan, O. Martinez-Rubi, B. Massart, F. Meynadier, S. Mignot, U. Munari, A. T. Nguyen, T. Nordlander, P. Ocvirk, K. S. O'Flaherty, A. Olias Sanz, P. Ortiz, J. Osorio, D. Oszkiewicz, A. Ouzounis, M. Palmer, P. Park, E. Pasquato, C. Peltzer, J. Peralta, F. Péturaud, T. Pieniluoma, E. Pigozzi, J. Poels, G. Prat, T. Prod'homme, F. Raison, J. M. Rebordao, D. Risquez, B. Rocca-Volmerange, S. Rosen, M. I. Ruiz-Fuertes, F. Russo, S. Sembay, I. Serraller Vizcaino, A. Short, A. Siebert, H. Silva, D. Sinachopoulos, E. Slezak, M. Soffel, D. Sosnowska, V. Straižys, M. ter Linden, D. Terrell, S. Theil, C. Tiede, L. Troisi, P. Tsalmantza, D. Tur, M. Vaccari, F. Vachier,

P. Valles, W. Van Hamme, L. Veltz, J. Virtanen, J. M. Wallut, R. Wichmann, M. I. Wilkinson, H. Ziaeepour, and S. Zschocke. The Gaia mission. *Astron. Astrophys.*, 595:A1, November 2016b. doi: 10.1051/0004-6361/201629272.

Gaia Collaboration, A. G. A. Brown, A. Vallenari, T. Prusti, J. H. J. de Bruijne, C. Babusiaux, C. A. L. Bailer-Jones, M. Biermann, D. W. Evans, L. Eyer, F. Jansen, C. Jordi, S. A. Klioner, U. Lammers, L. Lindegren, X. Luri, F. Mignard, C. Panem, D. Pourbaix, S. Randich, P. Sartoretti, H. I. Siddiqui, C. Soubiran, F. van Leeuwen, N. A. Walton, F. Arenou, U. Bastian, M. Cropper, R. Drimmel, D. Katz, M. G. Lattanzi, J. Bakker, C. Cacciari, J. Castañeda, L. Chaoul, N. Cheek, F. De Angeli, C. Fabricius, R. Guerra, B. Holl, E. Masana, R. Messineo, N. Mowlavi, K. Nienartowicz, P. Panuzzo, J. Portell, M. Riello, G. M. Seabroke, P. Tanga, F. Thévenin, G. Gracia-Abril, G. Comoretto, M. Garcia-Reinaldos, D. Teyssier, M. Altmann, R. Andrae, M. Audard, I. Bellas-Velidis, K. Benson, J. Berthier, R. Blomme, P. Burgess, G. Busso, B. Carry, A. Cellino, G. Clementini, M. Clotet, O. Creevey, M. Davidson, J. De Ridder, L. Delchambre, A. Dell'Oro, C. Ducourant, J. Fernández-Hernández, M. Fouesneau, Y. Frémat, L. Galluccio, M. García-Torres, J. González-Núñez, J. J. González-Vidal, E. Gosset, L. P. Guy, J. L. Halbwachs, N. C. Hambly, D. L. Harrison, J. Hernández, D. Hestroffer, S. T. Hodgkin, A. Hutton, G. Jasniewicz, A. Jean-Antoine-Piccolo, S. Jordan, A. J. Korn, A. Krone-Martins, A. C. Lanzafame, T. Lebzelter, W. Löffler, M. Manteiga, P. M. Marrese, J. M. Martín-Fleitas, A. Moitinho, A. Mora, K. Muinonen, J. Osinde, E. Pancino, T. Pauwels, J. M. Petit, A. Recio-Blanco, P. J. Richards, L. Rimoldini, A. C. Robin, L. M. Sarro, C. Siopis, M. Smith, A. Sozzetti, M. Süveges, J. Torra, W. van Reeven, U. Abbas, A. Abreu Aramburu, S. Accart, C. Aerts, G. Altavilla, M. A. Álvarez, R. Alvarez, J. Alves, R. I. Anderson, A. H. Andrei, E. Anglada Varela, E. Antiche, T. Antoja, B. Arcay, T. L. Astraatmadja, N. Bach, S. G. Baker, L. Balaguer-Núñez, P. Balm, C. Barache, C. Barata, D. Barbato, F. Barblan, P. S. Barklem, D. Barrado, M. Barros, M. A. Barstow, S. Bartholomé Muñoz, J. L. Bassilana, U. Becciani, M. Bellazzini, A. Berihuete, S. Bertone, L. Bianchi, O. Bienaymé, S. Blanco-Cuaresma, T. Boch, C. Boeche, A. Bombrun, R. Borrachero, D. Bossini, S. Bouquillon, G. Bourda, A. Bragaglia, L. Bramante, M. A. Breddels, A. Bressan, N. Brouillet, T. Brüsemeister, E. Brugaletta, B. Bucciarelli, A. Burlacu, D. Busonero, A. G. Butkevich, R. Buzzi, E. Caffau, R. Cancelliere, G. Cannizzaro, T. Cantat-Gaudin, R. Carballo, T. Carlucci, J. M. Carrasco, L. Casamiquela, M. Castellani, A. Castro-Ginard, P. Charlot, L. Chemin, A. Chiavassa, G. Cocozza, G. Costigan, S. Cowell, F. Crifo, M. Crosta, C. Crowley, J. Cuypers, C. Dafonte, Y. Damerdji, A. Dapergolas, P. David, M. David, P. de Laverny, F. De Luise, R. De March, D. de Martino, R. de Souza, A. de Torres, J. Debosscher, E. del Pozo, M. Delbo, A. Delgado, H. E. Delgado, P. Di Matteo, S. Diakite, C. Diener, E. Distefano,

C. Dolding, P. Drazinos, J. Durán, B. Edvardsson, H. Enke, K. Eriksson, P. Esquej, G. Eynard Bontemps, C. Fabre, M. Fabrizio, S. Faigler, A. J. Falcão, M. Farràs Casas, L. Federici, G. Fedorets, P. Fernique, F. Figueras, F. Filippi, K. Findeisen, A. Fonti, E. Fraile, M. Fraser, B. Frézouls, M. Gai, S. Galleti, D. Garabato, F. García-Sedano, A. Garofalo, N. Garralda, A. Gavel, P. Gavras, J. Gerssen, R. Geyer, P. Giacobbe, G. Gilmore, S. Girona, G. Giuffrida, F. Glass, M. Gomes, M. Granvik, A. Gueguen, A. Guerrier, J. Guiraud, R. Gutiérrez-Sánchez, R. Haigron, D. Hatzidimitriou, M. Hauser, M. Haywood, U. Heiter, A. Helmi, J. Heu, T. Hilger, D. Hobbs, W. Hofmann, G. Holland, H. E. Huckle, A. Hypki, V. Icardi, K. Janßen, G. Jevardat de Fombelle, P. G. Jonker, Á. L. Juhász, F. Julbe, A. Karampelas, A. Kewley, J. Klar, A. Kochoska, R. Kohley, K. Kolenberg, M. Kontizas, E. Kontizas, S. E. Koposov, G. Kordopatis, Z. Kostrzewa-Rutkowska, P. Koubsky, S. Lambert, A. F. Lanza, Y. Lasne, J. B. Lavigne, Y. Le Fustec, C. Le Poncin-Lafitte, Y. Lebreton, S. Leccia, N. Leclerc, I. Lecoeur-Taibi, H. Lenhardt, F. Leroux, S. Liao, E. Licata, H. E. P. Lindstrøm, T. A. Lister, E. Livanou, A. Lobel, M. López, S. Managau, R. G. Mann, G. Mantelet, O. Marchal, J. M. Marchant, M. Marconi, S. Marinoni, G. Marschalkó, D. J. Marshall, M. Martino, G. Marton, N. Mary, D. Massari, G. Matijevič, T. Mazeh, P. J. McMillan, S. Messina, D. Michalik, N. R. Millar, D. Molina, R. Molinaro, L. Molnár, P. Montegriffo, R. Mor, R. Morbidelli, T. Morel, D. Morris, A. F. Mulone, T. Muraveva, I. Musella, G. Nelemans, L. Nicastro, L. Noval, W. O'Mullane, C. Ordénovic, D. Ordóñez-Blanco, P. Osborne, C. Pagani, I. Pagano, F. Pailler, H. Palacin, L. Palaversa, A. Panahi, M. Pawlak, A. M. Piersimoni, F. X. Pineau, E. Plachy, G. Plum, E. Poggio, E. Poujoulet, A. Prša, L. Pulone, E. Racero, S. Ragaini, N. Rambaux, M. Ramos-Lerate, S. Regibo, C. Reylé, F. Riclet, V. Ripepi, A. Riva, A. Rivard, G. Rixon, T. Roegiers, M. Roelens, M. Romero-Gómez, N. Rowell, F. Royer, L. Ruiz-Dern, G. Sadowski, T. Sagristà Sellés, J. Sahlmann, J. Salgado, E. Salguero, N. Sanna, T. Santana-Ros, M. Sarasso, H. Savietto, M. Schultheis, E. Sciacca, M. Segol, J. C. Segovia, D. Ségransan, I. C. Shih, L. Siltala, A. F. Silva, R. L. Smart, K. W. Smith, E. Solano, F. Solitro, R. Sordo, S. Soria Nieto, J. Souchay, A. Spagna, F. Spoto, U. Stampa, I. A. Steele, H. Steidelmüller, C. A. Stephenson, H. Stoev, F. F. Suess, J. Surdej, L. Szabados, E. Szegedi-Elek, D. Tapiador, F. Taris, G. Tauran, M. B. Taylor, R. Teixeira, D. Terrett, P. Teyssandier, W. Thuillot, A. Titarenko, F. Torra Clotet, C. Turon, A. Ulla, E. Utrilla, S. Uzzi, M. Vaillant, G. Valentini, V. Valette, A. van Elteren, E. Van Hemelryck, M. van Leeuwen, M. Vaschetto, A. Vecchiato, J. Veljanoski, Y. Viala, D. Vicente, S. Vogt, C. von Essen, H. Voss, V. Votruba, S. Voutsinas, G. Walmsley, M. Weiler, O. Wertz, T. Wevers, Ł. Wyrzykowski, A. Yoldas, M. Žerjal, H. Ziaeepour, J. Zorec, S. Zschocke, S. Zucker, C. Zurbach, and T. Zwitter. Gaia Data Release 2. Summary of the contents and survey properties. *Astron. Astrophys.*, 616:A1, August 2018.

doi: 10.1051/0004-6361/201833051.

Gaia Collaboration, A. G. A. Brown, A. Vallenari, T. Prusti, J. H. J. de Bruijne, C. Babusiaux, M. Biermann, O. L. Creevey, D. W. Evans, L. Eyer, A. Hutton, F. Jansen, C. Jordi, S. A. Klioner, U. Lammers, L. Lindegren, X. Luri, F. Mignard, C. Panem, D. Pourbaix, S. Randich, P. Sartoretti, C. Soubiran, N. A. Walton, F. Arenou, C. A. L. Bailer-Jones, U. Bastian, M. Cropper, R. Drimmel, D. Katz, M. G. Lattanzi, F. van Leeuwen, J. Bakker, C. Cacciari, J. Castañeda, F. De Angeli, C. Ducourant, C. Fabricius, M. Fouesneau, Y. Frémat, R. Guerra, A. Guerrier, J. Guiraud, A. Jean-Antoine Piccolo, E. Masana, R. Messineo, N. Mowlavi, C. Nicolas, K. Nienartowicz, F. Pailler, P. Panuzzo, F. Riclet, W. Roux, G. M. Seabroke, R. Sordo, P. Tanga, F. Thévenin, G. Gracia-Abril, J. Portell, D. Teyssier, M. Altmann, R. Andrae, I. Bellas-Velidis, K. Benson, J. Berthier, R. Blomme, E. Brugaletta, P. W. Burgess, G. Busso, B. Carry, A. Cellino, N. Cheek, G. Clementini, Y. Damerdji, M. Davidson, L. Delchambre, A. Dell'Oro, J. Fernández-Hernández, L. Galluccio, P. García-Lario, M. Garcia-Reinaldos, J. González-Núñez, E. Gosset, R. Haigron, J. L. Halbwachs, N. C. Hambly, D. L. Harrison, D. Hatzidimitriou, U. Heiter, J. Hernández, D. Hestroffer, S. T. Hodgkin, B. Holl, K. Janßen, G. Jevardat de Fombelle, S. Jordan, A. Krone-Martins, A. C. Lanzafame, W. Löffler, A. Lorca, M. Manteiga, O. Marchal, P. M. Marrese, A. Moitinho, A. Mora, K. Muinonen, P. Osborne, E. Pancino, T. Pauwels, J. M. Petit, A. Recio-Blanco, P. J. Richards, M. Riello, L. Rimoldini, A. C. Robin, T. Roegiers, J. Rybizki, L. M. Sarro, C. Siopis, M. Smith, A. Sozzetti, A. Ulla, E. Utrilla, M. van Leeuwen, W. van Reeven, U. Abbas, A. Abreu Aramburu, S. Accart, C. Aerts, J. J. Aguado, M. Ajaj, G. Altavilla, M. A. Álvarez, J. Álvarez Cid-Fuentes, J. Alves, R. I. Anderson, E. Anglada Varela, T. Antoja, M. Audard, D. Baines, S. G. Baker, L. Balaguer-Núñez, E. Balbinot, Z. Balog, C. Barache, D. Barbato, M. Barros, M. A. Barstow, S. Bartolomé, J. L. Bassilana, N. Bauchet, A. Baudesson-Stella, U. Becciani, M. Bellazzini, M. Bernet, S. Bertone, L. Bianchi, S. Blanco-Cuaresma, T. Boch, A. Bombrun, D. Bossini, S. Bouquillon, A. Bragaglia, L. Bramante, E. Breedt, A. Bressan, N. Brouillet, B. Bucciarelli, A. Burlacu, D. Busonero, A. G. Butkevich, R. Buzzi, E. Caffau, R. Cancelliere, H. Cánovas, T. Cantat-Gaudin, R. Carballo, T. Carlucci, M. I. Carnerero, J. M. Carrasco, L. Casamiquela, M. Castellani, A. Castro-Ginard, P. Castro Sampol, L. Chaoul, P. Charlot, L. Chemin, A. Chiavassa, M. R. L. Cioni, G. Comoretto, W. J. Cooper, T. Cornez, S. Cowell, F. Crifo, M. Crosta, C. Crowley, C. Dafonte, A. Dapergolas, M. David, P. David, P. de Laverny, F. De Luise, R. De March, J. De Ridder, R. de Souza, P. de Teodoro, A. de Torres, E. F. del Peloso, E. del Pozo, M. Delbo, A. Delgado, H. E. Delgado, J. B. Delisle, P. Di Matteo, S. Diakite, C. Diener, E. Distefano, C. Dolding, D. Eappachen, B. Edvardsson, H. Enke, P. Esquej, C. Fabre, M. Fabrizio, S. Faigler, G. Fedorets, P. Fernique, A. Fienga, F. Figueras, C. Fouron, F. Fragkoudi, E. Fraile, F. Franke, M. Gai, D. Garabato, A. Garcia-Gutierrez, M. García-Torres, A. Garofalo, P. Gavras, E. Gerlach, R. Geyer, P. Giacobbe, G. Gilmore, S. Girona, G. Giuffrida, R. Gomel, A. Gomez, I. Gonzalez-Santamaria, J. J. González-Vidal, M. Granvik, R. Gutiérrez-Sánchez, L. P. Guy, M. Hauser, M. Haywood, A. Helmi, S. L. Hidalgo, T. Hilger, N. Hładczuk, D. Hobbs, G. Holland, H. E. Huckle, G. Jasniewicz, P. G. Jonker, J. Juaristi Campillo, F. Julbe, L. Karbevska, P. Kervella, S. Khanna, A. Kochoska, M. Kontizas, G. Kordopatis, A. J. Korn, Z. Kostrzewa-Rutkowska, K. Kruszyńska, S. Lambert, A. F. Lanza, Y. Lasne, J. F. Le Campion, Y. Le Fustec, Y. Lebreton, T. Lebzelter, S. Leccia, N. Leclerc, I. Lecoeur-Taibi, S. Liao, E. Licata, E. P. Lindstrøm, T. A. Lister, E. Livanou, A. Lobel, P. Madrero Pardo, S. Managau, R. G. Mann, J. M. Marchant, M. Marconi, M. M. S. Marcos Santos, S. Marinoni, F. Marocco, D. J. Marshall, L. Martin Polo, J. M. Martín-Fleitas, A. Masip, D. Massari, A. Mastrobuono-Battisti, T. Mazeh, P. J. McMillan, S. Messina, D. Michalik, N. R. Millar, A. Mints, D. Molina, R. Molinaro, L. Molnár, P. Montegriffo, R. Mor, R. Morbidelli, T. Morel, D. Morris, A. F. Mulone, D. Munoz, T. Muraveva, C. P. Murphy, I. Musella, L. Noval, C. Ordénovic, G. Orrù, J. Osinde, C. Pagani, I. Pagano, L. Palaversa, P. A. Palicio, A. Panahi, M. Pawlak, X. Peñalosa Esteller, A. Penttilä, A. M. Piersimoni, F. X. Pineau, E. Plachy, G. Plum, E. Poggio, E. Poretti, E. Poujoulet, A. Prša, L. Pulone, E. Racero, S. Ragaini, M. Rainer, C. M. Raiteri, N. Rambaux, P. Ramos, M. Ramos-Lerate, P. Re Fiorentin, S. Regibo, C. Reylé, V. Ripepi, A. Riva, G. Rixon, N. Robichon, C. Robin, M. Roelens, L. Rohrbasser, M. Romero-Gómez, N. Rowell, F. Royer, K. A. Rybicki, G. Sadowski, A. Sagristà Sellés, J. Sahlmann, J. Salgado, E. Salguero, N. Samaras, V. Sanchez Gimenez, N. Sanna, R. Santoveña, M. Sarasso, M. Schultheis, E. Sciacca, M. Segol, J. C. Segovia, D. Ségransan, D. Semeux, S. Shahaf, H. I. Siddiqui, A. Siebert, L. Siltala, E. Slezak, R. L. Smart, E. Solano, F. Solitro, D. Souami, J. Souchay, A. Spagna, F. Spoto, I. A. Steele, H. Steidelmüller, C. A. Stephenson, M. Süveges, L. Szabados, E. Szegedi-Elek, F. Taris, G. Tauran, M. B. Taylor, R. Teixeira, W. Thuillot, N. Tonello, F. Torra, J. Torra, C. Turon, N. Unger, M. Vaillant, E. van Dillen, O. Vanel, A. Vecchiato, Y. Viala, D. Vicente, S. Voutsinas, M. Weiler, T. Wevers, Ł. Wyrzykowski, A. Yoldas, P. Yvard, H. Zhao, J. Zorec, S. Zucker, C. Zurbach, and T. Zwitter. Gaia Early Data Release 3. Summary of the contents and survey properties. *Astron. Astrophys.*, 649:A1, May 2021. doi: 10.1051/0004-6361/202039657.

Gaia Collaboration, A. Vallenari, A. G. A. Brown, T. Prusti, J. H. J. de Bruijne, F. Arenou, C. Babusiaux, M. Biermann, O. L. Creevey, C. Ducourant, D. W. Evans, L. Eyer, R. Guerra, A. Hutton, C. Jordi, S. A. Klioner, U. L. Lammers, L. Lindegren, X. Luri, F. Mignard, C. Panem, D. Pourbaix, S. Randich, P. Sartoretti, C. Soubiran, P. Tanga, N. A. Walton, C. A. L. Bailer-Jones, U. Bastian, R. Drimmel, F. Jansen, D. Katz,

M. G. Lattanzi, F. van Leeuwen, J. Bakker, C. Cacciari, J. Castañeda, F. De Angeli, C. Fabricius, M. Fouesneau, Y. Frémat, L. Galluccio, A. Guerrier, U. Heiter, E. Masana, R. Messineo, N. Mowlavi, C. Nicolas, K. Nienartowicz, F. Pailler, P. Panuzzo, F. Riclet, W. Roux, G. M. Seabroke, R. Sordo, F. Thévenin, G. Gracia-Abril, J. Portell, D. Teyssier, M. Altmann, R. Andrae, M. Audard, I. Bellas-Velidis, K. Benson, J. Berthier, R. Blomme, P. W. Burgess, D. Busonero, G. Busso, H. Cánovas, B. Carry, A. Cellino, N. Cheek, G. Clementini, Y. Damerdji, M. Davidson, P. de Teodoro, M. Nuñez Campos, L. Delchambre, A. Dell'Oro, P. Esquej, J. Fernández-Hernández, E. Fraile, D. Garabato, P. García-Lario, E. Gosset, R. Haigron, J. L. Halbwachs, N. C. Hambly, D. L. Harrison, J. Hernández, D. Hestroffer, S. T. Hodgkin, B. Holl, K. Janßen, G. Jevardat de Fombelle, S. Jordan, A. Krone-Martins, A. C. Lanzafame, W. Löffler, O. Marchal, P. M. Marrese, A. Moitinho, K. Muinonen, P. Osborne, E. Pancino, T. Pauwels, A. Recio-Blanco, C. Reylé, M. Riello, L. Rimoldini, T. Roegiers, J. Rybizki, L. M. Sarro, C. Siopis, M. Smith, A. Sozzetti, E. Utrilla, M. van Leeuwen, U. Abbas, P. Ábrahám, A. Abreu Aramburu, C. Aerts, J. J. Aguado, M. Ajaj, F. Aldea-Montero, G. Altavilla, M. A. Álvarez, J. Alves, F. Anders, R. I. Anderson, E. Anglada Varela, T. Antoja, D. Baines, S. G. Baker, L. Balaguer-Núñez, E. Balbinot, Z. Balog, C. Barache, D. Barbato, M. Barros, M. A. Barstow, S. Bartolomé, J. L. Bassilana, N. Bauchet, U. Becciani, M. Bellazzini, A. Berihuete, M. Bernet, S. Bertone, L. Bianchi, A. Binnenfeld, S. Blanco-Cuaresma, A. Blazere, T. Boch, A. Bombrun, D. Bossini, S. Bouquillon, A. Bragaglia, L. Bramante, E. Breedt, A. Bressan, N. Brouillet, E. Brugaletta, B. Bucciarelli, A. Burlacu, A. G. Butkevich, R. Buzzi, E. Caffau, R. Cancelliere, T. Cantat-Gaudin, R. Carballo, T. Carlucci, M. I. Carnerero, J. M. Carrasco, L. Casamiquela, M. Castellani, A. Castro-Ginard, L. Chaoul, P. Charlot, L. Chemin, V. Chiaramida, A. Chiavassa, N. Chornay, G. Comoretto, G. Contursi, W. J. Cooper, T. Cornez, S. Cowell, F. Crifo, M. Cropper, M. Crosta, C. Crowley, C. Dafonte, A. Dapergolas, M. David, P. David, P. de Laverny, F. De Luise, R. De March, J. De Ridder, R. de Souza, A. de Torres, E. F. del Peloso, E. del Pozo, M. Delbo, A. Delgado, J. B. Delisle, C. Demouchy, T. E. Dharmawardena, P. Di Matteo, S. Diakite, C. Diener, E. Distefano, C. Dolding, B. Edvardsson, H. Enke, C. Fabre, M. Fabrizio, S. Faigler, G. Fedorets, P. Fernique, A. Fienga, F. Figueras, Y. Fournier, C. Fouron, F. Fragkoudi, M. Gai, A. Garcia-Gutierrez, M. Garcia-Reinaldos, M. García-Torres, A. Garofalo, A. Gavel, P. Gavras, E. Gerlach, R. Geyer, P. Giacobbe, G. Gilmore, S. Girona, G. Giuffrida, R. Gomel, A. Gomez, J. González-Núñez, I. González-Santamaría, J. J. González-Vidal, M. Granvik, P. Guillout, J. Guiraud, R. Gutiérrez-Sánchez, L. P. Guy, D. Hatzidimitriou, M. Hauser, M. Haywood, A. Helmer, A. Helmi, M. H. Sarmiento, S. L. Hidalgo, T. Hilger, N. Hładczuk, D. Hobbs, G. Holland, H. E. Huckle, K. Jardine, G. Jasniewicz, A. Jean-Antoine Piccolo, Ó. Jiménez-Arranz,

A. Jorissen, J. Juaristi Campillo, F. Julbe, L. Karbevska, P. Kervella, S. Khanna, M. Kontizas, G. Kordopatis, A. J. Korn, Á. Kóspál, Z. Kostrzewa-Rutkowska, K. Kruszyńska, M. Kun, P. Laizeau, S. Lambert, A. F. Lanza, Y. Lasne, J. F. Le Campion, Y. Lebreton, T. Lebzelter, S. Leccia, N. Leclerc, I. Lecoeur-Taibi, S. Liao, E. L. Licata, H. E. P. Lindstrøm, T. A. Lister, E. Livanou, A. Lobel, A. Lorca, C. Loup, P. Madrero Pardo, A. Magdaleno Romeo, S. Managau, R. G. Mann, M. Manteiga, J. M. Marchant, M. Marconi, J. Marcos, M. M. S. Marcos Santos, D. Marín Pina, S. Marinoni, F. Marocco, D. J. Marshall, L. Martin Polo, J. M. Martín-Fleitas, G. Marton, N. Mary, A. Masip, D. Massari, A. Mastrobuono-Battisti, T. Mazeh, P. J. McMillan, S. Messina, D. Michalik, N. R. Millar, A. Mints, D. Molina, R. Molinaro, L. Molnár, G. Monari, M. Monguió, P. Montegriffo, A. Montero, R. Mor, A. Mora, R. Morbidelli, T. Morel, D. Morris, T. Muraveva, C. P. Murphy, I. Musella, Z. Nagy, L. Noval, F. Ocaña, A. Ogden, C. Ordenovic, J. O. Osinde, C. Pagani, I. Pagano, L. Palaversa, P. A. Palicio, L. Pallas-Quintela, A. Panahi, S. Payne-Wardenaar, X. Peñalosa Esteller, A. Penttilä, B. Pichon, A. M. Piersimoni, F. X. Pineau, E. Plachy, G. Plum, E. Poggio, A. Prša, L. Pulone, E. Racero, S. Ragaini, M. Rainer, C. M. Raiteri, N. Rambaux, P. Ramos, M. Ramos-Lerate, P. Re Fiorentin, S. Regibo, P. J. Richards, C. Rios Diaz, V. Ripepi, A. Riva, H. W. Rix, G. Rixon, N. Robichon, A. C. Robin, C. Robin, M. Roelens, H. R. O. Rogues, L. Rohrbasser, M. Romero-Gómez, N. Rowell, F. Royer, D. Ruz Mieres, K. A. Rybicki, G. Sadowski, A. Sáez Núñez, A. Sagristà Sellés, J. Sahlmann, E. Salguero, N. Samaras, V. Sanchez Gimenez, N. Sanna, R. Santoveña, M. Sarasso, M. Schultheis, E. Sciacca, M. Segol, J. C. Segovia, D. Ségransan, D. Semeux, S. Shahaf, H. I. Siddiqui, A. Siebert, L. Siltala, A. Silvelo, E. Slezak, I. Slezak, R. L. Smart, O. N. Snaith, E. Solano, F. Solitro, D. Souami, J. Souchay, A. Spagna, L. Spina, F. Spoto, I. A. Steele, H. Steidelmüller, C. A. Stephenson, M. Süveges, J. Surdej, L. Szabados, E. Szegedi-Elek, F. Taris, M. B. Taylor, R. Teixeira, L. Tolomei, N. Tonello, F. Torra, J. Torra, G. Torralba Elipe, M. Trabucchi, A. T. Tsounis, C. Turon, A. Ulla, N. Unger, M. V. Vaillant, E. van Dillen, W. van Reeven, O. Vanel, A. Vecchiato, Y. Viala, D. Vicente, S. Voutsinas, M. Weiler, T. Wevers, Ł. Wyrzykowski, A. Yoldas, P. Yvard, H. Zhao, J. Zorec, S. Zucker, and T. Zwitter. Gaia Data Release 3. Summary of the content and survey properties. *Astron. Astrophys.*, 674: A1, June 2023. doi: 10.1051/0004-6361/202243940.

Boris T. Gänsicke, Matthias R. Schreiber, Odette Toloza, Nicola P. Gentile Fusillo, Detlev Koester, and Christopher J. Manser. Accretion of a giant planet onto a white dwarf star. *Nature*, 576(7785):61–64, December 2019. doi: 10.1038/s41586-019-1789-8.

J. A. Garbutt, S. G. Parsons, O. Toloza, B. T. Gänsicke, M. S. Hernandez, D. Koester, F. Lagos, R. Raddi, A. Rebassa-Mansergas, J. J. Ren, M. R. Schreiber, and M. Zorotovic.

The white dwarf binary pathways survey - X. Gaia orbits for known UV excess binaries. *Mon. Not. R. Astron. Soc.*, 529(4):4840–4855, April 2024. doi: 10.1093/mnras/stae807.

Hongwei Ge, Michael S. Hjellming, Ronald F. Webbink, Xuefei Chen, and Zhanwen Han. Adiabatic Mass Loss in Binary Stars. I. Computational Method. *Astrophys. J.*, 717(2): 724–738, July 2010. doi: 10.1088/0004-637X/717/2/724.

Hongwei Ge, Ronald F. Webbink, Xuefei Chen, and Zhanwen Han. Adiabatic Mass Loss in Binary Stars. II. From Zero-age Main Sequence to the Base of the Giant Branch. *Astrophys. J.*, 812(1):40, October 2015. doi: 10.1088/0004-637X/812/1/40.

Hongwei Ge, Ronald F. Webbink, Xuefei Chen, and Zhanwen Han. Adiabatic Mass Loss in Binary Stars. III. From the Base of the Red Giant Branch to the Tip of the Asymptotic Giant Branch. *Astrophys. J.*, 899(2):132, August 2020. doi: 10.3847/1538-4357/aba7b7.

S. Geier, S. Nesslinger, U. Heber, N. Przybilla, R. Napiwotzki, and R. P. Kudritzki. The hot subdwarf B + white dwarf binary KPD 1930+2752. A supernova type Ia progenitor candidate. *Astron. Astrophys.*, 464(1):299–307, March 2007. doi: 10.1051/0004-6361:20066098.

C. Genest-Beaulieu and P. Bergeron. A Comprehensive Spectroscopic and Photometric Analysis of DA and DB White Dwarfs from SDSS and Gaia. *Astrophys. J.*, 871(2):169, February 2019. doi: 10.3847/1538-4357/aafac6.

N. P. Gentile Fusillo, P. E. Tremblay, E. Cukanovaite, A. Vorontseva, R. Lallement, M. Hollands, B. T. Gänsicke, K. B. Burdge, J. McCleery, and S. Jordan. A catalogue of white dwarfs in Gaia EDR3. *Mon. Not. R. Astron. Soc.*, 508(3):3877–3896, December 2021. doi: 10.1093/mnras/stab2672.

Nicola Pietro Gentile Fusillo, Pier-Emmanuel Tremblay, Boris T. Gänsicke, Christopher J. Manser, Tim Cunningham, Elena Cukanovaite, Mark Hollands, Thomas Marsh, Roberto Raddi, Stefan Jordan, Silvia Toonen, Stephan Geier, Martin Barstow, and Jeffrey D. Cummings. A Gaia Data Release 2 catalogue of white dwarfs and a comparison with SDSS. *Mon. Not. R. Astron. Soc.*, 482(4):4570–4591, February 2019. doi: 10.1093/mnras/sty3016.

Maria Georgousi, Nikolaos Karnesis, Valeriya Korol, Mauro Pieroni, and Nikolaos Stergioulas. Gravitational waves from double white dwarfs as probes of the milky way. *Mon. Not. R. Astron. Soc.*, 519(2):2552–2566, February 2023. doi: 10.1093/mnras/stac3686.

A. Gianninas, P. Bergeron, and M. T. Ruiz. A Spectroscopic Survey and Analysis of Bright, Hydrogen-rich White Dwarfs. *Astrophys. J.*, 743(2):138, December 2011. doi: 10.1088/0004-637X/743/2/138.

Hila Glanz, Hagai B. Perets, Aakash Bhat, and Ruediger Pakmor. Origins of the fastest stars from merger-disruption of He-CO white dwarfs. *arXiv e-prints*, art. arXiv:2410.17306, October 2024. doi: 10.48550/arXiv.2410.17306.

P. Goldreich and D. Lynden-Bell. Io, a jovian unipolar inductor. *Astrophys. J.*, 156:59–78, April 1969. doi: 10.1086/149947.

Karl D. Gordon, Geoffrey C. Clayton, Marjorie Decleir, E. L. Fitzpatrick, Derck Massa, Karl A. Misselt, and Erik J. Tollerud. One Relation for All Wavelengths: The Far-ultraviolet to Mid-infrared Milky Way Spectroscopic R(V)-dependent Dust Extinction Relationship. *Astrophys. J.*, 950(2):86, June 2023. doi: 10.3847/1538-4357/accb59.

James Guillochon, Marius Dan, Enrico Ramirez-Ruiz, and Stephan Rosswog. Surface Detonations in Double Degenerate Binary Systems Triggered by Accretion Stream Instabilities. *Astrophys. J. Lett.*, 709(1):L64–L69, January 2010. doi: 10.1088/2041-8205/709/1/L64.

Jincheng Guo, Jingkun Zhao, Anestis Tziamtzis, Jifeng Liu, Lifang Li, Yong Zhang, Yonghui Hou, and Yuefei Wang. White dwarfs identified in LAMOST DR 2. *Mon. Not. R. Astron. Soc.*, 454(3):2787–2797, December 2015. doi: 10.1093/mnras/stv2104.

Vasilii V. Gvaramadze, Götz Gräfener, Norbert Langer, Olga V. Maryeva, Alexei Y. Kniazev, Alexander S. Moskvitin, and Olga I. Spiridonova. A massive white-dwarf merger product before final collapse. *Nature*, 569(7758):684–687, May 2019. doi: 10.1038/s41586-019-1216-1.

Pasi Hakala, Gavin Ramsay, Kinwah Wu, Linnea Hjalmarsdotter, Silva Järvinen, Arto Järvinen, and Mark Cropper. Spin up in RX J0806+15: the shortest period binary. *Mon. Not. R. Astron. Soc.*, 343(1):L10–L14, July 2003. doi: 10.1046/j.1365-8711.2003.06830.x.

Pasi Hakala, Gavin Ramsay, and Kristiina Byckling. Monitoring the spin up in RX J0806+15. *Mon. Not. R. Astron. Soc.*, 353(2):453–456, September 2004. doi: 10.1111/j.1365-2966.2004.08074.x.

Jean-Louis Halbwachs, Dimitri Pourbaix, Frédéric Arenou, Laurent Galluccio, Patrick Guillout, Nathalie Bauchet, Olivier Marchal, Gilles Sadowski, and David Teyssier. Gaia Data Release 3. Astrometric binary star processing. *Astron. Astrophys.*, 674:A9, June 2023. doi: 10.1051/0004-6361/202243969.

N. Hallakoun, D. Maoz, M. Kilic, T. Mazeh, A. Gianninas, E. Agol, K. J. Bell, S. Bloemen, W. R. Brown, J. Debes, S. Faigler, I. Kull, T. Kupfer, A. Loeb, B. M. Morris, and F. Mullally. SDSS J1152+0248: an eclipsing double white dwarf from the Kepler K2 campaign. *Mon. Not. R. Astron. Soc.*, 458(1):845–854, May 2016. doi: 10.1093/mnras/stw364.

Z. Han, Ph. Podsiadlowski, P. F. L. Maxted, T. R. Marsh, and N. Ivanova. The origin of subdwarf B stars - I. The formation channels. *Mon. Not. R. Astron. Soc.*, 336(2):449–466, October 2002. doi: 10.1046/j.1365-8711.2002.05752.x.

Zhan-Wen Han, Hong-Wei Ge, Xue-Fei Chen, and Hai-Liang Chen. Binary Population Synthesis. *Research in Astronomy and Astrophysics*, 20(10):161, October 2020. doi: 10.1088/1674-4527/20/10/161.

Zhanwen Han. The formation of double degenerates and related objects. *Mon. Not. R. Astron. Soc.*, 296(4):1019–1040, June 1998. doi: 10.1046/j.1365-8711.1998.01475.x.

Zhanwen Han and Ronald F. Webbink. Stability and energetics of mass transfer in double white dwarfs. *Astron. Astrophys.*, 349:L17–L20, September 1999.

U. Heber, R. Napiwotzki, and I. N. Reid. Rotation velocities of white dwarf stars. *Astron. Astrophys.*, 323:819–826, July 1997.

Tyler M. Heintz, J. J. Hermes, Kareem El-Badry, Charlie Walsh, Jennifer L. van Saders, C. E. Fields, and Detlev Koester. Testing White Dwarf Age Estimates Using Wide Double White Dwarf Binaries from Gaia EDR3. *Astrophys. J.*, 934(2):148, August 2022. doi: 10.3847/1538-4357/ac78d9.

Tyler M. Heintz, J. J. Hermes, P. E. Tremblay, Lou Baya Ould Rouis, Joshua S. Reding, B. C. Kaiser, and Jennifer L. van Saders. A Test of Spectroscopic Age Estimates of White Dwarfs Using Wide WD+WD Binaries. *Astrophys. J.*, 969(1):68, July 2024. doi: 10.3847/1538-4357/ad479b.

Coel Hellier. *Cataclysmic Variable Stars*. Springer, 2001.

J. J. Hermes, Mukremin Kilic, Warren R. Brown, D. E. Winget, Carlos Allende Prieto, A. Gianninas, Anjum S. Mukadam, Antonio Cabrera-Lavers, and Scott J. Kenyon. Rapid Orbital Decay in the 12.75-minute Binary White Dwarf J0651+2844. *Astrophys. J. Lett.*, 757(2):L21, October 2012. doi: 10.1088/2041-8205/757/2/L21.

J. J. Hermes, Warren R. Brown, Mukremin Kilic, A. Gianninas, Paul Chote, D. J. Sullivan, D. E. Winget, Keaton J. Bell, R. E. Falcon, K. I. Winget, Paul A. Mason, Samuel T. Harrold, and M. H. Montgomery. Radius Constraints from High-speed Photometry of

20 Low-mass White Dwarf Binaries. *Astrophys. J.*, 792(1):39, September 2014. doi: 10.1088/0004-637X/792/1/39.

J. B. Holberg, T. D. Oswalt, E. M. Sion, and G. P. McCook. The 25 parsec local white dwarf population. *Mon. Not. R. Astron. Soc.*, 462(3):2295–2318, November 2016. doi: 10.1093/mnras/stw1357.

M. A. Hollands, P. E. Tremblay, B. T. Gaensicke, N. P. Gentile-Fusillo, and S. Toonen. The Gaia 20 pc white dwarf sample. *arXiv e-prints*, art. arXiv:1805.12590, May 2018. doi: 10.48550/arXiv.1805.12590.

M. A. Hollands, P. E. Tremblay, B. T. Gänsicke, M. E. Camisassa, D. Koester, A. Aungwerojwit, P. Chote, A. H. Córsico, V. S. Dhillon, N. P. Gentile-Fusillo, M. J. Hoskin, P. Izquierdo, T. R. Marsh, and D. Steeghs. An ultra-massive white dwarf with a mixed hydrogen-carbon atmosphere as a likely merger remnant. *Nature Astronomy*, 4:663–669, March 2020. doi: 10.1038/s41550-020-1028-0.

J. R. Holt. Spectroscopic Determination of Stellar Rotation. *Astronomy and Astro-Physics (formerly The Sidereal Messenger)*, 12:646, January 1893.

K. Horne. An optimal extraction algorithm for CCD spectroscopy. *Publ. Astron. Soc. Pac.*, 98:609–617, June 1986. doi: 10.1086/131801.

Martin Horvat, Kyle E. Conroy, Herbert Pablo, Kelly M. Hambleton, Angela Kochoska, Joseph Giammarco, and Andrej Prša. Physics of Eclipsing Binaries. III. Spin-Orbit Misalignment. *Astrophys. J. Suppl. Ser.*, 237(2):26, August 2018. doi: 10.3847/1538-4365/aacd0f.

Martin Horvat, Kyle E. Conroy, David Jones, and Andrej Prša. Bolometric Treatment of Irradiation Effects: General Discussion and Application to Binary Stars. *Astrophys. J. Suppl. Ser.*, 240(2):36, February 2019. doi: 10.3847/1538-4365/aaffd7.

R. A. Hulse and J. H. Taylor. Discovery of a pulsar in a binary system. *Astrophys. J. Lett.*, 195:L51–L53, January 1975. doi: 10.1086/181708.

Jarrod R. Hurley, Christopher A. Tout, and Onno R. Pols. Evolution of binary stars and the effect of tides on binary populations. *Mon. Not. R. Astron. Soc.*, 329(4):897–928, February 2002. doi: 10.1046/j.1365-8711.2002.05038.x.

Jr. Iben, Icko and Alexander V. Tutukov. Evolutionary Scenarios for Intermediate-Mass Stars in Close Binaries. *Astrophys. J.*, 313:727, February 1987. doi: 10.1086/165011.

Keith Inight, Boris T. Gänsicke, Axel Schwope, Scott F. Anderson, Elmé Breedt, Joel R. Brownstein, Sebastian Demasi, Susanne Friedrich, J. J. Hermes, Knox S. Long, Timothy Mulvany, Gautham Adamane Pallathadka, Mara Salvato, Simone Scaringi, Matthias R. Schreiber, Guy S. Stringfellow, John R. Thorstensen, Gagik Tovmassian, and Nadia L. Zakamska. Cataclysmic variables from Sloan Digital Sky Survey - V (2020-2023) identified using machine learning. *Mon. Not. R. Astron. Soc.*, 536(2):1057–1076, January 2025. doi: 10.1093/mnras/stae2524.

G. L. Israel, W. Hummel, S. Covino, S. Campana, I. Appenzeller, W. Gässler, K. H. Mantel, G. Marconi, C. W. Mauche, U. Munari, I. Negueruela, H. Nicklas, G. Rupprecht, R. L. Smart, O. Stahl, and L. Stella. RX J0806.3+1527: A double degenerate binary with the shortest known orbital period (321s). *Astron. Astrophys.*, 386:L13–L17, May 2002. doi: 10.1051/0004-6361:20020314.

G. L. Israel, S. Covino, S. Dall'Osso, D. Fugazza, C. W. Mauche, L. Stella, S. Campana, V. Mangano, G. Marconi, S. Bagnulo, and U. Munari. Taking the pulse of the shortest orbital period binary system RX J0806.3+1527. *Memorie della Societa Astronomica Italiana Supplementi*, 5:148–153, January 2004.

A. G. Istrate, P. Marchant, T. M. Tauris, N. Langer, R. J. Stancliffe, and L. Grassitelli. Models of low-mass helium white dwarfs including gravitational settling, thermal and chemical diffusion, and rotational mixing. *Astron. Astrophys.*, 595:A35, October 2016. doi: 10.1051/0004-6361/201628874.

N. Ivanova, S. Justham, J. L. Avendano Nandez, and J. C. Lombardi. Identification of the Long-Sought Common-Envelope Events. *Science*, 339(6118):433, January 2013a. doi: 10.1126/science.1225540.

N. Ivanova, S. Justham, X. Chen, O. De Marco, C. L. Fryer, E. Gaburov, H. Ge, E. Glebbeek, Z. Han, X. D. Li, G. Lu, T. Marsh, P. Podsiadlowski, A. Potter, N. Soker, R. Taam, T. M. Tauris, E. P. J. van den Heuvel, and R. F. Webbink. Common envelope evolution: where we stand and how we can move forward. *Astron. Astrophys. Rev.*, 21:59, February 2013b. doi: 10.1007/s00159-013-0059-2.

Paula Izquierdo, Boris T. Gänsicke, Pablo Rodríguez-Gil, Detlev Koester, Odette Toloza, Nicola P. Gentile Fusillo, Anna F. Pala, and Pier-Emmanuel Tremblay. Systematic uncertainties in the characterization of helium-dominated metal-polluted white dwarf atmospheres. *Mon. Not. R. Astron. Soc.*, 520(2):2843–2866, April 2023. doi: 10.1093/mnras/stad282.

J. H. Jeans. The Stability of a Spherical Nebula. *Philosophical Transactions of the Royal Society of London Series A*, 199:1–53, January 1902. doi: 10.1098/rsta.1902.0012.

Adam S. Jermyn, Evan B. Bauer, Josiah Schwab, R. Farmer, Warrick H. Ball, Earl P. Bellinger, Aaron Dotter, Meridith Joyce, Pablo Marchant, Joey S. G. Mombarg, William M. Wolf, Tin Long Sunny Wong, Giulia C. Cinquegrana, Eoin Farrell, R. Smolec, Anne Thoul, Matteo Cantiello, Falk Herwig, Odette Toloza, Lars Bildsten, Richard H. D. Townsend, and F. X. Timmes. Modules for Experiments in Stellar Astrophysics (MESA): Time-dependent Convection, Energy Conservation, Automatic Differentiation, and Infrastructure. *Astrophys. J. Suppl. Ser.*, 265(1):15, March 2023. doi: 10.3847/1538-4365/acae8d.

Noelia Jiménez, Patricia B. Tissera, and Francesca Matteucci. Type Ia Supernova Progenitors and Chemical Enrichment in Hydrodynamical Simulations. I. The Single-degenerate Scenario. *Astrophys. J.*, 810(2):137, September 2015. doi: 10.1088/0004-637X/810/2/137.

F. M. Jiménez-Esteban, S. Torres, A. Rebassa-Mansergas, P. Cruz, R. Murillo-Ojeda, E. Solano, C. Rodrigo, and M. E. Camisassa. Spectral classification of the 100 pc white dwarf population from Gaia-DR3 and the virtual observatory. *Mon. Not. R. Astron. Soc.*, 518(4):5106–5122, February 2023. doi: 10.1093/mnras/stac3382.

David Jones, Kyle E. Conroy, Martin Horvat, Joseph Giammarco, Angela Kochoska, Herbert Pablo, Alex J. Brown, Paulina Sowicka, and Andrej Prša. Physics of Eclipsing Binaries. IV. The Impact of Interstellar Extinction on the Light Curves of Eclipsing Binaries. *Astrophys. J. Suppl. Ser.*, 247(2):63, April 2020. doi: 10.3847/1538-4365/ab7927.

Vassiliki Kalogera and Gordon Baym. The Maximum Mass of a Neutron Star. *Astrophys. J. Lett.*, 470:L61, October 1996. doi: 10.1086/310296.

David L. Kaplan, Lars Bildsten, and Justin D. R. Steinfadt. Orbital Evolution of Compact White Dwarf Binaries. *Astrophys. J.*, 758(1):64, October 2012. doi: 10.1088/0004-637X/758/1/64.

C. A. Karl, R. Napiwotzki, G. Nelemans, N. Christlieb, D. Koester, U. Heber, and D. Reimers. Binaries discovered by the SPY project. III. HE 2209-1444: A massive, short period double degenerate. *Astron. Astrophys.*, 410:663–669, November 2003. doi: 10.1051/0004-6361:20031278.

Adela Kawka, Gordon P. Briggs, Stéphane Vennes, Lilia Ferrario, Ernst Paunzen, and Dayal T. Wickramasinghe. A fast spinning magnetic white dwarf in the double degenerate, super-Chandrasekhar system NLTT 12758. *Mon. Not. R. Astron. Soc.*, 466(1): 1127–1139, April 2017. doi: 10.1093/mnras/stw3149.

Adela Kawka, Lilia Ferrario, and Stéphane Vennes. The non-explosive stellar merging origin of the ultra-massive carbon-rich white dwarfs. *Mon. Not. R. Astron. Soc.*, 520(4): 6299–6311, April 2023. doi: 10.1093/mnras/stad553.

Pascal M. Keller, Elmé Breedt, Simon Hodgkin, Vasily Belokurov, James Wild, Ignacio García-Soriano, and Jacob L. Wise. Eclipsing white dwarf binaries in Gaia and the Zwicky Transient Faaccility. *Mon. Not. R. Astron. Soc.*, 509(3):4171–4188, January 2022. doi: 10.1093/mnras/stab3293.

S. O. Kepler, Detlev Koester, Ingrid Pelisoli, Alejandra D. Romero, and Gustavo Ourique. White dwarf and subdwarf stars in the Sloan Digital Sky Survey Data Release 16. *Mon. Not. R. Astron. Soc.*, 507(3):4646–4660, November 2021. doi: 10.1093/mnras/stab2411.

Mukremin Kilic, Warren R. Brown, Carlos Allende Prieto, S. J. Kenyon, and J. A. Panei. The Discovery of Binary White Dwarfs that will Merge Within 500 Myr. *Astrophys. J.*, 716(1):122–130, June 2010. doi: 10.1088/0004-637X/716/1/122.

Mukremin Kilic, A. Bédard, P. Bergeron, and Alekzander Kosakowski. Two new double-lined spectroscopic binary white dwarfs. *Mon. Not. R. Astron. Soc.*, 493(2):2805–2816, April 2020a. doi: 10.1093/mnras/staa466.

Mukremin Kilic, P. Bergeron, Alekzander Kosakowski, Warren R. Brown, Marcel A. Agüeros, and Simon Blouin. The 100 pc White Dwarf Sample in the SDSS Footprint. *Astrophys. J.*, 898(1):84, July 2020b. doi: 10.3847/1538-4357/ab9b8d.

Mukremin Kilic, A. Bédard, and P. Bergeron. Hidden in plain sight: a double-lined white dwarf binary 26 pc away and a distant cousin. *Mon. Not. R. Astron. Soc.*, 502(4):4972–4980, April 2021a. doi: 10.1093/mnras/stab439.

Mukremin Kilic, Warren R. Brown, A. Bédard, and Alekzander Kosakowski. The Discovery of Two LISA Sources within 0.5 kpc. *Astrophys. J. Lett.*, 918(1):L14, September 2021b. doi: 10.3847/2041-8213/ac1e2b.

Mukremin Kilic, Adam G. Moss, Alekzander Kosakowski, P. Bergeron, Annamarie A. Conly, Warren R. Brown, Silvia Toonen, Kurtis A. Williams, and P. Dufour. The merger fraction of ultramassive white dwarfs. *Mon. Not. R. Astron. Soc.*, 518(2):2341–2353, January 2023. doi: 10.1093/mnras/stac3182.

Mukremin Kilic, Pierre Bergeron, Simon Blouin, Adam Moss, Warren R. Brown, Antoine Bedard, Gracyn Jewett, and Marcel A. Agueros. The 100 pc White Dwarf Sample in the SDSS Footprint II. A New Look at the Spectral Evolution of White Dwarfs. *arXiv e-prints*, art. arXiv:2412.04611, December 2024. doi: 10.48550/arXiv.2412.04611.

D. Kilkenny, D. O'Donoghue, H. L. Worters, C. Koen, N. Hambly, and H. MacGillivray. The Edinburgh-Cape Blue Object Survey - IV. Zone 3: Galactic latitudes -40° > b > -50°. *Mon. Not. R. Astron. Soc.*, 453(2):1879–1887, October 2015. doi: 10.1093/mnras/stv1771.

Bokyoung Kim, Sebastien Lépine, and Ilija Medan. A Catalog of 531 White Dwarf Candidates in the Local Galactic Halo from Gaia Data Release 2. *Astrophys. J.*, 899(1):83, August 2020. doi: 10.3847/1538-4357/aba523.

S. J. Kleinman, S. O. Kepler, D. Koester, Ingrid Pelisoli, Viviane Peçanha, A. Nitta, J. E. S. Costa, J. Krzesinski, P. Dufour, F. R. Lachapelle, P. Bergeron, Ching-Wa Yip, Hugh C. Harris, Daniel J. Eisenstein, L. Althaus, and A. Córsico. SDSS DR7 White Dwarf Catalog. *Astrophys. J. Suppl. Ser.*, 204(1):5, January 2013. doi: 10.1088/0067-0049/204/1/5.

Christian Knigge, Isabelle Baraffe, and Joseph Patterson. The Evolution of Cataclysmic Variables as Revealed by Their Donor Stars. *Astrophys. J. Suppl. Ser.*, 194(2):28, June 2011. doi: 10.1088/0067-0049/194/2/28.

D. Koester. White dwarf spectra and atmosphere models. *Mem. Soc. Astron. Italiana*, 81: 921–931, January 2010.

D. Koester, S. Dreizler, V. Weidemann, and N. F. Allard. Search for rotation in white dwarfs. *Astron. Astrophys.*, 338:612–622, October 1998.

Zdenek Kopal. *Close binary systems*. 1959.

V. Korol, S. Toonen, A. Klein, V. Belokurov, F. Vincenzo, R. Buscicchio, D. Gerosa, C. J. Moore, E. Roebber, E. M. Rossi, and A. Vecchio. Populations of double white dwarfs in Milky Way satellites and their detectability with LISA. *Astron. Astrophys.*, 638:A153, June 2020. doi: 10.1051/0004-6361/202037764.

Valeriya Korol, Elena M. Rossi, Paul J. Groot, Gijs Nelemans, Silvia Toonen, and Anthony G. A. Brown. Prospects for detection of detached double white dwarf binaries with Gaia, LSST and LISA. *Mon. Not. R. Astron. Soc.*, 470(2):1894–1910, September 2017. doi: 10.1093/mnras/stx1285.

Valeriya Korol, Vasily Belokurov, and Silvia Toonen. A gap in the double white dwarf separation distribution caused by the common-envelope evolution: astrometric evidence from Gaia. *Mon. Not. R. Astron. Soc.*, 515(1):1228–1246, September 2022a. doi: 10.1093/mnras/stac1686.

Valeriya Korol, Na'ama Hallakoun, Silvia Toonen, and Nikolaos Karnesis. Observationally driven Galactic double white dwarf population for LISA. *Mon. Not. R. Astron. Soc.*, 511(4):5936–5947, April 2022b. doi: 10.1093/mnras/stac415.

Valeriya Korol, Riccardo Buscicchio, Ruediger Pakmor, Javier Morán-Fraile, Christopher J. Moore, and Selma E. de Mink. Expected insights into Type Ia supernovae from LISA's gravitational wave observations. *Astron. Astrophys.*, 691:A44, November 2024. doi: 10.1051/0004-6361/202451380.

A. Kosakowski, M. Kilic, W. R. Brown, P. Bergeron, and T. Kupfer. Four new deeply eclipsing white dwarfs in Zwicky Transient Facility. *Mon. Not. R. Astron. Soc.*, 516(1):720–730, October 2022. doi: 10.1093/mnras/stac1146.

Alekzander Kosakowski, Warren R. Brown, Mukremin Kilic, Thomas Kupfer, Antoine Bédard, A. Gianninas, Marcel A. Agüeros, and Manuel Barrientos. The ELM Survey South. II. Two Dozen New Low-mass White Dwarf Binaries. *Astrophys. J.*, 950(2):141, June 2023. doi: 10.3847/1538-4357/acd187.

M. Kromer and S. A. Sim. Time-dependent three-dimensional spectrum synthesis for Type Ia supernovae. *Mon. Not. R. Astron. Soc.*, 398(4):1809–1826, October 2009. doi: 10.1111/j.1365-2966.2009.15256.x.

M. Kromer, S. A. Sim, M. Fink, F. K. Röpke, I. R. Seitenzahl, and W. Hillebrandt. Double-detonation Sub-Chandrasekhar Supernovae: Synthetic Observables for Minimum Helium Shell Mass Models. *Astrophys. J.*, 719(2):1067–1082, August 2010. doi: 10.1088/0004-637X/719/2/1067.

T. Kupfer, V. Korol, S. Shah, G. Nelemans, T. R. Marsh, G. Ramsay, P. J. Groot, D. T. H. Steeghs, and E. M. Rossi. LISA verification binaries with updated distances from Gaia Data Release 2. *Mon. Not. R. Astron. Soc.*, 480(1):302–309, October 2018. doi: 10.1093/mnras/sty1545.

Thomas Kupfer, Valeriya Korol, Tyson B. Littenberg, Sweta Shah, Etienne Savalle, Paul J. Groot, Thomas R. Marsh, Maude Le Jeune, Gijs Nelemans, Anna F. Pala, Antoine Petiteau, Gavin Ramsay, Danny Steeghs, and Stanislav Babak. LISA Galactic Binaries with Astrometry from Gaia DR3. *Astrophys. J.*, 963(2):100, March 2024. doi: 10.3847/1538-4357/ad2068.

E. Lacchin, F. Calura, and E. Vesperini. On the role of Type Ia supernovae in the second-generation star formation in globular clusters. *Mon. Not. R. Astron. Soc.*, 506(4):5951–5968, October 2021. doi: 10.1093/mnras/stab2061.

R. Lallement, J. L. Vergely, C. Babusiaux, and N. L. J. Cox. Updated Gaia-2MASS 3D maps of Galactic interstellar dust. *Astron. Astrophys.*, 661:A147, May 2022. doi: 10.1051/0004-6361/202142846.

Astrid Lamberts, Sarah Blunt, Tyson B. Littenberg, Shea Garrison-Kimmel, Thomas Kupfer, and Robyn E. Sanderson. Predicting the LISA white dwarf binary population in the Milky Way with cosmological simulations. *Mon. Not. R. Astron. Soc.*, 490(4): 5888–5903, December 2019. doi: 10.1093/mnras/stz2834.

Lev Davidovich Landau and E. M. Lifshitz. *The classical theory of fields*. 1971.

Dustin Lang, David W. Hogg, Keir Mierle, Michael Blanton, and Sam Roweis. Astrometry.net: Blind Astrometric Calibration of Arbitrary Astronomical Images. *Astron. J.*, 139 (5):1782–1800, May 2010. doi: 10.1088/0004-6256/139/5/1782.

Weidong Li, Ryan Chornock, Jesse Leaman, Alexei V. Filippenko, Dovi Poznanski, Xiaofeng Wang, Mohan Ganeshalingam, and Filippo Mannucci. Nearby supernova rates from the Lick Observatory Supernova Search - III. The rate-size relation, and the rates as a function of galaxy Hubble type and colour. *Mon. Not. R. Astron. Soc.*, 412(3):1473–1507, April 2011. doi: 10.1111/j.1365-2966.2011.18162.x.

Zhenwei Li, Xuefei Chen, Hai-Liang Chen, and Zhanwen Han. Formation of Extremely Low-mass White Dwarfs in Double Degenerates. *Astrophys. J.*, 871(2):148, February 2019. doi: 10.3847/1538-4357/aaf9a1.

Zhenwei Li, Xuefei Chen, Hongwei Ge, Hai-Liang Chen, and Zhanwen Han. Influence of a mass transfer stability criterion on double white dwarf populations. *Astron. Astrophys.*, 669:A82, January 2023. doi: 10.1051/0004-6361/202243893.

James Liebert, P. Bergeron, and J. B. Holberg. The Formation Rate and Mass and Luminosity Functions of DA White Dwarfs from the Palomar Green Survey. *Astrophys. J. Suppl. Ser.*, 156(1):47–68, January 2005. doi: 10.1086/425738.

Zheng-Wei Liu, Friedrich K. Röpke, and Zhanwen Han. Type Ia Supernova Explosions in Binary Systems: A Review. *Research in Astronomy and Astrophysics*, 23(8):082001, August 2023. doi: 10.1088/1674-4527/acd89e.

Eli Livne. Successive Detonations in Accreting White Dwarfs as an Alternative Mechanism for Type I Supernovae. *Astrophys. J. Lett.*, 354:L53, May 1990. doi: 10.1086/185721.

N. R. Lomb. Least-Squares Frequency Analysis of Unequally Spaced Data. *Astrophys. Space Sci.*, 39(2):447–462, February 1976. doi: 10.1007/BF00648343.

Changqing Luo, Jiao Li, Chuanjie Zheng, Dongdong Liu, Zhenwei Li, Yangping Luo, Peter Nemeth, Bo Zhang, Jianping Xiong, Bo Wang, Song Wang, Yu Bai, Qingzheng Li, Pei Wang, Zhanwen Han, Jifeng Liu, Yang Huang, Xuefei Chen, and Chao Liu. A born ultramassive white dwarf-hot subdwarf super-Chandrasekhar candidate. *arXiv e-prints*, art. arXiv:2404.04835, April 2024. doi: 10.48550/arXiv.2404.04835.

Jun Luo, Li-Sheng Chen, Hui-Zong Duan, Yun-Gui Gong, Shoucun Hu, Jianghui Ji, Qi Liu, Jianwei Mei, Vadim Milyukov, Mikhail Sazhin, Cheng-Gang Shao, Viktor T. Toth, Hai-Bo Tu, Yamin Wang, Yan Wang, Hsien-Chi Yeh, Ming-Sheng Zhan, Yonghe Zhang, Vladimir Zharov, and Ze-Bing Zhou. TianQin: a space-borne gravitational wave detector. *Classical and Quantum Gravity*, 33(3):035010, February 2016. doi: 10.1088/0264-9381/33/3/035010.

C. Maitra, F. Haberl, G. Vasilopoulos, A. Rau, A. Schwope, S. Friedrich, D. A. H. Buckley, F. Valdes, D. Lang, and S. A. Macfarlane. eRASSUJ060839.5-704014: A double degenerate ultra-compact binary in the direction of the LMC. *arXiv e-prints*, art. arXiv:2401.17293, January 2024. doi: 10.48550/arXiv.2401.17293.

Christopher J. Manser, Paula Izquierdo, Boris T. Gänsicke, Andrew Swan, Detlev Koester, Akshay Robert, Siyi Xu, Keith Inight, Ben Amroota, N. P. Gentile Fusillo, Sergey E. Koposov, Bokyoung Kim, Arjun Dey, Carlos Allende Prieto, J. Aguilar, S. Ahlen, R. Blum, D. Brooks, T. Claybaugh, A. P. Cooper, K. Dawson, A. de la Macorra, P. Doel, J. E. Forero-Romero, E. Gaztañaga, S. Gontcho A Gontcho, K. Honscheid, T. Kisner, A. Kremin, A. Lambert, M. Landriau, L. Le Guillou, Michael E. Levi, T. S. Li, A. Meisner, R. Miquel, J. Moustakas, J. Nie, N. Palanque-Delabrouille, W. J. Percival, C. Poppett, F. Prada, M. Rezaie, G. Rossi, E. Sanchez, E. F. Schlafly, D. Schlegel, M. Schubnell, H. Seo, J. Silber, G. Tarlé, B. A. Weaver, Z. Zhou, and H. Zou. The DESI Early Data Release White Dwarf Catalogue. *arXiv e-prints*, art. arXiv:2402.18641, February 2024. doi: 10.48550/arXiv.2402.18641.

D. Maoz and F. Mannucci. Type-Ia Supernova Rates and the Progenitor Problem: A Review. *Publ. Astron. Soc. Aust.*, 29(4):447–465, January 2012. doi: 10.1071/AS11052.

Dan Maoz and Na'ama Hallakoun. The binary fraction, separation distribution, and merger rate of white dwarfs from SPY. *Mon. Not. R. Astron. Soc.*, 467(2):1414–1425, May 2017. doi: 10.1093/mnras/stx102.

Dan Maoz, Carles Badenes, and Steven J. Bickerton. Characterizing the Galactic White Dwarf Binary Population with Sparsely Sampled Radial Velocity Data. *Astrophys. J.*, 751(2):143, June 2012. doi: 10.1088/0004-637X/751/2/143.

Dan Maoz, Filippo Mannucci, and Gijs Nelemans. Observational Clues to the Progenitors of Type Ia Supernovae. *Annu. Rev. Astron. Astrophys.*, 52:107–170, August 2014. doi: 10.1146/annurev-astro-082812-141031.

Dan Maoz, Na'ama Hallakoun, and Carles Badenes. The separation distribution and merger rate of double white dwarfs: improved constraints. *Mon. Not. R. Astron. Soc.*, 476(2): 2584–2590, May 2018. doi: 10.1093/mnras/sty339.

T. R. Marsh. The Extraction of Highly Distorted Spectra. *Publ. Astron. Soc. Pac.*, 101: 1032, November 1989. doi: 10.1086/132570.

T. R. Marsh. The discovery of a short-period double-degenerate binary star. *Mon. Not. R. Astron. Soc.*, 275(1):L1–L5, July 1995. doi: 10.1093/mnras/275.1.L1.

T. R. Marsh. Gravitational lensing in eclipsing binary stars. *Mon. Not. R. Astron. Soc.*, 324 (3):547–552, June 2001. doi: 10.1046/j.1365-8711.2001.04293.x.

T. R. Marsh. Double white dwarfs and LISA. *Classical and Quantum Gravity*, 28(9): 094019, May 2011. doi: 10.1088/0264-9381/28/9/094019.

T. R. Marsh and D. Steeghs. V407 Vul: a direct impact accretor. *Mon. Not. R. Astron. Soc.*, 331(1):L7–L11, March 2002. doi: 10.1046/j.1365-8711.2002.05346.x.

T. R. Marsh, V. S. Dhillon, and S. R. Duck. Low-Mass White Dwarfs Need Friends - Five New Double-Degenerate Close Binary Stars. *Mon. Not. R. Astron. Soc.*, 275:828, August 1995. doi: 10.1093/mnras/275.3.828.

T. R. Marsh, G. Nelemans, and D. Steeghs. Mass transfer between double white dwarfs. *Mon. Not. R. Astron. Soc.*, 350(1):113–128, May 2004. doi: 10.1111/j.1365-2966.2004.07564.x.

Tom Marsh. molly: 1D astronomical spectra analyzer. Astrophysics Source Code Library, record ascl:1907.012, July 2019.

J. L. Marshall, Scott Burles, Ian B. Thompson, Stephen A. Shectman, Bruce C. Bigelow, Gregory Burley, Christoph Birk, Jorge Estrada, Patricio Jones, Matthew Smith, Vince Kowal, Jerson Castillo, Robert Storts, and Greg Ortiz. The MagE spectrograph. In Ian S. McLean and Mark M. Casali, editors, *Ground-based and Airborne Instrumentation* *for Astronomy II*, volume 7014 of *Society of Photo-Optical Instrumentation Engineers (SPIE) Conference Series*, page 701454, July 2008. doi: 10.1117/12.789972.

Elena Mason, G. L. Israel, S. Dall'Osso, L. Stella, U. Munari, G. Marconi, K. O'Brian, S. Covino, and D. Fugazza. VLT Phase Resolved Optical Spectroscopy of the Ultra-Compact Binary HM Cnc. *arXiv e-prints*, art. arXiv:1003.1986, March 2010.

P. F. L. Maxted and T. R. Marsh. The fraction of double degenerates among DA white dwarfs. *Mon. Not. R. Astron. Soc.*, 307(1):122–132, July 1999. doi: 10.1046/j.1365-8711.1999.02635.x.

P. F. L. Maxted, T. R. Marsh, and R. C. North. KPD 1930+2752: a candidate Type Ia supernova progenitor. *Mon. Not. R. Astron. Soc.*, 317(3):L41–L44, September 2000. doi: 10.1046/j.1365-8711.2000.03856.x.

P. F. L. Maxted, M. R. Burleigh, T. R. Marsh, and N. P. Bannister. PG 1115+166 - a long-period DA+DB binary. *Mon. Not. R. Astron. Soc.*, 334(4):833–839, August 2002a. doi: 10.1046/j.1365-8711.2002.05545.x.

P. F. L. Maxted, T. R. Marsh, and C. K. J. Moran. The mass ratio distribution of short-period double degenerate stars. *Mon. Not. R. Astron. Soc.*, 332(3):745–753, May 2002b. doi: 10.1046/j.1365-8711.2002.05368.x.

Jack McCleery, Pier-Emmanuel Tremblay, Nicola Pietro Gentile Fusillo, Mark A. Hollands, Boris T. Gänsicke, Paula Izquierdo, Silvia Toonen, Tim Cunningham, and Alberto Rebassa-Mansergas. Gaia white dwarfs within 40 pc II: the volume-limited Northern hemisphere sample. *Mon. Not. R. Astron. Soc.*, 499(2):1890–1908, December 2020. doi: 10.1093/mnras/staa2030.

D. B. McLaughlin. Some results of a spectrographic study of the Algol system. *Astrophys. J.*, 60:22–31, July 1924. doi: 10.1086/142826.

C. J. Moore, R. H. Cole, and C. P. L. Berry. Gravitational-wave sensitivity curves. *Classical and Quantum Gravity*, 32(1):015014, January 2015. doi: 10.1088/0264-9381/32/1/015014.

C. Moran, T. R. Marsh, and A. Bragaglia. A detached double degenerate with a 1.4-h orbital period. *Mon. Not. R. Astron. Soc.*, 288(2):538–544, June 1997. doi: 10.1093/mnras/288.2.538.

James Munday. Jamesmunday98/wd-bass: v1.0.0, May 2024. URL `https://doi.org/10.5281/zenodo.11188044`.

James Munday, T. R. Marsh, Mark Hollands, Ingrid Pelisoli, Danny Steeghs, Pasi Hakala, Elmé Breedt, Alex Brown, V. S. Dhillon, Martin J. Dyer, Matthew Green, Paul Kerry, S. P. Littlefair, Steven G. Parsons, Dave Sahman, Sorawit Somjit, Boonchoo Sukaum, and James Wild. Two decades of optical timing of the shortest-period binary star system HM Cancri. *Mon. Not. R. Astron. Soc.*, 518(4):5123–5139, February 2023. doi: 10.1093/mnras/stac3385.

James Munday, Ingrid Pelisoli, P. E. Tremblay, T. R. Marsh, Gijs Nelemans, Antoine Bédard, Silvia Toonen, Elmé Breedt, Tim Cunningham, Mairi W. O'Brien, and Harry Dawson. The DBL Survey I: discovery of 34 double-lined double white dwarf binaries. *Mon. Not. R. Astron. Soc.*, 532(2):2534–2556, August 2024. doi: 10.1093/mnras/stae1645.

James Munday, Ruediger Pakmor, Ingrid Pelisoli, David Jones, Snehalata Sahu, Pier-Emmanuel Tremblay, Abinaya Swaruba Rajamuthukumar, Gijs Nelemans, Mark Magee, Silvia Toonen, Antoine Bédard, and Tim Cunningham. A super-Chandrasekhar mass type Ia supernova progenitor at 49 pc set to detonate in 23 Gyr. *Nature Astronomy*, April 2025. doi: 10.1038/s41550-025-02528-4.

J. L. A. Nandez, N. Ivanova, and J. C. Jr Lombardi. Recombination energy in double white dwarf formation. *Mon. Not. R. Astron. Soc.*, 450:L39–L43, June 2015. doi: 10.1093/mnrasl/slv043.

R. Napiwotzki. LTE or NLTE for the analysis of hot white dwarf and subdwarf B stars? *Astron. Astrophys.*, 322:256–265, June 1997.

R. Napiwotzki, D. Koester, G. Nelemans, L. Yungelson, N. Christlieb, A. Renzini, D. Reimers, H. Drechsel, and B. Leibundgut. Binaries discovered by the SPY project. II. HE 1414-0848: A double degenerate with a mass close to the Chandrasekhar limit. *Astron. Astrophys.*, 386:957–963, May 2002. doi: 10.1051/0004-6361:20020361.

R. Napiwotzki, C. A. Karl, T. Lisker, S. Catalán, H. Drechsel, U. Heber, D. Homeier, D. Koester, B. Leibundgut, T. R. Marsh, S. Moehler, G. Nelemans, D. Reimers, A. Renzini, A. Ströer, and L. Yungelson. The ESO supernovae type Ia progenitor survey (SPY). The radial velocities of 643 DA white dwarfs. *Astron. Astrophys.*, 638:A131, June 2020. doi: 10.1051/0004-6361/201629648.

Ralf Napiwotzki. The galactic population of white dwarfs. In *Journal of Physics Conference Series*, volume 172 of *Journal of Physics Conference Series*, page 012004. IOP, June 2009. doi: 10.1088/1742-6596/172/1/012004.

Tim Naylor. An optimal extraction algorithm for imaging photometry. *Mon. Not. R. Astron. Soc.*, 296(2):339–346, May 1998. doi: 10.1046/j.1365-8711.1998.01314.x.

G. Nelemans, F. Verbunt, L. R. Yungelson, and Simon F. Portegies Zwart. Reconstructing the evolution of double helium white dwarfs: envelope loss without spiral-in. *Astron. Astrophys.*, 360:1011–1018, August 2000. doi: 10.48550/arXiv.astro-ph/0006216.

G. Nelemans, S. F. Portegies Zwart, F. Verbunt, and L. R. Yungelson. Population synthesis for double white dwarfs. II. Semi-detached systems: AM CVn stars. *Astron. Astrophys.*, 368:939–949, March 2001a. doi: 10.1051/0004-6361:20010049.

G. Nelemans, L. R. Yungelson, and S. F. Portegies Zwart. The gravitational wave signal from the Galactic disk population of binaries containing two compact objects. *Astron. Astrophys.*, 375:890–898, September 2001b. doi: 10.1051/0004-6361:20010683.

G. Nelemans, L. R. Yungelson, S. F. Portegies Zwart, and F. Verbunt. Population synthesis for double white dwarfs . I. Close detached systems. *Astron. Astrophys.*, 365:491–507, January 2001c. doi: 10.1051/0004-6361:20000147.

G. Nelemans, R. Napiwotzki, C. Karl, T. R. Marsh, B. Voss, G. Roelofs, R. G. Izzard, M. Montgomery, T. Reerink, N. Christlieb, and D. Reimers. Binaries discovered by the SPYproject. IV. Five single-lined DA double white dwarfs. *Astron. Astrophys.*, 440(3): 1087–1095, September 2005. doi: 10.1051/0004-6361:20053174.

Gijs Nelemans, Holly Preece, Karel Temmink, James Munday, and Onno Pols. The first phase of mass transfer in low-mass binaries: Neither stable nor a common envelope. *Astron. Astrophys.*, 700:A219, August 2025. doi: 10.1051/0004-6361/202555129.

P. Neunteufel, S. C. Yoon, and N. Langer. Models for the evolution of close binaries with He-star and white dwarf components towards Type Ia supernova explosions. *Astron. Astrophys.*, 589:A43, May 2016. doi: 10.1051/0004-6361/201527845.

Samaya Nissanke, Michele Vallisneri, Gijs Nelemans, and Thomas A. Prince. Gravitational-wave Emission from Compact Galactic Binaries. *Astrophys. J.*, 758(2): 131, October 2012. doi: 10.1088/0004-637X/758/2/131.

T. Noguchi, H. Maehara, and M. Kondo. A search for ultraviolet-excess objects. *Annals of the Tokyo Astronomical Observatory*, 18:55–70, January 1980.

K. Nomoto. Accreting white dwarf models for type I supernovae. I - Presupernova evolution and triggering mechanisms. *Astrophys. J.*, 253:798–810, February 1982. doi: 10.1086/159682.

K. Nomoto, S. Miyaji, D. Sugimoto, and K. Yokoi. Collapse of Accreting White Dwarf to Form a Neutron Star. In H. M. van Horn, V. Weidemann, and M. P. Savedoff, editors, *IAU Colloq. 53: White Dwarfs and Variable Degenerate Stars*, page 56, January 1979.

Ken'ichi Nomoto and Yoji Kondo. Conditions for Accretion-induced Collapse of White Dwarfs. *Astrophys. J. Lett.*, 367:L19, January 1991. doi: 10.1086/185922.

A. J. Norton, C. A. Haswell, and G. A. Wynn. Face-on, stream-fed intermediate polars: An alternative model for RX J1914.4+2456 and RX J0806.3+1527. *Astron. Astrophys.*, 419: 1025–1033, June 2004. doi: 10.1051/0004-6361:20035906.

Mairi W. O'Brien, P. E. Tremblay, N. P. Gentile Fusillo, M. A. Hollands, B. T. Gänsicke, D. Koester, I. Pelisoli, E. Cukanovaite, T. Cunningham, A. E. Doyle, A. Elms, J. Farihi, J. J. Hermes, J. Holberg, S. Jordan, B. L. Klein, S. J. Kleinman, C. J. Manser, D. De Martino, T. R. Marsh, J. McCleery, C. Melis, A. Nitta, S. G. Parsons, R. Raddi, A. Rebassa-Mansergas, M. R. Schreiber, R. Silvotti, D. Steeghs, O. Toloza, S. Toonen, S. Torres, A. J. Weinberger, and B. Zuckerman. Gaia white dwarfs within 40 pc - III. Spectroscopic observations of new candidates in the Southern hemisphere. *Mon. Not. R. Astron. Soc.*, 518(2):3055–3073, January 2023. doi: 10.1093/mnras/stac3303.

Mairi W. O'Brien, P. E. Tremblay, B. L. Klein, D. Koester, C. Melis, A. Bédard, E. Cukanovaite, T. Cunningham, A. E. Doyle, B. T. Gänsicke, N. P. Gentile Fusillo, M. A. Hollands, J. McCleery, I. Pelisoli, S. Toonen, A. J. Weinberger, and B. Zuckerman. The 40 pc sample of white dwarfs from Gaia. *Mon. Not. R. Astron. Soc.*, 527(3): 8687–8705, January 2024. doi: 10.1093/mnras/stad3773.

B. Paczyński. Evolutionary Processes in Close Binary Systems. *Annu. Rev. Astron. Astrophys.*, 9:183, January 1971. doi: 10.1146/annurev.aa.09.090171.001151.

R. Pakmor, S. Hachinger, F. K. Röpke, and W. Hillebrandt. Violent mergers of nearly equal-mass white dwarf as progenitors of subluminous Type Ia supernovae. *Astron. Astrophys.*, 528:A117, April 2011. doi: 10.1051/0004-6361/201015653.

R. Pakmor, P. Edelmann, F. K. Röpke, and W. Hillebrandt. Stellar GADGET: a smoothed particle hydrodynamics code for stellar astrophysics and its application to Type Ia supernovae from white dwarf mergers. *Mon. Not. R. Astron. Soc.*, 424(3):2222–2231, August 2012a. doi: 10.1111/j.1365-2966.2012.21383.x.

R. Pakmor, M. Kromer, S. Taubenberger, S. A. Sim, F. K. Röpke, and W. Hillebrandt. Normal Type Ia Supernovae from Violent Mergers of White Dwarf Binaries. *Astrophys. J. Lett.*, 747(1):L10, March 2012b. doi: 10.1088/2041-8205/747/1/L10.

R. Pakmor, M. Kromer, S. Taubenberger, and V. Springel. Helium-ignited Violent Mergers as a Unified Model for Normal and Rapidly Declining Type Ia Supernovae. *Astrophys. J. Lett.*, 770:L8, June 2013. doi: 10.1088/2041-8205/770/1/L8.

R. Pakmor, V. Springel, A. Bauer, P. Mocz, D. J. Munoz, S. T. Ohlmann, K. Schaal, and C. Zhu. Improving the convergence properties of the moving-mesh code AREPO. *Mon. Not. R. Astron. Soc.*, 455:1134–1143, January 2016. doi: 10.1093/mnras/stv2380.

R. Pakmor, Y. Zenati, H. B. Perets, and S. Toonen. Thermonuclear explosion of a massive hybrid HeCO white dwarf triggered by a He detonation on a companion. *Mon. Not. R. Astron. Soc.*, 503(4):4734–4747, June 2021. doi: 10.1093/mnras/stab686.

R. Pakmor, F. P. Callan, C. E. Collins, S. E. de Mink, A. Holas, W. E. Kerzendorf, M. Kromer, P. G. Neunteufel, John T. O'Brien, F. K. Röpke, A. J. Ruiter, I. R. Seitenzahl, Luke J. Shingles, S. A. Sim, and S. Taubenberger. On the fate of the secondary white dwarf in double-degenerate double-detonation Type Ia supernovae. *Mon. Not. R. Astron. Soc.*, 517(4):5260–5271, December 2022. doi: 10.1093/mnras/stac3107.

Rüdiger Pakmor, Markus Kromer, Friedrich K. Röpke, Stuart A. Sim, Ashley J. Ruiter, and Wolfgang Hillebrandt. Sub-luminous type Ia supernovae from the mergers of equal-mass white dwarfs with mass ~0.9M_{solar}. *Nature*, 463(7277):61–64, January 2010. doi: 10.1038/nature08642.

Rüdiger Pakmor, Ivo R. Seitenzahl, Ashley J. Ruiter, Stuart A. Sim, Friedrich K. Röpke, Stefan Taubenberger, Rebekka Bieri, and Stéphane Blondin. Type Ia supernova explosion models are inherently multidimensional. *Astron. Astrophys.*, 686:A227, June 2024. doi: 10.1051/0004-6361/202449637.

Tony Pan, Daniel Kasen, and Abraham Loeb. Pair-instability supernovae at the epoch of reionization. *Mon. Not. R. Astron. Soc.*, 422(3):2701–2711, May 2012. doi: 10.1111/j.1365-2966.2012.20837.x.

S. G. Parsons, B. T. Gänsicke, T. R. Marsh, R. P. Ashley, M. C. P. Bours, E. Breedt, M. R. Burleigh, C. M. Copperwheat, V. S. Dhillon, M. Green, L. K. Hardy, J. J. Hermes, P. Irawati, P. Kerry, S. P. Littlefair, M. J. McAllister, S. Rattanasoon, A. Rebassa-Mansergas, D. I. Sahman, and M. R. Schreiber. Testing the white dwarf mass-radius relationship with eclipsing binaries. *Mon. Not. R. Astron. Soc.*, 470(4):4473–4492, October 2017. doi: 10.1093/mnras/stx1522.

Steven G. Parsons, Alexander J. Brown, Stuart P. Littlefair, Vikram S. Dhillon, Thomas R. Marsh, J. J. Hermes, Alina G. Istrate, Elmé Breedt, Martin J. Dyer, Matthew J. Green, and David I. Sahman. A pulsating white dwarf in an eclipsing binary. *Nature Astronomy*, 4:690–696, March 2020. doi: 10.1038/s41550-020-1037-z.

E. M. Pauli, R. Napiwotzki, U. Heber, M. Altmann, and M. Odenkirchen. 3D kinematics of white dwarfs from the SPY project. II. *Astron. Astrophys.*, 447(1):173–184, February 2006. doi: 10.1051/0004-6361:20052730.

B. Paxton, L. Bildsten, A. Dotter, F. Herwig, P. Lesaffre, and F. Timmes. Modules for Experiments in Stellar Astrophysics (MESA). *Astrophys. J. Suppl. Ser.*, 192:3, jan 2011. doi: 10.1088/0067-0049/192/1/3.

B. Paxton, M. Cantiello, P. Arras, L. Bildsten, E. F. Brown, A. Dotter, C. Mankovich, M. H. Montgomery, D. Stello, F. X. Timmes, and R. Townsend. Modules for Experiments in Stellar Astrophysics (MESA): Planets, Oscillations, Rotation, and Massive Stars. *Astrophys. J. Suppl. Ser.*, 208:4, sep 2013. doi: 10.1088/0067-0049/208/1/4.

B. Paxton, P. Marchant, J. Schwab, E. B. Bauer, L. Bildsten, M. Cantiello, L. Dessart, R. Farmer, H. Hu, N. Langer, R. H. D. Townsend, D. M. Townsley, and F. X. Timmes. Modules for Experiments in Stellar Astrophysics (MESA): Binaries, Pulsations, and Explosions. *Astrophys. J. Suppl. Ser.*, 220:15, sep 2015. doi: 10.1088/0067-0049/220/1/15.

B. Paxton, J. Schwab, E. B. Bauer, L. Bildsten, S. Blinnikov, P. Duffell, R. Farmer, J. A. Goldberg, P. Marchant, E. Sorokina, A. Thoul, R. H. D. Townsend, and F. X. Timmes. Modules for Experiments in Stellar Astrophysics (MESA): Convective Boundaries, Element Diffusion, and Massive Star Explosions. *Astrophys. J. Suppl. Ser.*, 234:34, feb 2018. doi: 10.3847/1538-4365/aaa5a8.

Bill Paxton, R. Smolec, Josiah Schwab, A. Gautschy, Lars Bildsten, Matteo Cantiello, Aaron Dotter, R. Farmer, Jared A. Goldberg, Adam S. Jermyn, S. M. Kanbur, Pablo Marchant, Anne Thoul, Richard H. D. Townsend, William M. Wolf, Michael Zhang, and F. X. Timmes. Modules for Experiments in Stellar Astrophysics (MESA): Pulsating Variable Stars, Rotation, Convective Boundaries, and Energy Conservation. *Astrophys. J. Suppl. Ser.*, 243(1):10, Jul 2019. doi: 10.3847/1538-4365/ab2241.

Ingrid Pelisoli, T. R. Marsh, R. P. Ashley, Pasi Hakala, A. Aungwerojwit, K. Burdge, E. Breedt, A. J. Brown, K. Chanthorn, V. S. Dhillon, M. J. Dyer, M. J. Green, P. Kerry, S. P. Littlefair, S. G. Parsons, D. I. Sahman, J. F. Wild, and S. Yotthanathong. Optical detection of the rapidly spinning white dwarf in V1460 Her. *Mon. Not. R. Astron. Soc.*, 507(4):6132–6139, November 2021a. doi: 10.1093/mnras/stab2511.

Ingrid Pelisoli, P. Neunteufel, S. Geier, T. Kupfer, U. Heber, A. Irrgang, D. Schneider, A. Bastian, J. van Roestel, V. Schaffenroth, and B. N. Barlow. A hot subdwarf-white dwarf super-Chandrasekhar candidate supernova Ia progenitor. *Nature Astronomy*, 5: 1052–1061, July 2021b. doi: 10.1038/s41550-021-01413-0.

P. C. Peters. Gravitational Radiation and the Motion of Two Point Masses. *Physical Review*, 136(4B):1224–1232, November 1964. doi: 10.1103/PhysRev.136.B1224.

Anthony L. Piro. Tidal Interactions in Merging White Dwarf Binaries. *Astrophys. J. Lett.*, 740(2):L53, October 2011. doi: 10.1088/2041-8205/740/2/L53.

Anthony L. Piro. Inferring the Presence of Tides in Detached White Dwarf Binaries. *Astrophys. J. Lett.*, 885(1):L2, November 2019. doi: 10.3847/2041-8213/ab44c4.

Abigail Polin, Peter Nugent, and Daniel Kasen. Observational Predictions for Sub-Chandrasekhar Mass Explosions: Further Evidence for Multiple Progenitor Systems for Type Ia Supernovae. *Astrophys. J.*, 873(1):84, March 2019. doi: 10.3847/1538-4357/aafb6a.

P. G. Prada Moroni and O. Straniero. Very low-mass white dwarfs with a C-O core. *Astron. Astrophys.*, 507(3):1575–1583, December 2009. doi: 10.1051/0004-6361/200912847.

Adrian M. Price-Whelan. Gala: A python package for galactic dynamics. *The Journal of Open Source Software*, 2(18), oct 2017. doi: 10.21105/joss.00388. URL `https://doi.org/10.21105%2Fjoss.00388`.

J. Prochaska, Joseph Hennawi, Kyle Westfall, Ryan Cooke, Feige Wang, Tiffany Hsyu, Frederick Davies, Emanuele Farina, and Debora Pelliccia. PypeIt: The Python Spectroscopic Data Reduction Pipeline. *The Journal of Open Source Software*, 5(56):2308, December 2020. doi: 10.21105/joss.02308.

A. Prša and T. Zwitter. A Computational Guide to Physics of Eclipsing Binaries. I. Demonstrations and Perspectives. *Astrophys. J.*, 628(1):426–438, July 2005. doi: 10.1086/430591.

A. Prša, K. E. Conroy, M. Horvat, H. Pablo, A. Kochoska, S. Bloemen, J. Giammarco, K. M. Hambleton, and P. Degroote. Physics Of Eclipsing Binaries. II. Toward the Increased Model Fidelity. *Astrophys. J. Suppl. Ser.*, 227(2):29, December 2016. doi: 10.3847/1538-4365/227/2/29.

Deepak Raghavan, Harold A. McAlister, Todd J. Henry, David W. Latham, Geoffrey W. Marcy, Brian D. Mason, Douglas R. Gies, Russel J. White, and Theo A. ten Brummelaar. A Survey of Stellar Families: Multiplicity of Solar-type Stars. *Astrophys. J. Suppl. Ser.*, 190(1):1–42, September 2010. doi: 10.1088/0067-0049/190/1/1.

Gavin Ramsay and Pasi Hakala. RApid Temporal Survey (RATS) - I. Overview and first results. *Mon. Not. R. Astron. Soc.*, 360(1):314–321, June 2005. doi: 10.1111/j.1365-2966.2005.09035.x.

Gavin Ramsay, Pasi Hakala, and Mark Cropper. RX J0806+15: the shortest period binary? *Mon. Not. R. Astron. Soc.*, 332(1):L7–L10, May 2002. doi: 10.1046/j.1365-8711.2002.05471.x.

Gavin Ramsay, Catherine Brocksopp, Kinwah Wu, Bruce Slee, and Curtis J. Saxton. A search for electron cyclotron maser emission from compact binaries. *Mon. Not. R. Astron. Soc.*, 382(1):461–465, November 2007. doi: 10.1111/j.1365-2966.2007.12393.x.

S. Rappaport, F. Verbunt, and P. C. Joss. A new technique for calculations of binary stellar evolution application to magnetic braking. *Astrophys. J.*, 275:713–731, December 1983. doi: 10.1086/161569.

A. Rebassa-Mansergas, S. G. Parsons, E. García-Berro, B. T. Gänsicke, M. R. Schreiber, M. Rybicka, and D. Koester. Orbital periods and component masses of three double white dwarfs. *Mon. Not. R. Astron. Soc.*, 466(2):1575–1581, April 2017. doi: 10.1093/mnras/stw3155.

A. Rebassa-Mansergas, S. Toonen, V. Korol, and S. Torres. Where are the double-degenerate progenitors of Type Ia supernovae? *Mon. Not. R. Astron. Soc.*, 482(3):3656–3668, January 2019. doi: 10.1093/mnras/sty2965.

D. Reichart, M. Nysewander, J. Moran, J. Bartelme, M. Bayliss, A. Foster, J. C. Clemens, P. Price, C. Evans, J. Salmonson, S. Trammell, B. Carney, J. Keohane, and R. Gotwals. PROMPT: Panchromatic Robotic Optical Monitoring and Polarimetry Telescopes. *Nuovo Cimento C Geophysics Space Physics C*, 28(4):767, July 2005. doi: 10.1393/ncc/i2005-10149-6.

K. Reinsch, J. Steiper, and S. Dreizler. Spectral Analysis and Constraints on the Nature of the Ultra-Compact Binary RX J0806.3+1527. In R. Napiwotzki and M. R. Burleigh, editors, *15th European Workshop on White Dwarfs*, volume 372 of *Astronomical Society of the Pacific Conference Series*, page 419, September 2007.

Liangliang Ren, Chengyuan Li, Bo Ma, Sihao Cheng, Shun-Jia Huang, Baitian Tang, and Yi-ming Hu. A Systematic Search for Short-period Close White Dwarf Binary Candidates Based on Gaia EDR3 Catalog and Zwicky Transient Facility Data. *Astrophys. J. Suppl. Ser.*, 264(2):39, February 2023. doi: 10.3847/1538-4365/aca09e.

George R. Ricker, Joshua N. Winn, Roland Vanderspek, David W. Latham, Gáspár Á. Bakos, Jacob L. Bean, Zachory K. Berta-Thompson, Timothy M. Brown, Lars Buchhave, Nathaniel R. Butler, R. Paul Butler, William J. Chaplin, David Charbonneau, Jørgen Christensen-Dalsgaard, Mark Clampin, Drake Deming, John Doty, Nathan De

Lee, Courtney Dressing, Edward W. Dunham, Michael Endl, Francois Fressin, Jian Ge, Thomas Henning, Matthew J. Holman, Andrew W. Howard, Shigeru Ida, Jon M. Jenkins, Garrett Jernigan, John Asher Johnson, Lisa Kaltenegger, Nobuyuki Kawai, Hans Kjeldsen, Gregory Laughlin, Alan M. Levine, Douglas Lin, Jack J. Lissauer, Phillip MacQueen, Geoffrey Marcy, Peter R. McCullough, Timothy D. Morton, Norio Narita, Martin Paegert, Enric Palle, Francesco Pepe, Joshua Pepper, Andreas Quirrenbach, Stephen A. Rinehart, Dimitar Sasselov, Bun'ei Sato, Sara Seager, Alessandro Sozzetti, Keivan G. Stassun, Peter Sullivan, Andrew Szentgyorgyi, Guillermo Torres, Stephane Udry, and Joel Villasenor. Transiting Exoplanet Survey Satellite (TESS). *Journal of Astronomical Telescopes, Instruments, and Systems*, 1:014003, January 2015. doi: 10.1117/1.JATIS.1.1.014003.

H. Ritter. Turning on and off mass transfer in cataclysmic binaries. *Astron. Astrophys.*, 202: 93–100, aug 1988.

Edward L. Robinson and Allen W. Shafter. An Upper Limit to the Space Density of Short-period Noninteracting Binary White Dwarfs. *Astrophys. J.*, 322:296, November 1987. doi: 10.1086/165725.

Travis Robson, Neil J. Cornish, and Chang Liu. The construction and use of LISA sensitivity curves. *Classical and Quantum Gravity*, 36(10):105011, May 2019. doi: 10.1088/1361-6382/ab1101.

Gijs H. A. Roelofs, Arne Rau, Tom R. Marsh, Danny Steeghs, Paul J. Groot, and Gijs Nelemans. Spectroscopic Evidence for a 5.4 Minute Orbital Period in HM Cancri. *Astrophys. J. Lett.*, 711(2):L138–L142, March 2010. doi: 10.1088/2041-8205/711/2/L138.

A. D. Romero, F. Campos, and S. O. Kepler. The age-metallicity dependence for white dwarf stars. *Mon. Not. R. Astron. Soc.*, 450(4):3708–3723, July 2015. doi: 10.1093/mnras/stv848.

Alejandra D. Romero, S. O. Kepler, S. R. G. Joyce, G. R. Lauffer, and A. H. Córsico. The white dwarf mass-radius relation and its dependence on the hydrogen envelope. *Mon. Not. R. Astron. Soc.*, 484(2):2711–2724, April 2019. doi: 10.1093/mnras/stz160.

R. A. Rossiter. On the detection of an effect of rotation during eclipse in the velocity of the brigher component of beta Lyrae, and on the constancy of velocity of this system. *Astrophys. J.*, 60:15–21, July 1924. doi: 10.1086/142825.

Rex A. Saffer, James Liebert, and Edward W. Olszewski. Discovery of a Close Detached Binary DA White Dwarf System. *Astrophys. J.*, 334:947, November 1988. doi: 10.1086/166888.

Snehalata Sahu, Boris T. Gänsicke, Pier-Emmanuel Tremblay, Detlev Koester, J. J. Hermes, David J. Wilson, Odette Toloza, Matthew J. Hoskin, Jay Farihi, Christopher J. Manser, and Seth Redfield. An HST COS ultraviolet spectroscopic survey of 311 DA white dwarfs - I. Fundamental parameters and comparative studies. *Mon. Not. R. Astron. Soc.*, 526(4): 5800–5823, December 2023. doi: 10.1093/mnras/stad2663.

Sedighe Sajadian. Study of Self-lensing/Eclipsing Signals in Edge-on Double White-dwarf Systems. *Astron. J.*, 169(3):164, March 2025. doi: 10.3847/1538-3881/adab74.

Hugues Sana and Christopher J. Evans. The multiplicity of massive stars. In Coralie Neiner, Gregg Wade, Georges Meynet, and Geraldine Peters, editors, *Active OB Stars: Structure, Evolution, Mass Loss, and Critical Limits*, volume 272 of *IAU Symposium*, pages 474–485, July 2011. doi: 10.1017/S1743921311011124.

J. D. Scargle. Studies in astronomical time series analysis. II. Statistical aspects of spectral analysis of unevenly spaced data. *Astrophys. J.*, 263:835–853, December 1982. doi: 10.1086/160554.

V. Schaffenroth, I. Pelisoli, B. N. Barlow, S. Geier, and T. Kupfer. Hot subdwarfs in close binaries observed from space. I. Orbital, atmospheric, and absolute parameters, and the nature of their companions. *Astron. Astrophys.*, 666:A182, October 2022. doi: 10.1051/0004-6361/202244214.

Peter Scherbak and Jim Fuller. White dwarf binaries suggest a common envelope efficiency α 1/3. *Mon. Not. R. Astron. Soc.*, 518(3):3966–3984, January 2023. doi: 10.1093/mnras/stac3313.

M. R. Schreiber and B. T. Gänsicke. The age, life expectancy, and space density of Post Common Envelope Binaries. *Astron. Astrophys.*, 406:305–321, July 2003. doi: 10.1051/0004-6361:20030801.

Matthias R. Schreiber, Diogo Belloni, Boris T. Gänsicke, Steven G. Parsons, and Monica Zorotovic. The origin and evolution of magnetic white dwarfs in close binary stars. *Nature Astronomy*, 5:648–654, January 2021. doi: 10.1038/s41550-021-01346-8.

Matthias R. Schreiber, Diogo Belloni, Monica Zorotovic, Sarai Zapata, Boris T. Gänsicke, and Steven G. Parsons. Magnetic dynamos in white dwarfs - III. Explaining the occurrence of strong magnetic fields in close double white dwarfs. *Mon. Not. R. Astron. Soc.*, 513(2):3090–3103, June 2022. doi: 10.1093/mnras/stac1076.

Josiah Schwab. Hot subdwarfs formed from the merger of two He white dwarfs. *Mon. Not. R. Astron. Soc.*, 476(4):5303–5311, June 2018. doi: 10.1093/mnras/sty586.

Josiah Schwab. Evolutionary Models for R Coronae Borealis Stars. *Astrophys. J.*, 885(1): 27, November 2019. doi: 10.3847/1538-4357/ab425d.

Josiah Schwab, Ken J. Shen, Eliot Quataert, Marius Dan, and Stephan Rosswog. The viscous evolution of white dwarf merger remnants. *Mon. Not. R. Astron. Soc.*, 427(1): 190–203, November 2012. doi: 10.1111/j.1365-2966.2012.21993.x.

Ivo R. Seitenzahl, Casey A. Meakin, Dean M. Townsley, Don Q. Lamb, and James W. Truran. Spontaneous Initiation of Detonations in White Dwarf Environments: Determination of Critical Sizes. *Astrophys. J.*, 696(1):515–527, May 2009. doi: 10.1088/0004-637X/696/1/515.

Ken J. Shen. Every Interacting Double White Dwarf Binary May Merge. *Astrophys. J. Lett.*, 805(1):L6, May 2015. doi: 10.1088/2041-8205/805/1/L6.

Ken J. Shen and Lars Bildsten. The Ignition of Carbon Detonations via Converging Shock Waves in White Dwarfs. *Astrophys. J.*, 785(1):61, April 2014. doi: 10.1088/0004-637X/785/1/61.

Ken J. Shen, Lars Bildsten, Daniel Kasen, and Eliot Quataert. The Long-term Evolution of Double White Dwarf Mergers. *Astrophys. J.*, 748(1):35, March 2012. doi: 10.1088/0004-637X/748/1/35.

Ken J. Shen, Douglas Boubert, Boris T. Gänsicke, Saurabh W. Jha, Jennifer E. Andrews, Laura Chomiuk, Ryan J. Foley, Morgan Fraser, Mariusz Gromadzki, James Guillochon, Marissa M. Kotze, Kate Maguire, Matthew R. Siebert, Nathan Smith, Jay Strader, Carles Badenes, Wolfgang E. Kerzendorf, Detlev Koester, Markus Kromer, Broxton Miles, Rüdiger Pakmor, Josiah Schwab, Odette Toloza, Silvia Toonen, Dean M. Townsley, and Brian J. Williams. Three Hypervelocity White Dwarfs in Gaia DR2: Evidence for Dynamically Driven Double-degenerate Double-detonation Type Ia Supernovae. *Astrophys. J.*, 865(1):15, September 2018a. doi: 10.3847/1538-4357/aad55b.

Ken J. Shen, Daniel Kasen, Broxton J. Miles, and Dean M. Townsley. Sub-Chandrasekhar-mass White Dwarf Detonations Revisited. *Astrophys. J.*, 854(1):52, February 2018b. doi: 10.3847/1538-4357/aaa8de.

Ken J. Shen, Samuel J. Boos, Dean M. Townsley, and Daniel Kasen. Multidimensional Radiative Transfer Calculations of Double Detonations of Sub-Chandrasekhar-mass White Dwarfs. *Astrophys. J.*, 922(1):68, November 2021. doi: 10.3847/1538-4357/ac2304.

Ken J. Shen, Simon Blouin, and Katelyn Breivik. The Q Branch Cooling Anomaly Can Be Explained by Mergers of White Dwarfs and Subgiant Stars. *Astrophys. J. Lett.*, 955(2): L33, October 2023. doi: 10.3847/2041-8213/acf57b.

Ken J. Shen, Samuel J. Boos, and Dean M. Townsley. Almost All Carbon/Oxygen White Dwarfs Can Host Double Detonations. *Astrophys. J.*, 975(1):127, November 2024. doi: 10.3847/1538-4357/ad7379.

I. S. Shklovskii. Possible Causes of the Secular Increase in Pulsar Periods. *Soviet Astron.*, 13:562, February 1970.

S. A. Sim. Multidimensional simulations of radiative transfer in Type Ia supernovae. *Mon. Not. R. Astron. Soc.*, 375(1):154–162, February 2007. doi: 10.1111/j.1365-2966.2006.11271.x.

S. A. Sim, F. K. Röpke, W. Hillebrandt, M. Kromer, R. Pakmor, M. Fink, A. J. Ruiter, and I. R. Seitenzahl. Detonations in Sub-Chandrasekhar-mass C+O White Dwarfs. *Astrophys. J. Lett.*, 714(1):L52–L57, May 2010. doi: 10.1088/2041-8205/714/1/L52.

Edward M. Sion, Jan-Erik Solheim, Paula Szkody, Boris T. Gaensicke, and Steve B. Howell. The First Direct Spectroscopic Detection of a White Dwarf Primary in an AM CVn System. *Astrophys. J. Lett.*, 636(2):L125–L128, January 2006. doi: 10.1086/500085.

Noam Soker. Supernovae in 2023 (review): possible breakthroughs by late observations. *The Open Journal of Astrophysics*, 7:31, April 2024. doi: 10.33232/001c.117147.

J. E. Solheim. AM CVn Stars: Status and Challenges. *Publ. Astron. Soc. Pac.*, 122(896): 1133, October 2010. doi: 10.1086/656680.

V. Springel. E pur si muove: Galilean-invariant cosmological hydrodynamical simulations on a moving mesh. *Mon. Not. R. Astron. Soc.*, 401:791–851, January 2010. doi: 10.1111/j.1365-2966.2009.15715.x.

Seppe Staelens and Gijs Nelemans. Likelihood of white dwarf binaries to dominate the astrophysical gravitational wave background in the mHz band. *Astron. Astrophys.*, 683: A139, March 2024. doi: 10.1051/0004-6361/202348429.

Justin D. R. Steinfadt, David L. Kaplan, Avi Shporer, Lars Bildsten, and Steve B. Howell. Discovery of the Eclipsing Detached Double White Dwarf Binary NLTT 11748. *Astrophys. J. Lett.*, 716(2):L146–L151, June 2010. doi: 10.1088/2041-8205/716/2/L146.

Tod E. Strohmayer. Precision X-Ray Timing of RX J0806.3+1527 with Chandra: Evidence for Gravitational Radiation from an Ultracompact Binary. *Astrophys. J.*, 627(2):920–925, July 2005. doi: 10.1086/430439.

Tod E. Strohmayer. High-Resolution X-Ray Spectroscopy of RX J0806.3+1527 with Chandra. *Astrophys. J. Lett.*, 679(2):L109, June 2008. doi: 10.1086/589439.

Tod E. Strohmayer. A Real-time View of Orbital Evolution in HM Cancri. *Astrophys. J. Lett.*, 912(1):L8, May 2021. doi: 10.3847/2041-8213/abf3cc.

K. D. Temmink, O. R. Pols, S. Justham, A. G. Istrate, and S. Toonen. Coping with loss. Stability of mass transfer from post-main-sequence donor stars. *Astron. Astrophys.*, 669:A45, January 2023. doi: 10.1051/0004-6361/202244137.

J. L. Tonry, L. Denneau, A. N. Heinze, B. Stalder, K. W. Smith, S. J. Smartt, C. W. Stubbs, H. J. Weiland, and A. Rest. ATLAS: A High-cadence All-sky Survey System. *Publ. Astron. Soc. Pac.*, 130(988):064505, June 2018. doi: 10.1088/1538-3873/aabadf.

S. Toonen and G. Nelemans. The effect of common-envelope evolution on the visible population of post-common-envelope binaries. *Astron. Astrophys.*, 557:A87, September 2013. doi: 10.1051/0004-6361/201321753.

S. Toonen, G. Nelemans, and S. Portegies Zwart. Supernova Type Ia progenitors from merging double white dwarfs. Using a new population synthesis model. *Astron. Astrophys.*, 546:A70, October 2012. doi: 10.1051/0004-6361/201218966.

S. Toonen, M. Hollands, B. T. Gänsicke, and T. Boekholt. The binarity of the local white dwarf population. *Astron. Astrophys.*, 602:A16, June 2017. doi: 10.1051/0004-6361/201629978.

S. Toonen, H. B. Perets, and A. S. Hamers. Rate of WD-WD head-on collisions in isolated triples is too low to explain standard type Ia supernovae. *Astron. Astrophys.*, 610:A22, February 2018. doi: 10.1051/0004-6361/201731874.

A. Toubiana, N. Karnesis, A. Lamberts, and M. C. Miller. The interacting double white dwarf population with LISA: Stochastic foreground and resolved sources. *Astron. Astrophys.*, 692:A165, December 2024. doi: 10.1051/0004-6361/202450174.

P. E. Tremblay and P. Bergeron. Spectroscopic Analysis of DA White Dwarfs: Stark Broadening of Hydrogen Lines Including Nonideal Effects. *Astrophys. J.*, 696(2):1755–1770, May 2009. doi: 10.1088/0004-637X/696/2/1755.

P. E. Tremblay, P. Bergeron, and A. Gianninas. An Improved Spectroscopic Analysis of DA White Dwarfs from the Sloan Digital Sky Survey Data Release 4. *Astrophys. J.*, 730 (2):128, April 2011. doi: 10.1088/0004-637X/730/2/128.

P. E. Tremblay, H. G. Ludwig, M. Steffen, and B. Freytag. Spectroscopic analysis of DA white dwarfs with 3D model atmospheres. *Astron. Astrophys.*, 559:A104, November 2013a. doi: 10.1051/0004-6361/201322318.

P. E. Tremblay, H. G. Ludwig, M. Steffen, and B. Freytag. Pure-hydrogen 3D model atmospheres of cool white dwarfs. *Astron. Astrophys.*, 552:A13, April 2013b. doi: 10.1051/0004-6361/201220813.

P. E. Tremblay, A. Gianninas, M. Kilic, H. G. Ludwig, M. Steffen, B. Freytag, and J. J. Hermes. 3D Model Atmospheres for Extremely Low-mass White Dwarfs. *Astrophys. J.*, 809(2):148, August 2015. doi: 10.1088/0004-637X/809/2/148.

P. E. Tremblay, J. Cummings, J. S. Kalirai, B. T. Gänsicke, N. Gentile-Fusillo, and R. Raddi. The field white dwarf mass distribution. *Mon. Not. R. Astron. Soc.*, 461(2):2100–2114, September 2016. doi: 10.1093/mnras/stw1447.

P. E. Tremblay, E. Cukanovaite, N. P. Gentile Fusillo, T. Cunningham, and M. A. Hollands. Fundamental parameter accuracy of DA and DB white dwarfs in Gaia Data Release 2. *Mon. Not. R. Astron. Soc.*, 482(4):5222–5232, February 2019. doi: 10.1093/mnras/sty3067.

M. V. van der Sluys, F. Verbunt, and O. R. Pols. Modelling the formation of double white dwarfs. *Astron. Astrophys.*, 460(1):209–228, December 2006. doi: 10.1051/0004-6361:20065066.

J. van Roestel, T. Kupfer, M. J. Green, T. L. S. Wong, L. Bildsten, K. Burdge, T. Prince, T. R. Marsh, P. Szkody, C. Fremling, M. J. Graham, V. S. Dhillon, S. P. Littlefair, E. C. Bellm, M. Coughlin, D. A. Duev, D. A. Goldstein, R. R. Laher, B. Rusholme, R. Riddle, R. Dekany, and S. R. Kulkarni. Discovery and characterization of five new eclipsing AM CVn systems. *Mon. Not. R. Astron. Soc.*, 512(4):5440–5461, June 2022. doi: 10.1093/mnras/stab2421.

Jan van Roestel, Leah Creter, Thomas Kupfer, Paula Szkody, Jim Fuller, Matthew J. Green, R. Michael Rich, John Sepikas, Kevin Burdge, Ilaria Caiazzo, Przemek Mróz, Thomas A. Prince, Dmitry A. Duev, Matthew J. Graham, David L. Shupe, Russ R. Laher, Ashish A. Mahabal, and Frank J. Masci. A Systematic Search for Outbursting AM CVn Systems with the Zwicky Transient Facility. *Astron. J.*, 162(3):113, September 2021. doi: 10.3847/1538-3881/ac0622.

Jacob T. VanderPlas and Željko Ivezić. Periodograms for Multiband Astronomical Time Series. *Astrophys. J.*, 812(1):18, October 2015. doi: 10.1088/0004-637X/812/1/18.

S. Vennes, J. R. Thorstensen, A. Kawka, P. Németh, J. N. Skinner, A. Pigulski, Ste&şacute, M. licki, Z. Kołaczkowski, and P. Śródka. Discovery of a Bright, Extremely Low Mass White Dwarf in a Close Double Degenerate System. *Astrophys. J. Lett.*, 737(1):L16, August 2011. doi: 10.1088/2041-8205/737/1/L16.

F. Verbunt and P. Hut. Magnetic braking and tidal energy dissipation in close binaries. *Astron. Astrophys.*, 127(1):161–163, October 1983.

F. Verbunt and C. Zwaan. Magnetic braking in low-mass X-ray binaries. *Astron. Astrophys.*, 100:L7–L9, July 1981.

Frank Verbunt and Saul Rappaport. Mass Transfer Instabilities Due to Angular Momentum Flows in Close Binaries. *Astrophys. J.*, 332:193, September 1988. doi: 10.1086/166645.

Olivier Vincent, P. Bergeron, and P. Dufour. Data-driven selection and spectral classification of white dwarf stars. *Mon. Not. R. Astron. Soc.*, 521(1):760–771, May 2023. doi: 10.1093/mnras/stad580.

T. Wagg, K. Breivik, and S. E. de Mink. LEGWORK: A Python Package for Computing the Evolution and Detectability of Stellar-origin Gravitational-wave Sources with Space-based Detectors. *Astrophys. J. Suppl. Ser.*, 260(2):52, June 2022a. doi: 10.3847/1538-4365/ac5c52.

Tom Wagg, Katelyn Breivik, and Selma de Mink. LEGWORK: A python package for computing the evolution and detectability of stellar-origin gravitational-wave sources with space-based detectors. *The Journal of Open Source Software*, 7(70):3998, February 2022b. doi: 10.21105/joss.03998.

R. F. Webbink. Double white dwarfs as progenitors of R Coronae Borealis stars and type I supernovae. *Astrophys. J.*, 277:355–360, February 1984. doi: 10.1086/161701.

Rainer Weinberger, Volker Springel, and Rüdiger Pakmor. The AREPO Public Code Release. *Astrophys. J. Suppl. Ser.*, 248(2):32, June 2020. doi: 10.3847/1538-4365/ab908c.

Jonathan B. Whitmore and Michael T. Murphy. Impact of instrumental systematic errors on fine-structure constant measurements with quasar spectra. *Mon. Not. R. Astron. Soc.*, 447(1):446–462, February 2015. doi: 10.1093/mnras/stu2420.

Jonathan B. Whitmore, Michael T. Murphy, and Kim Griest. Wavelength Calibration of the VLT-UVES Spectrograph. *Astrophys. J.*, 723(1):89–99, November 2010. doi: 10.1088/0004-637X/723/1/89.

Robert E. Wilson and Edward J. Devinney. Realization of Accurate Close-Binary Light Curves: Application to MR Cygni. *Astrophys. J.*, 166:605, June 1971. doi: 10.1086/150986.

Christian Wolf, Christopher A. Onken, Lance C. Luvaul, Brian P. Schmidt, Michael S. Bessell, Seo-Won Chang, Gary S. Da Costa, Dougal Mackey, Tony Martin-Jones, Simon J. Murphy, Tim Preston, Richard A. Scalzo, Li Shao, Jon Smillie, Patrick Tisserand, Marc C. White, and Fang Yuan. SkyMapper Southern Survey: First Data Release (DR1). *Publ. Astron. Soc. Aust.*, 35:e010, February 2018. doi: 10.1017/pasa.2018.5.

Tin Long Sunny Wong and Lars Bildsten. Mass Transfer and Stellar Evolution of the White Dwarfs in AM CVn Binaries. *Astrophys. J.*, 923(1):125, December 2021. doi: 10.3847/1538-4357/ac2b2a.

T. E. Woods, N. Ivanova, M. V. van der Sluys, and S. Chaichenets. On the Formation of Double White Dwarfs through Stable Mass Transfer and a Common Envelope. *Astrophys. J.*, 744(1):12, January 2012. doi: 10.1088/0004-637X/744/1/12.

Kinwah Wu, Mark Cropper, Gavin Ramsay, and Kazuhiro Sekiguchi. An electrically powered binary star? *Mon. Not. R. Astron. Soc.*, 331(1):221–227, March 2002. doi: 10.1046/j.1365-8711.2002.05190.x.

Natsuko Yamaguchi, Kareem El-Badry, Jim Fuller, David W. Latham, Phillip A. Cargile, Tsevi Mazeh, Sahar Shahaf, Allyson Bieryla, Lars A. Buchhave, and Melissa Hobson. Wide post-common envelope binaries containing ultramassive white dwarfs: evidence for efficient envelope ejection in massive asymptotic giant branch stars. *Mon. Not. R. Astron. Soc.*, 527(4):11719–11739, February 2024. doi: 10.1093/mnras/stad4005.

Bo-Bing Ye, Xuefeng Zhang, Ming-Yue Zhou, Yan Wang, Hui-Min Yuan, Defeng Gu, Yanwei Ding, Jinxiu Zhang, Jianwei Mei, and Jun Luo. Optimizing orbits for TianQin. *International Journal of Modern Physics D*, 28(9):1950121, January 2019. doi: 10.1142/S0218271819501219.

Derek York. Least squares fitting of a straight line with correlated errors. *Earth and Planetary Science Letters*, 5:320–324, January 1968. doi: 10.1016/S0012-821X(68)80059-7.

J. P. Zahn. Tidal friction in close binary systems. *Astron. Astrophys.*, 57:383–394, May 1977.

Yossef Zenati, Silvia Toonen, and Hagai B. Perets. Formation and evolution of hybrid He-CO white dwarfs and their properties. *Mon. Not. R. Astron. Soc.*, 482(1):1135–1142, January 2019. doi: 10.1093/mnras/sty2723.

Xianfei Zhang and C. Simon Jeffery. Evolutionary models for double helium white dwarf mergers and the formation of helium-rich hot subdwarfs. *Mon. Not. R. Astron. Soc.*, 419 (1):452–464, January 2012. doi: 10.1111/j.1365-2966.2011.19711.x.

B. Zuckerman, D. Koester, I. N. Reid, and M. Hünsch. Metal Lines in DA White Dwarfs. *Astrophys. J.*, 596(1):477–495, October 2003. doi: 10.1086/377492.